

**TELEOPERATED MRI-GUIDED PROSTATE NEEDLE
PLACEMENT**

by

Reza Seifabadi

A thesis submitted to the Department of Mechanical and Material Engineering

In conformity with the requirements for

the degree of Doctor of Philosophy

Queen's University

Kingston, Ontario, Canada

(May, 2013)

Copyright ©Reza Seifabadi, 2013

Abstract

Most robotic systems reported for MRI-guided prostate interventions use manual needle insertion, based on a previously acquired image, which requires withdrawing the patient from the scanner multiple times during the procedure. This makes the intervention longer, more expensive and elongating the discomfort to patient and, most importantly, less accurate due to the virtually inevitable motion of the target. As a remedy, automated needle placement methods were proposed, putting human supervision out of the control loop. This thesis presents the development of enabling technologies for human-operated in-room master-slave needle placement under real-time MRI guidance, while the patient is kept in the scanner and having the process of needle placement under continuous control of the physician. The feasibility of teleoperated needle insertion was demonstrated by developing a 1-DOF (degree of freedom) MRI-compatible master-slave system, which was integrated with a 4-DOF robot for transperineal prostate biopsy and brachytherapy. An accuracy study was conducted on a robotic system for MRI-guided prostate needle placement. Different error sources were identified and quantified. This study concluded that errors occurring during needle insertion have the most significant contribution to needle placement error. In order to compensate for these errors, teleoperated needle steering under real-time MRI guidance was proposed. A 2-DOF piezo-actuated MRI-compatible needle steering module was developed and integrated with the aforementioned 4-DOF transperineal robot, yielding a fully actuated 6-DOF (x, y, z, yaw, pitch, roll) robotic platform for MRI-guided prostate interventions. A novel MRI-compatible master robot was also developed to enable teleoperated needle steering inside the MRI room. MRI-compatible controller hardware and software were developed. A novel MRI-compatible force/torque sensor was devised using Fiber Bragg Grating for force measurement in MRI room. Phantom experiments proved the feasibility

of teleoperated needle steering under real-time MRI guidance. A system was also developed for real-time 3D shape tracking of a bevel-tip needle with Fiber Bragg Grating sensors embedded along the needle shaft. The needle profile was overlaid on the real-time MR image, yielding real time navigation with accuracy better than 0.5 mm. The experimental system is presently being refitted for clinical safety and feasibility trials on real patients.

Co-Authorship

This dissertation is presented in a manuscript format. The manuscript chapters are based on journal paper publications that are either accepted or to-be-submitted:

Chapter 2: R. Seifabadi, I. Iordachita, and G. Fichtinger “Robot-assisted MRI-guided Prostate Needle Placement: Need for Teleoperated Needle Steering,” to be submitted to *IEEE Transactions on Biomedical Engineering (TBME)*.

Chapter 3: R. Seifabadi, S. E. Song, A. Krieger, N. B. Cho, J. Tokuda, G. Fichtinger and I. Iordachita, "Robotic system for MRI-guided prostate biopsy: feasibility of teleoperated needle insertion and ex vivo phantom study," *International Journal of Computer Assisted Radiology and Surgery*, vol. 7, pp. 181-190, 2012.

Chapter 4: R. Seifabadi, N. B. J. Cho, S. E. Song, J. Tokuda, N. Hata, C. M. Tempany, G. Fichtinger and I. Iordachita, "Accuracy study of a robotic system for MRI-guided prostate needle placement," *The International Journal of Medical Robotics and Computer Assisted Surgery*, Published online: 8 JUN 2012, DOI: 10.1002/rcs.1440.

Chapter 5: R. Seifabadi, I. Iordachita, and G. Fichtinger “Teleoperated needle steering under real-time MRI guidance for prostate interventions: a feasibility study”, to be submitted to the *IEEE/ASME Transactions on Mechatronics*.

Chapter 6: R. Seifabadi, E. Escobar Gomez, F. Aalamifar, G. Fichtinger, and I. Iordachita “Real-time tracking of a bevel-tip needle with varying insertion depth: toward teleoperated MRI-guided needle steering”, to be submitted to the *IEEE Transactions on Biomedical Engineering (TBME)*.

The work presented in this dissertation is my own work, with co-authors acting primarily in an advisory capacity or assistance during experiment. I. Iordachita and G. Fichtinger were my advisors. The other co-authors have made the following contributions:

Chapter 3: S. E. Song, N. B. Cho, and J. Tokuda assisted during the MRI phantom experiment. I adapted A. Krieger's needle insertion module and controller hardware for my system.

Chapter 4: N. B. J. Cho, S. E. Song, J. Tokuda assisted during the MRI phantom experiment. N. Hata and C. M. Tempany were co-PIs of the project.

Chapter 6: E. Escobar Gomez performed the computer simulation for finding optimum locations of the FBG sensors based on the mathematical model and methodology that I developed. He also prepared the calibration setup, modified an existing MATLAB code to get data from interrogator, and performed the calibration. F. Aalamifar implemented visualization of the needle in 3D slicer.

Acknowledgements

I would like to express my sincere gratitude to my advisor professor Gabor Fichtinger for inviting me to the Laboratory for Percutaneous Surgery (Perk Lab), continuously supporting and advising me over the years, and for giving me the opportunity of going to the Johns Hopkins University as a visiting scholar. I would like also to sincerely thank Professor Iulian Iordachita, my mentor at the Johns Hopkins University, for his enormous technical contributions to my thesis, his guidance, understanding, patience, and friendship during the three years of my work at the Johns Hopkins University.

I would like to thank Professors Russell Taylor and Louis Whitcomb for hosting me at the Laboratory of Computational Sensing and Robotics (LCSR) during my long stay at the Johns Hopkins University. I would also like to sincerely thank all LCSR faculty and students.

It is my pleasure to thank those who made this thesis possible: Dr. Reza Monfaredi, with whom I developed the force sensor, my wife Fereshteh Aalamifar, who developed the 3D visualization of the smart needle and was a key person during most of the experiments reported in this thesis, and Esteban Escobar Gomez, with whom I developed the smart needle. I would also thank Nathan Cho, my colleague at LCSR, and my collaborators from Harvard Medical School: Professors Clare Tempany and Nobuhiko Hata, and Drs. Junichi Tokuda and Sam Song. I would like to also thank Professor Kevin Cleary and Dr. Stanley Fricke from Children's National Medical Center, Washington DC, for providing access to their MRI scanners and for the technical support for my experiments. I also thank Mr. Hugh Wall from the Johns Hopkins Hospital for the technical assistance during MRI experiments. I would sincerely thank my colleagues, Professor Gregory Fischer and Dr. Hao Su from Worcester Polytechnique Institute for their technical support and encouragement during the years of my research.

I would like to thank all my labmates at Johns Hopkins, especially Dr. Hassan Rivaz, Berk Gonenc, Xingchi He, Dr. Sohrab Eslami, Ehsan Azimi, Marcin Balicki, Kevin Olds, Ryan Hearty, Dr. Amy Blank, and Dr. Ehsan Dehghan.

I would like to thank all my labmates and friends at Queen's, especially Paweena U-Thainual, Dr. Andras Lasso, Dr. Tamas Ungi, Hossein Sadjadi, Yashar Madjidi, Helen Xu, Hadi Tadayyon, Siavash Khallaghi, Narges Ahmidi, Vahid Nazari, Sasan Taghizadeh, Farhad Imani, Hamed Sadeghi, and Dr. Mohammad Omidyeganeh.

I would like to thank my loving parents who gave me the chance to come to Canada for higher education and my brothers and my sister for their continuous encouragement and support.

Last but not the least, my wholehearted gratitude goes to my wife Fereshteh Aalamifar, who not only was my colleague and contributed to this dissertation, but also unfailingly supported me by love during this long journey. Without her, this dissertation could not be possible.

Dedication

To my dearest wife and my loving parents ...

تقدیم به همسر عزیزم و پدر و مادر عزیز تر از جانم ...

Statement of Originality

I hereby certify that all of the work described within this thesis is the original work of the author. Any published (or unpublished) ideas and/or techniques from the work of others are fully acknowledged in accordance with the standard referencing practices.

(Reza Seifabadi)

(May, 2013)

Table of Contents

Abstract	ii
Co-Authorship	iv
Acknowledgements.....	vi
Statement of Originality.....	ix
Chapter 1 Introduction	1
1.1 Motivation.....	1
1.2 Objectives	4
1.3 Contributions	4
1.4 Thesis outline.....	6
References.....	6
Chapter 2 Robot-assisted MRI-guided prostate biopsy and brachytherapy: need for teleoperated needle steering	10
2.1 Introduction.....	10
2.2 Engineering challenges of MRI-compatible robotics	15
2.2.1 MRI-compatibility	15
2.2.2 Confined workspace.....	18
2.2.3 RF heating.....	19
2.2.4 Electromagnetic interference	19
2.2.5 Robot-to-image registration	19
2.3 Manual devices used for prostate biopsy and brachytherapy.....	21
2.4 Computer-controlled robotic systems for prostate biopsy and brachytherapy.....	23
2.4.1 Transrectal access	23
2.4.2 Transperineal access	25
2.4.3 Transgluteal access	28
2.5 Case for teleoperated needle steering under MRI guidance.....	30
2.5.1 Error sources in MRI-guided robotic needle placement	30
2.5.2 Methods of compensation for error caused during needle insertion	31
2.5.3 Different methods of needle steering	32
2.5.4 Teleoperated approach for MRI-guided bevel-tip needle steering.....	33
2.5.5 Previous work on teleoperated needle insertion under MRI guidance.....	34

2.6 Enabling technologies for teleoperated needle steering under MRI guidance.....	35
2.6.1 MRI-compatible haptic devices	35
2.6.2 MRI-compatible force sensor.....	36
2.6.3 Real-time target tracking.....	38
2.6.4 Real-time needle tracking	38
2.7 Conclusions.....	39
References.....	39
Chapter 3 Robotic system for MRI-guided prostate biopsy: feasibility of teleoperated needle insertion and ex vivo phantom study	59
3.1 Introduction.....	59
3.2 System design	64
3.2.1 System components	64
3.2.2 Robot kinematics	66
3.2.3 Variable workspace.....	67
3.2.4 Sterilization	68
3.3 Needle driver module design	69
3.3.1 Needle driver (slave robot)	71
3.3.2 Master device	74
3.3.3 Needle driver control unit	74
3.4 Experiments and results	75
3.4.1 Ex vivo accuracy evaluation with manual insertion	75
3.4.2 Position tracking evaluation of the master-slave needle driver.....	78
3.5 Discussion.....	78
3.6 Conclusions and future work	79
References.....	80
Chapter 4 Accuracy study of a robotic system for MRI-guided prostate needle placement.....	87
4.1 Introduction.....	88
4.2 Error sources and components	90
4.2.1 Classification of error sources.....	90
4.2.2 Identification of robotic system error components	92
4.3 Methods and materials	93
4.3.1 Z-frame registration accuracy evaluation	94

4.3.2 Z-frame to robot registration accuracy evaluation	95
4.3.3 Needle artifact shift evaluation	95
4.3.4 The manipulator's accuracy	96
4.3.5 Total error of the robotic system.....	103
4.3.6 Overall needle placement error	105
4.4 Results.....	106
4.4.1 Error components of the robotic system	106
4.4.2 Total error of robotic system.....	108
4.4.3 Overall needle placement error	109
4.4.4 Due-to-insertion inaccuracy	109
4.5 Discussions	110
4.6 Conclusions.....	111
References.....	112
Chapter 5 Teleoperated needle steering under real-time MRI guidance for prostate interventions: a feasibility study	118
5.1 Introduction.....	119
5.1.1 Previous work on teleoperated needle insertion under MRI guidance.....	121
5.1.2 Case for teleoperated needle steering under MRI guidance.....	122
5.2 System architecture and components.....	125
5.2.1 Base robot system architecture and components	126
5.2.2 Teleoperated needle steering system architecture and components.....	129
5.3 Slave robot	131
5.3.1 Motors selection.....	132
5.3.2 Linear stage	133
5.3.3 Rotary stage	134
5.3.4 Needle	134
5.3.5 Power analysis	134
5.4 Master robot.....	135
5.4.1 Linear stage.....	136
5.4.2 Rotary stage	140
5.5 Controller	141
5.5.1 Controller hardware	141

5.5.2 Controller architecture	143
5.5.3 Controller software	144
5.6 MRI-Compatible force sensor.....	145
5.7 Experiments and results	146
5.7.1 MRI-compatibility	146
5.7.2 System functionality	150
5.7.3 Feasibility of teleoperated needle steering in phantom trial on bench-top setup	152
5.7.4 Feasibility of teleoperated needle steering under real-time MRI guidance	155
5.8 Conclusions and future work	157
References.....	159
Chapter 6 Needle tracking with embedded Fiber Bragg Gratings	167
6.1 Introduction.....	167
6.2 Design considerations	170
6.3 Tip position estimation	171
6.4 Sensor localization	173
6.4.1 Modeling	174
6.4.2 Optimization	176
6.5 Fabrication	180
6.6 Calibration	182
6.7 Preliminary evaluation with one inflection point.....	184
6.8 Real-time visualization	187
6.9 Conclusions and future work	189
References.....	189
Chapter 7 Conclusions and future work.....	193
7.1 Conclusions.....	193
7.2 Future work.....	195
References.....	197
Appendix A.....	198
A.1 Introduction.....	199
A.2 Sensor design	204
A.2.1 Mechanical design.....	204
A.2.2 Finite element analysis.....	209

A.3 Sensor fabrication and FBG installation	210
A.4 Sensor calibration and results	212
A.5 Conclusions.....	214
References	215
Appendix B.....	218
B.1 Introduction.....	220
B.2 Materials and Methods.....	222
B.2.1 Pneumatic robot with 4-DOF parallel kinematic structure.....	222
B.2.2 System configuration.....	224
B.2.3 User interface for needle insertion path planning.....	226
B.2.4 Targeting experiment	227
B.3 Results	231
B.4 Discussion	232
References	236

List of Figures

Figure 1.1: (a) TRUS-guided prostate biopsy and (b) TRUS-guided prostate brachytherapy	2
Figure 2.1: Prostate and the neighboring organs	11
Figure 2.2: (a) MRI room and (b) Control room.....	13
Figure 2.3: Different patient poses during prostate needle placement.....	21
Figure 2.4: SYMBIS Surgical System	35
Figure 3.1: Latest prototype of the pneumatically actuated 4-DOF robot	62
Figure 3.2: Diagram of system components and information flow	64
Figure 3.3: Robot kinematics.....	67
Figure 3.4: 2D view of robot workspace when front/rear triangles links length are changed	68
Figure 3.5: Robot is covered by a sterilized drape with a small hole on it for needle travel.	69
Figure 3.6: Schematic view of the overall master-slave system.....	71
Figure 3.7: The needle driver.....	72
Figure 3.8: The needle driver is installed on the pneumatic robot.....	73
Figure 3.9: The master device.....	74
Figure 3.10: Galil motion controller and AB5 Nanomotion amplifier.	75
Figure 3.11: Overall needle placement error in ex vivo phantom experiment.....	77
Figure 3.12: Position tracking of the master-slave needle insertion module.	78
Figure 4.1: The 4-DOF pneumatic robot for MRI-guided transperineal prostate biopsy	90
Figure 4.2: Different error sources contributing to a robotic system for MRI-guided needle placement.....	92
Figure 4.3: (a) Robot inverse kinematics and (b) front and back triangle coordinate systems can be translated and rotated arbitrarily due to the manufacturing inaccuracies.....	97
Figure 4.4: (a) Data collection strategy for measuring actual T_1 and T_2 and (b) actual geometric parameter.	99
Figure 4.5: (a) The experimental setup, (b) robot calibration and accuracy analysis with two tracking probes.....	100
Figure 4.6: Needle placement in a soft phantom for measuring of the robotic system total error and the artifact shift	104
Figure 4.7: (a) The manipulator's needle placement accuracy before and after sterilization and (b) repeatability in XYZ space before and after sterilization.	108

Figure 4.8: Distribution of the total error for the robotic system.....	109
Figure 4.9: Summary of the error distribution of the studied robotic system in phantom	111
Figure 4.10: The front (back) planar mechanism of different parallel robots.....	112
Figure 5.1: Schematic of the entire system components.....	126
Figure 5.2: Base robot.....	127
Figure 5.3: MRI-compatible needle steering slave robot with 2-DOF	131
Figure 5.4: Integration of the slave and the base robot yields a 6-DOF fully actuated robot.....	132
Figure 5.5: Force variation for a 20G bevel-tip needle into prostate phantom CIRS 053	135
Figure 5.6: Prototype of the master robot.	136
Figure 5.7: Peaucellier-Lipkin mechanism.	137
Figure 5.8: The input-output relationship remains satisfactorily linear if β is bounded	139
Figure 5.9: Top, front and side views of the master robot.	140
Figure 5.10: (a) Master-slave controller box outside view, (b) different components, and (c) Power supply box.....	142
Figure 5.11: Controller architecture for master-slave system.	144
Figure 5.12: MRI-compatible force sensor prototype [43].	145
Figure 5.13: SNR results.....	149
Figure 5.14: Visual comparison of different imaging sequences for the baseline while the system is moving.....	150
Figure 5.15: Position tracking when needle is moving in free space.....	151
Figure 5.16: Position tracking when needle is inserted into phantom.	152
Figure 5.17: Bench-top phantom experiment to evaluate effectiveness of bevel-tip needle steering in error compensation.....	153
Figure 5.18: The effectiveness of a simple steering method.....	154
Figure 5.19: Experiment setup for teleoperated needle steering under MRI guidance	155
Figure 5.20: Phantom used in teleoperated needle steering experiment under MRI guidance. ...	156
Figure 5.21: Real-time MR image of the needle during insertion	157
Figure 6.1: Teleoperated needle steering under real-time MRI guidance.....	168
Figure 6.2: A 20G bevel-tip needle with 3 optical fibers at 120-degree configuration	170
Figure 6.3: Needle with one and two inflection points	171
Figure 6.4: Free body diagram (FBD) for the bevel-tip needle during insertion.	174
Figure 6.5: Case 2	177

Figure 6.6: Case 3	179
Figure 6.7: Case 4.	179
Figure 6.8: Maximum possible error in tip approximation for any load configuration as a function of insertion depth.	180
Figure 6.9: (a) Jigs and milling machine for making three grooves along the 0.6 mm needle at 120-degree configuration, (b) Needle prototype.....	182
Figure 6.10: Calibration and experimental setup.....	183
Figure 6.11: Experimental results for needle tip position estimation for different depths and needle orientations	186
Figure 6.12: Data flow from FBGs to 3D Slicer.....	187
Figure 6.13: Real-time visualization of a 20G × 110 mm needle in 3D Slicer.....	189
Figure A. 1: (a) Motivation and (b) MRI-compatibility.	200
Figure A. 2: 2-DOF force/torque sensor with radial FBG installation, first design.....	206
Figure A. 3: Modified sensor with axial FBG installation configuration.	207
Figure A. 4: FE analysis for the axial force active elements.	209
Figure A. 5: FE analysis for the active elements involved in axial torque measurement.	210
Figure A. 6: (a) Different pieces of the active element and (b) The exploded view of the final fabricated parts.....	211
Figure A. 7: (a) Assembled sensor, (b) Sensor prototype after installing the FBGs.....	211
Figure A. 8: Calibration setup.....	213
Figure A. 9: Calibration results.....	213
Figure B. 1: 4-DOF MRI-compatible pneumatic robot	223
Figure B. 2: System architecture and components.....	225
Figure B. 3: The screenshot of the navigation software based on 3D Slicer	226
Figure B. 4: Robot sterilization.....	228
Figure B. 5: MRI needle placement accuracy.....	231
Figure B. 6: Accuracy results.....	232

List of Tables

Table 2.1: Manually actuated devices for MRI-guided prostate biopsy and brachytherapy.....	24
Table 2.2: Robotic systems for MRI-guided prostate biopsy and brachytherapy.....	29
Table 3.1: Comparison of different piezo motors.....	72
Table 3.2: Results of needle placement accuracy evaluation	77
Table 4.1: Different sources of error in robot assisted prostate needle placement under MRI guidance.....	91
Table 4.2: Calibration of the geometric parameters (mm).....	101
Table 4.3: Results of the needle artifact shift.....	107
Table 4.4: Joint space accuracy (mm).....	107
Table 5.1: Controller parameters.....	144
Table 5.2: Imaging parameters used for SNR tests.....	148
Table 6.1: Parameters used for optimization.....	176
Table 6.2: Sensor optimal locations.....	180

Chapter 1

Introduction

1.1 Motivation

Prostate cancer is the most common cancer in men in North America and the western hemisphere. As of 2012, it is the most common cancer in males in Canada with 26,500 estimated new cases which is 14.2% of all cancers [1]. Every year in the United States, approximately 1.5 million prostate biopsy procedures are performed [2]. If prostate-specific antigen (PSA) levels go above a certain threshold, patients are advised for biopsy, which means taking a small sample from any suspicious lesions observed inside the prostate capsule in ultrasound or MR images. If the result is positive and depending on the stage of the cancer, patients receive one or a combination of different therapies such as chemotherapy, radiation therapy, prostatectomy, ablation, etc. Many patients choose low dose rate (LDR) brachytherapy as a minimally invasive treatment for its advantages, such as minimal trauma and quick recovery. Low dose brachytherapy (hereafter referred to as brachytherapy) means the permanent placement of 60-120 radioactive seeds into the prostate, based on a dosimetry plan (Figure 1.1b), so that the seeds locally irradiate cancerous tumors. In contemporary practice, both biopsy and brachytherapy procedures require inserting needles into the prostate under transrectal ultrasound (TRUS) guidance (Figure 1.1). Usually, the biopsy is performed transrectally while brachytherapy is delivered transperineally.

Ultrasound guidance is the gold standard method for these two procedures, since it is real-time, relatively inexpensive, and non-invasive. However, the image quality is rarely sufficient to show cancerous lesions and instead, it shows the prostate boundary. As a result, the prostate biopsy is

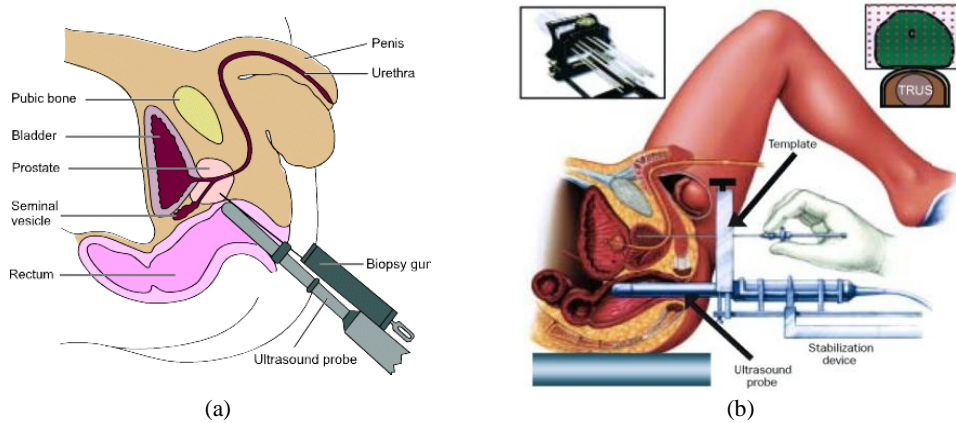


Figure 1.1. (a) TRUS-guided prostate biopsy¹ and (b) TRUS-guided prostate brachytherapy [3].

performed in a so-called systematic manner, meaning that 6-12 cores are removed from peripheral zone (PZ), the origin of more than 70% of tumors [4]. This results in a significant number of false-negative biopsies and the detection rate is between 20-40% [4]. In brachytherapy also, the seeds are barely visible since they are very small and also because their visibility is hampered by the speckle shadow artifact [5].

MRI is a superior imaging modality owing to its excellent visualization of the prostate gland, lesions, surrounding tissues, and its noninvasive nature [6]. Advances with endorectal coils and phased array pelvic have significantly improved the ability of MRI to visualize prostate tissues [7]. MRI was first used for prostate imaging in 1980's. Although it is relatively more expensive, the visualization is significantly better than with TRUS. It can even provide real-time (> 2 Hz) imaging under some circumstances.

¹ Nottingham Urology Group: <http://www.nottinghamurologygroup.co.uk/> accessed May 2013]

MRI-guided manual prostate biopsy was introduced first in 1995 by Schenck *et al.* in [8]. The effectiveness of MRI-guided brachytherapy was initially reported by D'Amico in 1998 [9]. Following this pioneering work, many research groups around the world have tried to implement this technique with closed 1.5T, and 3T scanners.

Manual needle placement procedure inside an MRI scanner has some shortcomings. 1) It is hard to access to the patient, because the MRI scanner is a fairly confined space (typically, $\varnothing = 60 \text{ cm} \times 200 \text{ cm}$). This means patient should be removed from the bore twice for each biopsy, once after acquiring target localization image for needle insertion and once after acquiring a confirmation image for taking out the sample. This results in a longer procedure, which is more expensive (due to longer MRI time and personnel time) and less comfortable for the patient. It also causes patient movement which contributes to targeting error. 2) In manual brachytherapy (Figure 1.1b), usually a grid template is used, the targeting resolution of which is limited to 5 mm. Also, it does not offer angulated needle trajectories and in case of larger prostates (over about 55 cc), the needle may hit the pubic arch when trying to reach the anterior part of prostate (this is called pubic arch interference-PAI). These deficiencies are motivations for a robot-assisted approach, where the needle placement can be performed under live MRI with higher accuracy and repeatability than a manual approach.

Since 2000 when the first robot was introduced to assist MRI-guided prostate biopsy and brachytherapy [10], several research groups have tried to develop robotic systems for MRI-guided prostate biopsy and brachytherapy. Chapter 2 will thoroughly review the robots reported in the literaturesince then and compare them from different perspectives. Such systems can be categorized into two groups: 1) manually actuated devices developed for MRI-guided prostate biopsy and brachytherapy, and 2) computer controlled systems developed for MRI-guided

prostate biopsy and brachytherapy. The first group has the main disadvantage of many patient removals from the scanner. The second group can be categorized into two subtypes: 1) Robots with manual needle insertion; these robots only position and orient the needle toward the target based and the insertion is still performed manually by the clinician. The main shortcoming of these systems is the numerous patient removals from the scanner (most of the reported robotic devices fall in this category). 2) Robots with automated needle placement. The major concern about the latter systems is excluding the clinician from the control loop thus compromising patient safety.

1.2 Objectives

The overarching aim of this thesis is to improve the efficacy of needle placement using a physician-operated in-room, master-slave robot for MRI-guided prostate biopsy and brachytherapy. In this manner, the patient remains inside the scanner and benefits from real-time MR imaging while the clinician has continuous supervision over the procedure.

1.3 Contributions

- 1- *I developed a 1-DOF MRI-compatible master-slave system and added it to an existing transperineal 4-DOF robot [11] to remotely perform needle insertion.* The slave is piezo-actuated. The master is an MRI-compatible master device with manual actuation. Details of this feasibility study and the preliminary results have been published in [12].
- 2- *I studied the accuracy of needle placement in a robot-assisted approach for MRI-guided prostate biopsy and brachytherapy.* This is the first systematic study on the different sources that contribute to the error during robot-assisted MRI-guided prostate needle placement. This study has been published in [13].

- 3- *I developed an MRI-compatible master-slave system for teleoperated bevel-tip needle steering under real-time MRI-guidance in order to compensate for the errors occurring during needle insertion. This is the most significant contribution of this dissertation. The slave robot is a 2-DOF piezo-actuated needle steering module that is integrated with the transperineal robot [11], yielding a fully actuated 6-DOF (3 translations + 3 rotations) MRI-compatible robot for prostate needle placement. Details of this study, the results of MRI-compatibility, effectiveness of needle steering in error compensation, and the feasibility of steering under real-time MRI guidance is reported in Chapter 5. The 4-DOF base robot positions the needle toward the target (macro positioning) while the slave robot provides needle insertion and fine adjustments (micro positioning).*
- 4- *I co-developed a 2-DOF MRI-compatible force sensor for measuring axial force and torque using Fiber Bragg Grating (FBG) sensors. The purpose of developing such sensor was to address the non-backdrivability of the master robot originating from the inherent friction of the piezo motors, and to enable bilateral (i.e. with force feedback) teleoperated needle steering. The sensor was prototyped, calibrated, and tested successfully. The results were published in [14] and were also filed as a United States patent [15].*
- 5- *I developed a method of real-time 3D shape needle tracking which is faster and more accurate than real-time MRI by using FBG sensors and displayed the 3D shape of the needle in 3D Slicer. The accuracy of needle-tip tracking was found to be better than 0.5 mm for any clinically required insertion depth ranging from 0-110 mm. Detail of this study is reported in Chapter 6.*
- 6- *I wrote a review paper on MRI-guided robotic prostate biopsy and brachytherapy. I present a comparative study of MRI-guided robotic systems for prostate biopsy and brachytherapy and*

prove the need for teleoperated needle steering under MRI guidance. Details of this study are reported in Chapter 2.

1.4 Thesis outline

Manuscript format is used to present this dissertation. In Chapter 2, a thorough literature review is performed on the previously reported manually actuated and robotic devices for MRI-guided prostate biopsy and brachytherapy. The need for teleoperated needle steering under real-time MRI guidance is justified. In Chapter 3, a feasibility study of the teleoperated needle insertion under MRI-guidance is presented. In Chapter 4, an accuracy study of a robotic system for MRI-guided prostate needle placement is presented. In Chapter 5, the development of a teleoperated needle steering system for prostate needle placement under real-time MRI guidance is discussed. In Chapter 6, real-time 3D shape needle tracking using FBG sensors is presented. In Chapter 7, the contributions are reviewed, and further directions are suggested. In Appendix A, development of a decoupled 2-DOF force sensor using FBGs is presented. In Appendix B, a preclinical study of the transperineal robot, reported in [11], is presented. The majority of the contents of this dissertation have been published in various papers, explained on the Co-authorship page and in the introduction of the appendices.

References

- [1] <http://www.cancer.ca>
- [2] R. Siegel, D. Naishadham and A. Jemal, "Cancer statistics, 2012," *CA: A Cancer Journal for Clinicians*, 2012.

- [3] T. M. Pisansky, D. G. Gold, K. M. Furutani, O. K. Macdonald, R. H. McLaren, L. A. Mynderse, T. M. Wilson, J. R. Hebl and R. Choo, "High-dose-rate brachytherapy in the curative treatment of patients with localized prostate cancer," in *Mayo Clinic Proceedings*, 2008, pp. 1364-1372.
- [4] C. Tempany, S. Straus, N. Hata and S. Haker, "MR - guided prostate interventions," *Journal of Magnetic Resonance Imaging*, vol. 27, pp. 356-367, 2008.
- [5] B. H. Han, K. Wallner, G. Merrick, W. Butler, S. Sutlief and J. Sylvester, "Prostate brachytherapy seed identification on post-implant TRUS images," *Med. Phys.*, vol. 30, pp. 898, 2003.
- [6] A. Wefer, H. Hricak, D. Vigneron, F. Coakley, Y. Lu, J. Wefer, U. Mueller-Lisse, P. Carroll and J. Kurhanewicz, "Sextant localization of prostate cancer: comparison of sextant biopsy, magnetic resonance imaging and magnetic resonance spectroscopic imaging with step section histology," *J. Urol.*, vol. 164, pp. 400-404, 2000.
- [7] A. Krieger, I. Iordachita, S. E. Song, N. B. Cho, P. Guion, G. Fichtinger and L. L. Whitcomb, "Development and preliminary evaluation of an actuated MRI-compatible robotic device for MRI-guided prostate intervention," in *Robotics and Automation (ICRA), 2010 IEEE International Conference on*, 2010, pp. 1066-1073.
- [8] J. F. Schenck, F. A. Jolesz, P. B. Roemer, H. E. Cline, W. E. Lorensen, R. Kikinis, S. G. Silverman, C. J. Hardy, W. D. Barber, and E. T. Laskaris. "Superconducting open configuration MR imaging system for image-guided therapy," *Radiology*, vol. 195, pp. 805-814, 1995.

- [9] A. V. D'amico, C. Tempany, R. Cormack, N. Hata, M. Jinzaki, K. Tuncali, M. Weinstein and J. Richie, "Transperineal magnetic resonance image guided prostate biopsy," *J. Urol.*, vol. 164, pp. 385-387, 2000.
- [10] K. Chinzei, N. Hata, F. Jolesz and R. Kikinis, "Surgical assist robot for the active navigation in the intraoperative MRI: Hardware design issues," in *Intelligent Robots and Systems, 2000.(IROS 2000). Proceedings. 2000 IEEE/RSJ International Conference on, 2000*, pp. 727-732.
- [11] S. E. Song, N. B. Cho, G. Fischer, N. Hata, C. Tempany, G. Fichtinger and I. Iordachita, "Development of a pneumatic robot for MRI-guided transperineal prostate biopsy and brachytherapy: New approaches," in *Robotics and Automation (ICRA), 2010 IEEE International Conference on, 2010*, pp. 2580-2585.
- [12] R. Seifabadi, S. E. Song, A. Krieger, N. B. Cho, J. Tokuda, G. Fichtinger and I. Iordachita, "Robotic system for MRI-guided prostate biopsy: feasibility of teleoperated needle insertion and ex vivo phantom study," *International Journal of Computer Assisted Radiology and Surgery*, vol. 7, pp. 181-190, 2012.
- [13] R. Seifabadi, N. B. J. Cho, S. E. Song, J. Tokuda, N. Hata, C. M. Tempany, G. Fichtinger and I. Iordachita, "Accuracy study of a robotic system for MRI-guided prostate needle placement," *The International Journal of Medical Robotics and Computer Assisted Surgery*, 2012.

- [14] R. Monfaredi, R. Seifabadi, G. Fichtinger, and I. Iordachita, "Design of a decoupled MRI-compatible force sensor for robot-assisted prostate interventions," *In SPIE Medical Imaging*, pp. 867118-867118, 2013.
- [15] R. Monfaredi, I. Iordachita, and R. Seifabadi, "MRI-compatible force/toque sensor with fiber Bragg gratings", JHU reference #C12338, March 2013, to be filed as a *United States Patent*.

Chapter 2

Robot-assisted MRI-guided prostate biopsy and brachytherapy: need for teleoperated needle steering

This chapter is an engineering review of robot-assisted MRI-guided prostate needle placement. MRI-compatible robots developed for prostate biopsy and brachytherapy found in the literature are reviewed and compared from different perspectives. After summarizing the previous work, I demonstrate the need for teleoperated needle insertion and steering and enabling technologies such as needle shape tracking, target tracking, and MRI-compatible force and shape sensing.

2.1 Introduction

²[Prostate is the male's reproductive organ (Figure 2.1). Prostate cancer is a very important disease in today's world. It is expected that by the year 2015, 450,000 new cases will be diagnosed in the United States [1]. Approximately 1.5 million prostate biopsy procedures are performed yearly in US [2]. If the prostate-specific antigen (PSA) level goes above a certain threshold, it can be a sign of prostate cancer. To confirm this, a biopsy is performed which means taking a small sample from suspicious lesions observed inside the prostate capsule viewed in ultrasound or MRI diagnostic images. If the result is positive and depending on the stage of the cancer, patients

² The materials provided between the brackets have some overlap with the introduction part in Chapter 1 and/or Chapter 5. This is due to the fact that each chapter is a manuscript which is either published or to be published and should have a single complete story.

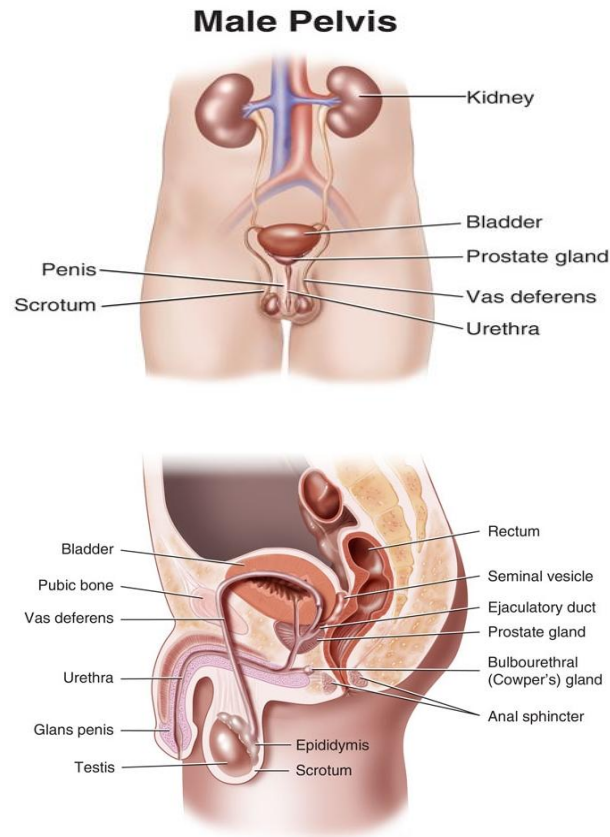


Figure 2.1. Prostate and the neighboring organs³

are advised to take one or a combination of different therapies including chemotherapy, radiation therapy, prostatectomy, ablation, etc. Many patients choose low dose rate (LDR) brachytherapy as a minimally invasive treatment for its advantages such as minimal trauma and quick recovery. LDR is suitable for patients with a localised tumour and good prognosis. Brachytherapy entails the permanent placement of 60-120 radioactive seeds into the prostate (Figure 1.1b) so that the seeds locally irradiate cancerous tumors. Both biopsy and brachytherapy procedures involve manually inserting needles into the prostate along a straight trajectory with transrectal ultrasound

³ Source: <http://www.google.ca/images> [downloaded May 2010].

(TRUS) guidance (Figure 1.1). Typically, a biopsy is performed transrectally while brachytherapy is performed transperineally with the aid of a grid template. One reason is that biopsy requires less number of needle insertion (typically 6-12) and the patient can tolerate transrectal insertion without anesthesia. Transperineal prostate access is relatively easier but is more traumatic.

Ultrasound is the gold standard method for these two procedures since it is real-time, relatively inexpensive, non-invasive, and easy to use. However, the image quality is rarely sufficient to show cancerous lesions - instead, it shows the prostate boundary. As a result, a prostate biopsy is performed in a “systematic way” whereby 6-12 equally-distant cores are removed from peripheral zone (PZ), the origin of more than 70% tumors. This results in a significant number of false-negative biopsies and the detection rate is between 20-40% [1]. Also in brachytherapy, the seeds are barely visible since they are very small and visibility is hampered by the speckle shadow artifact [3].

Magnetic resonance imaging (MRI) is a superior imaging modality because it is non-invasiveness, gives an excellent visualization of the prostate gland, lesions, and surrounding tissues (Figure 2.2). MRI was initially used for prostate imaging in the 1980s. Although it is more expensive than ultrasound⁴, the visualization is significantly better. It can even provide real-time (> 2 Hz) imaging.]

⁴ According to Canadian Diagnostic Corporation (CDC), abdominal scan with a 1.5 T MRI costs \$1600 while Ultrasound costs \$500 as of May 2013.



(a)



(b)

Figure 2.2. (a) MRI room and (b) Control room.

MRI-guided manual prostate biopsy was introduced first in 1995 by Schenck *et al.* in [4]. The effectiveness of MRI-guided brachytherapy was initially reported by D'Amico *et al.* in 1998 [5]. Since then, a few teams have tried to implement these techniques with closed 1.5T and 3T MRI scanners. Recently, Moore *et al.* [6] and Yakar *et al.* [7] [6] in different studies have thoroughly reviewed attempts on manual prostate biopsy using MRI. Yakar *et al.* [7] briefly reviewed studies

with manual MRI-guided prostate brachytherapy as well as other focal therapies using MRI including ablation and focused ultrasound.

In-bore MRI-guided manual procedures have some shortcomings. First, it is hard to access the patient since the MRI scanner is a fairly confined space (typically, $\text{Ø } 60 \text{ cm} \times 200 \text{ cm}$). This means the patient must be removed from scanner, once for insertion and once for extraction. In that case, targeting is performed based on a previously taken image. Because of this, real-time MRI imaging cannot be used in a manual procedure. Also, moving the patient in and out of MRI scanner can lead to targeting error due to the inevitable patient movements. Secondly, in brachytherapy, a grid template with holes 5 mm apart is used, limiting the targeting resolution to 5mm. Also, since it does not offer angulated needle trajectories, the procedure is likely to hit the pubic arch when trying to reach the anterior part of the prostate in patients with larger prostates (called pubic arch interference-PAI). These deficiencies are motivations for a robot-assisted approach since the needle placement can be performed under live MRI with higher accuracy and repeatability.

Since 2000 when the first MRI-compatible robot was introduced for prostate needle placement in open MRI, many devices and robots have been developed for MRI-guided prostate biopsy and brachytherapy. Based on our search via Google Scholar and PubMed, since 2005 only the following review papers with “robot”, “MRI”, and “prostate” keywords in the title have been published: [8], [9], [10], and [11]. Except [10], the other papers are written by clinical fellows with little focus on engineering perspectives and missing a lot of contemporary and recent studies. The only engineering review, i.e., [10] is 5 years old at the time of writing this chapter. Thus, we believe that an engineering review covering old and recently developed systems in addition to stating the current directions of this field is missing in the literature. In this study, we

focus on robotic manipulators controlled by computers. However, we also cover manipulators that are manually actuated.

The chapter is organized as follows: in section 2.1, engineering challenges of MRI-compatible robotics are discussed. In section 2.3, manually actuated devices for MRI-guided prostate biopsy and brachytherapy are discussed. In section 2.4, robots for MRI-guided prostate biopsy and brachytherapy are listed and reviewed in detail. After reviewing previous studies in this field, I demonstrate the need for teleoperated needle steering in order to compensate for the errors caused during needle insertion. In section 2.5, different sources that contribute to targeting error are briefly summarized and then, possible solutions found in the literature to reduce these errors are reviewed. Next, different methods of needle steering are reviewed and the significance of having human in the loop is realized. In section 2.6, requirements and technologies to enable teleoperated bevel-tip needle steering under MRI-guidance such as MRI-compatible haptic devices, target tracking, needle tracking and MRI-compatible force sensors are reviewed and discussed. The chapter ends with conclusions in section 2.7.

2.2 Engineering challenges of MRI-compatible robotics

2.2.1 MRI-compatibility

Constraints that factor into the MRI-compatibility of a device are defined as follows: 1) the device does not develop a risk to patient and clinicians' safety - this can be either flying objects due to the magnetic force or radio frequency heating caused by metal components; 2) the device can properly function inside an MRI scanner while the machine is operating; 3) the image artifacts caused by the device are insignificant. In the following paragraphs, we review the most important factors that play a role in MRI-compatibility.

Materials: In an MRI room, there is a large static magnetic field (usually 3T in today's scanners and up to 8T in research scanners) as well as a high frequency varying magnetic field. As a result, ferromagnetic materials (Fe, Co, Ni) cannot be used since they can fly and injure people in the room and can develop noise into image. Conductive materials also should be avoided due to RF heating and the noise caused by eddy current [12]. Plastic materials such as cast acrylic, Ultem, ABS, and polycarbonate are commonly used in such an environment. Recently, an interesting research was conducted on the force and image artifacts caused by metals in MRI-compatible devices [13]. Twelve commonly-used metals with sufficient rigidity and low enough susceptibility such as brass, phosphor-bronze, inconel, aluminum, stainless steel 304, etc. were selected. The specimens, cylinders $\text{\O} 12.7 \text{ mm} \times 127 \text{ mm}$, were placed at the iso-center of a 3T Siemens scanner. The study discovered that the force was proportional to the metal susceptibility. The artifacts size increased with susceptibility, echo time, and use of turbo spin echo over gradient echo sequence.

Actuators: The most commonly used actuators in medical robotics, DC and stepper motor, cannot be used in MRI room since they operate based on electromagnetic principles and lead to electromagnetic interference (EMI). However, they can be placed at a far distance from the scanner and anchored safely. The power can then be transmitted to the scanner in some way, e.g. with cable and pulleys or rod and shaft [14]. This method has not gained interest for its obvious limitations and for causing EMI. Piezo motors, ultrasonic piezo motors, and pneumatic drivers are widely used instead of DC and stepper motors.

Pneumatic actuators are the best solution for MRI applications on principle. They neither introduce any EMI nor any patient safety risk. The air source is usually available in the MRI room. The only issue with pneumatic actuators is their highly nonlinear behavior due to the air

compressibility as well as friction in the piston and valves, making their position control very challenging [10]. A ratchet-like pneumatic actuator for an MRI-compatible robot and a wobble-motor were introduced in [15] and [16], respectively, having less control issues. Stoianovici *et al.* in [17] developed a new generation of pneumatic actuators (called PneuStep) that work similarly to a stepper motor but with the air pressure controlled by a set of piezo valves placed outside of MRI room that solves the control issues of pneumatic motors. However, this kind of actuator has a complex and expensive design [18] and has not been commercialized. Nevertheless, pneumatic actuators have been continually used for MRI-compatible robots [19], [20], [21], [22].

Piezo motors and ultrasonic piezo motors have been widely used in MRI robots since the beginning of this field. Piezo motors consist of certain ceramic materials that change their shape if excited by an external source of voltage. Since this change in shape is very small, the voltage must change its polarity with high frequency to make a larger translation. Ultrasonic motors are piezo motors with an ultrasonic frequency for the electrical signal excitation (i.e. > 20 kHz). The main issue with piezo motors is EMI. This is caused by: 1) the cables carrying electrical signal to the motors - this issue can be resolved by careful shielding and grounding of the cables; 2) the high frequency noise developed by piezo motor drivers interfering with the magnetic field of the MRI scanner. This issue has been resolved by an integrated driver and controller which has almost no influence on MR image [23]. Other criticisms about piezo motors are the high voltage that drives the motor [10] and their non-backdrivability [24]. Solutions to the latter problem include using some small excitation to overcome the inherent friction or using a force sensor and admittance control [25].

Hydraulic actuators have also been used for fMRI studies [26], [27] as well as breast biopsy [28]. Similar to pneumatic, hydraulic actuators have no effect on MRI on principle. The pump can be

placed outside of the scanner room. Unlike pneumatic actuators, hydraulic actuators do not have the air compressability issue making their motion control less challenging. The primary concern about hydraulic actuation is the risk of leakage [10].

Other types of actuation have also been reported. In [29], a binary manipulation method was proposed using dielectric elastomer actuators (DEA) for prostate transperineal interventions. Despite its MRI-compatibility, low cost and simple design, the power it produced was not sufficient. Recently, air muscles replaced the DEA with better results in force, precision, and size [30]. Lorentz actuators are typical electromagnetic motors without ferromagnetic material and use a scanner magnetic field to run. Still, their output torque is limited and they require a challenging calibration for each scanner they are used with [18]. Chang *et al.* in [31] reported an active steerable needle. They embedded optical fibers into a slender needle made of shape memory alloy (SMA) to pass through a laser with 0.8 W. The heating makes the needle tip deflect up to few millimeters. The effectiveness of this method inside tissue however was not investigated. A review on other methods of actuation such as electroactive, ion conducting polymers, and electrorheological fluid brakes is provided in [14].

2.2.2 Confined workspace

Open-configuration MRI such as the double-donut-configuration offers easy access to the patient for MRI interventions. However, magnetic field and therefore, signal-to-noise-ratio (SNR) are low. Most of high field MRI scanners ($>1.5T$) have a diameter of 60 cm and are 2 m long thus making it very difficult to access to patient. The MRI table also takes up some of this space thus making it more confined. More recent closed MRIs such as the Siemens Verio 3T have larger diameter (70 cm) and are shorter (173 cm).

2.2.3 RF heating

Conductive materials can develop eddy current when placed in MRI scanner resulting in local heating. This is a major problem in designing needles, RF coils, and other devices [32].

2.2.4 Electromagnetic interference

Any device that produces an electromagnetic field such as electronic circuits (motor drivers, force sensor amplifiers, controller, etc) and magnetic and nonmagnetic metals can distort the homogeneity of the magnetic field and results in EMI. EMI reduces SNR which leads to deterioration of image quality. This is why electronic circuits (if placed inside MRI room) should be RF shielded. All cables transmitting electrical signal to/from motors and encoders must be well shielded and grounded to minimize EMI.

2.2.5 Robot-to-image registration

In MRI-guided prostate biopsy and brachytherapy, targets defined in the MRI coordinate system are referred to as RAS (right-left, anterior-posterior, and superior-inferior). This coordinate system is different from the robot coordinate system (XYZ). Therefore, a transformation is sought between the image and robot coordinate system. This procedure is known as registration or calibration. This transformation matrix (4×4) is one of the key sources that can influence the accuracy of the MRI-guided robotic procedures [10], [33]. To calculate this transformation, the following methods are available: joint encoding, active markers, passive markers, and optical tracking [34].

- 1- *Joint encoding* needs a rigid mount to the MRI scanner in a repeatable manner and a pre-calibration. Then, optical encoders reveal the position of the robots or devices [35].
- 2- *Active markers*: Two types of active markers have been reported: gradient field sensing markers, and micro tracking coils:

- 2-1) *Gradient field sensing* markers use the gradient field of MRI to measure the position and orientation of the devices in MRI scanner. The EndoScout® tracking system (Robin Medical Inc., Baltimore, MD, USA), for instance, is a 6-DOF sensor that gives the full position and orientation within an MRI in real-time [36]. It has been used for manual intraoperative needle placement as well as the robotic MRI-guided breast biopsy. The big advantage of this method over micro tracking coils is that it uses the conventional imaging sequences. But it requires a one-time careful calibration over the entire region of interest for every MRI it is used with [33].
- 2-2) *Micro tracking coils* method uses three or more micro coils and custom-made imaging sequences [37]. By combining the information attained by all sensors, the 6-DOF position and orientation is achieved. The advantages of this method are high accuracy (< 0.3 degree, 0.2 mm) and high speed (20 Hz). The disadvantages of this method are scanner programming, limiting the number of available channels, and making tracking devices complex and expensive.
- 3- *Passive markers*, alternatively called fiducial markers, are small markers typically filled with gadolinium and water and are clearly visible in MRI. They can be automatically segmented in the MR image and used for registration. Susil *et al.* in [38] used passive markers for MRI-guided high dose rate (HDR) brachytherapy. Beyersdrof *et al.* [39] embedded passive markers in a sleeve coaxial to the transrectal biopsy device. The main drawback of this method is that it entails a lot of T1 or T2-weighted imaging which takes a significant amount of time. Krieger *et al.* in [33] used a similar idea but combined it with joint encoding. A single-slice stereotactic method for robot-to-CT image registration was proposed by Susil *et al.* in [40] called Z-frame. Z-frame is a cube with three Z-pattern on three adjacent faces

giving full 6-DOF position with only one slice (although more slices are taken to improve accuracy over the region of interest). The Z-frame has been used in MRI-guided robotic transperineal prostate biopsy and brachytherapy [19], [41], [44], as well as in manual biopsy with a 2-DOF needle-guiding template grid [46]. Patriciu *et al.* in [47] proposed a new method of tracking passive markers for their MRI-guided transperineal automated brachytherapy. The markers were a combination of an ellipse, a line, and some control points, all placed around the seed injector module (i.e. coaxial with needle).

2.3 Manual devices used for prostate biopsy and brachytherapy

In this section, manually actuated devices used in MRI-guided prostate biopsy and brachytherapy are listed. These devices were used with both open and closed MRI scanners. Open scanners offer near real-time imaging as well as easy access to the patient while closed MRI offers higher SNR images. Figure 2.3 shows different patient positions during prostate needle placement.

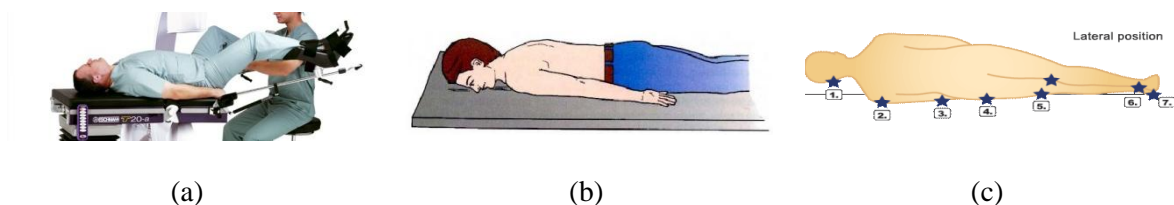


Figure 2.3. Different patient poses during prostate needle placement: (a) lithomy, (b) prone, and (c) lateral decubitus (side)⁵.

In open MRI, the following devices have been reported in literature. D’Amico *et al.* in [5] used a 0.5 T open scanner and a needle-guiding template with small holes 5 mm apart for transperineal biopsy. Hata *et al.* in [48] used a similar approach. Template-to-MRI registration was performed using an optical tracking system and software was developed to assist targeting. Zangos *et al.* in

⁵ Source: <http://www.google.ca/images>, [downloaded Oct. 2010].

[49] used a 0.2 T scanner for transgluteal prostate biopsy. They reported patient experiments using this method and concluded that the method is feasible and safe.

In closed MRI, the following devices have been reported in literature. Menard *et al.* in [50] used a grid template attached to a passive arm for high dose rate transperineal brachytherapy in multiple patient experiments. Patients were placed on their side with an endorectal MRI coil placed for enhanced imaging. Fichtinger *et al.* in [51] reported a 3-DOF transrectal prostate biopsy device with the patient in prone position. The device was actuated manually using flexible shafts from outside of the scanner. Beyersdorff *et al.* in [39] developed a transrectal prostate biopsy device. The needle guide was visible in MRI. They reported 12 patient experiments. A company called Invivo (Invivo, Schwerin, Germany) developed a commercial device similar to one reported in [39]. Engelhard *et al.* in [52] used the same robot for 37 patients in supine position. Krieger *et al.* in [53] and Susil *et al.* in [54] developed a transrectal robot for prostate biopsy, marker placement, and therapeutic injection which was an extension of the robot presented in [51]. The 2-DOF system called APT (access to prostate tissue) was designed for a 3T scanner. The system was actuated using two flexible shafts from outside of the bore. It utilized an endorectal coil and a hybrid tracking method as mentioned in [33]. The design of APT system was modified in APT II [55] to be more compact and portable. Flexible shafts were removed and the device was manually actuated. 3D Slicer software⁶ was used for navigation and planning. APT was tested on 50 patients successfully. Tokuda *et al.* in [46] reported an in-bore setup and software for a 3T MRI-guided transperineal prostate biopsy. They used a custom-made template with holes 5 mm apart which can translate up-down and left-right. They used Z-frame to register the template to the MRI. 10 patient experiments were reported in a 3T scanner and the accuracy was 5.4 mm. Cepek

⁶ www.slicer.org

et al. in [56] developed a transperineal 2-DOF needle guide device for prostate biopsy and brachytherapy. The device was actuated manually from outside of the bore using two long handles. An optical encoder was used to measure the position of the needle guide after the initial robot-to-image registration. A handheld user interface with two grids of LEDs (one for the target and one for the current position of the needle) was developed to be placed next to the scanner and helped the physician with needle placement. Christoforou *et al.* in [57] developed a manually actuated general purpose manipulator with 6-DOF. They performed phantom experiments under MRI guidance. The robot is similar to Innomotion (Innomedic, Germany [58]), in which an arm hangs over the patient and reaches inside the scanner. Table 2.1 compares the manual devices reviewed in this section.

2.4 Computer-controlled robotic systems for prostate biopsy and brachytherapy

Since 2000, different robots (devices controlled by a computer) have been reported for MRI-guided prostate biopsy and brachytherapy. These robots can be categorized in different ways. One way is to sort them according to the way of reaching to the prostate, i.e. transrectal, transperineal and transgluteal.

2.4.1 Transrectal access

Elhawary *et al.* reported a 5-DOF prototype robotic system using linear piezo-ceramic motors (PiezoLEG, Piezomotor Inc., Uppsala, Sweden) for transrectal prostate biopsy in a 1.5T MRI [59]. This system employed a remotely driven touch-screen needle insertion console placed inside the scanner room. Tse *et al.* in [60] used a simple 1-DOF master robot with the same transrectal robot.

Table 2.1: Manually actuated devices for MRI-guided prostate biopsy and brachytherapy.

Primary Author	Reference	Year	Status	Access approach	Patient position	MRI Magnitude & type	Biopsy or Brachytherapy	Registration method	Country	Commercialized	DOF	Endorectal coil	Encoded
D'Amico	[5]	2000	C	TP	L	0.5T O	BX	PM	USA	No	0*	No	No
Hata	[48]	2001		TP	L		BX	OT	USA	No	0	No	No
Fichtinger	[51]	2002	P	TR	Pr	>1.5 C	BX	AM	USA	No	3	N/A	No
Menard	[50]	2004	C	TP	LD	1.5T C	HDR	PM	USA	No	0	Yes	No
Zangos	[49]	2005	C	TG	LD	0.2T O	BX	PM	GER	No	0	Yes	No
Beyersdorff	[39]	2005	C	TR	Pr	1.5T C	BX	PM	GER	Yes	5	No	No
Krieger	[53]	2005	C	TR	Pr	3T C	BX	HB	USA	No	2	Yes	Yes
Engelhard	[52]	2006	C	TR	Pr	1.5T C	BX	PM	GER	Yes	5	Yes	No
Susil	[54]	2006	C	TR	Pr	3T C	BX	HB	USA	No	2	Yes	Yes
Krieger	[55]	2011	C	TR	Pr	3T C	BX	HB	USA	No	2	Yes	Yes
Tokuda	[46]	2012	C	TP	S	3T C	BX	PM	USA	No	2	No	No
Cepek	[56]	2012	P	TP	S	3T C	BX, LDR	PM	CAN	No	2	N/A	Yes
Christoforou	[57]	2012	P	TP, TG	S	3T C	Gen	PM	GRE E	No	6	N/A	Yes

Status: **C** = Clinical, **P** = Phantom study

Access approach: **TP** = Transperineal, **TR** = Transrectal, **TG** = Transgluteal

Patient position: **L** = lithomy, **Pr** = Prone, **S** = Supine, **LD** = Lateral Decubitus

MRI type: **C** = Closed, **O** = Open

BX = Biopsy, **LDR** = Low-dose Rate Brachytherapy, **HDR** = High-dose Rate Brachytherapy

Registration method: **OT** = Optical Tracking, **PM** = Passive Marker, **AM** = Active Marker, **HB** = Hybrid

*0-DOF means a fixed template grid was used.

The master robot was placed in control room. Krieger *et al.* in [61] introduced a motorized version of the previously mentioned APT robot where the roll and pitch movements were actuated using Nanomotion (Nanomotion Ltd, Yokneam, Israe) piezo motors with the insertion performed manually outside of the bore. They reported that the robot and controller introduced significant noise to MR image.

Unlike manual APT robots, no phantom, animal, or patient experiment was reported using this robot. Later, a conceptual design was performed to make the motorized APT robot smaller and the needle insertion actuated [62]. This design however was not prototyped. Schouten *et al.* in [63] used a 5-DOF pneumatically actuated robot for transrectal prostate biopsy under real-time MRI guidance with patient in prone position. They tested this robot for 13 patients and compared the results with manual biopsy. Robotic procedure was found to be slower and slightly less accurate.

2.4.2 Transperineal access

Primary MRI-guided transperineal prostate intervention was studied in an open MRI scanner [35] and [64]. The robot was anchored on top of the scanner in order to minimize EMI caused by the Shinsei ultrasonic motors (Shinsei Co., Tokyo, Japan). The work was further extended in [65] and the accuracy and repeatability of the system was evaluated in [66]. This system was designed to guide the needle for biopsy and brachytherapy and the insertion was performed manually [67]. Tadakuma *et al.* in [29] developed an MRI-compatible robot for transperineal needle placement in the prostate using dielectric elastomer actuators (DEAs). The accuracy of the robot was reported, but the MRI-compatibility, registration, and phantom experiment were not reported. Invention of PneuStep [17] was followed by development of MrBot which is a fully automated MRI Stealth pneumatic robot for transperineal prostate biopsy and brachytherapy [68]. It was designed for a patient in lateral decubitus position which makes the preoperative and intraoperative image registration more challenging. The robot has 6-DOF: 5 for needle positioning using a parallel structure that was optimized for maximum rigidity, and 1 for insertion. An automated seed injector was also developed and tested in phantom [69], [47] for the MrBot using fast needle insertion to reduce needle deflection. The accuracy of the MRI-guided

seed placement in gel phantom including all sources of error was 1.15 mm. The system was also tested on canine [70] and the accuracy of needle placement and seed placement were 2.02 mm and 2.5 mm, respectively. This robotic system has not been tested on any patient apparently due to excluding physician from the control loop. A pneumatically actuated robot was developed for transperineal prostate biopsy and brachytherapy as reported by Fischer *et al.* in [19]. The robot was 4-DOF even though the angulations were disabled in the reported experiments. The insertion was manual meaning that patient had to be removed for each insertion and sampling and patient position was supine. The accuracy of the manipulator outside of tissue was sub-millimeter. It was designed for a 3T MRI and for transperineal MRI-guided prostate biopsy and brachytherapy. MRI-compatibility showed negligible SNR reduction. The robot used Z-frame for registration with an accuracy of 2.6 mm [71]. A software strategy was reported in [71] for this robotic system with intuitive needle guidance tools, such as interactive target planning, 3D anatomy visualization, and current needle position. Song *et al.* in [41] developed the second-generation of the manipulator. The controller was identical to the first version and the robot was still pneumatically actuated. The main advantage of the second-generation was the increase rigidity due to the parallel structure with a significantly smaller force required for actuation. In addition, the actuators were easier to control since a timing belt with damping characteristics was used for power transmission. An MRI-compatibility study of the second-version manipulator was reported in [72]. A feasibility study of teleoperated needle insertion using this robot integrated with a piezo-actuated needle driver was reported by Seifabadi *et al.* in [73]. Tokuda *et al.* in [74] reported using this robot for angulated needle placement in a 3T scanner. Seifabadi *et al.* in [33] reported an accuracy study of the robotic system including all sources of error in phantom experiment concluding 2.5 mm error in needle placement. Seifabadi *et al.* in [24] reported a

conceptual design for teleoperated steering of a 20G needle using an MRI-compatible 2-DOF master and a 2-DOF MRI-compatible slave robot integrated with the transperineal robot making it fully actuated (x, y, z, yaw, pitch, and roll). Eslami *et al.* in [75] reported the third generation of this system. The manipulator has the same kinematic architecture as the second version with some modification in order to eliminate the unintended rotation of the needle guide. The actuation method was changed to piezo motors and lead screws were used instead of the timing belt. Goldenberg *et al.* in [76] developed a 6-DOF robotic system employing Shinsei ultrasonic actuators for MRI-guided transperineal prostate intervention. As expected, Shinsei motor drivers resulted in noticeable SNR reduction. The accuracy of the system was 2 mm in a phantom study. van den Bosch *et al.* in [77] reported a 5-DOF manually actuated robot equipped with a hydraulically and pneumatically actuated tapping device [78] and [79], which significantly reduces prostate displacement and deformation. The device uses hydraulic actuators for the insertion DOF and a pneumatic actuator for tapping purpose (i.e. small oscillations). They used this robot for 4 gold marker placements into the patient under a 1.5T MRI guidance. Su *et al.* in [44] reported a 6-DOF piezo-actuated robot with bevel-tip needle steering capability for transrectal prostate brachytherapy under real-time MRI-guidance. The robot consisted of a Cartesian 3-DOF stage plus a 3-DOF module for seed implantation. SNR reduction was 2% because of using the controller developed in [24]. They used Z-frame to register their robot to MRI. The Z-frame was permanently attached to the robot to reduce errors. In [45], they used the same 6-DOF robot but with a concentric active cannula which allows MRI-guided steerable curved active cannula. Abdelaziz *et al.* in [80], [81] reported the feasibility of cable driven robots for transperineal prostate intervention. Design challenges were reported in [80] and the tension and length of the cables were studied in [81]. The system was designed for cryoablation, but can

be easily used for biopsy and brachytherapy. Miron *et al.* in [18] reported an MRI-compatible pneumatic actuation manipulator for transperineal prostate interventions which uses embedded air-muscles operated in a binary fashion similar to [29]. In addition to high accuracy, the technology offers compactness, MRI-compatibility, simplicity and low cost. 20 embedded air-muscles distributed in four star-like polymer structures were used. MRI-compatibility tests revealed no observable effects on the signal-to-noise ratio and the accuracy of the robot-only outside of tissue was under 0.5 mm. Song *et al.* in [82] reported a motorized 2-DOF needle guide template using Shinsei motors that mimics the transperineal ultrasound-guided brachytherapy template. In order to eliminate EMI, they placed the motors over 50 cm away from iso-center and transmitted power using timing belts. The “smart template” guides the needle with higher accuracy than the grid needle-guiding. Insertion was performed manually. This robot can be used for multiple patient experiments since it adds a minimum number of extra requirements to the current clinical workflow. The SNR reduction was reported to be negligible and the accuracy in phantom under MRI guidance was sub millimeter.

2.4.3 Transgluteal access

Zangos *et al.* in [83] used the Innomotion robot for transgluteal approach in a cadaver study at 1.5T. Innomotion is a 5-DOF (3 translations + 2 rotations) CT/MRI-compatible robot for general purposes. It is a commercial robot and used in operating rooms for sciatic pain and facet joint treatments, biopsies, drainages, and CT-guided osteosynthesis. It is anchored to the MRI table using a C-shaped support (the patient passes through the 40 cm C shape). The robot has a long arm which is placed over the patient and does manipulation inside the closed MRI gantry. The robot is pneumatically actuated and passive markers and optical encoders were used to track the needle. Insertion is performed manually. A remote center of motion (RCM) mechanism is used at

Table 2.2: Robotic systems for MRI-guided prostate biopsy and brachytherapy.

Primary Author	Ref	Year	Status	Access approach	Patient position	Insertion method	MRI type & Magnitude	Actuation method	Biopsy or Brachytherapy	Registration method	Country	Commercialized	DOF	Endorectal coil	Clinician in loop
Chinzei	[64] [65] [66] [67]	2000	P	TP	L	M	0.5 T O	UM	BX BT	PM	USA	No	5	No	Yes
Stoianovici	[17][68] [69][70] [47]	2007	An	TP	LD	A	3T C	HPN	BT	PM	USA	No	6	Yes	No
Zangos	[83] [84]	2008	C	TG	LD	M	1.5 T C	PN	BX	PM	GER	Yes	5	Yes	Yes
Tadakuma	[29]	2008	D	TP	L	M	3T C	DEA	BX BT	None	USA	No	2	No	Yes
Goldenberg	[76]	2008	P	TP	L	A	3T C	UM	RF A	PC	CA	No	6	No	No
Fischer	[19]	2008	P	TP	L	M	3T C	PN	BX BT	PM	USA	No	4	No	Yes
Elhawary	[59][60]	2010	P	TR	Pr	TO	1.5 T C	PZ	BX	PM	UK	No	5 + 1	Yes	Yes
Krieger	[61]	2010	P	TR	Pr	M	3T C	PZ	BX	PM	USA	No	2	Yes	Yes
Song	[41]	2010	P	TP	L	M	3T C	PN	BX BT	PM	USA	No	4	No	Yes
van der Bosch	[77]	2010	C	TP	L	A	1.5 T C	PN + HY	MP	PM	NL	No	5	No	No
Su	[44][45]	2011	P	TP	L	A + ST	3T C	PZ	BX BT	PM	USA	No	6	No	No
Bohren	[62]	2012	D	TR	Pr	A	3T C	PZ	BX	PM	USA	No	3	No	No
Schouten	[63]	2012	C	TR	Pr	M	3T C	PN	BX	PM	NL	No	5	No	Yes
Abdelaziz	[80][81]	2012	P	TP	L	M	1.5 T C	DC	CA	PM	FR	No	4	No	Yes
Seifabadi	[24]	2013	P	TP	L	TO + ST	3T C	PN+P Z	BX BT	PM	USA	No	6 + 2	No	Yes
Miron	[18]	2013	P	TP	L	M	3T C	HPN	BX BT	PM	CA	No	4	No	Yes
Eslami	[75]	2013	D	TP	L	M	3T C	UM	BX BT	PM	USA	No	4	No	Yes

Status: **P** = Phantom study, **C** = Clinical study, **D** = Design, **An** = Animal study

Access approach: **TP** = Transperineal, **TR** = Transrectal, **TG** = Transgluteal

Patient position: **L** = Lithomy, **Pr** = Prone, **S** = Supine, **LD** = Lateral Decubitus

Insertion method: **M** = Manual, **A** = Automated, **TO** = Teleoperated, **ST** = (with) Steering

MRI type: **C** = Closed, **O** = Open

Actuation method: **PZ** = Piezo motor, **UM** = Ultrasonic motor, **HPN** = House made Pneumatic motor, **PN** = Pneumatic, **HY** = Hydraulic, **DC** = DC motor, **DEA** = Dielectric Elastomer Actuator

BX = Biopsy, **BT** = (low dose) Brachytherapy, **RFA** = Radio Frequency Ablation, **MP** = Marker Placement, **CA** = Cryo Ablation

Registration method: **PM** = Passive Marker, **PC** = Passive Coil

the end effector. The robot was used on 16 patients for MRI-guided spine injection. The mechanical accuracy of the robot was sub-millimeter. Zangos *et al.* in [84] reported using Innomotion for prostate biopsy in 20 patients. The procedure was successful with no complications. The median time for the whole procedure was reported to be 40 min. Table 2.2 compares the robots developed for MRI-guided prostate biopsy and brachytherapy.

2.5 Case for teleoperated needle steering under MRI guidance

2.5.1 Error sources in MRI-guided robotic needle placement

An accuracy study of robotic systems for MRI-guided prostate needle placement was presented in [33]. The maximum tolerable error in biopsy is 5 mm which is the radius of a clinically significant tumore assuming that it has a spherical shape. Between intrinsic and extrinsic sources, the former is of particular interest from the robotic point of view. This source of error consists of robotic system errors (registration error, manipulators' inaccuracies, and the needle artifact) and error caused by needle-tissue interaction (needle deflection, prostate motion, and displacement). Among these two parts, the robotic sources are smaller according to literature. For example, Seifabadi *et al.* in [33] concluded that of the 2.5 mm overall error in phantom under MRI guidance, 1.3 mm was caused by intrinsic sources and 2.13 mm by the extrinsic sources (errors are vectors). Stoianovici *et al.* in [68] reported the overall error being 1.15 mm in a phantom study. In [71] and [77], the overall error in a phantom study was reported to be 2.6 mm and 2 mm, respectively. But when inserting a needle into a real prostate, the error is larger. For instance, Tokuda *et al.* in [46] reported an average 5.4 mm error in prostate biopsy and Blumenfeld *et al.* in [85] reported 6.8 mm error for MRI-guided prostate biopsy in 10 cases. The finding that errors caused by needle-tissue interaction are larger is somewhat straightforward, since the real tissue and perineum are stiffer than phantom tissue. Furthermore, the gland rotates and deforms,

something that is difficult to mimic in phantoms. In conclusion, the error caused during needle insertion is of particular importance and attention. This error may be even more significant in brachytherapy, where many needles have to be inserted into prostate to deploy radioactive seeds. In the following sections, different methods for compensation of this error are reviewed.

2.5.2 Methods of compensation for error caused during needle insertion

Numerous studies have been reported on methods of error estimation/prediction and error compensation during needle insertion. Abolhassani *et al.* in [86] reviewed these methods in detail. They grouped methods for error estimation/prediction into three categories: 1) methods that help control the accuracy of needle insertion by modeling insertion forces [87], 2) methods that estimate the error by modeling tissue deformation during needle insertion ([88] and [89]), and 3) methods that estimate the error by modeling needle deflection [90]. Methods of error estimation are not in the scope of this study. Instead, in this chapter, we focus on different insertion techniques that robots can offer to compensate for errors. We found the following methods in the literature that reduced the error caused during needle insertion:

- 1- Lagerburg *et al.* in [78] proposed a tapping method to decrease the insertion force. Tapping means the oscillation of needle during insertion which results in reducing friction and therefore, decreasing the force between the needle and the tissue. As the insertion force becomes smaller, prostate motion and deformation as well as the needle deflection decreases. The efficacy of tapping was investigated in 30 patients who underwent transperineal ultrasound-guided brachytherapy. The needle placement error reduced from a mean of 5.9 mm to 0.9 mm [range of 0 - 2.0 mm] as a result of tapping as reported in [79]. Although this results are quite remarkable, this method has not been used by others;

- 2- Patriciu *et al.* in [47] suggested fast needle insertion during MRI-guided transperineal prostate brachytherapy to reduce the error caused by prostate motion. The method was 1.15 mm accurate in seed placement in phantom and 2.5 mm in a canine study. We think that this method may place some risk on patient's safety due to the high speed of the needle;
- 3- Badaan *et al.* in [91] reported continuous spinning of the needle as a practical solution to lower insertion force. The main concern about this method is possible tissue damage as a result of the needle spinning.

In addition to the abovementioned limitations, these methods cannot entirely eliminate the error and rather reduce the error to some extent since they assume the target does not move during the needle insertion. A possible improved approach that addresses this issue is flexible needle steering, meaning a technique to maneuver the needle tip inside the tissue under visual guidance until it reaches the target.

2.5.3 Different methods of needle steering

Three methods have been proposed for steering a flexible needle inside tissue: 1) moving the base of the needle laterally from outside of the tissue during needle insertion [92]. Similar to the steering technique that DiMaio *et al.* presented in [92], Glozman *et al.* in [93] and [94] performed fast path planning and image-guided tracking for the needle in order to avoid obstacles and reach targets. Disadvantages of this method are the large lateral displacement of the needle base and requirement of applying a large force to the tissue. 2) Multiple concentric tubing with pre-bent inner stylet: this method was proposed independently by two teams [95] and [96]. The feasibility of multiple concentric tubing under MRI guidance has recently been reported by Su *et al.* in [45] using the same 6-DOF piezo-actuated robot for transperineal prostate brachytherapy [44]. This method is effective when reaching a target in a cavity. But if targets are located deep inside

tissues, it may not be as effective unless the needle is very close to the target [97]. 3) bevel-tip needle steering [98]: if a bevel-tip needle is inserted into tissue, it bends due to the asymmetric forces applied to the tip. If the needle is rotated 180 degrees, the needle bends in the opposite direction. Compared with the first method, this technique reduces trauma to the patient and compared with the second approach has the advantage of using standard needles and a simple robotic system. In fact, bevel-tip needle steering only needs a combination of linear and rotary movements of needle. Bevel tip needles are commonly used in prostate brachytherapy to make the seed deployment easier. They are also used commonly in biopsy since they enable manual needle steering that physicians naturally do to compensate for the needle deflection.

Bevel-tip needle steering under real-time MRI seems to be the most effective way to compensate for the error introduced during needle insertion, considering the limitations of other two methods as mentioned above. Although this idea was initially proposed to avoid obstacles, it can be used to improve accuracy as well.

2.5.4 Teleoperated approach for MRI-guided bevel-tip needle steering

Robot-assisted bevel-tip needle steering can be automated or performed by a human-operated master-slave system. Each of these approaches has advantages and disadvantages as discussed in [23]. The automated approach may be faster and lead to less traumatic to the patient since it requires the fewer number of insertions. However, it relies on knowledge of tissue and needle deformation as the needle is inserted. There is no such model available yet which can precisely predict needle-tissue deformation and prostate motion. On the other hand, human-operated needle steering does not entail a model of needle-tissue interaction since it is performed in a trial and error fashion. The biggest advantage, however, is having continuous human supervision during

the procedure. For the advantages mentioned above, master-slave bevel-tip needle steering seems to be a promising approach to compensate for the error caused during needle insertion.

2.5.5 Previous work on teleoperated needle insertion under MRI guidance

Teleoperated needle insertion under MRI-guidance was reported in the literature. Kokes *et al.* in [28] reported a 1-DOF hydraulically actuated needle insertion device for breast radio frequency ablation (RFA) under MRI guidance using a PHANTOM haptic device placed outside of the MRI room. They used a commercial non-MRI-compatible force sensor on the slave side to monitor the force applied to the needle to detect suspicious tissues that feel harder than their surroundings. Yang *et al.* in [20] (the same group) proposed a pneumatically actuated version of the 1-DOF system. They used a 3-DOF MRI-compatible force sensor to monitor the force [112]. Elhawary *et al.* in [59] reported a 5-DOF robotic system using linear piezo-ceramic motors for transrectal prostate biopsy in 1.5T MRI. This system employed a remotely-driven touch-screen needle insertion console placed inside the scanner room. Tse *et al.* in [60] reported a 1-DOF master robot to command the same robot from outside of the scanner room. Su *et al.* in [43] reported design requirements for teleoperated needle insertion under real-time MRI for prostate brachytherapy. They proposed using a commercial haptic device as the master robot to command the needle driver from outside of the room. Seifabadi *et al.* in [73] reported the feasibility of teleoperated needle insertion with a single DOF piezo-actuated needle insertion device integrated with a 4-DOF pneumatically actuated robot for transperineal biopsy and brachytherapy [41] and commanding it remotely by an MRI-compatible manually actuated master device. Piccin *et al.* in [99] reported development of a single-DOF master device to remotely command the needle driver module of a 5-DOF CT/MRI-guided patient-mounted needle placement robot. IMRIS (Winnipeg, Canada) has recently developed a master console like da Vinci (Intuitive Surgical co., CA, USA)

to remotely perform intraoperative intervention under MRI guidance (Figure 2.4) using two NeuroArms⁷ (an MRI-compatible robot for MRI-guided brain needle placement [100]) as the slave robots.

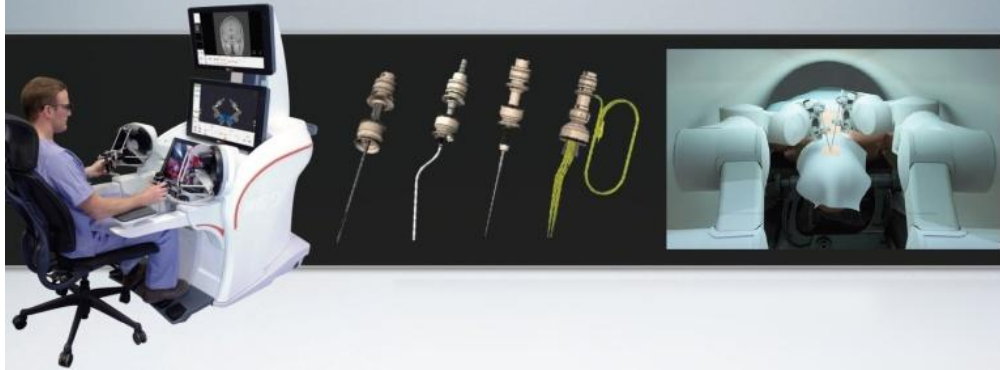


Figure 2.4: SYMBIS Surgical System - the new MRI-compatible robotic neurosurgery platform⁸.

2.6 Enabling technologies for teleoperated needle steering under MRI guidance

2.6.1 MRI-compatible haptic devices

Clinicians prefer to stay inside the operating room during interventions. This means that the master robot should be MRI-compatible. Since commercial haptic devices are not designed to be MRI-compatible, such haptic devices should be developed for the needle steering task. Fischer *et al.* in [101] proposed two simple conceptual designs of haptic devices for teleoperated prostate brachytherapy under MRI guidance for the (slave) robot reported in [44]. Seifabadi *et al.* in [24] designed a 2-DOF master robot that enables needle steering using piezo actuation (see Chapter 5). A Pecullier-Lipkin mechanism was used to convert the rotary motion of a piezo motor into

⁷ <http://www.neuroarm.org/> [Accessed on May 2013]

⁸ http://surgrob.blogspot.com/2012/11/symbis-surgical-system-new-neurarm-mr.html?goback=%2Egde_1771311_member_187500688 [Accessed on May 2013]

linear motion. The actuators were attached to the master robot's base in order to minimize the moving inertia. The design and study of MRI-compatible haptic device have also been reported in the context of fMRI (neuroscience study of the brain under functional MRI imaging) as reported in [26], [27].

2.6.2 MRI-compatible force sensor

For teleoperated needle insertion and steering, it is beneficial to measure and feedback the forces applied to the needle to the clinician's hand through the master robot, so that the clinician could have a more realistic feeling of performing the insertion procedure. A force sensor is also desired on the master side for bilateral teleoperation [102]. Another motivation is to address the non-backdrivability of the piezo motors as mentioned previously [24]. Non-backdrivability means that the motion cannot be initiated. Despite the need for MRI-compatible force sensors, no such commercial sensors are available. ATI (ATI Industrial Automation, Apex, NC, USA) has developed a non-magnetic version of the commonly used Nano17 but the strain gauges utilized can interfere with the magnetic field of MRI.

MRI-compatible technologies such as hydrostatic pressure sensing, optical micrometry, absolute light intensity, differential light intensity, and differential optic fiber have been reported in the literature[42]. Tada *et al.* in [103] developed an optical 2-axis force sensor (x, y) without any metal or electronic components in the sensing element using photo sensors and optical fibers. The force sensor had no SNR distortion and the results showed linear and decoupled readings. In [104], the same group developed a three-axis MRI-compatible force sensor using a new MRI-compatible optical micrometry. Optoelectronic devices and pairs of optical fibers were used to measure forces in three directions. Chapuis *et al.* in [105] designed a simple and efficient 1-DOF torque sensor based on light intensity measurement over optical fibers for a fMRI study. Tokuno

et al. in [106] used a parallel plate structure to develop a 1-DOF MRI-compatible optical force sensor. It utilized an optical micrometry based on differential measures of light intensity. The sensor's head components were made of glass fiber to reduce hysteresis behavior. A 3-DOF MRI-compatible force sensor based on optical sensing principle and using a flexible structure was reported in [107]. This sensor only measured forces, and was bulky for the small range of forces that it can measure ($\pm 3\text{N}$). Polygerinos *et al.* in [108] presented a prototype design and development of a small MRI-compatible fiber-optic force sensor for sensing axial and lateral forces during MRI-guided cardiac catheterization. In [108] and [109], they reviewed other fiber-optic force/pressure sensors for catheters. In [110], they developed a triaxial force sensor for cardiac catheterization. In their work, a fiber-optic cable interrogated a reflective surface at a predefined distance inside a catheter shaft based on light intensity modulation.

Tan *et al.* in [111] developed a 3-DOF axial force sensor with small coupling effects between DOFs. Due to the hysteresis behavior of the plastic materials used, it was necessary to model the hysteresis behavior. In addition, the sensor was very bulky ($50\times 50\times 50\text{ mm}$) in comparison with the small range of force it was designed for ($0\sim 6\text{ N}$). This force sensor was used later for the breast RFA robot reported in [20]. Su *et al.* in [42] developed a 3-DOF force/torque sensor (two DOF torques and one force). This sensor was designed to be used in the transperineal robot for prostate brachytherapy reported in [44]. Monfaredi *et al.* in [25] reported a decoupled MRI-compatible 2-DOF force/torque sensor using FBG sensors for robot-assisted MRI-guided prostate interventions. Despite its small footprint ($\varnothing = 14\text{ mm}$, Height = 17 mm), it was able to measure axial forces between $\pm 20\text{N}$ and axial torque of $\pm 200\text{ Nmm}$ with 0.1 N and 1 Nmm resolution. The sensor by design was decoupled and therefore, the calibration was straightforward. Ataollahi *et al.* in [112] reported a novel force sensing approach employing a prismatic-tip optical fiber

inside an ortho-planar spring structure. The sensor was 1-DOF for compression force only. Moerman *et al.* in [113] used FBG sensors to measure forces up to 15 N for a novel MRI-compatible soft tissue indenter. Hora *et al.* in [114] reported a 2-DOF force sensor using non-magnetic materials and optical fibers to measure interaction force between the user and the fMRI 2-DOF joystick.

2.6.3 Real-time target tracking

In order to enable needle steering under real-time MRI guidance, both the needle tip and target must be tracked in real-time with an update frequency better than 10 Hz. Real-time 3D target tracking was reported in MRI-guided focused ultrasound ablations by Reis *et al.* in [115] for moving tissues. Target tracking is a medical image computing task and is beyond the scope of this study.

2.6.4 Real-time needle tracking

Autonomous image-based tracking of the needle tip in real-time is a challenging task due to the following reasons: 1) it is difficult to capture 3D shape of the needle in 2D image plane, 2) needle leaves a large artifact on the image, and 3) real-time MRI has some latency (~500 ms). Localization of needle tip within image artifact has been studied in [116]. One alternative approach which does not require real-time MRI is tracking the needle shape and tip by embedding 3 optical fibers along the needle shaft and placing some FBG sensors at certain locations in order to estimate the needle curve from the strain information as suggested by Park *et al.* [117]. This method offers a more accurate method to track the needle tip with higher bandwidth than real-time MRI.

2.7 Conclusions

In this chapter, we thoroughly reviewed the previous work on MRI-guided robot-assisted prostate biopsy and brachytherapy systems. We discussed the sensors, actuators, and design challenges of this field. Manually actuated and robotic systems developed for prostate biopsy and brachytherapy under MRI-guidance were reviewed in detail and compared. To the best of our knowledge, there is not such a detailed study in literature. Then, we made the case of why teleoperated needle steering under real-time MRI is presently of particular interest in this field. Afterward, technologies that enable teleoperated needle steering under MRI-guidance were discussed.

References

- [1] C. M. Tempany, S. Straus, N. Hata and S. Haker, "MR - guided prostate interventions," *Journal of Magnetic Resonance Imaging*, vol. 27, pp. 356-367, 2008.
- [2] R. Siegel, D. Naishadham and A. Jemal, "Cancer statistics, 2012," *CA: A Cancer Journal for Clinicians*, 2012.
- [3] B. H. Han, K. Wallner, G. Merrick, W. Butler, S. Sutlief and J. Sylvester, "Prostate brachytherapy seed identification on post-implant TRUS images," *Med. Phys.*, vol. 30, pp. 898, 2003.
- [4] J. F. Schenck, F. A. Jolesz, P. B. Roemer, H. E. Cline, W. E. Lorensen, R. Kikinis, S. G. Silverman, C. J. Hardy, W. D. Barber, and E. T. Laskaris. "Superconducting open configuration MR imaging system for image-guided therapy," *Radiology*, vol. 195, pp. 805–814, 1995.

- [5] A. V. D'Amico, R. Cormack, C. M. Tempany, S. Kumar, G. Topulos, H. M. Kooy and C. N. Coleman, "Real-time magnetic resonance image-guided interstitial brachytherapy in the treatment of select patients with clinically localized prostate cancer," *International Journal of Radiation, Oncology, Biology Physics*, vol. 42, pp. 507-515, 1998.
- [6] M. Moore, N. L. Robertson, N. Arsanious, T. Middleton, A. Villers, L. Klotz, S. S. Taneja and M. Emberton, "Image-Guided Prostate Biopsy Using Magnetic Resonance Imaging-Derived Targets: A Systematic Review," *Eur. Urol.*, 2012.
- [7] D. Yakar and J. J. Fütterer, "MR-Guided Prostate Biopsy," *Interventional Magnetic Resonance Imaging*, pp. 227-235, 2012.
- [8] J. G. R. Bomers, J. P. M. Sedelaar, J. O. Barentsz and J. J. Fütterer, "MRI-Guided Interventions for the Treatment of Prostate Cancer," *Am. J. Roentgenol.*, vol. 199, pp. 714-720, 2012.
- [9] J. J. Fütterer and J. O. Barentsz, "MRI-guided and robotic-assisted prostate biopsy," *Curr. Opin. Urol.*, vol. 22, pp. 316-319, 2012.
- [10] K. J. Macura and D. Stoianovici, "Advancements in Magnetic Resonance-Guided Robotic Interventions in the Prostate," *Topics in Magnetic Resonance Imaging: TMRI*, vol. 19, pp. 297, 2008.
- [11] K. M. Pondman, J. J. Fütterer, B. ten Haken, L. J. Schultze Kool, J. A. Witjes, T. Hambroek, K. J. Macura and J. O. Barentsz, "MR-guided biopsy of the prostate: an overview of techniques and a systematic review," *Eur. Urol.*, vol. 54, pp. 517-527, 2008.

- [12] A. Krieger. "Advances in magnetic resonance image guided robotic intervention". *Ph.D. dissertation, Dept. Mech. Eng., Johns Hopkins Univ., Baltimore, MD, 2008.*
- [13] K. E. Bannan, W. B. Handler, C. Wyenberg, B. A. Chronik, and S. P. Salisbury, "Prediction of Force and Image Artifacts Under MRI for Metals Used in Medical Devices,". *IEEE/ASME Transactions on Mechatronics*, vol. 18(3), pp. 954 – 962, 2013.
- [14] R. Gassert, A. Yamamoto, D. Chapuis, L. Dovat, H. Bleuler and E. Burdet, "Actuation methods for applications in MR environments," *Concepts in Magnetic Resonance Part B: Magnetic Resonance Engineering*, vol. 29, pp. 191-209, 2006.
- [15] I. Bricault, N. Zemiti, E. Jouniaux, C. Fouard, E. Taillant, F. Dorandeu and P. Cinquin, "Light puncture robot for CT and MRI interventions," *Engineering in Medicine and Biology Magazine, IEEE*, vol. 27, pp. 42-50, 2008.
- [16] K. Suzumori, T. Hashimoto, K. Uzuka and I. Enomoto, "Pneumatic direct-drive stepping motor for robots," in *Intelligent Robots and Systems, 2002. IEEE/RSJ International Conference on, 2002*, pp. 2031-2036.
- [17] D. Stoianovici, A. Patriciu, D. Petrisor, D. Mazilu and L. Kavoussi, "A new type of motor: pneumatic step motor," *Mechatronics, IEEE/ASME Transactions on*, vol. 12, pp. 98-106, 2007.
- [18] G. Miron, A. Girard, J. S. Plante and M. Lepage, "Design and Manufacturing of Embedded Air-Muscles for a Magnetic Resonance Imaging Compatible Prostate Cancer Binary Manipulator," *Journal of Mechanical Design*, 2013.

- [19] G. S. Fischer, I. Iordachita, C. Csoma, J. Tokuda, S. P. DiMaio, C. M. Tempany, N. Hata and G. Fichtinger, "MRI-compatible pneumatic robot for transperineal prostate needle placement," *Mechatronics, IEEE/ASME Transactions on*, vol. 13, pp. 295-305, 2008.
- [20] B. Yang, U. X. Tan, A. B. McMillan, R. Gullapalli and J. P. Desai, "Design and control of a 1-DOF MRI-compatible pneumatically actuated robot with long transmission lines," *Mechatronics, IEEE/ASME Transactions on*, vol. 16, pp. 1040-1048, 2011.
- [21] M. G. Schouten, J. G. R. Bomers, D. Yakar, H. Huisman, E. Rothgang, D. Bosboom, T. W. J. Scheenen, S. Misra and J. J. Fütterer, "Evaluation of a robotic technique for transrectal MRI-guided prostate biopsies," *Eur. Radiol.*, vol. 22, pp. 476-483, 2012.
- [22] S. Jiang, W. Feng, P. Zheng, J. Liu and J. Yang, "Pneumatic position servo control of magnetic resonance compatible needle insertion robot," *Proc. Inst. Mech. Eng. Part C*, 2012.
- [23] G. Cole, K. Harrington, H. Su, A. Camilo, J. Pilitsis and G. Fischer, "Closed-loop actuated surgical system utilizing real-time in-situ MRI guidance," in *12th International Symposium on Experimental Robotics-ISER*, 2010, pp. 2489-2495.
- [24] R. Seifabadi, I. Iordachita and G. Fichtinger, "Design of a teleoperated needle steering system for MRI-guided prostate interventions," in *Biomedical Robotics and Biomechatronics (BioRob), 2012 4th IEEE RAS & EMBS International Conference on*, 2012, pp. 793-798.

- [25] R. Monfaredi, R. Seifabadi, G. Fichtinger, and I. Iordachita, "Design of a decoupled MRI-compatible force sensor for robot-assisted prostate interventions," *In SPIE Medical Imaging*, pp. 867118-867118, 2013.
- [26] R. Gassert, R. Moser, E. Burdet and H. Bleuler, "MRI/fMRI-compatible robotic system with force feedback for interaction with human motion," *Mechatronics, IEEE/ASME Transactions on*, vol. 11, pp. 216-224, 2006.
- [27] E. Burdet, R. Gassert, G. Gowrishankar, D. Chapuis and H. Bleuler, "fMRI-compatible haptic interfaces to investigate human motor control," *Experimental Robotics IX*, pp. 25-34, 2006.
- [28] R. Kokes, K. Lister, R. Gullapalli, B. Zhang, A. MacMillan, H. Richard and J. P. Desai, "Towards a teleoperated needle driver robot with haptic feedback for RFA of breast tumors under continuous MRI," *Med. Image Anal.*, vol. 13, pp. 445-455, 2009.
- [29] K. Tadakuma, L. DeVita, J. Plante, Y. Shaoze and S. Dubowsky, "The experimental study of a precision parallel manipulator with binary actuation: With application to MRI cancer treatment," in *Robotics and Automation, 2008. ICRA 2008. IEEE International Conference on*, 2008, pp. 2503-2508.
- [30] S. Proulx and J. S. Plante, "Design and Experimental Assessment of an Elastically Averaged Binary Manipulator Using Pneumatic Air Muscles for Magnetic Resonance Imaging Guided Prostate Interventions," *Journal of Mechanical Design*, vol. 133, 2011.
- [31] S. C. Ryu, Z. F. Quek, P. Renaud, R. J. Black, B. L. Daniel and M. R. Cutkosky, "An optical actuation system and curvature sensor for a MR-compatible active needle," in

- Robotics and Automation (ICRA), 2012 IEEE International Conference on*, 2012, pp. 1589-1594.
- [32] R. Gassert, E. Burdet and K. Chinzei, "Opportunities and challenges in MR-compatible robotics," *Engineering in Medicine and Biology Magazine, IEEE*, vol. 27, pp. 15-22, 2008.
- [33] R. Seifabadi, N. B. J. Cho, S. E. Song, J. Tokuda, N. Hata, C. M. Tempany, G. Fichtinger and I. Iordachita, "Accuracy study of a robotic system for MRI - guided prostate needle placement," *The International Journal of Medical Robotics and Computer Assisted Surgery*, 2012.
- [34] A. Krieger, G. Metzger, G. Fichtinger, E. Atalar and L. Whitcomb, "A hybrid method for 6-DOF tracking of MRI-compatible robotic interventional devices," in *Robotics and Automation, 2006. ICRA 2006. Proceedings 2006 IEEE International Conference on*, 2006, pp. 3844-3849.
- [35] K. Chinzei, N. Hata, F. Jolesz and R. Kikinis, "Surgical assist robot for the active navigation in the intraoperative MRI: Hardware design issues," in *Intelligent Robots and Systems, 2000.(IROS 2000). Proceedings. 2000 IEEE/RSJ International Conference on*, 2000, pp. 727-732.
- [36] S. Hushek, B. Fetics, and R. Moser, "Initial clinical experience with a passive electromagnetic 3D locator system," in *Proc. 5th Interventional MRI Symposium*, 2004.

- [37] R. C. Susil, A. Krieger, J. A. Derbyshire, A. Tanacs, L. L. Whitcomb, G. Fichtinger and E. Atalar, "System for MR Image-guided Prostate Interventions: Canine Study 1," *Radiology*, vol. 228, pp. 886-894, 2003.
- [38] R. C. Susil, K. Camphausen, P. Choyke, E. R. McVeigh, G. S. Gustafson, H. Ning, R. W. Miller, E. Atalar, C. N. Coleman and C. Ménard, "System for prostate brachytherapy and biopsy in a standard 1.5T MRI scanner," *Magnetic Resonance in Medicine*, vol. 52, pp. 683-687, 2004.
- [39] D. Beyersdorff, A. Winkel, B. Hamm, S. Lenk, S. A. Loening and M. Taupitz, "MR Imaging-guided Prostate Biopsy with a Closed MR Unit at 1.5T: Initial Results1," *Radiology*, vol. 234, pp. 576-581, 2005.
- [40] R. Susil, J. Anderson and R. Taylor, "A single image registration method for CT guided interventions," in *Medical Image Computing and Computer-Assisted Intervention—MICCAI'99*, 1999, pp. 798-808.
- [41] S. E. Song, N. B. Cho, G. Fischer, N. Hata, C. Tempny, G. Fichtinger and I. Iordachita, "Development of a pneumatic robot for MRI-guided transperineal prostate biopsy and brachytherapy: New approaches," in *Robotics and Automation (ICRA), 2010 IEEE International Conference on*, 2010, pp. 2580-2585.
- [42] H. Su and G. S. Fischer, "A 3-axis optical force/torque sensor for prostate needle placement in magnetic resonance imaging environments," in *Technologies for Practical Robot Applications, 2009. TePRA 2009. IEEE International Conference on*, 2009, pp. 5-9.

- [43] H. Su, W. Shang, G. A. Cole, K. Harrington and G. S. Fischer, "Haptic system design for MRI-guided needle based prostate brachytherapy," in *Haptics Symposium, 2010 IEEE*, 2010, pp. 483-488.
- [44] H. Su, M. Zervas, G. A. Cole, C. Furlong and G. S. Fischer, "Real-time MRI-guided needle placement robot with integrated fiber-optic force sensing," in *Robotics and Automation (ICRA), 2011 IEEE International Conference on*, 2011, pp. 1583-1588.
- [45] H. Su, D. C. Cardona, W. Shang, A. Camilo, G. A. Cole, D. C. Rucker, R. Webster and G. S. Fischer, "A MRI-guided concentric tube continuum robot with piezoelectric actuation: A feasibility study," in *Robotics and Automation (ICRA), 2012 IEEE International Conference on*, 2012, pp. 1939-1945.
- [46] J. Tokuda, K. Tuncali, I. Iordachita, S. E. Song, A. Fedorov, S. Oguro, A. Lasso, F. M. Fennessy, C. M. Tempany and N. Hata, "In-bore setup and software for 3T MRI-guided transperineal prostate biopsy," *Phys. Med. Biol.*, vol. 57, pp. 5823, 2012.
- [47] A. Patriciu, D. Petrisor, M. Muntener, D. Mazilu, M. Schär and D. Stoianovici, "Automatic brachytherapy seed placement under MRI guidance," *IEEE Trans. Biomed. Eng.*, vol. 54, pp. 1499, 2007.
- [48] N. Hata, M. Jinzaki, D. Kacher, R. Cormak, D. Gering, A. Nabavi, S. G. Silverman, A. V. D'Amico, R. Kikinis and F. A. Jolesz, "MR imaging-guided prostate biopsy with surgical navigation software: Device validation and feasibility1," *Radiology*, vol. 220, pp. 263-268, 2001.

- [49] S. Zangos, K. Eichler, K. Engelmann, M. Ahmed, S. Dettmer, C. Herzog, W. Pegios, A. Wetter, T. Lehnert and M. G. Mack, "MR-guided transgluteal biopsies with an open low-field system in patients with clinically suspected prostate cancer: technique and preliminary results," *Eur. Radiol.*, vol. 15, pp. 174-182, 2005.
- [50] C. Ménard, R. C. Susil, P. Choyke, G. S. Gustafson, W. Kammerer, H. Ning, R. W. Miller, K. L. Ullman, N. Sears Crouse and S. Smith, "MRI-guided HDR prostate brachytherapy in standard 1.5T scanner," *International Journal of Radiation Oncology* Biology* Physics*, vol. 59, pp. 1414-1423, 2004.
- [51] G. Fichtinger, A. Krieger, R. Susil, A. Tanacs, L. Whitcomb and E. Atalar, "Transrectal prostate biopsy inside closed MRI scanner with remote actuation, under real-time image guidance," *Medical Image Computing and Computer-Assisted Intervention—MICCAI 2002*, pp. 91-98, 2002.
- [52] K. Engelhard, H. Hollenbach, B. Kiefer, A. Winkel, K. Goeb and D. Engehausen, "Prostate biopsy in the supine position in a standard 1.5-T scanner under real time MR-imaging control using a MR-compatible endorectal biopsy device," *Eur. Radiol.*, vol. 16, pp. 1237-1243, 2006.
- [53] A. Krieger, R. C. Susil, C. Ménard, J. A. Coleman, G. Fichtinger, E. Atalar and L. L. Whitcomb, "Design of a novel MRI-compatible manipulator for image guided prostate interventions," *Biomedical Engineering, IEEE Transactions on*, vol. 52, pp. 306-313, 2005.

- [54] R. C. Susil, C. Ménard, A. Krieger, J. A. Coleman, K. Camphausen, P. Choyke, G. Fichtinger, L. L. Whitcomb, C. N. Coleman and E. Atalar, "Transrectal prostate biopsy and fiducial marker placement in a standard 1.5T magnetic resonance imaging scanner," *J. Urol.*, vol. 175, pp. 113-120, 2006.
- [55] A. Krieger, I. I. Iordachita, P. Guion, A. K. Singh, A. Kaushal, C. Ménard, P. A. Pinto, K. Camphausen, G. Fichtinger and L. L. Whitcomb, "An MRI-compatible robotic system with hybrid tracking for MRI-guided prostate intervention," *Biomedical Engineering, IEEE Transactions on*, vol. 58, pp. 3049-3060, 2011.
- [56] J. Cepek, B. Chronik, U. Lindner, J. Trachtenberg and A. Fenster, "Development of an MRI-Compatible Device for Prostate Focal Therapy," *Medical Image Computing and Computer-Assisted Intervention–MICCAI 2012*, pp. 455-462, 2012.
- [57] E. G. Christoforou, I. Seimenis, E. Andreou and N. V. Tsekos, "Development and initial testing of a general-purpose, MR-compatible, manually-actuated manipulator for image-guided interventions," in *Biomedical Robotics and Biomechatronics (BioRob), 2012 4th IEEE RAS & EMBS International Conference on*, 2012, pp. 737-742.
- [58] A. Melzer, B. Gutmann, T. Remmele, R. Wolf, A. Lukoscheck, M. Bock, H. Bardenheuer and H. Fischer, "Innomotion for percutaneous image-guided interventions," *Engineering in Medicine and Biology Magazine, IEEE*, vol. 27, pp. 66-73, 2008.
- [59] H. Elhawary, Z. Tse, M. Rea, A. Zivanovic, B. Davies, C. Besant, N. de Souza, D. McRobbie, I. Young and M. Lamperth, "Robotic system for transrectal biopsy of the

- prostate: Real-time guidance under MRI," *Engineering in Medicine and Biology Magazine, IEEE*, vol. 29, pp. 78-86, 2010.
- [60] Z. Tse, H. Elhawary, M. Rea, I. Young, B. Davis and M. Lamperth, "A haptic unit designed for magnetic-resonance-guided biopsy," *Proc. Inst. Mech. Eng. Part H J. Eng. Med.*, vol. 223, pp. 159-172, 2009.
- [61] A. Krieger, S. E. Song, N. B. Cho, I. Iordachita, P. Guion, G. Fichtinger, L. L. Whitcomb, "Development and Evaluation of an Actuated MRI-Compatible Robotic System for MRI-Guided Prostate Intervention," *Mechatronics, IEEE/ASME Transactions on*, vol. 18, pp. 273-284, 2013.
- [62] J. Bohren, I. Iordachita and L. L. Whitcomb, "Design requirements and feasibility study for a 3-DOF MRI-compatible robotic device for MRI-guided prostate intervention," in *Robotics and Automation (ICRA), 2012 IEEE International Conference on*, 2012, pp. 677-682.
- [63] G. Schouten, J. G. R. Bomers, D. Yakar, H. Huisman, E. Rothgang, D. Bosboom, T. W. J. Scheenen, S. Misra and J. J. Fütterer, "Evaluation of a robotic technique for transrectal MRI-guided prostate biopsies," *Eur. Radiol.*, vol. 22, pp. 476-483, 2012.
- [64] K. Chinzei and K. Miller, "Towards MRI guided surgical manipulator." *Medical Science Monitor: International Medical Journal of Experimental and Clinical Research*, vol. 7, pp. 153, 2001.
- [65] Y. Koseki, N. Koyachi, T. Arai and K. Chinzei, "Remote actuation mechanism for MR-compatible manipulator using leverage and parallelogram-workspace analysis, workspace

- control, and stiffness evaluation," in *Robotics and Automation, 2003. Proceedings. ICRA'03. IEEE International Conference on*, 2003, pp. 652-657.
- [66] Y. Koseki, R. Kikinis, F. Jolesz and K. Chinzei, "Precise evaluation of positioning repeatability of MR-compatible manipulator inside MRI," *Medical Image Computing and Computer-Assisted Intervention—MICCAI 2004*, pp. 192-199, 2004.
- [67] S. DiMaio, S. Pieper, K. Chinzei, N. Hata, S. Haker, D. Kacher, G. Fichtinger, C. Tempany and R. Kikinis, "Robot-assisted needle placement in open MRI: system architecture, integration and validation," *Computer Aided Surgery*, vol. 12, pp. 15-24, 2007.
- [68] D. Stoianovici, D. Song, D. Petrisor, D. Ursu, D. Mazilu, M. Mutener, M. Schar and A. Patriciu, "'MRI Stealth" robot for prostate interventions," *Minimally Invasive Therapy & Allied Technologies*, vol. 16, pp. 241-248, 2007.
- [69] M. Muntener, A. Patriciu, D. Petrisor, D. Mazilu, H. Bagga, L. Kavoussi, K. Cleary and D. Stoianovici, "Magnetic resonance imaging compatible robotic system for fully automated brachytherapy seed placement," *Urology*, vol. 68, pp. 1313-1317, 2006.
- [70] M. Muntener, A. Patriciu, D. Petrisor, M. Schär, D. Ursu, D. Y. Song and D. Stoianovici, "Transperineal Prostate Intervention: Robot for Fully Automated MR Imaging—System Description and Proof of Principle in a Canine Model," *Radiology*, vol. 247, pp. 543-549, 2008.
- [71] J. Tokuda, G. Fischer, C. Csoma, S. DiMaio, D. Gobbi, G. Fichtinger, C. Tempany and N. Hata, "Software strategy for robotic transperineal prostate therapy in closed-bore

MRI," *Medical Image Computing and Computer-Assisted Intervention–MICCAI 2008*, pp. 701-709, 2008.

- [72] S. Song S, N. B. Cho, J. Tokuda, N. Hata, C. M. Tempany, G. Fichtinger, I. Iordachita, "MRI compatibility study of a pneumatically actuated robotic system for transperineal prostate needle placement," *CARS 2010 - Proceedings of the 24th International Congress and Exhibition. Int J CARS*, vol. 5 (1), pp. 26-27.
- [73] R. Seifabadi, S. E. Song, A. Krieger, N. B. Cho, J. Tokuda, G. Fichtinger and I. Iordachita, "Robotic system for MRI-guided prostate biopsy: feasibility of teleoperated needle insertion and ex vivo phantom study," *International Journal of Computer Assisted Radiology and Surgery*, vol. 7, pp. 181-190, 2012.
- [74] J. Tokuda, S. E. Song, G. S. Fischer, I. I. Iordachita, R. Seifabadi, N. B. Cho, K. Tuncali, G. Fichtinger, C. M. Tempany and N. Hata, "Preclinical evaluation of an MRI-compatible pneumatic robot for angulated needle placement in transperineal prostate interventions," *International Journal of Computer Assisted Radiology and Surgery*, vol. 7(6), pp. 949-957, 2012.
- [75] S. Eslami, GS. Fischer, J. Tokuda, N. Hata, CM. Tempany, and I. Iordachita., "Towards Clinically Optimized MRI-guided Surgical Manipulator for Minimally Invasive Prostate Percutaneous Interventions: Constructive Design," in *Robotics and Automation, 2013. ICRA 2013. IEEE International Conference on*, in press.

- [76] A. Goldenberg, J. Trachtenberg, W. Kucharczyk, Y. Yi, M. Haider, L. Ma, R. Weersink and C. Raoufi, "Robotic system for closed-bore MRI-guided prostatic interventions," *Mechatronics, IEEE/ASME Transactions on*, vol. 13, pp. 374-379, 2008.
- [77] M. R. van den Bosch, M. R. Moman, M. van Vulpen, J. J. Battermann, E. Duiveman, L. J. van Schelven, H. de Leeuw, J. J. W. Lagendijk and M. A. Moerland, "MRI-guided robotic system for transperineal prostate interventions: proof of principle," *Phys. Med. Biol.*, vol. 55(5), pp. 133-140, 2010.
- [78] V. Lagerburg, M. Moerland, M. Konings, R. Van de Vosse, J. Lagendijk and J. Battermann, "Development of a tapping device: a new needle insertion method for prostate brachytherapy," *Phys. Med. Biol.*, vol. 51, pp. 891, 2006.
- [79] V. Lagerburg, M. A. Moerland, M. van Vulpen and J. J. W. Lagendijk, "A new robotic needle insertion method to minimise attendant prostate motion," *Radiotherapy and Oncology*, vol. 80, pp. 73-77, 2006.
- [80] S. Abdelaziz, L. Esteveny, P. Renaud, B. Bayle, L. Barbé, M. De Mathelin and A. Gangi, "Design considerations for a novel MRI-compatible manipulator for prostate cryoablation," *International Journal of Computer Assisted Radiology and Surgery*, vol. 6, pp. 811-819, 2011.
- [81] S. Abdelaziz, L. Esteveny, L. Barbé, P. Renaud, B. Bayle and M. de Mathelin, "Development of a MR-compatible cable-driven manipulator: Design and technological issues," in *Robotics and Automation (ICRA), 2012 IEEE International Conference on*, 2012, pp. 1488-1494.

- [82] S. Song, J. Tokuda, K. Tuncali, C. Tempany, E. Zhang and N. Hata, "Development and Preliminary Evaluation of a Motorized Needle Guide Template for MRI-guided Targeted Prostate Biopsy," 2013.
- [83] S. Zangos, C. Herzog, K. Eichler, R. Hammerstingl, A. Lukoschek, S. Guthmann, B. Gutmann, U. J. Schoepf, P. Costello and T. J. Vogl, "MR-compatible assistance system for puncture in a high-field system: device and feasibility of transgluteal biopsies of the prostate gland," *Eur. Radiol.*, vol. 17, pp. 1118-1124, 2007.
- [84] S. Zangos, A. Melzer, K. Eichler, C. Sadighi, A. Thalhammer, B. Bodelle, R. Wolf, T. Gruber-Rouh, D. Proschek and R. Hammerstingl, "MR-compatible assistance system for biopsy in a high-field-strength system: initial results in patients with suspicious prostate lesions," *Radiology*, vol. 259, pp. 903-910, 2011.
- [85] P. Blumenfeld, N. Hata, S. DiMaio, K. Zou, S. Haker, G. Fichtinger and C. Tempany, "Transperineal prostate biopsy under magnetic resonance image guidance: a needle placement accuracy study," *Journal of Magnetic Resonance Imaging*, vol. 26, pp. 688-694, 2007.
- [86] N. Abolhassani, R. Patel and M. Moallem, "Needle insertion into soft tissue: A survey," *Med. Eng. Phys.*, vol. 29, pp. 413-431, 2007.
- [87] C. Simone and A. M. Okamura, "Modeling of needle insertion forces for robot-assisted percutaneous therapy," in *Robotics and Automation, 2002. Proceedings. ICRA'02. IEEE International Conference on*, 2002, pp. 2085-2091.

- [88] S. P. DiMaio and S. Salcudean, "Needle steering and motion planning in soft tissues," *Biomedical Engineering, IEEE Transactions on*, vol. 52, pp. 965-974, 2005.
- [89] R. Alterovitz, K. Goldberg, J. Pouliot, R. Taschereau and I. C. Hsu, "Needle insertion and radioactive seed implantation in human tissues: Simulation and sensitivity analysis," in *Robotics and Automation, 2003. Proceedings. ICRA'03. IEEE International Conference on*, 2003, pp. 1793-1799.
- [90] H. Kataoka, T. Washio, M. Audette and K. Mizuhara, "A model for relations between needle deflection, force, and thickness on needle penetration," in *Medical Image Computing and Computer-Assisted Intervention—MICCAI 2001*, pp. 966-974.
- [91] S. Badaan, D. Petrisor, C. Kim, P. Mozer, D. Mazilu, L. Gruionu, A. Patriciu, K. Cleary and D. Stoianovici, "Does needle rotation improve lesion targeting?" *The International Journal of Medical Robotics and Computer Assisted Surgery*, vol. 7, pp. 138-147, 2011.
- [92] S. DiMaio and S. Salcudean, "Needle steering and model-based trajectory planning," *Medical Image Computing and Computer-Assisted Intervention-MICCAI 2003*, pp. 33-40, 2003.
- [93] D. Glozman and M. Shoham, "Image-guided robotic flexible needle steering," *Robotics, IEEE Transactions on*, vol. 23, pp. 459-467, 2007.
- [94] D. Glozman and M. Shoham, "Flexible needle steering and optimal trajectory planning for percutaneous therapies," *Medical Image Computing and Computer-Assisted Intervention—MICCAI 2004*, pp. 137-144, 2004.

- [95] E. Dupont, J. Lock, B. Itkowitz and E. Butler, "Design and control of concentric-tube robots," *Robotics, IEEE Transactions on*, vol. 26, pp. 209-225, 2010.
- [96] D. C. Rucker, B. A. Jones and R. J. Webster, "A geometrically exact model for externally loaded concentric-tube continuum robots," *Robotics, IEEE Transactions on*, vol. 26, pp. 769-780, 2010.
- [97] C. Walsh, "Image-guided robots for dot-matrix ablation," *PhD dissertation*, Dept. Mech. Eng., *Massachusetts Institute of technology (MIT)*, Chapter 5, 2010.
- [98] J. Webster III, J. S. Kim, N. J. Cowan, G. S. Chirikjian and A. M. Okamura, "Nonholonomic modeling of needle steering," *The International Journal of Robotics Research*, vol. 25, pp. 509-525, 2006.
- [99] O. Piccin, L. Barbé, B. Bayle, M. De Mathelin and A. Gangi, "A force feedback teleoperated needle insertion device for percutaneous procedures," *The International Journal of Robotics Research*, vol. 28, pp. 1154-1168, 2009.
- [100] G. R. Sutherland, P. B. McBeth and D. F. Louw, "NeuroArm: An MR compatible robot for microsurgery," in *International Congress Series*, 2003, pp. 504-508.
- [101] G. S. Fischer, and H. Su, "apparatus and methods for MRI-compatible haptic interface," *U.S. Patent No. 20,120,265,051*, 2012.
- [102] R. Seifabadi, S. Rezaei, S. S. Ghidary, M. Zareinejad and M. Saadat, "To enhance transparency of a piezo-actuated tele-micromanipulator using passive bilateral control," *Robotica*, vol. 28, pp. 689-703, 2010.

- [103] M. Tada, S. Sasaki and T. Ogasawara, "Development of an optical 2-axis force sensor usable in MRI environments," in *Sensors, 2002. Proceedings of IEEE, 2002*, pp. 984-989.
- [104] M. Tada and T. Kanade, "Design of an MR-compatible three-axis force sensor," in *Intelligent Robots and Systems, 2005.(IROS 2005). 2005 IEEE/RSJ International Conference on, 2005*, pp. 3505-3510.
- [105] D. Chapuis, R. Gassert, L. Sacher, E. Burdet and H. Bleuler, "Design of a simple MRI/fMRI-compatible force/torque sensor," in *Intelligent Robots and Systems, 2004.(IROS 2004). Proceedings. 2004 IEEE/RSJ International Conference on, 2004*, pp. 2593-2599.
- [106] T. Tokuno, M. Tada and K. Umeda, "High-precision mri-compatible force sensor with parallel plate structure," in *Biomedical Robotics and Biomechatronics, 2008. BioRob 2008. 2nd IEEE RAS & EMBS International Conference on, 2008*, pp. 33-38.
- [107] P. Puangmali, K. Althoefer and L. D. Seneviratne, "Novel design of a 3-axis optical fiber force sensor for applications in magnetic resonance environments," in *Robotics and Automation, 2009. ICRA'09. IEEE International Conference on, 2009*, pp. 3682-3687.
- [108] P. Polygerinos, P. Puangmali, T. Schaeffter, R. Razavi, L. D. Seneviratne and K. Althoefer, "Novel miniature MRI-compatible fiber-optic force sensor for cardiac catheterization procedures," in *Robotics and Automation (ICRA), 2010 IEEE International Conference on, 2010*, pp. 2598-2603.

- [109] P. Polygerinos, D. Zbyszewski, T. Schaeffter, R. Razavi, L. D. Seneviratne and K. Althoefer, "MRI-compatible fiber-optic force sensors for catheterization procedures," *Sensors Journal, IEEE*, vol. 10, pp. 1598-1608, 2010.
- [110] P. Polygerinos, L. D. Seneviratne, R. Razavi, T. Schaeffter and K. Althoefer, "Triaxial Catheter-Tip Force Sensor for MRI-Guided Cardiac Procedures," 2013.
- [111] X. Tan, B. Yang, R. Gullapalli and J. P. Desai, "Triaxial MRI-compatible fiber-optic force sensor," *Robotics, IEEE Transactions on*, vol. 27, pp. 65-74, 2011.
- [112] A. Ataollahi, A. S. Fallah, L. D. Seneviratne, P. Dasgupta and K. Althoefer, "Novel Force Sensing Approach Employing Prismatic-Tip Optical Fiber Inside an Orthoplanar Spring Structure," 2013 .
- [113] M. Moerman, A. M. J. Sprengers, A. J. Nederveen and C. K. Simms, "A novel MRI-compatible soft tissue indenter and fibre Bragg grating force sensor," *Med. Eng. Phys.*, 2012.
- [114] M. Hara, G. Matthey, A. Yamamoto, D. Chapuis, R. Gassert, H. Bleuler and T. Higuchi, "Development of a 2-DOF electrostatic haptic joystick for MRI/fMRI applications," in *Robotics and Automation, 2009. ICRA'09. IEEE International Conference on*, 2009, pp. 1479-1484.
- [115] M. Ries, B. D. de Senneville, S. Roujol, Y. Berber, B. Quesson and C. Moonen, "Real - time 3D target tracking in MRI guided focused ultrasound ablations in moving tissues," *Magnetic Resonance in Medicine*, vol. 64, pp. 1704-1712, 2010.

- [116] S. E. Song, N. B. Cho, I. Iordachita, P. Guion, G. Fichtinger, K. Camphausen, L. L. Whitcomb, "Biopsy Needle Artifact Localization in MRI-guided Robotic Transrectal Prostate Intervention," *Biomedical Engineering, IEEE Transactions on*, Jul; vol. 59, pp. 1902-1911, 2012.
- [117] Y. L. Park, S. Elayaperumal, B. Daniel, S. C. Ryu, M. Shin, J. Savall, R. J. Black, B. Moslehi and M. R. Cutkosky, "Real-time estimation of 3-D needle shape and deflection for MRI-guided interventions," *Mechatronics, IEEE/ASME Transactions on*, vol. 15, pp. 906-915, 2010.

Chapter 3

Robotic system for MRI-guided prostate biopsy: feasibility of teleoperated needle insertion and ex vivo phantom study

Purpose: Magnetic Resonance Imaging (MRI) combined with robotic assistance has the potential to improve on clinical outcomes of biopsy and local treatment of prostate cancer. **Methods:** We report the workspace optimization and phantom evaluation of a five Degrees of Freedom (DOF) parallel pneumatically actuated modular robot for MRI-guided prostate biopsy. To shorten procedure time and consequently increase patient comfort and system accuracy, a prototype of an MRI-compatible master-slave needle driver module using piezo motors was also added to the base robot. **Results:** Variable size workspace was achieved using appropriate link length, compared to the previous design. The targeting accuracy demonstrated an average error of 2.5 mm (STD = 1.37 mm) in a realistic phantom inside a 3T magnet with a bevel-tip 18G needle. The average position tracking error of the master-slave needle driver was always below 0.1 mm. **Conclusion:** Phantom experiments showed sufficient accuracy for manual prostate biopsy. Also, the implementation of teleoperated needle insertion was feasible and accurate. These two together suggest the feasibility of accurate fully actuated needle placement into prostate while keeping the clinician supervision over the task.

3.1 Introduction

Prostate cancer is the most common cancer in men in the United States. In 2010, over 200,000 men were expected to be diagnosed with prostate cancer with over 32,000 deaths of this disease [1]. Early stage cancer detection is critically important to ensure patient survival. Despite its poor specificity, PSA level is used to determine which patient is a candidate for core needle biopsy.

Each year approximately 1.5 million prostate biopsy procedures are performed only in the United States [2]. For this reason, a surgical biopsy needle is inserted into a predefined target position inside the prostate under image guidance.

Transrectal ultrasound (TRUS) guidance is the “Gold Standard” navigation method for the biopsy due to its real-time nature, relative low cost, and ease of use. However, this imaging modality is not capable of visualizing cancer [3] but rather the contour of prostate, resulting in a significant number of false-negatives in conventional TRUS-guided systematic biopsy, where 6 to 12 cores, equally distributed within the prostate, are sampled.

MRI is a superior imaging modality, primarily due to its high sensitivity for detecting prostate tumors, excellent soft tissue contrast, high spatial resolution, and multi-planar volumetric imaging capabilities [4]. Despite its unique capabilities, MRI has two main limitations when it comes to a robotic approach: strong magnetic field (1.5T or greater) that requires MRI-compatibility of surgical devices, sensors, and actuators as well as physical limitation of in-bore access and workspace.

Several MRI-compatible robots have been reported for prostate intervention. The robotic systems can be categorized into transrectal, transperineal, and transgluteal depending upon the anatomical access method used [8].

1) *Transrectal approach*: In [5]-[7] two generations of MRI-guided systems were developed for transrectal prostate biopsies, therapeutic injections, and marker placements. APT I, had 2-DOF (roll and pitch) and was actuated manually through two flexible shafts coming out of the bore. APT II was used in many clinical procedures at a few healthcare institutions. In [8] a motorized APT was introduced where the roll and pitch movements were actuated using piezo motors. In [9] Beyersdorff *et al.* and in [10] Engelhard *et al.* developed MRI-guided transrectal needle biopsies

in patient studies with a system (Invivo Germany GmbH, Schwerin, Germany) employing manual alignment of a needle sleeve. Elhawary *et al.* reported a prototype robotic system using linear piezo-ceramic motors for transrectal prostate biopsy [11]. This system employed remotely driven needle driver module with haptic force feedback on the master side.

2) *Transperineal Approach*: MRI-guided transperineal prostate intervention was primarily studied in patient experiment inside an open MRI scanner [12] and then conventional closed MRI scanner [13]. In [14] and [15], Chinzei *et al.* and Di Maio *et al.* designed systems to assist transperineal intra-prostatic needle placement. In [16] Tadakuma *et al.* developed an MRI-compatible robot for transperineal needle placement into prostate using dielectric elastomer actuators (DEAs). In [17], Stoianovici *et al.* developed a fully automated pneumatically actuated device for transperineal brachytherapy seed placement in phantom. In [18] Fischer *et al.* developed a pneumatic 2-DOF robot for transperineal prostate needle placement in phantom. In [19] Goldenberg *et al.* developed a robotic system employing ultrasonic piezo actuators for MRI-guided transperineal prostate intervention. In [20] van den Bosch *et al.* reported a hydraulically and pneumatically actuated tapping device to alleviate prostate displacement and deformation during needle insertion. Su reported a 3-DOF Cartesian robot for MRI-guided transperineal needle alignment with a 3-DOF needle steering module for teleoperated and autonomous seed implantation [21] and [22].

3) *Transgluteal Approach*: In [23], Zangos *et al.* proposed and clinically validated the feasibility of manual transgluteal approach with an open 0.2T MRI scanner. In [24] Zangos *et al.* used the Innomotion robot for transgluteal approach in a cadaver study at 1.5T.

With use of low friction MRI-compatible pneumatic actuators, a high field 3T MRI-guided prostate intervention system was developed for transperineal needle placement procedures. Figure 3.1 shows the latest robot prototype that provides 4-DOF surgical needle alignment in MRI

coordinate with a platform for the manual needle insertion as the 5-th DOF. The previous reports focused on pneumatic actuator control, workspace design and targeting functions [25], signal-to-noise ratio (SNR) test for MRI-compatibility [26], and overall system integration and procedural description [27]. In this study, we report the latest workspace optimization of the robot and targeting accuracy assessment in a commercial prostate phantom. Also, the robot sterilization is addressed.

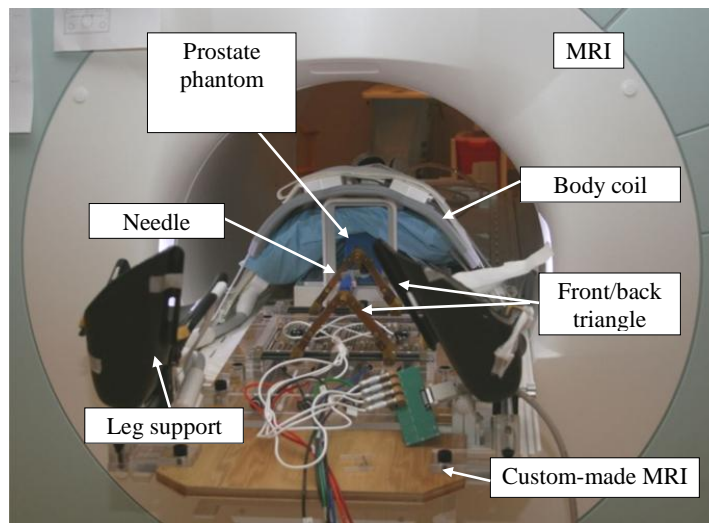


Figure 3.1: Latest prototype of the pneumatically actuated 4-DOF robot for MRI-guided transperineal prostate needle placement: experiment inside a 3T magnet using a prostate phantom.

Although this robot is able to align the surgical needle toward a predefined target inside prostate, the needle needs to be inserted manually. For this reason, the patient has to be pulled out of the bore twice for each biopsy, i.e. once for manual insertion and once for tissue removal after taking confirmation image. In order to shorten the procedure time, we have proposed adding a teleoperated needle driver module on the robot which can eliminate the first move-out. This

needle driver is a separate MRI-compatible module driven remotely by a master device placed outside the bore. In this manner, the procedure time can be notably shortened providing patient comfort and the target movement caused by patient motion can be reduced. For the same reason, it may reduce the necessity of confirmation imaging, as well.

Several teleoperated needle placement systems under MRI guidance have been investigated. In [28] Kokes *et al.* reported a teleoperated hydraulic needle driver robot with haptic feedback for radio frequency ablation of breast tumors under continuous MRI guidance. In [29] Su *et al.* reported a 3-DOF teleoperated needle driver installed on a 3-DOF Cartesian linear stage for brachytherapy. In [30] Tse *et al.* reported a 5-DOF robot for needle alignment with a single DOF teleoperated module for transrectal prostate biopsy.

Unlike previously discussed systems, our master device is designed to be placed inside the scanner room as surgeons prefer to be close to the patient during the interventional procedure. This means that conventional (non-MRI compatible) haptic devices cannot be deployed due to the high magnetic field. This chapter reports the preliminary study of a human-controlled needle drive added to an existing robot.

The chapter is organized as follows: system architecture and procedure are discussed in section II. In section III, teleoperated needle driver module is introduced and discussed. Workspace optimization is briefly discussed, as well. In section IV, the overall system needle placement accuracy is evaluated in phantom experiment inside a 3T magnet. Also, the performance of the proposed teleoperated needle insertion driver is evaluated. This chapter is continued by discussion in section V and ended by conclusions and future work in section VI.

3.2 System design

3.2.1 System components

Figure 3.2 shows a diagram of the system components and information flow. In the MRI suite (left side), the patient and the robot are placed inside the scanner and the robot controller is placed at 3 m distance from the scanner's bore. The medical air supply available in a standard hospital is used to run the pneumatic robot. The controller sends the pressure signals (commands) to the robot pneumatic actuators and receives position feedback from the robot optical encoders. There is no

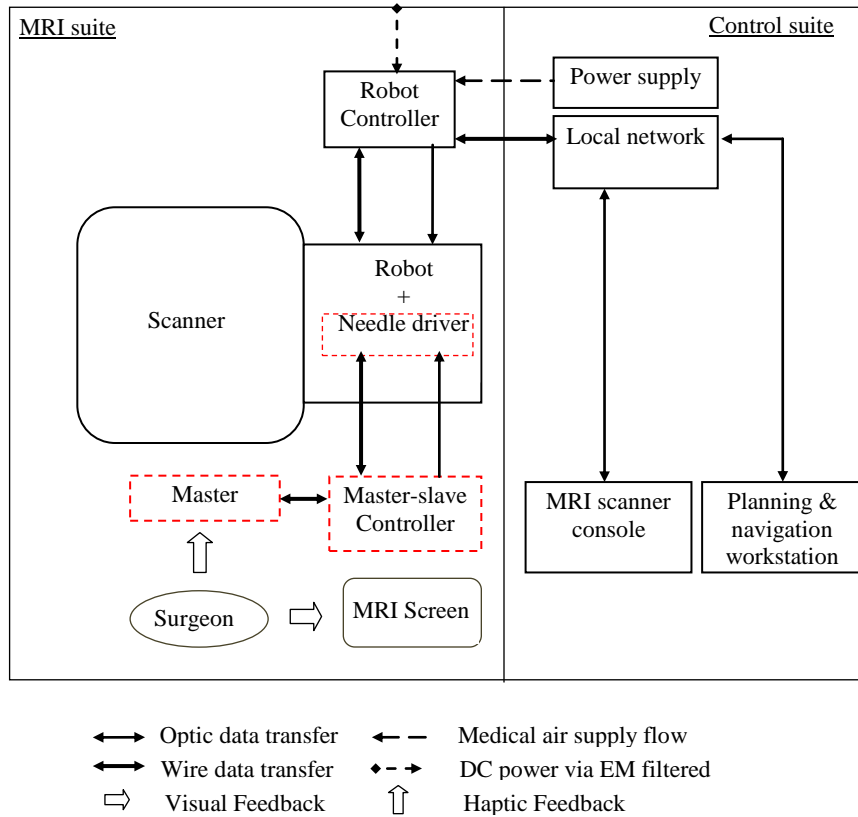


Figure 3.2: Diagram of the system components and information flow: dashed-line boxes show newly added components to the previous setup.

electrical communication between the controller and the robot in order to keep the electromagnetic interference (EMI) minimized. The power supply of the controller is placed in the control room to further reduce the EMI. In the control room (right side), the MRI scanner console is placed. 3D Slicer is running on a Linux-based workstation called planning workstation. Intraoperative MR images are imported from the scanner console to 3D Slicer. Target positions are selected by the clinician in this software and sent as commands to the robot controller. A local network is established among the planning and navigation workstation, the scanner console, and the robot controller. Data communication between the network and robot controller is via fiber-optic Ethernet to avoid EMI.

Dashed-line squares show newly added components to the existing system as discussed above. These components include the master device, the slave (needle driver module), and the master-slave control units. Currently, the needle driver controller is not integrated with the robot controller. The surgeon stands next to the scanner and moves the master console while observing the real-time image. The slave follows the master and performs insertion.

To avoid interference with the pubic arch and urethra, a 4-DOF parallel kinematic structure was proposed [25] (Figure 3.1). The pyramid structure of the robot helps to maximize the use of ‘under-legs’ space and minimize ‘between-legs’ space. If necessary, the workspace can be shifted vertically by inserting a spacer. Timing belts and pulleys transmit each pneumatic cylinder movement to the prismatic manipulation of front and rear triangular structures. These pulleys and timing belts function as external damping mechanism as well to stabilize the cylinder’s dynamic behavior and solve some of the difficulties associated with control of pneumatic actuators. MRI-

compatible optical encoders were used for position sensing. The moving parts were made of Ultem which is sufficiently rigid and MRI-compatible. The needle was located on the linkage connecting the front and back mechanisms.

The controller operates inside the scanner room, approximately 3 m away from the 3T scanner, without functional difficulties or significant image quality degradation [18]. The controller is placed inside an EMI-shielded enclosure and contains the embedded Linux PC providing low-level servo control, the piezoelectric valves, pressure sensors, and the fiber-optic Ethernet media converter. A customized graphical user interface (GUI) specifically designed for the prostate intervention is used with the robot [34].

In case of robot failure, the robot is removed and the procedure is continued manually using a template grid similar to the standard ultrasound-guided procedure [35] and [36].

3.2.2 Robot kinematics

The robot comprises two identical planar mechanisms, front and rear triangles, as shown in Figure 3.3. Each planar parallel structure can move its end-effector within the corresponding plane with the use of two pneumatic actuators. As these two mechanisms are coupled together with a variable-length link and two spherical joints at ends, yaw and pitch orientations are generated as well as x and y translations, resulting in 4 DOF. The insertion is performed manually. Each of the 2-DOF mechanisms provides a workspace covering a circle of 50 mm diameter (Figure 3.3b).

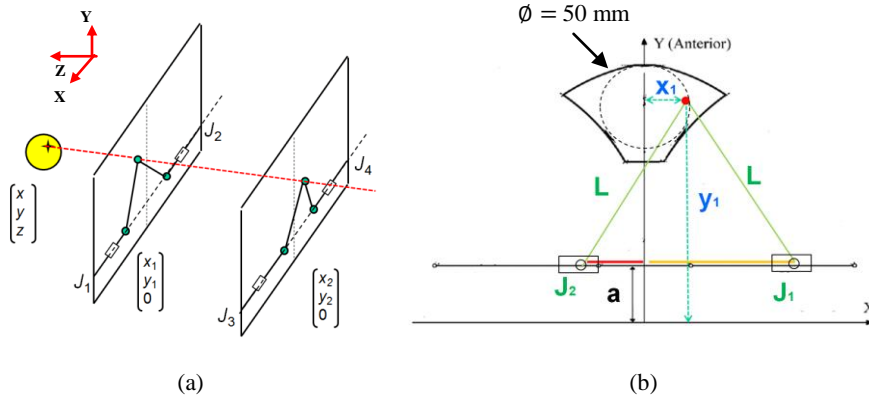


Figure 3.3: Robot kinematics: (a) The manipulator consists of a pair of identical 2-DOF planar mechanisms and (b) planar mechanism workspace and in-plane inverse kinematics relationship are shown.

The way the robot reaches a target (i.e. the inverse kinematics) is as follows: first, a target and a straight trajectory (considering pubic arc/urethra avoidance) are specified by the clinician in the navigation software. These target and trajectory are given in MRI coordinate system, thus needed to be transformed into robot coordinate system. For this reason, Z-frame is used [37]. Then, the intersection of the line defined by the target and the trajectory with the front and rear planes gives us (x_1, y_1) and (x_2, y_2) as shown in Figure 3.3a. Then, each 2-DOF planar mechanism must move as follows so that the effectors reach those coordinates (Figure 3.3b):

$$J_1 = x_1 + \sqrt{(L^2 - (y_1 - a)^2)}, \quad J_2 = x_1 - \sqrt{(L^2 - (y_1 - a)^2)}$$

where J_1 and J_2 are x coordinate of each actuator. Similar relationship holds for J_3 and J_4 (back triangular mechanisms) by replacing x_2 and y_2 for x_1 and y_1 .

3.2.3 Variable workspace

The robot was designed with variable link length so that robot's workspace can easily be modified or intraoperatively changed depending upon the prostate size and height relative to the

table. Considering the robot kinematics (Figure 3.3a), the rear triangle requires larger manipulation range because the front triangle is fundamentally responsible for needle entry area and the rear triangle is responsible for angulations. Also, since the insertion angle is usually upwards i.e. posterior-to-anterior, a shorter rear triangle link length would be beneficial. Originally, 120 mm link length was designed for all triangle links. However, 120 mm / 100 mm for front triangle link, and 120 mm / 100 mm / 80 mm for rear triangle are currently available. Figure 3.4 shows an axial view of 120 mm front - 120 mm rear workspace (a) and 120 mm front - 80 mm rear workspace (b). As seen, the 2D workspace has enlarged because of shortening the back links.

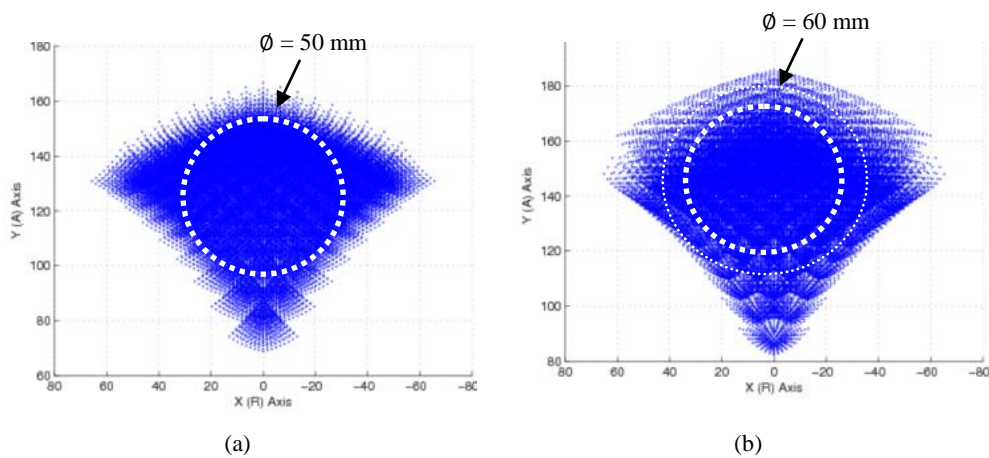


Figure 3.4: 2D view of robot workspace when front/rear triangles links length are changed: (a) 120/120: a sphere of 50 mm diameter represents a relatively large prostate and (b) 120/80: the 2D workspace is enlarged because of shortening the back links.

3.2.4 Sterilization

Prostate biopsies that are performed through the rectum do not require sterilization. In contrast, we propose a system for transperineal access that requires some degree of sterilization. Compared to the conventional prostate biopsy system in which a disposable grid template is used, the brass

tube in the front triangle which guides the needle through (Figure 3.8) is not disposable and rather permanently attached to the links by the front spherical joint. Hence, for the current version, we proposed to dismantle the top parts (Figure 3.8, dashed-line area) as an assembly and send to the plasma sterilization before each procedure. The non-sterile parts are covered by a plastic drape with a small hole for the needle to travel through (Figure 3.5). The use of a drape did not show interference with the robot's movement.

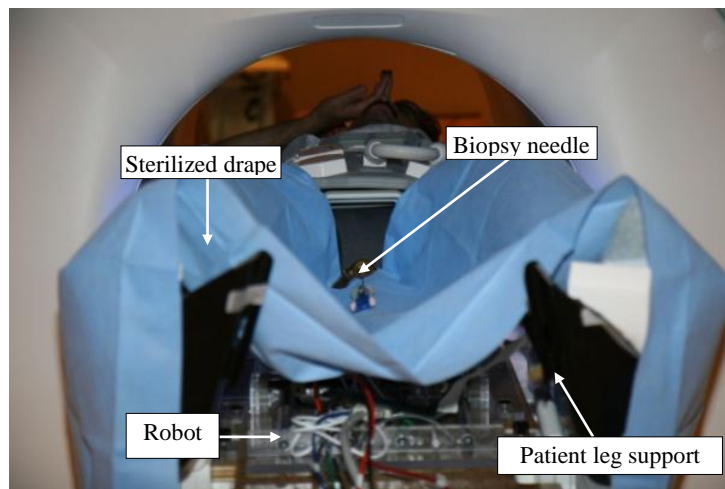


Figure 3.5: Robot is covered by a sterilized drape with a small hole on it for needle travel.

3.3 Needle driver module design

The clinical workflow of this robotic system is as follows:

- 1) Patient is placed inside the bore;
- 2) The Z-frame is placed at a pre-defined position on the custom-made MRI board;
- 3) The Z-frame is scanned and 3D Slicer finds the transformation matrix from the MRI coordinates to robot coordinates;
- 4) The Z-frame is removed;

- 5) The robot is placed between the patient's legs on a pre-defined position on the custom-made MRI board;
- 6) An intraoperative MR image of the anatomy is acquired and imported into the navigation software;
- 7) One target and needle trajectory is specified in the planning workstation;
- 8) The planning software (3D Slicer) sends the transformation matrix and target information to the robot controller;
- 9) The controller solves the inverse kinematics problem and commands the robot actuators to orient the needle toward the target;
- 10) The patient is pulled out of the bore;
- 11) The surgeon inserts the needle manually;
- 12) The patient is placed back into the bore;
- 13) A confirmation image is taken;
- 14) The needle tip is compared with the planned target in the axial plane and the targeting error is found;
- 15) If the error is acceptable (< 5 mm), the patient is pulled out for tissue removal and next targeting starts from (7); otherwise, the patient is pulled out for needle removal and redoing the insertion. The 5 mm is the radius of a clinically significant tumor assuming that the tumor is spherical. This means the accuracy of the needle placement should be better than 5 mm.

The important issue with the manual insertion is that the second move-out followed by move-in (underlined above) not only extends the procedure duration by itself, but also raises the risk of targeting failure because of patient movement thus causing repetition of items 7-15. Hence, this

study aims to eliminate manual needle insertion so as to reduce the procedure time and boost patient comfort. Automated needle insertion is not the solution due to safety issues. The solution proposed here is a teleoperated needle insertion. As depicted in Figure 3.6, the surgeon stands in MRI room, next to the patient and operates an MRI-compatible master device. Also, the surgeon will be able to benefit from real-time MR image through a monitor placed inside the MRI room.

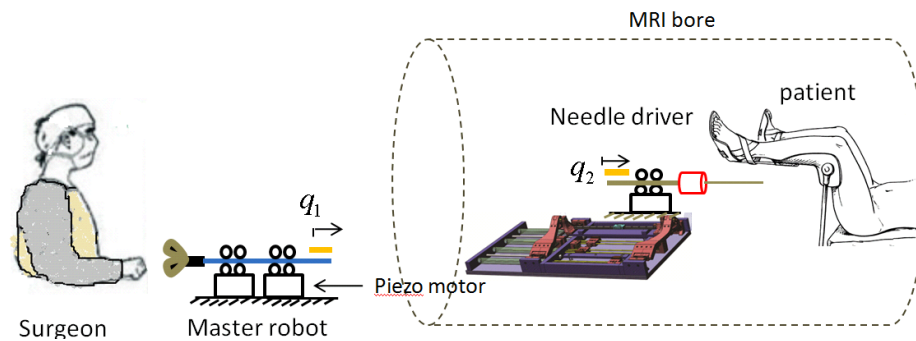


Figure 3.6: Schematic view of the overall master-slave system. The surgeon interacts with a master device to insert a needle at remote site under MRI guidance.

The requirements for such system are summarized as follows:

- 1) The needle driver should precisely follow the master position not only in free space movement, but also during the insertion (i.e. $q_1 = q_2$);
- 2) The system should be MRI-compatible with negligible SNR deterioration;
- 3) The needle driver should be sufficiently compact so that it can be mounted on the base robot;
- 4) The slave must be sufficiently strong so penetrates the needle into the tissue (at least 8.9 N [30]).

3.3.1 Needle driver (slave robot)

The needle driver is designed to be installed on the linkage between the front and rear triangles. The needle driver is located close to the scanner's iso-center. Therefore, MRI-compatibility

becomes the first concern for actuator selection. Based upon previous experience, pneumatic actuators are hard to control especially when they are configured as a master-slave system. This is due mainly to the air compressibility and their inherent nonlinearity of the pneumatic actuator. Nevertheless, nonlinear control strategies are available for pneumatic control. An alternative to pneumatic actuator is piezo motor which provides high precision and ease of control. Moreover, piezo motor generates enough force in a small footprint. We compared three different types of commercial piezo motors: Nanomotion Ltd. (Yoqneam, Israel), PI PILine (Physik Instrumente, Karlsruhe, Germany) and Piezomotor PiezoLEG (Piezomotor AB, Upsala, Sweden). Table 3.1 shows the comparison.

Table 3.1: Comparison of different piezo motors.

Motor	MRI compatible	Max Thrust [N]
Nanomotion	✓	Up to 32
PI	×	Not available
PiezoLEG	✓	10

The nanomotion motor was selected since it provides enough thrust and is MRI-compatible.

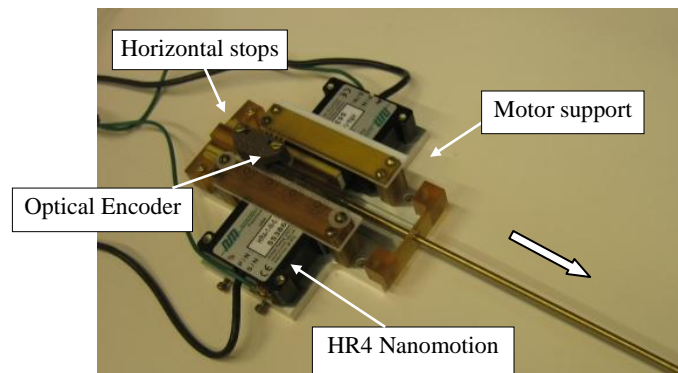


Figure 3.7: The needle driver: two HR4 Nanomotion motors (28 N together) are placed against each other. Optical encoder is employed for position feedback.

In order to achieve the given clinical task, the module should:

- Provide sufficient thrust;
- Be sufficiently compact so that it can be installed on the top of the robot;
- Be MRI-compatible (minimum image degradation);
- Be as frictionless as possible since mechanical friction obstructs the needle-tissue interaction.

To measure position, optical encoders are employed: modular EM1 electro optical encoders (US Digital, Vancouver, Washington), along with a 500 lines per inch (LPI) code strip. Figure 3.7 shows a close-up view of the stage using two Nanomotion HR4 motors with four motor elements each (28 N together). The speed of the needle insertion is 30 mm/sec. This stage was previously used as the linear stage for the motorized APT robot [8]. A pair of HR4 Nanomotion motors were axially pre-loaded against each other on ceramic drive strips and provided linear motion of a drive shaft that slides axially forward and backward on an aluminum plate. Vertical and horizontal stops were used to limit vertical movement and define end stops for travel. All materials were non-metallic (Ultem, plastic, or ceramic) except the motor plate that was made of Aluminum for increased rigidity. Figure 3.8 shows this module installed on the robot.

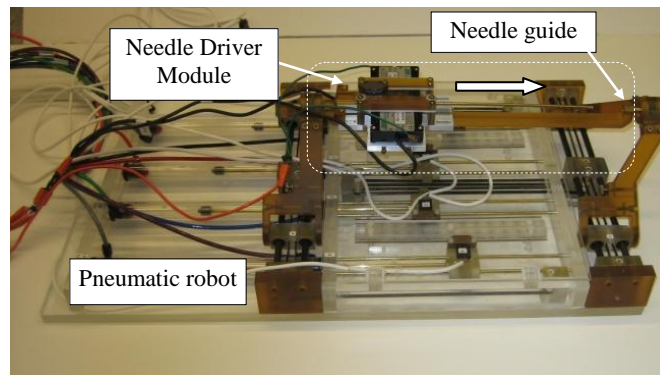


Figure 3.8: The needle driver is installed on the pneumatic robot. Dashed-line area shows sterilizable parts.

3.3.2 Master device

In our preliminary prototype (Figure 3.9), the master device is manually actuated. It consists of an MRI-compatible slide and rail (Iigus Inc., East Providence, RI) which mimics the needle insertion. To measure position, optical encoding was employed with 500 lines per inch (LPI) code strip. In the next step, a linear module similar to the needle driver will replace the current master device in order to generate haptic force feedback on surgeon's fingers.

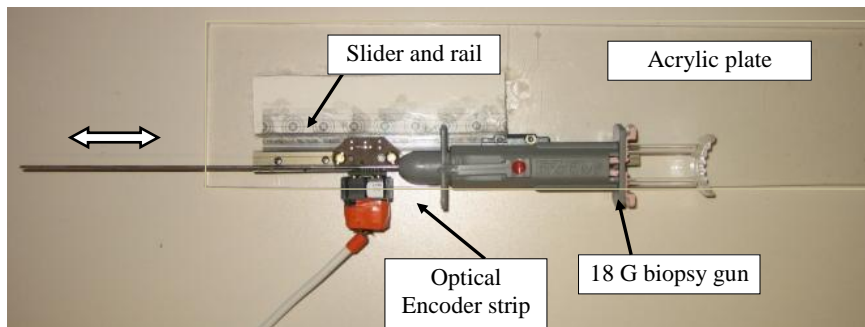


Figure 3.9: The master device: a biopsy gun is translated by a slider on a rail affixed to the cast acrylic plate. Optical encoder is used for position measurement.

3.3.3 Needle driver control unit

The needle driver controller unit consists of two Nanomotion AB5 motor amplifiers, a DMC-21x3 Ethernet motion controller (Galil Motion Control, Rocklin, California) (Figure 3.10), and a PC workstation on which GalilTools (the software to command the controller and to monitor sensor signals) runs. A 24 V DC power supply is used to run the controller and amplifier. If shielded properly, the SNR deterioration as a result of using AB5 amplifiers would be negligible as long as the motor is not moving (even if the motor is on) [8]. However, in our application, the motor is running while the scanner is operating which may impact the SNR noticeably. For this

reason, the AB5 should be replaced with a custom-made amplifier that eliminates the high frequency noises that exist on the sinusoidal voltages that excite the piezo crystals.

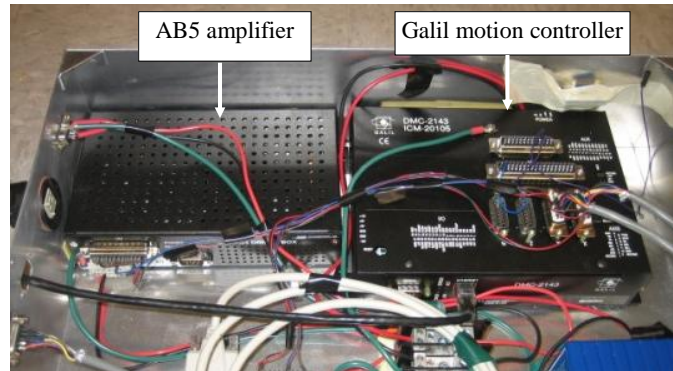


Figure 3.10: Galil motion controller and AB5 Nanomotion amplifier.

3.4 Experiments and results

3.4.1 Ex vivo accuracy evaluation with manual insertion

In previous studies, we evaluated the system in three series of preliminary experiments: 1) manipulator positioning accuracy and repeatability test [25], 2) signal-to-noise ratio (SNR) test for MRI-compatibility [26], and 3) patient compatibility and comfort tests for system integration and procedural feasibility [27]. Here, we performed an ex vivo experiment (Figure 3.1) using a commercial prostate intervention training phantom (Model 053 Ultrasound Prostate Training Phantom, Computerized Imaging Reference Systems, Inc., Norfolk, VA, USA). The objective of this experiment was to evaluate the overall accuracy of needle placement in prostate biopsy procedures. The prostate phantom was placed and fixed in a height typical in a real clinical procedure. In the beginning, the Z-frame was secured on the predefined position on the custom-made MRI table. The image of the Z-frame was acquired using 3D Fast Low Angle Shot (FLASH) (TR/TE: 12 ms/1.97 ms; acquisition matrix: 256×256; flip angle 45°; field of view:

160×160 mm; slice thickness: 2 mm; receiver bandwidth: 400 Hz/pixel; number of averages: 3). After imaging the Z-frame, the images were imported in 3D Slicer and the transformation matrix from RAS to robot coordinate (XYZ) was calculated by the software. The prostate phantom was then imaged and imported to the navigation software. The image of the phantom was acquired using 2D Turbo Spin Echo (TSE) sequence (TR/TE = 5250/100 ms; acquisition matrix = 320×224; flip angle = 150°; field of view = 140×140 mm; slice thickness = 3 mm; receiver bandwidth = 203 Hz/pixel). Then, the Z-frame was removed and the robot was placed in a certain pose on MRI board. In 3D Slicer, a total of 15 targets were randomly picked within the prostate capsule, as indicated in Table 3.2. These targets were chosen in different area of the prostate capsule to ensure the reported average error is independent of the target location. The software sent those targets and corresponding needle trajectories (in quaternion format) to the robot controller along with the RAS-to-XYZ transformation matrix (calculated by Z-frame registration) via Ethernet cable. After a 18G×20 cm bevel-tip needle (MRI Bio Gun, E-Z-EM, Westbury, NY) was inserted for each target, a confirmation image was acquired around the target with a half Fourier acquisition single shot turbo spin echo (HASTE) sequence (TR/TE = 1000/102 ms; matrix = 320×179; flip angle = 150°; field of view = 280×224 mm; slice thickness = 2 mm; receiver bandwidth = 780 Hz/pixel) along axial and sagittal plane in order to measure the 2D needle placement error. The 2D needle placement error was defined as the distance between the predefined target and the center of the needle artifact on the same axial plane, as obtained. The error in S direction (normal to the axial image plane) was ignored as the needle artifact was visible in a slice before and after the predefined target. Moreover, the biopsy sample is typically 15-20 mm implying that few millimeters of error in needle direction is practically insignificant. The error components in R and A direction (entitled Err_R and Err_A, respectively) as well as the

overall in-plane error (entitled Err_Total) for each target are provided in Table 3.2. Figure 3.11 shows the histogram of the overall in-plane error for each target as well as the average error. Target 13 was an outlier and it was eliminated. The results are discussed in the next section.

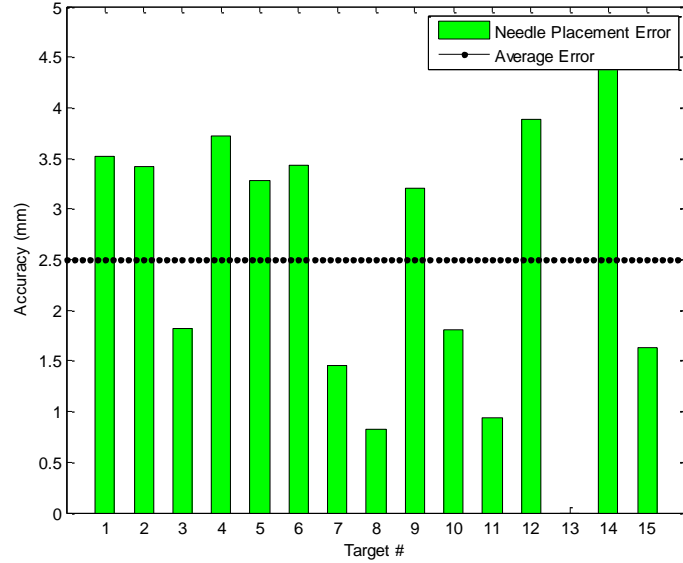


Figure 3.11: Overall needle placement error in ex vivo phantom experiment: the needle was bevel-tip 18G × 20 cm.

Table 3.2: Results of needle placement accuracy evaluation in realistic phantom in a 3T magnet (mm).

Target #	1	2	3	4	5	6	7	8	9	10	11	12	13	14	15	Avg	STD
R	9.0	20.4	9.6	15.3	2.1	2.4	9.6	15.6	11.1	15.0	11.0	13.0	0	2.4	9.6	-	-
A	16.3	15.8	28.3	21.5	15.8	24.0	10.9	11.5	12.0	17.0	22.0	18.0	0	24.0	10.9	-	-
S	12.5	12.5	12.5	22.0	22.0	22.0	32.0	32.0	12.5	12.5	12.5	20.0	0	25.0	25.0	-	-
Err_R	-1.3	2.1	0.3	3.7	2.6	0.5	-0.4	0.2	3.2	1.7	0.8	-1.2	0	3.5	-1.2	1.0	1.73
Err_A	3.2	2.7	-1.8	-0.4	2	3.4	1.4	0.8	0.1	-0.6	-0.5	3.7	0	3.1	1.1	1.2	1.74
Err_Total	3.5	3.4	1.8	3.7	3.2	3.4	1.4	0.8	3.2	1.8	0.9	3.8	0	4.6	1.6	2.5	1.37

3.4.2 Position tracking evaluation of the master-slave needle driver

The performance of the master-slave insertion module is explored separately as shown in Figure 3.12. The main experimental objective of the needle driver system was to test whether the needle driver follows the command sent by the master device. A simple code was written in G-language (the programming language of Galil motion controller). The controller on the slave side was a proportional-integral (PI) controller with the $K_P = 100$ and $K_I = 20$. The master was moved back and forth over a 40 mm range of motion for 20 sec and it was expected that the slave follows the master without any delay. As seen, the needle driver was following the master accurately without noticeable delay. The average error of position tracking was 0.03 mm. This experiment was repeated 3 times and the error was below 0.1 mm in all cases.

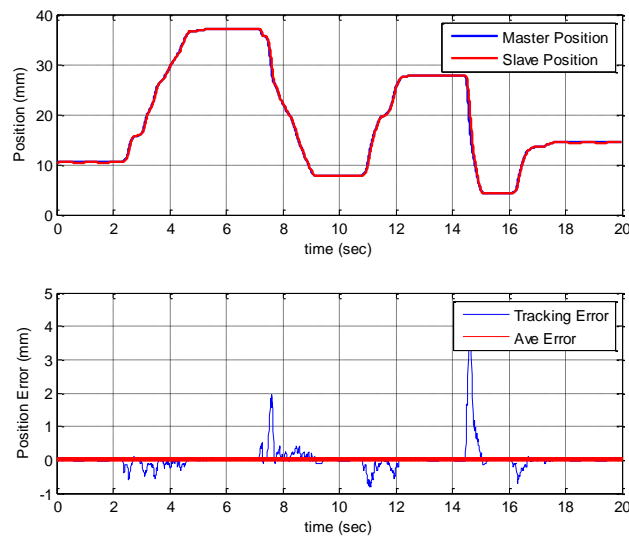


Figure 3.12: Position tracking of the master-slave needle insertion module.

3.5 Discussion

The required accuracy is determined by the clinically significant size of prostate cancer foci. Although there is no standard yet, it is generally agreed that 5 mm accuracy is sufficient for

biopsy [38]. As seen in Figure 3.11 and Table 3.2, the average of the overall system needle placement error (i.e. including the manipulator error and the registration error) for the manual insertion approach is 2.5 mm (STD = 1.37, max = 3.8 mm) which seems adequate. However, due to prostate motion in real clinical procedure, the clinical targeting error is expected to be somewhat larger [39].

Since the master-slave needle insertion system is only responsible for the needle insertion (i.e. the 5th DOF) and its motion is decoupled from the 4-DOF robot, it should not affect the 4-DOF robot targeting accuracy (i.e. the needle alignment). Also, Figure 3.12 shows that the slave followed the master with high accuracy and with no noticeable time delay. Hence, the results of the two experiments together suggest that the proposed 4-DOF robotic system has acceptable accuracy.

3.6 Conclusions and future work

A transperineal pneumatic robot was developed for MRI-guided prostatic biopsy. The robot addressed problems associated with previously developed MRI-guided prostate robot systems, including workspace limitation, needle placement accuracy, sterilization, and MRI-compatibility. Pre-patient mockup trial was carried out in order to investigate the overall system needle placement accuracy. As the latest development, a prototype of a needle driver module was introduced. This needle driver module was added to the robot and can run remotely by a master device placed close to scanner. In conclusion, the overall concept, design and implementation showed the feasibility in initial phantom experiments. Work continues toward a clinically certifiable implementation. Also, we are considering possible solutions for an MRI-compatible force measurement technology in order to feedback the insertion force to clinician's hand. Studies have been carried out on MRI-compatible force sensors ([32] and the references therein) that are not commercially available and have various limitations. The only commercially available

technology is FBG force sensors [33]. After implementing FBG force sensors, a tool will be given to the clinician so that they can distinguish between different stages of needle advancement.

References

- [1] American Cancer Society. Cancer Facts and Figures 2010. *American Cancer Society*, Atlanta, 2010.
- [2] Jemal, R. Siegel, E. Ward, Y. Hao, J. Xu, and M. J. Thun. *Cancer Statistics*, 2009. CA: A Cancer Journal for Clinicians, page caac.20006, 2009.
- [3] M. K. Terris, E. M. Wallen, and T. A. Stamey, "Comparison of mid-lobe versus lateral systematic sextant biopsies in detection of prostate cancer," *Urol. Int.*, vol. 59, pp. 239–242, 1997.
- [4] K. K. Yu and H. Hricak, "Imaging prostate cancer," in *Radiol Clin North Am*, vol. 38(1), pp. 59–85, 2000.
- [5] S. L. Chowning, R. C. Susil, A. Krieger, G. Fichtinger, L. L. Whitcomb and E. Atalar, "A preliminary analysis and model of prostate injection distributions," *Prostate*, vol. 66, pp. 344-357, 2006.
- [6] A. Krieger, G. Metzger, G. Fichtinger, E. Atalar and L. Whitcomb, "A hybrid method for 6-DOF tracking of MRI-compatible robotic interventional devices," in *Robotics and Automation, 2006. ICRA 2006. Proceedings 2006 IEEE International Conference on*, 2006, pp. 3844-3849.

- [7] A. Krieger, R. Susil, A. Tanacs, G. Fichtinger, L. Whitcomb, and E. Atalar, "A MRI-compatible device for MRI-guided transrectal prostate biopsy," *International Society of Magnetic Resonance Imaging in Medicine*, Tenth Scientific Meeting, pp. 338, 2002.
- [8] A. Krieger, I. Iordachita, S. Song, N. B. Cho, P. Guion, G. Fichtinger and L. L. Whitcomb, "Development and preliminary evaluation of an actuated MRI-compatible robotic device for MRI-guided prostate intervention," in *Robotics and Automation (ICRA), 2010 IEEE International Conference on*, 2010, pp. 1066-1073.
- [9] D. Beyersdorff, A. Winkel, B. Hamm, S. Lenk, S. A. Loening and M. Taupitz, "MR Imaging-guided Prostate Biopsy with a Closed MR Unit at 1.5T: Initial Results1," *Radiology*, vol. 234, pp. 576-581, 2005.
- [10] K. Engelhard, H. Hollenbach, B. Kiefer, A. Winkel, K. Goeb and D. Engehausen, "Prostate biopsy in the supine position in a standard 1.5-T scanner under real time MR-imaging control using a MR-compatible endorectal biopsy device," *Eur. Radiol.*, vol. 16, pp. 1237-1243, 2006.
- [11] H. Elhawary, A. Zivanovic, M. Rea, B. Davies, C. Besant, D. McRobbie, N. de Souza, I. Young and M. Lampérth, "The feasibility of MR-image guided prostate biopsy using piezoceramic motors inside or near to the magnet isocentre," in *Medical Image Computing and Computer-Assisted Intervention—MICCAI 2006* Anonymous Springer, 2006, pp. 519-526.

- [12] A. V. D'amico, C. Tempany, R. Cormack, N. Hata, M. Jinzaki, K. Tuncali, M. Weinstein and J. Richie, "Transperineal magnetic resonance image guided prostate biopsy," *J. Urol.*, vol. 164, pp. 385-387, 2000.
- [13] R. C. Susil, K. Camphausen, P. Choyke, E. R. McVeigh, G. S. Gustafson, H. Ning, R. W. Miller, E. Atalar, C. N. Coleman and C. Ménard, "System for prostate brachytherapy and biopsy in a standard 1.5T MRI scanner," *Magnetic Resonance in Medicine*, vol. 52, pp. 683-687, 2004.
- [14] K. Chinzei, N. Hata, F. A. Jolesz and R. Kikinis, "MR compatible surgical assist robot: System integration and preliminary feasibility study," in *Medical Image Computing and Computer-Assisted Intervention–MICCAI 2000*, 2000, pp. 921-930.
- [15] S. DiMaio, S. Pieper, K. Chinzei, N. Hata, S. Haker, D. Kacher, G. Fichtinger, C. Tempany and R. Kikinis, "Robot-assisted needle placement in open MRI: system architecture, integration and validation," *Computer Aided Surgery*, vol. 12, pp. 15-24, 2007.
- [16] K. Tadakuma, L. DeVita, J. Plante, Y. Shaoze and S. Dubowsky, "The experimental study of a precision parallel manipulator with binary actuation: With application to MRI cancer treatment," in *Robotics and Automation, 2008. ICRA 2008. IEEE International Conference on*, 2008, pp. 2503-2508.
- [17] D. Stoianovici, D. Song, D. Petrisor, D. Ursu, D. Mazilu, M. Mutener, M. Schar and A. Patriciu, "'MRI Stealth' robot for prostate interventions," *Minimally Invasive Therapy & Allied Technologies*, vol. 16, pp. 241-248, 2007.

- [18] G. S. Fischer, I. Iordachita, C. Csoma, J. Tokuda, S. P. DiMaio, C. M. Tempny, N. Hata and G. Fichtinger, "MRI-compatible pneumatic robot for transperineal prostate needle placement," *Mechatronics, IEEE/ASME Transactions on*, vol. 13, pp. 295-305, 2008.
- [19] A. Goldenberg, J. Trachtenberg, W. Kucharczyk, Y. Yi, M. Haider, L. Ma, R. Weersink and C. Raoufi, "Robotic system for closed-bore MRI-guided prostatic interventions," *Mechatronics, IEEE/ASME Transactions on*, vol. 13, pp. 374-379, 2008.
- [20] M. R. van den Bosch, M. R. Moman, M. van Vulpen, J. J. Battermann, E. Duiveman, L. J. van Schelven, H. de Leeuw, J. J. W. Lagendijk and M. A. Moerland, "MRI-guided robotic system for transperineal prostate interventions: proof of principle," *Phys. Med. Biol.*, vol. 55, pp. N133, 2010.
- [21] H. Su, K. Harrington, G. Cole, G. Fischer, "Modular Needle Steering Driver for MRI-guided Transperineal Prostate Intervention," in *Robotics and Automation (ICRA), 2010 IEEE International Conference on, Workshop on Snakes, Worms and Catheters*, 2010.
- [22] H. Su, M. Zervas, G. Cole, C. Furlong, G. Fischer, "Real-time MRI-Guided Needle Placement Robot with Integrated Fiber Optic Force Sensing ", in *Robotics and Automation (ICRA), 2011 IEEE International Conference on*, pp. 1583-1588, 2011.
- [23] S. Zangos, K. Eichler, K. Engelmann, M. Ahmed, S. Dettmer, C. Herzog, W. Pegios, A. Wetter, T. Lehnert and M. G. Mack, "MR-guided transgluteal biopsies with an open low-field system in patients with clinically suspected prostate cancer: technique and preliminary results," *Eur. Radiol.*, vol. 15, pp. 174-182, 2005.

- [24] S. Zangos, C. Herzog, K. Eichler, R. Hammerstingl, A. Lukoschek, S. Guthmann, B. Gutmann, U. J. Schoepf, P. Costello, and T. J. Vogl. MR-compatible assistance system for puncture in a high-field system: device and feasibility transgluteal biopsies of the prostate gland. *Eur. Radiol.*, vol. 17(4), pp. 1118–1124, 2007.
- [25] S. Song, N. Cho, G. Ficsher, N. Hata, C. Tempany, G. Fichtinger, and I. Iordachita. “Development of a Pneumatic Robot for MRI-guided Transperineal Prostate Biopsy and Brachytherapy: New Approaches,” in *Robotics and Automation (ICRA), 2010 IEEE International Conference on*, pp. 2580-85, 2010.
- [26] S. Song, N. Cho, J. Tokuda, N. Hata, C. Tempany, G. Fichtinger, and I. Iordachita. “MRI compatibility study of a pneumatically actuated robotic system for transperineal prostate needle placement,” *Proceeding of Computer Assisted Radiology and Surgery (CARS)*, 2010.
- [27] S. Song, N. Cho, J. Tokuda, N. Hata, C. Tempany, G. Fichtinger and I. Iordachita, “Preliminary evaluation of a MRI-compatible modular robotic system for MRI-guided prostate interventions,” in *Biomedical Robotics and Biomechatronics (BioRob), 2010 3rd IEEE RAS and EMBS International Conference on*, 2010, pp. 796-801.
- [28] R. Kokes., K. Lister, R. Gullapalli, B. Zhang, A. MacMillan, H. Richard, J. P. Desai, “Towards a teleoperated needle driver robot with haptic feedback for RFA of breast tumors under continuous MRI,” *Medical Image Analysis*, vol. 13, pp. 445–455, 2009.

- [29] H. Su, W. Shang, G. A. Cole, K. Harrington and G. S. Fischer, "Haptic system design for MRI-guided needle based prostate brachytherapy," in *Haptics Symposium, 2010 IEEE*, 2010, pp. 483-488.
- [30] Z. Tse, H. Elhawary, M. Rea, I. Young, B. Davis and M. Lamperth, "A haptic unit designed for magnetic-resonance-guided biopsy," *Proc. Inst. Mech. Eng. Part H J. Eng. Med.*, vol. 223, pp. 159-172, 2009.
- [31] P. Mewes, J. Tokuda, S. P. DiMaio, G. S. Fischer, C. Csoma, D. G. Gobi, C. Tempany, G. Fichtinger, and N. Hata, "An integrated MRI and robot control software system for an MR-compatible robot in prostate intervention," in *Robotics and Automation (ICRA), IEEE International Conference on, 2008*, pp. 295-305, 2008.
- [32] H. Su and G. S. Fischer, "A 3-axis optical force/torque sensor for prostate needle placement in magnetic resonance imaging environments," in *Technologies for Practical Robot Applications, 2009. TePRA 2009. IEEE International Conference on, 2009*, pp. 5-9.
- [33] Y-L. Park, S. Elayaperumal, B.L. Daniel, E. Kaye, K.B. Pauly, R.J. Black, and M.R. Cutkosky, "MRI-compatible Haptics: Feasibility of using optical fiber Bragg grating strain-sensors to detect deflection of needles in an MRI environment," *International Society for Magnetic Resonance in Medicine (ISMRM)*, 2008.
- [34] J. Tokuda, G. Fischer, X et al, "OpenIGTLink: an open network protocol for image-guided therapy environment," *Int J Med Robotics Comput Assist Surg.*, vol. 5(4), pp. 423-434, 2009.

- [35] K. Tuncali, J. Tokuda, I. Iordachita, S.E. Song, A. Fedorov, S. Oguro, A. Lasso, FM Fennessy, Y. Tang, CM Tempny, N. Hata, "3T MRI-guided Transperineal Targeted Prostate Biopsy: Clinical Feasibility, Safety, and Early Results", *International Society for Magnetic Resonance in Medicine (ISMRM)*, 2011.
- [36] J. Tokuda, K. Tuncali, I. Iordachita, S.E. Song, A. Fedorov, S. Oguro, A. Lasso, FM Fennessy, Y. Tang, CM Tempny, N. Hata, "Preliminary Accuracy Evaluation of 3T MRI-guided Transperineal Prostate Biopsy with Grid Template", *International Society for Magnetic Resonance in Medicine (ISMRM)*, 2011.
- [37] K. Masamune, G. Fichtinger, A. Patriciu, I. Sakuma, T. Dohi, Stoianovici D: System for Robotically Assisted Percutaneous Procedures With Computed Tomography Guidance, *Jour of Comp Aided Surg*, vol. 6, pp. 370-383, 2001.
- [38] Van der Kwast, Theodorus H, T. Wolters, A. Evans and M. Roobol, "Single prostatic cancer foci on prostate biopsy," *European Urology Supplements*, vol. 7, pp. 549-556, 2008.
- [39] H. Xu, A. Lasso, S. Vikal, P. Guion, A. Krieger, A. Kaushal, L. L. Whitcomb and G. Fichtinger, "MRI-guided robotic prostate biopsy: A clinical accuracy validation," in *Medical Image Computing and Computer-Assisted Intervention–MICCAI 2010* Anonymous Springer, 2010, pp. 383-391.

Chapter 4

Accuracy study of a robotic system for MRI-guided prostate needle placement

Background: Accurate needle placement is the first concern in percutaneous MRI-guided prostate interventions. In this phantom study, different sources contributing to the overall needle placement error of an MRI-guided robot for prostate biopsy have been identified, quantified, and minimized to the possible extent. In this study, we considered 3 mm as the accuracy limit. Since the focus of this study is placed on the errors caused by the robotic system, the phantom study is quite representative of the actual procedure. Methods and Materials: The overall needle placement error of the system was evaluated in a prostate phantom. This error was broken into two parts: the error associated with the robotic system (called before-insertion error) and the error associated with needle-tissue interaction (called due-to-insertion error). The before-insertion error was measured directly in a soft phantom and different sources contributing into this part were identified and quantified. A calibration methodology was developed to minimize the 4-DOF manipulator's error. The due-to-insertion error was indirectly approximated by comparing the overall error and the before-insertion error. The effect of sterilization on the manipulator's accuracy and repeatability was also studied. Results: The average overall system error in a phantom study was 2.5 mm (STD = 1.1 mm). The average robotic system error in soft phantom was 1.3 mm (STD = 0.7 mm). Assuming orthogonal error components, the needle-tissue interaction error was approximated to be 2.13 mm thus having larger contribution to the overall error. The average susceptibility artifact shift was 0.2 mm. The manipulator's targeting accuracy was 0.71 mm (STD = 0.21mm) after robot calibration. The robot's repeatability was 0.13 mm.

Sterilization had no noticeable influence on the robot's accuracy and repeatability. Conclusions: The experimental methodology presented in this chapter may help researchers to identify, quantify, and minimize different sources contributing into the overall needle placement error of an MRI-guided robotic system for prostate needle placement. In the robotic system analyzed here, the overall error of the studied system remained within the acceptable range.

4.1 Introduction

Prostate cancer is the most common cancer in men in the United States [1]. The definitive diagnostic method for this disease is core needle biopsy. According to the statistics, each year approximately 1.5 million prostate biopsy procedures are performed only in the United States [2]. Transrectal ultrasound (TRUS) guidance is the "Gold Standard" navigation method for biopsy due to its real-time nature, relative low cost, and ease of use. However, this imaging modality is not capable of visualizing cancer but rather the contour of prostate, resulting in a significant number of false-negatives in conventional TRUS-guided systematic biopsy [3], where 6-12 cores equally distributed within the prostate are sampled.

Magnetic Resonance Imaging (MRI) has the potential to improve prostate biopsy due to its high sensitivity for detecting prostate tumors, excellent soft tissue contrast, high spatial resolution, and multi-planar volumetric imaging capabilities [4]. Manual transperineal prostate biopsy has been reported in [5] and [6]. Due to limited accuracy, needle placement with template grid was proposed in [7]. Unfortunately, the template does not allow for arbitrary needle trajectory. Robotic systems can assist in solving this issue. Several MRI-compatible robots have been reported for prostate interventions using transrectal, transperineal, and transgluteal access to the prostate. MRI-guided transperineal prostate interventions were studied in patient experiments inside open MRI scanner by Chinzei *et al.* [8]. In [9], Di Maio *et al.* designed systems to assist

transperineal intra-prostatic needle placement. In [10] Tadakuma *et al.* developed an MRI-compatible robot for transperineal needle placement using dielectric elastomer actuators (DEAs). In [11] Stoianovici *et al.* developed a pneumatically actuated device for transperineal brachytherapy seed placement. In [12] Fischer *et al.* developed a pneumatic 2-DOF robot for transperineal prostate needle placement. In [13] Goldenberg *et al.* developed a robotic system employing ultrasonic actuators for MRI-guided transperineal prostate intervention. In [14] van den Bosch *et al.* reported a hydraulically and pneumatically actuated tapping device to alleviate undesirable prostate displacement and deformation. Su *et al.* reported a 3-DOF Cartesian robot for MRI-guided transperineal needle alignment integrated with a 3-DOF needle steering module for teleoperated and autonomous seed implantation [15] and [16].

The required needle placement accuracy in prostate biopsy is determined by the clinically significant size of prostate cancer foci. There is no general agreement on this value. In [17] 0.5 mL tumor volume was proposed as the limit for the significant prostate cancer foci. A 0.5 mL spherical shaped tumor has radius of almost 5 mm which means the needle placement accuracy should be better than 5 mm. In this study, we consider 3 mm as the accuracy limit since we are conducting phantom studies which cannot reproduce prostate motion.

To ensure the overall error in needle placement remains below the threshold, systematic accuracy assessment is necessary in order to identify and quantify all error components. Prior accuracy assessment studies focused only on manual MRI-guided transperineal prostate biopsy with use of the needle-guiding grid [18] and [19]. In this study however, we provide a systematic accuracy assessment method for robotic MRI-guided prostate biopsy. In addition, a calibration methodology is proposed and implemented based on the manipulator's kinematics in order to minimize the error introduced by this key element of the whole system. Figure 4.1 shows a

prototype of the specific manipulators studied in this chapter. The system is an MRI-guided prostate intervention robot for transperineal needle placement with pneumatic actuation which provides 4-Degree of Freedom (DOF) needle positioning in MRI coordinates [20]-[22]. Although the calibration process proposed here is specific to this robot, our approach (discussed in section 3.4) can be applied to manipulators of different kinematics.

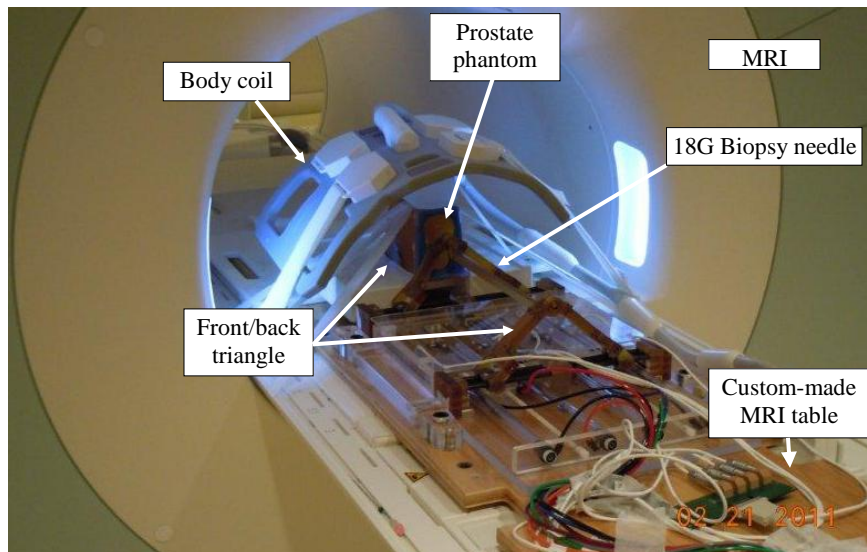


Figure 4.1: The 4-DOF pneumatic robot for MRI-guided transperineal prostate biopsy used in this study.

4.2 Error sources and components

4.2.1 Classification of error sources

We define the needle placement error in robotic prostate biopsy as the distance between the center of the needle artifact and the predefined target position both measured in the MR image. This error has two main components: intrinsic and extrinsic errors. Intrinsic error comprises: 1) error associated with the robotic system which occurs before needle insertion, 2) error introduced by needle-tissue interaction i.e. needle deflection, and prostate motion and deformation which

occurs as a result of needle insertion. Extrinsic error is introduced by patient motion, bladder filling, tissue deformation generated by surgical tools such as endorectal imaging coil probe. Table 4.1 categorizes different sources of needle placement error with the corresponding components and the method by which each part can be minimized.

In our phantom study, extrinsic errors were ignored. In fact, the focus of this study is placed on intrinsic errors, particularly the error associated with the robotic system. The other intrinsic error component, i.e. the error introduced by needle-tissue interaction was indirectly approximated as well.

Table 4.1: Different sources of error in robot assisted prostate needle placement under MRI guidance.

	Error Source	Different parts	Minimization solution
Intrinsic	1. Robotic system	a) fiducial frame registration b) fiducial frame to robot registration c) susceptibility artifact shift d) manipulator's inaccuracy	<ul style="list-style-type: none"> ✓ fiducial markers calibration ✓ permanent attachment of fiducials to the robot [16] and [23] ✓ artifact study ✓ manipulator calibration
	2. Needle-tissue interaction	a) prostate displacement b) prostate deformation c) needle deflection	<ul style="list-style-type: none"> ✓ FEA* [24], needle spinning [25], fast insertion [23], needle tapping [26] ✓ FEA, needle spinning, fast insertion, needle tapping ✓ deflection modeling, image-guided needle steering [25]
Extrinsic	1. Patient motion	-	<ul style="list-style-type: none"> ✓ reducing the procedure duration ✓ anesthesia ✓ teleoperated insertion [21] ✓ error measurement and compensation [27]
	2. Probe related	-	<ul style="list-style-type: none"> ✓ no endo-rectal probe ✓ error measurement and compensation [28]
	3. Bladder filling	-	-

*FEA: Finite Element Analysis

4.2.2 Identification of robotic system error components

To identify robotic system error components, the targeting workflow is reviewed (Figure 4.2): first, the target and needle trajectory are specified by the clinician in the 3D Slicer based navigation software. Both the target and the needle trajectories are expressed in the RAS coordinate system (see Figure 4.2) and should be converted to the robot coordinate system (XYZ). For this reason, a fiducial frame called Z-frame is used [29].

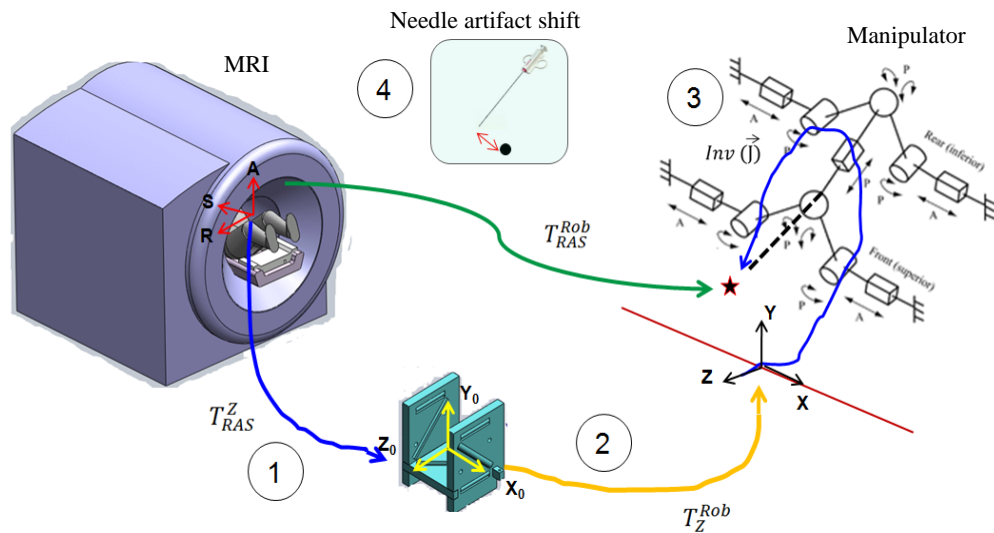


Figure 4.2: Different error sources contributing to a robotic system for MRI-guided needle placement: Z-frame registration error, robot to Z-frame registration error, the manipulator’s error, and the artifact shift.

The origin and the rotation matrix representing the three orthogonal vectors of the Z-frame are sent by the navigation software to the robot controller along with the target position and needle trajectory. Then, the target position and corresponding needle trajectory in XYZ are found as follows:

$$\begin{aligned}
[x, y, z]_{Rob}^T &= T_Z^{Rob} \cdot T_{RAS}^Z [x, y, z]_{RAS}^T, \\
[u, v, w]_{Rob}^T &= T_Z^{Rob} \cdot T_{RAS}^Z [u, v, w]_{RAS}^T
\end{aligned}
\tag{4-1}$$

where $[x, y, z]$ and $[u, v, w]$ are target position and needle trajectory, respectively. T_{RAS}^Z and T_Z^{Rob} are transformations from the RAS to Z-frame and from Z-frame to robot coordinates, respectively. When the target position and needle trajectory are specified in the robot coordinate system, the robot controller solves the inverse kinematic problem in order to reach that target position and sends the command to each actuator. Then, the robot moves to align the needle with the target. Next, the needle is inserted manually for the calculated depth. Finally, confirmation images are taken. The distance between the needle susceptibility artifact and pre-planned target is computed as the targeting error.

Based on the targeting workflow, four possible sources of error were identified in association with the robotic system: 1) RAS to Z-frame transformation error referred to as Z-frame registration error, 2) Z-frame to robot (XYZ) transformation error, 3) manipulator's needle positioning error, and 4) and positional error due to susceptibility artifact shift. In the following sections, we propose quantification and reduction methods for each of them.

4.3 Methods and materials

In this section, we propose methods for measurement of each component of the robotic system error. For the error introduced by the manipulator, a calibration method is proposed in order to reduce this error. Then, the total error of the robotic system (i.e. the overall error before insertion) and the overall error are separately quantified.

4.3.1 Z-frame registration accuracy evaluation

The Z-frame is used to register the scanner (RAS) and robot coordinate systems (Figure 4.2). The idea of using Z-frame was proposed in [29]. The Z-frame has seven rigid tubes with 7.5 mm inner diameters filled with a contrast agent (MR Spots, Beekley, Bristol, CT) placed on three adjacent faces of a 60 mm cube, thus forming a Z-shape in the images. The seven tubes are automatically detected on cross-sectional MR images of the Z-frame in 3D Slicer, providing the location and orientation of the Z-frame in the MRI coordinate system. Since the Z-frame is attached in a predefined position relative to the robot on the custom-made MRI table, the position of the target can be transformed from image coordinates to robot coordinates. This registration procedure can be imprecise. For this reason, a calibration methodology was proposed and evaluated in [19]. Summary of the method is as follows: registration error is usually provided as Target Registration Error (TRE). TRE can be defined as follows [30]:

$$\text{TRE} = \sqrt{\frac{\sum_{i=1}^N \|q_i - F(p_i)\|^2}{N}} \quad (4-2)$$

where N is the number of targets, q_i is actual measurement of targets in MRI coordinate, F is the calibration transformation (rotation and translation matrices) found after Z-frame registration, and p_i is the desired position to be reached in phantom coordinate system. A geometric phantom of 40 targets (p_i) within the typical position of an average prostate gland was placed in a tank of water and then imaged (q_i). The transformation matrix (4×4) was found in parallel by imaging the Z-frame (i.e. $F(\cdot)$). Then, these targets were uploaded in 3D Slicer and were tried to be reached. In order to eliminate any other errors and focus only on the registration error, the robot was replaced by a “simulator”. Then, simulator computes $F(p_i)$ based on the robot inverse kinematics and

marked it as a virtual point in 3D Slicer. These transformed points ($F(p_i)$) were then compared to the actual measurement in MR image (q_i) according to equation (4-2) and the TRE was reported.

4.3.2 Z-frame to robot registration accuracy evaluation

By design, Z-frame and robot coordinate are aligned and T_{Rob}^Z should be a pure translation. This source has a small contribution to the overall system inaccuracy since this translation does not involve kinematic parameters unlike other sources. This error can be negligible if the manufacturing accuracy of the robot parts is adequate (i.e. < 0.1 mm accuracy). Physical measurements showed that this error is negligible in our robotic system. To eliminate this error source permanently, the Z-frame should be rigidly attached to the robot [16] and [23].

4.3.3 Needle artifact shift evaluation

The surgical needle is not directly visible in MRI. Instead, it leaves a dark void on the image referred to as susceptibility needle artifact which is introduced by signal loss in the vicinity of the needle. The size, shape and location of the artifact depend on imaging parameters, needle material and shape, needle orientation relative to the static field B_0 , and frequency encoding direction [31]. Assuming that the center of masses of the artifacts in different slices represent the axis of the needle, the shape and size of the artifact become less important. The problem is how to relate the location of the needle artifact (the central axis of the void) and the true position of the needle. A few studies have been reported on this topic as reviewed in [31] and [18]. Unfortunately, the results of those studies are not applicable to the problem we are studying since the needle orientation and imaging parameters are different. We decided to follow the approach described in [31]. We selected different target positions within prostate capsule. For each target, we consecutively inserted two needles, a 1.5 mm glass needle as the ground truth and an 18G biopsy needle, into a custom-made soft phantom. The imaging parameters during needle insertions were

as follows: 2D Turbo Spin Echo (TSE) sequence (TR/TE = 3000/103 ms; acquisition matrix = 320×205; flip angle 140 deg; field of view = 192×240; thickness = 2 mm; receiver bandwidth = 252 Hz/pixel). The artifact introduced by the glass needle was significantly smaller than the void introduced by the biopsy needle. The in-plane distance between the central axes of the two artifacts was defined as the susceptibility needle artifact shift. The error normal to the plane was ignored (see section 3.6).

4.3.4 The manipulator's accuracy

In this section, the robot is first calibrated in order to compensate for manufacturing errors. Then, the robot accuracy is quantified using optical tracking system.

Calibration of the manipulator: The manipulator's kinematic parameters can differ from designed values due to manufacturing inaccuracies. Since the robot is mainly made of plastic for MRI-compatibility, this issue can be more significant. To minimize this important source of error, a calibration method is proposed. We approach this problem by considering the robot inverse kinematics as follows: the robot comprises a pair of planar 2-DOF mechanisms coupled to each other by an adjustable linkage and two spherical joints at ends (Figure 4.3a). After the target and the needle trajectory are transformed into the robot coordinate, the line defined by the target position and the needle trajectory is intersected with the front and back triangle planes as depicted in Figure 4.3a, yielding (x_1, y_1) and (x_2, y_2) . Then, the front and back 2-DOF planar mechanisms (Figure 4.3a) are kinematically structured by using prismatic actuators in order to achieve the following displacements:

$$\begin{aligned} J_1 &= x_1 + \sqrt{(L^2 - (y_1 - a)^2)} \\ J_2 &= x_1 - \sqrt{(L^2 - (y_1 - a)^2)} \end{aligned} \tag{4-3}$$

where J_1 and J_2 are the displacements of the actuators. A similar relationship exists for J_3 and J_4 (back triangular mechanisms) with replacing x_2 and y_2 for x_1 and y_1 . As seen in equation (4-3), two sets of parameters are involved in the needle tip position: (x, y) which we call kinematic parameters, and (L, a) which we call geometric parameters. Due to manufacturing errors, the front and back triangle planes might be displaced and mis-oriented arbitrarily thus impacting (x, y) . Also, due to these inaccuracies, geometric parameters might be different from desired values. In the following sections, we will propose methods for reducing these errors.

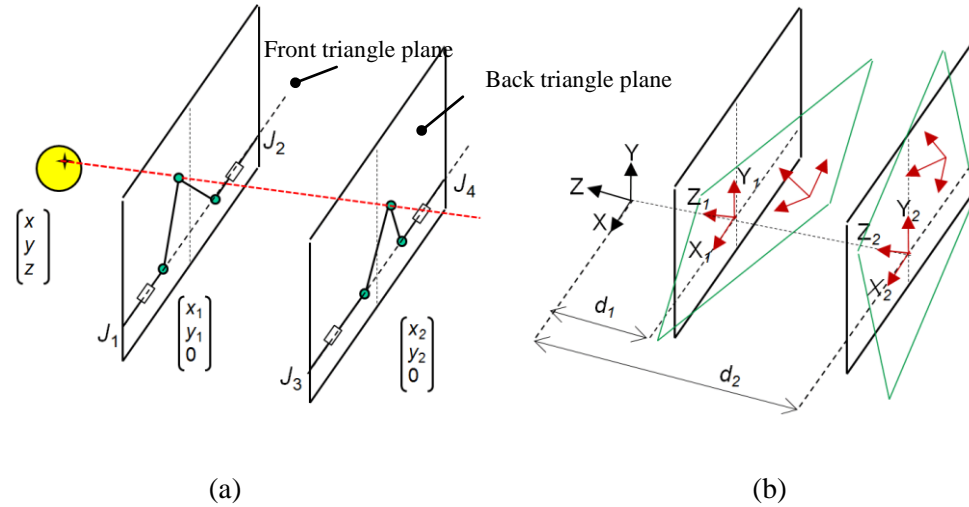


Figure 4.3: (a) Robot inverse kinematics and (b) front and back triangle coordinate systems can be translated and rotated arbitrarily due to the manufacturing inaccuracies.

A) *Modification to kinematic parameters:* Three local coordinate systems can be defined as depicted in Figure 4.3b: XYZ, the robot coordinate system, $X_1Y_1Z_1$ the front triangle coordinate system, and $X_2Y_2Z_2$ the back triangle coordinate system. Ideally, $X_1Y_1Z_1$ and $X_2Y_2Z_2$ are perfectly aligned with XYZ with their origins placed at $(0, 0, -d_1)$ and $(0, 0, -d_2)$, respectively in XYZ coordinates, where d_1 and d_2 are constant values. However, post - fabrication measurements are needed to find the actual values. Theoretically, origin displacement and rotation of the $X_1Y_1Z_1$

and $X_2Y_2Z_2$ can take place in all three directions (Figure 4.3b). Physically however, the rotation is constrained to the Y axis and the shift of origin is constrained in the X and Z directions since the front and rear triangles are sitting on the same plane i.e. robot base plane. In order to compensate for this disorientation and displacement, two transformation matrices are defined as follows: $T_1 = [R_1, TR_1; 0\ 0\ 0\ 1]^T$ and $T_2 = [R_2, TR_2; 0\ 0\ 0\ 1]^T$ where T_1 and T_2 are transformations from XYZ to $X_1Y_1Z_1$ and $X_2Y_2Z_2$, respectively. In an ideal world, R_i is identity and $TR_i = [0, 0, -d_i]$ where $i = \{1, 2\}$. These transformation matrices should be applied to the target and needle trajectory vectors before they are used in the robot inverse kinematics in order to compensate for errors.

In order to quantify R_1 and R_2 , we should find the true XYZ, $X_1Y_1Z_1$ and $X_2Y_2Z_2$. We used an optical tracking system and collected data as depicted in Figure 4.4a. X is defined by two sufficiently distant points on the front edge of the robot base plate (point 1). X_1 is defined by pivots 1 and 2 which are holes drilled precisely along the actuator's 1 and 2 axes. Likewise, X_2 is defined by pivots 3 and 4. Three out of the four pivot points define a plane whose normal defines the Y, Y_1 and Y_2 direction respectively. Y, Y_1 and Y_2 are parallel since the front and back triangles rest on the same plane (robot base plate). Z, Z_1 and Z_2 are found by cross production of the X and Y unit vectors.

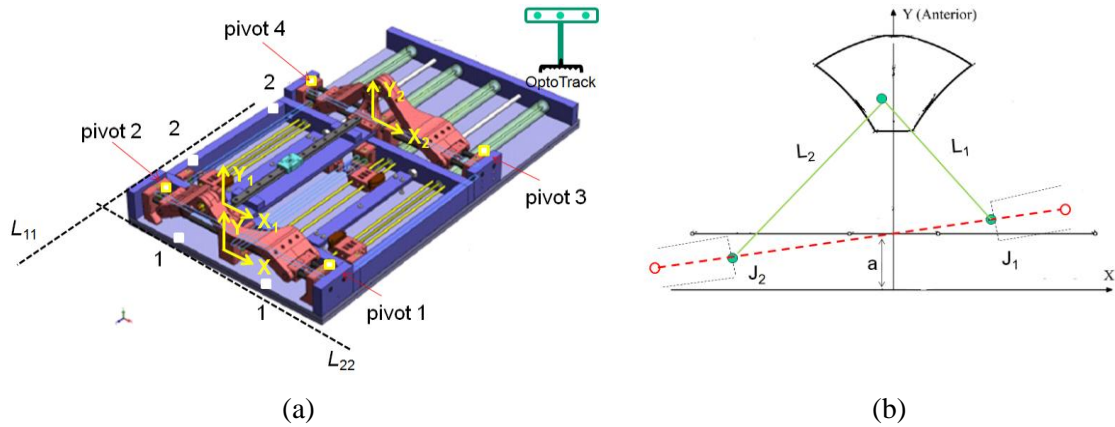


Figure 4.4: (a) Data collection strategy for measuring actual T_1 and T_2 and (b) actual geometric parameter.

The translation in X direction is found by comparing the distance between the midpoints of the pivot points and line L_{11} and the corresponding design values. The translation in Y direction is found by comparing the distance between the midpoints of the pivot points and line L_{22} and the corresponding design values. The experimental setup is shown in Figure 4.5a.

It comprised of the robot, robot controller, an optical tracking device (Optotrak 3020 NDI, Waterloo, Canada) and two 6-DOF tracking probes (Figure 4.5b), one for point data collection and one for needle tip measurement. According to the catalog of the device, the RMS accuracy at 2.5 m distance is 0.1 mm in x and y direction and 0.15 mm in z direction. Precision was 0.11 mm in our study based on the optical tracking probe pivot calibration that we conducted in the beginning of the experiment. However, it should be noted that accuracy of the tracking system may vary depending upon the distance between the camera and the measuring point. For this reason, we put the robot at a distance recommended by the company relative to the optical tracking system. At this distance, the accuracy is optimal and supposedly, as claimed by the manufacturer. We also used a rigid dynamic reference body clamped next to the robot (dark plate

clamped next to the robot as indicated in Figure 4.5b) in order to eliminate the effect of unwanted movement in the head of the optical tracking system.

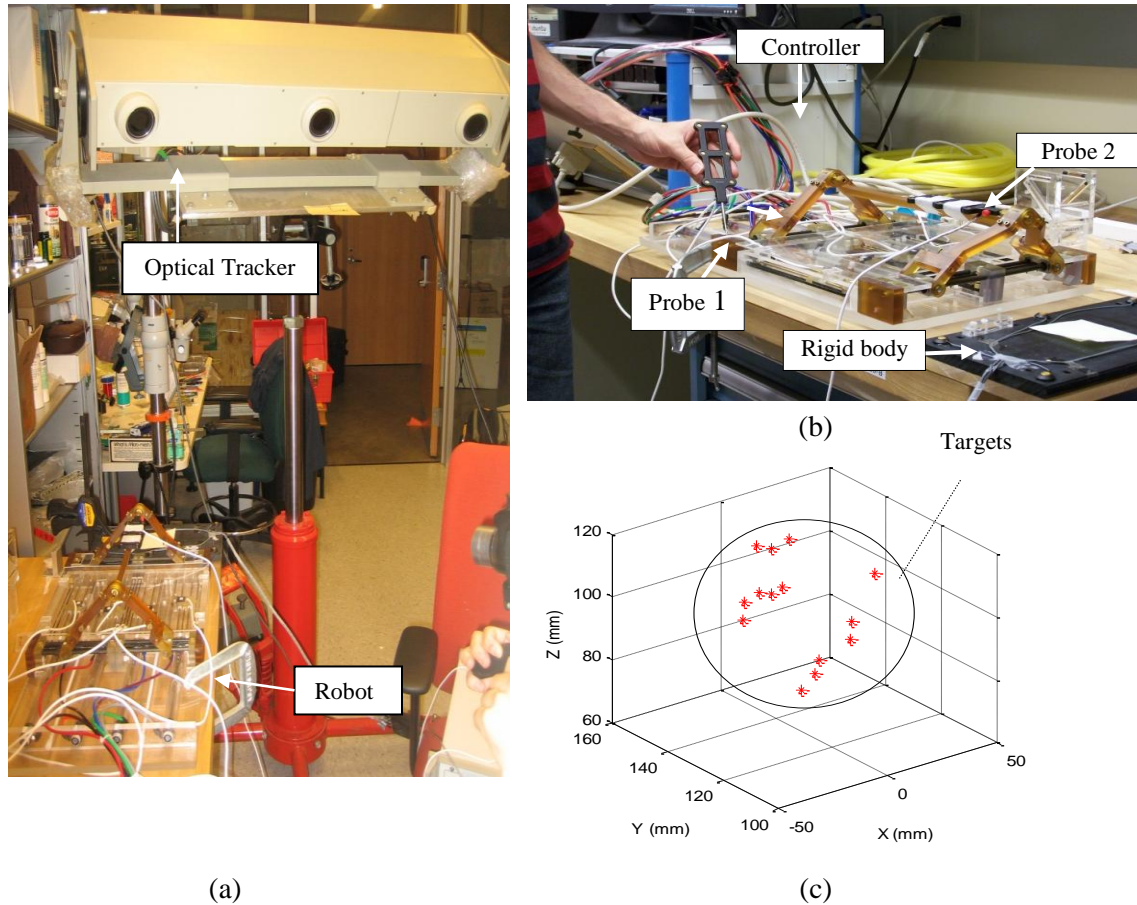


Figure 4.5: (a) The experimental setup, (b) robot calibration and accuracy analysis with two tracking probes, probe 1 for calibration and probe 2 for needle tip measurement, and (c) selected target positions within prostate boundary in XYZ coordinate system.

The necessary reference data points were collected as explained before and depicted in Figure 4.4a. For each point, an average of 200 data points (STD < 0.1 mm) was collected to ensure consistency.

T_1 and T_2 were computed as discussed and are provided below:

$$T_1 = \begin{bmatrix} 1 & -0.001 & 0.0055 & 0.58 \\ 0.001 & 1 & -0.0009 & 0 \\ -0.0055 & 0.0009 & 1 & -19.40 \\ 0 & 0 & 0 & 1 \end{bmatrix},$$

$$T_2 = \begin{bmatrix} 1 & -0.001 & 0.0052 & 2.14 \\ 0.0011 & 1 & -0.0009 & 0 \\ -0.0052 & 0.0009 & 1 & 297.82 \\ 0 & 0 & 0 & 1 \end{bmatrix} \quad (4-4)$$

Although the rotation part was close to identity, it can compensate for up to 4 mm error on the backplane as the backplane is located 320 mm apart from the target. The translation shifts in the X and Z directions were below 2 mm, considering that $d_1 = -18.5$ mm and $d_2 = 300.5$ mm.

B) Geometric parameter updates: These parameters include L_1 , L_2 , a_1 , and L_3 , L_4 , and a_2 as shown in Figure 4.4b. In order to find L_1 and L_2 , J_1 and J_2 were set at designated positions. The end-effector position was measured by an optical tracking system as shown in Figure 4.5a. Having these three points, L_1 and L_2 were found. L_3 and L_4 were found in the same way while the constant a_1 and a_2 were directly measured. The updated geometric parameters are shown in Table 4.2. The measured parameters closely matched the designed parameters.

Table 4.2: Calibration of the geometric parameters (mm).

	L_1	L_2	L_3	L_4	a_1	a_2
Measured	119.0	119.4	120.0	120.1	30.8	30.0
Designed	120.0	120.0	120.0	120.0	30.0	30.0

C) Inverse and forward kinematics modification: The kinematic parameters as well as geometric parameters must be updated after performing robot calibration. Hence, the robot inverse and forward kinematics are modified as shown in equations (4-6).

Updated inverse kinematics:

$$\begin{aligned}
J_1 &= x_1 + \sqrt{L_1^2 - (y_1 - a_1)^2}, \quad J_2 = x_1 - \sqrt{L_2^2 - (y_1 - a_1)^2}, \\
J_3 &= x_2 + \sqrt{L_3^2 - (y_2 - a_2)^2}, \quad J_4 = x_2 - \sqrt{L_4^2 - (y_2 - a_2)^2}
\end{aligned} \tag{4-5}$$

Updated forward kinematics:

$$x_1 = \frac{J_1 + J_2 + \sqrt{L_2^2 - (y_1 - a_1)^2} - \sqrt{L_1^2 - (y_1 - a_1)^2}}{2} \tag{4-6}$$

$$y_1 = a_1 + \sqrt{\chi}$$

where $\chi = \xi_1 - \left[\frac{\xi_3^2 + \xi_1 - \xi_2}{2\xi_3} \right]^2$, and $\xi_3 = J_1 - J_2$, $\xi_1 = L_1^2$, $\xi_2 = L_2^2$

$$x_2 = \frac{J_3 + J_4 + \sqrt{L_4^2 - (y_2 - a_2)^2} - \sqrt{L_3^2 - (y_2 - a_2)^2}}{2} \tag{4-7}$$

$$y_2 = a_2 + \sqrt{\psi}$$

where $\psi = \zeta_1 - \left[\frac{\zeta_3^2 + \zeta_1 - \zeta_2}{2\zeta_3} \right]^2$, and $\zeta_3 = J_3 - J_4$, $\zeta_1 = L_3^2$, $\zeta_2 = L_4^2$.

Having (x_1, y_1) and (x_2, y_2) and needle depth d , the target P and the needle trajectory vector l are obtained as follows:

$$P_1^T = [x_1 \ y_1 \ z_1]_{Rob} = T_1^{-1}[x_1 \ y_1 \ z_1], \tag{4-8}$$

$$P_2^T = [x_2 \ y_2 \ z_2]_{Rob} = T_2^{-1}[x_2 \ y_2 \ z_2]$$

and

$$l = [u \ v \ w]_{Rob} = P_2 - P_1, \quad (4-9)$$

$$P = P_1 + d \times l$$

Manipulator's accuracy assessment: Robot accuracy is evaluated in two different space domains: joint space (i.e. J_1 , J_2 , J_3 , and J_4) and robot space (i.e. needle tip in XYZ) in order to separate inaccuracy of actuator and other sources (e.g. encoder reading errors, joint tolerances, etc.) which cannot be systematically fixed. The experimental procedure was as follows: an optical tracking probe was placed into the front needle guide as indicated in Figure 4.5b in order to obtain the needle tip position. Data were recorded relative to the rigid dynamic reference body clamped next to the robot. First, the robot was registered to the optical tracking coordinates by collecting 4 pivot points as shown in Figure 4.4a. Then, 14 target positions were chosen within the robot's workspace (Figure 4.5c). The robot was commanded to those targets. Each time, all 4 encoder readings were recorded for joint space accuracy evaluation and the needle tip was recorded by the optical tracking probe for needle placement accuracy evaluation. Both probes were pivot-calibrated prior to measurement. Joint space error was defined as the difference between the sent command and the actual reading. Robot targeting accuracy was defined as the distance between the desired points calculated based on the updated forward kinematics and the corresponding points measured with optical tracking system.

4.3.5 Total error of the robotic system

The total error introduced by the robotic system (including all four sub-sources as listed in Table 4.1) was measured in a separate experiment as depicted in Figure 4.6.



Figure 4.6: Needle placement in a soft phantom for measuring of the robotic system total error and the artifact shift. CIRS 053 prostate phantom was customized to eliminate needle deflection.

A phantom was made by removing the perineum mimicking rubber layer and replacing the inside gel of a commercial prostate intervention training phantom (CIRS 053, Computerized Imaging Reference Systems, Inc., Norfolk, VA) with Soft Plastic (M-F Manufacturing, Inc., Ft. Worth, TX, USA). The liquid softener and liquid plastic were mixed at a ratio to eliminate the error introduced by needle-tissue interaction which in this experiment is caused by needle deflection.

The phantom and the Z-frame were secured on the custom-made MRI table. The image of the Z-frame was acquired using 3D Fast Low Angle Shot (FLASH) (TR/TE: 12 ms/1.97 ms; acquisition matrix: 256×256; flip angle 45°; field of view: 160×160 mm; slice thickness: 2 mm; receiver bandwidth: 400 Hz/pixel; number of averages 3). Next, the image was loaded into 3D Slicer and the transformation matrix from RAS to robot coordinate (XYZ) was calculated by the software. The prostate phantom was then imaged and the DICOM images were imported to the navigation software. The images of the phantom were acquired using 2D Turbo Spin Echo (TSE) sequence (TR/TE = 5250/100 ms; acquisition matrix = 320×224; flip

angle = 150°; field of view = 140×140 mm; slice thickness = 3 mm; receiver bandwidth = 203 Hz/pixel). Then, the Z-frame was removed and the robot was placed in a pre-defined pose on MRI board. In 3D Slicer, 9 target locations were randomly selected within the prostate region. These targets were chosen in different areas of the prostate capsule to ensure that the reported average error is independent of the target location. The software sent those targets and needle trajectories to the robot controller along with the RAS-to-XYZ transformation matrix (calculated by Z-frame registration). After each glass needle insertion, a confirmation image was acquired around the target with 2D Turbo Spin Echo (TSE) sequence (TR/TE = 3000/103 ms; acquisition matrix = 320×205; flip angle 140 deg; field of view = 192×240; thickness = 2 mm; receiver bandwidth = 252 Hz/pixel) in the axial plane in order to measure the 2D needle placement error. The 2D needle placement error was defined as the distance between the predefined target and the center of the needle artifact on the same axial plane.

4.3.6 Overall needle placement error

The overall needle placement error was evaluated in the same way as explained in the previous section but instead with the use of a multi-modality commercial prostate intervention training phantom (CIRS 053) in its original shape. The prostate phantom was imaged and the images were imported into the navigation software. A total of 15 targets were randomly selected in the prostate capsule. After inserting a 18G × 20 cm needle with bevel-shaped tip (MRI Bio Gun, E-Z-EM, Westbury, NY, USA) at each target, a confirmation image was taken. The 2D needle placement error was defined as the distance between the center of the needle artifact on the same axial plane and the predefined target. The error in S direction (normal to the axial image plane) was ignored as the needle artifact was visible in a slide before and after the predefined target. Also, the biopsy

sample is typically 15-20 mm long implying that few millimeters of error along the needle is clinically insignificant.

4.4 Results

4.4.1 Error components of the robotic system

Z-frame registration error measurement: The robot-to-image registration error defined as TRE was 1.8 mm for the inner area of the prostate capsule [19].

Z-frame to robot calibration error measurement: This error was negligible as discussed in section 4.2.

Susceptibility artifact shift measurement: Table 4.3 shows the results. Er_R and Er_A are error in R and A direction, respectively. Er_{Tot} is the total error. The results show that the artifact shift is approximately 0.2 mm in average (i.e. $1.29 - 1.09 = 0.2$ mm).

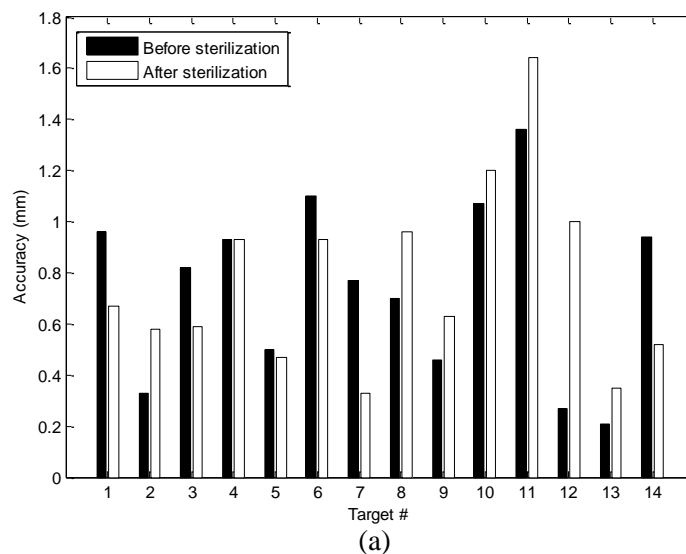
Manipulator's error measurement: As shown in Table 4.4, the average of joint space error was 0.2 mm (STD = 0.22 mm). The average needle positioning accuracy was 0.74 mm (STD = 0.33 mm), shown in Figure 4.7a. For each target shown in Figure 4.7a, the error was defined as the average absolute distance between the measured needle tip (i.e. the probe tip) and the target calculated from the forward kinematics. Repeatability was defined as the standard deviation of the error over 10 repetitions for reaching each target (Figure 4.7b). The mean value of the robot repeatability was 0.13 mm. Although the accuracy of the optical tracking system used for the manipulator's accuracy evaluation was not better than 0.15 mm, we think that this accuracy is still adequate for this study since the error of the manipulator is almost 5 times larger (0.74 mm).

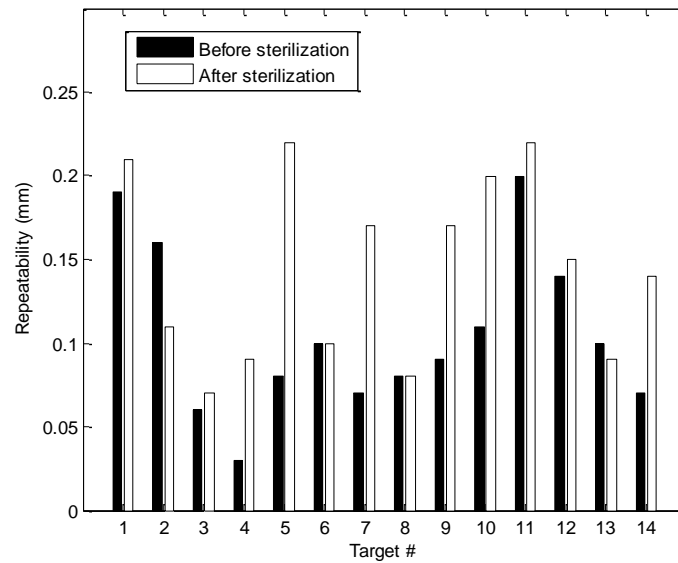
Table 4.3: Results of the needle artifact shift.

Targets	Glass needle			Titanium needle		
	Er _R	Er _A	Er _{Tot}	Er _R	Er _A	Er _{Tot}
#1	-0.10	-1.33	1.33	0.30	-0.13	0.32
#2	-0.74	0.20	0.76	-0.24	0.50	0.55
#4	-2.50	-1.50	2.91	-1.80	-1.40	2.28
#5	-0.70	-0.30	0.76	0.20	-0.30	0.36
#6	1.16	0.90	1.46	1.76	1.50	2.36
#7	-0.06	-0.85	0.85	-0.40	-0.35	0.53
#8	-0.40	1.40	1.40	-0.10	1.20	1.20
#9	-1.30	0.60	1.43	-1.30	0.00	1.30
Avg	-0.46	-0.14	1.29	-0.08	0.09	1.09
STD	1.05	1.00	0.70	1.07	0.87	0.76

Table 4.4: Joint space accuracy (mm).

	Axis 1	Axis 2	Axis 3	Axis 4	Avg
High	0.83	0.83	0.31	0.86	-
Low	-0.56	-0.24	-0.17	-0.26	-
Avg	0.20	0.29	0.17	0.11	0.20
STD	0.27	0.30	0.14	0.19	0.22





(b)

Figure 4.7: (a) The manipulator’s needle placement accuracy before and after sterilization and (b) repeatability in XYZ space before and after sterilization.

Effect of sterilization on robot accuracy: The robot sterilization protocol was as follows: 1) remove the top part of the robot (Figure 4.6) and send to sterilization as a sub-ensemble, 2) gross cleaning, 3) enzymatic cleaning, 4) gas sterilization, and 5) remount. Due to disassembly, heating, moisture absorption, and other effects, the robot’s accuracy and repeatability might be affected. To investigate this issue, the accuracy and repeatability assessments were repeated after robot sterilization. The results in Figure 4.7 show negligible difference. It should be noted that the differences shown here are not only because of sterilization since the robot does not have 0 mm precision (= repeatability).

4.4.2 Total error of robotic system

Figure 4.8 shows the distribution of the total error before needle insertion, i.e. the intrinsic error of the robotic system. The average error is 1.3 mm.

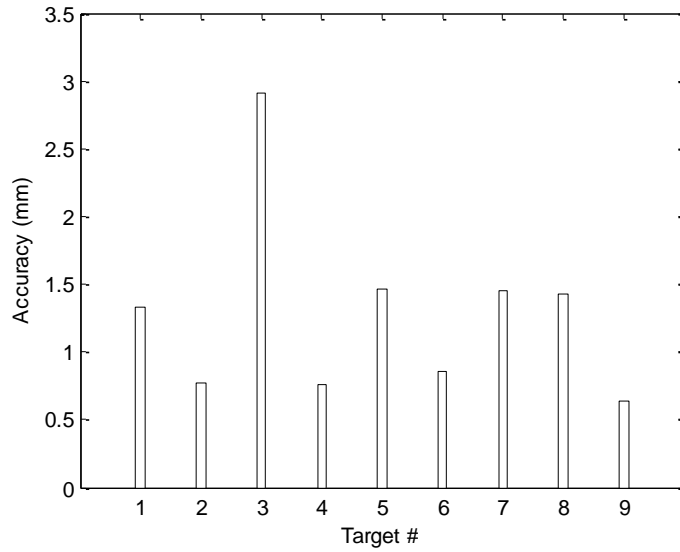


Figure 4.8: Distribution of the total error for the robotic system.

4.4.3 Overall needle placement error

The overall average error yielded by the experiment described in section 3.6, was 2.5 mm (STD = 1.37 mm) which is within the acceptable range for prostate biopsy [21].

4.4.4 Due-to-insertion inaccuracy

As seen, the average overall needle placement error and the total error associated with the robotic system are known. With the assumption of no extrinsic error (which seems realistic in a phantom experiment), the total error due to insertion can be approximated as follows (it is a rough approximation since error components are vectors):

$$\begin{aligned}
 Error_{due-to-insertion} &\approx \sqrt{(\overline{Error}_{overall}^2 - \overline{Error}_{robotic\ sys}^2)} \\
 &= \sqrt{(2.5^2 - 1.3^2)} = 2.13\ mm
 \end{aligned}
 \tag{4-10}$$

This implies that in our phantom experiments, due-to-insertion error is almost twice as large as the robotic system error.

4.5 Discussions

The overall needle placement error in phantom experiment was 2.5 mm which is acceptable for prostate cancer diagnosis. The overall error was broken into two parts: the error associated with the robotic system and the error introduced due to insertion. Robotic system was responsible for 1.3 mm and the insertion was responsible for 2.13 mm, assuming the error components are orthogonal. The error due to the robotic system consists of the manipulator's inaccuracy (0.71 mm), artifact shift (0.2 mm), and fiducial marker registration error (1.8 mm). The summation of absolute values of each part exceeds the total error (i.e. $(1.8 + 0.7 + 0.2) \text{ mm} = 2.7 \text{ mm} > 1.3 \text{ mm}$) because the error vectors may cancel out one another in some directions. Figure 4.9 shows this error distribution. The error due to the manipulator (robot) is relatively small compared to the fiducial registration error which indicates the effectiveness of the calibration process. The 2.13 mm error is an approximation of the due-to-insertion error and is mainly introduced by needle deflection. This error is highly dependent on the tissue properties and insertion depth. The calibration method proposed in this chapter is somehow particular to this robot because parallel robots are unique in kinematics [32] and therefore, they require their own way of calibration. In fact, the conventional methods of calibration for serial robots are not applicable to parallel robots and for this reason, it was to the interest of this research. However, the methodology we proposed in this chapter can still be customized for some other robot structures. This is due to the fact that our robot kinematic architecture has some features in common with some of its contemporary robots.

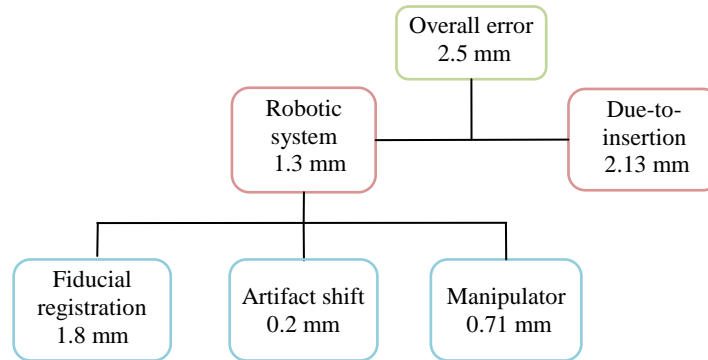


Figure 4.9: Summary of the error distribution (average values) of the studied robotic system in phantom MRI-guided prostate biopsy.

To understand it better, consider the kinematic architecture of MrBot [11], SABiR [32], and the Twin Pantograph [33]. Similar to our robot, these parallel robots comprise of two identical planar mechanisms and by combining the motion of these planar linkages, angulations (pitch and yaw) are generated. More interestingly, the architecture of the planar mechanisms of these robots are almost the same (Figure 4.10) but with different kinematic configurations. For example, the prismatic joints are replaced with revolute joints in Pantograph and SUBiR and or the location of prismatic joints are switched for the case of MrBot. Therefore, the study presented in this chapter can be customized for those kinematic structures as well or for robots with similar structure.

4.6 Conclusions

In this study, different sources contributing into the error of robot-assisted prostate biopsy under MRI guidance were identified. In particular, the error introduced by the robotic system was analyzed. All error components were quantified. A calibration method was proposed in order to

minimize the robot's inaccuracy as an important source of error. As a result, the overall error of the system in phantom experiment remained within the acceptable clinical range.

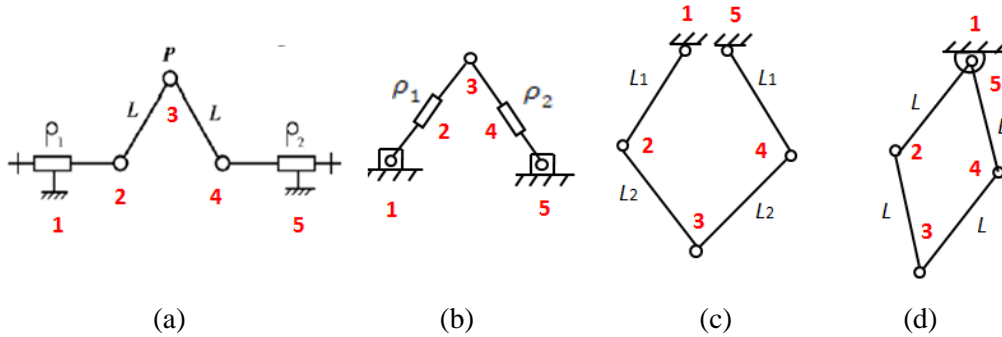


Figure 4.10: The front (back) planar mechanism of different parallel robots: (a) our robot, (b) MrBot, and (c) Twin Pantograph, and (d) SABiR. All of them have 5 joints and 5 linkages. In (a) and (b), two joints are prismatic, but in (c) and (d), all joints are revolute.

References

- [1] American Cancer Society, Cancer Facts and Figures 2011: <http://www.cancer.org>.
- [2] R. Siegel, E. Ward, O. Brawley, and A. Jemal. Cancer Statistics, 2011. The impact of eliminating socioeconomic and racial disparities on premature cancer deaths, Figure 1, DOI: 10.3322/caac.20121.
- [3] K. Eichler, S. Hempel, J. Wilby, L. Myers, L. M. Bachmann and J. Kleijnen, "Diagnostic value of systematic biopsy methods in the investigation of prostate cancer: a systematic review," *J. Urol.*, vol. 175, pp. 1605-1612, 2006.
- [4] K. K. Yu and H. Hricak, "Imaging prostate cancer," *Radiol. Clin. North Am.*, vol. 38, pp. 59-85, 2000.

- [5] A. V. D'amico, C. Tempany, R. Cormack, N. Hata, M. Jinzaki, K. Tuncali, M. Weinstein and J. Richie, "Transperineal magnetic resonance image guided prostate biopsy," *J. Urol.*, vol. 164, pp. 385-387, 2000.
- [6] N. Hata, M. Jinzaki, D. Kacher, R. Cormak, D. Gering, A. Nabavi, S. G. Silverman, A. V. D'Amico, R. Kikinis and F. A. Jolesz, "MR imaging-guided prostate biopsy with surgical navigation software: Device validation and feasibility1," *Radiology*, vol. 220, pp. 263-268, 2001.
- [7] R. C. Susil, K. Camphausen, P. Choyke, E. R. McVeigh, G. S. Gustafson, H. Ning, R. W. Miller, E. Atalar, C. N. Coleman and C. Ménard, "System for prostate brachytherapy and biopsy in a standard 1.5T MRI scanner," *Magnetic Resonance in Medicine*, vol. 52, pp. 683-687, 2004.
- [8] K. Chinzei, N. Hata, F. A. Jolesz and R. Kikinis, "MR compatible surgical assist robot: System integration and preliminary feasibility study," in *Medical Image Computing and Computer-Assisted Intervention–MICCAI 2000*, 2000, pp. 921-930.
- [9] S. DiMaio, S. Pieper, K. Chinzei, N. Hata, S. Haker, D. Kacher, G. Fichtinger, C. Tempany and R. Kikinis, "Robot-assisted needle placement in open MRI: system architecture, integration and validation," *Computer Aided Surgery*, vol. 12, pp. 15-24, 2007.
- [10] K. Tadakuma, L. DeVita, J. Plante, Y. Shaoze and S. Dubowsky, "The experimental study of a precision parallel manipulator with binary actuation: With application to MRI

- cancer treatment," in *Robotics and Automation, 2008. ICRA 2008. IEEE International Conference on*, 2008, pp. 2503-2508.
- [11] D. Stoianovici, D. Song, D. Petrisor, D. Ursu, D. Mazilu, M. Mutener, M. Schar and A. Patriciu, "'MRI Stealth' robot for prostate interventions," *Minimally Invasive Therapy & Allied Technologies*, vol. 16, pp. 241-248, 2007.
- [12] G. S. Fischer, I. Iordachita, C. Csoma, J. Tokuda, S. P. DiMaio, C. M. Tempny, N. Hata and G. Fichtinger, "MRI-compatible pneumatic robot for transperineal prostate needle placement," *Mechatronics, IEEE/ASME Transactions on*, vol. 13, pp. 295-305, 2008.
- [13] A. Goldenberg, J. Trachtenberg, W. Kucharczyk, Y. Yi, M. Haider, L. Ma, R. Weersink and C. Raoufi, "Robotic system for closed-bore MRI-guided prostatic interventions," *Mechatronics, IEEE/ASME Transactions on*, vol. 13, pp. 374-379, 2008.
- [14] M. R. van den Bosch, M. R. Moman, M. van Vulpen, J. J. Battermann, E. Duiveman, L. J. van Schelven, H. de Leeuw, J. J. W. Lagendijk and M. A. Moerland, "MRI-guided robotic system for transperineal prostate interventions: proof of principle," *Phys. Med. Biol.*, vol. 55(5), pp. 133-140, 2010.
- [15] H. Su, W. Shang, G. A. Cole, K. Harrington and G. S. Fischer, "Haptic system design for MRI-guided needle based prostate brachytherapy," in *Haptics Symposium, 2010 IEEE*, 2010, pp. 483-488.
- [16] H. Su, M. Zervas, G. A. Cole, C. Furlong and G. S. Fischer, "Real-time MRI-guided needle placement robot with integrated fiber-optic force sensing," in *Robotics and Automation (ICRA), 2011 IEEE International Conference on*, 2011, pp. 1583-1588.

- [17] J. B. Bak, S. K. Landas and G. P. Haas, "Characterization of prostate cancer missed by sextant biopsy," *Clinical Prostate Cancer*, vol. 2, pp. 115-118, 2003.
- [18] P. Blumenfeld, N. Hata, S. DiMaio, K. Zou, S. Haker, G. Fichtinger and C. Tempany, "Transperineal prostate biopsy under magnetic resonance image guidance: a needle placement accuracy study," *Journal of Magnetic Resonance Imaging*, vol. 26, pp. 688-694, 2007.
- [19] J. Tokuda, G. S. Fischer, S.P. DiMaio, D. G. Gobbi, C. Csoma, P.W. Mewes, G. Fichtinger, C. M. Tempany, and N. Hata. Integrated navigation and control software system for MRI-guided robotic prostate interventions. *Computerized Medical Imaging and Graphics*, vol. 34(1), pp. 3-8, 2010.
- [20] S. E. Song, N. B. Cho, G. Fischer, N. Hata, C. Tempany, G. Fichtinger and I. Iordachita, "Development of a pneumatic robot for MRI-guided transperineal prostate biopsy and brachytherapy: New approaches," in *Robotics and Automation (ICRA), 2010 IEEE International Conference on*, 2010, pp. 2580-2585.
- [21] R. Seifabadi, S. E. Song, A. Krieger, N. B. Cho, J. Tokuda, G. Fichtinger and I. Iordachita, "Robotic system for MRI-guided prostate biopsy: feasibility of teleoperated needle insertion and ex vivo phantom study," *International Journal of Computer Assisted Radiology and Surgery*, vol. 7, pp. 181-190, 2012.
- [22] S. Song, N. Hata, I. Iordachita, G. Fichtinger, C. Tempany and J. Tokuda, "A workspace-orientated needle-guiding robot for 3T MRI-guided transperineal prostate

- intervention: evaluation of in-bore workspace and MRI compatibility," *The International Journal of Medical Robotics and Computer Assisted Surgery*, 2012.
- [23] A. Patriciu, D. Petrisor, M. Muntener, D. Mazilu, M. Schär and D. Stoianovici, "Automatic brachytherapy seed placement under MRI guidance," *IEEE Trans. Biomed. Eng.*, vol. 54, pp. 1499-1506, 2007.
- [24] E. Dehghan and S. E. Salcudean. Needle insertion parameter optimization for brachytherapy. *Robotics, IEEE Transactions on*, vol. 25(2), pp. 303-315, 2009.
- [25] N. Abolhassani, R. Patel and F. Ayazi, "Effects of different insertion methods on reducing needle deflection," in *Engineering in Medicine and Biology Society, 2007. EMBS 2007. 29th Annual International Conference of the IEEE*, 2007, pp. 491-494.
- [26] V. Lagerburg, M. A. Moerland, M. van Vulpen, and J. W. Lagendik. A new robotic needle insertion method to minimize attendant prostate motion. *Radiotherapy and Oncology*, vol. 80(1), pp. 73-77, 2006.
- [27] H. Xu, A. Lasso, S. Vikal, P. Guion, A. Krieger, A. Kaushal, L. L. Whitcomb and G. Fichtinger, "MRI-guided robotic prostate biopsy: A clinical accuracy validation," in *Medical Image Computing and Computer-Assisted Intervention–MICCAI 2010* Anonymous Springer, 2010, pp. 383-391.
- [28] Y. Hu, T. J. Carter, H. U. Ahmed, M. Emberton, C. Allen, D. J. Hawkes and D. C. Barratt, "Modelling prostate motion for data fusion during image-guided

- interventions," *Medical Imaging, IEEE Transactions on*, vol. 30, pp. 1887-1900, 2011.
- [29] K. Masamune, G. Fichtinger, A. Patriciu, I. Sakuma, T. Dohi, and D. Stoianovici. System for robotically assisted percutaneous procedures with computed tomography guidance. *Journal of Computer Aided Surgery*, vol.6, pp.370-383, 2001.
- [30] T. Peters, K. Cleary. Image-Guided Interventions: Technology and Applications. *Springer*, pp. 447, 2008.
- [31] S. Song, N. B. Cho, I. I. Iordachita, P. Guion, G. Fichtinger and L. L. Whitcomb, "A study of needle image artifact localization in confirmation imaging of MRI-guided robotic prostate biopsy," in *Robotics and Automation (ICRA), 2011 IEEE International Conference on*, 2011, pp. 4834-4839.
- [32] O. Bebek, M. J. Hwang and M. C. Cavusoglu, "Design of a parallel robot for needle-based interventions on small animals," in *IEEE/ASME Transactions on Mechatronics*, published online 2011.
- [33] M. R. Sirouspour, S. P. DiMaio, S. Salcudean, P. Abolmaesumi and C. Jones, "Haptic interface control-design issues and experiments with a planar device," in *Robotics and Automation, 2000. Proceedings. ICRA'00. IEEE International Conference on*, 2000, pp. 789-794.

Chapter 5

Teleoperated needle steering under real-time MRI guidance for prostate interventions: a feasibility study

Most robotic systems reported for MRI-guided prostate interventions use manual needle insertion, based on previously acquired images, which requires removing the patient from the scanner multiple times during the procedure. This makes the intervention longer, more expensive and prolonging the discomfort to patient and, most importantly, less accurate due to the virtually inevitable motion of the target. As a remedy, automated needle placement techniques were proposed, removing human supervision from the control loop. This chapter proposes the feasibility of a human-operated in-room master-slave bevel-tip needle steering under real-time MRI guidance, in which the patient is kept in the scanner at all times and the process of needle placement is under continuous control of the physician. Bevel-tip needle steering is proposed in order to compensate for the targeting error due to needle-tissue interaction. Therefore, a 2-DOF piezo-actuated MRI-compatible needle steering module is developed and integrated with an existing 4-DOF transperineal robot creating a fully actuated 6-DOF (x , y , z , yaw, pitch, and roll) robotic platform for MRI-guided prostate interventions. A novel piezo-actuated MRI-compatible 2-DOF master robot is also developed to enable teleoperated needle steering. An MRI-compatible 2-DOF force/torque sensor was developed to be used on the master side. The MRI-compatibility results of the system demonstrated small signal to noise ratio (SNR) loss. Robot functionality was not influenced by the magnetic field. The feasibility of teleoperated bevel-tip needle steering using the proposed system was shown in phantom experiment once in a bench-top experiment

and once under real-time MRI-guidance. The targeting error was significantly reduced as the result of bevel-tip needle steering.

5.1 Introduction

Prostate cancer is the most common cancer for men in the United States and other western countries. Every year, approximately 1.5 million prostate biopsy procedures are performed in the United States alone [1]. If the prostate specific antigen (PSA) level goes above a certain threshold, patients are advised to undergo a biopsy which is usually performed under transrectal ultrasound (TRUS) guidance. If the result is positive, and depending on the stage of cancer, patients are advised to take one or a combination of different treatments such as radiation therapy, chemotherapy, ablation, etc. Many patients choose low dose brachytherapy (LDR) since it is a minimally invasive treatment method and has a short recovery time. Brachytherapy requires placing 60-120 radioactive seeds into the prostate using needles so that the radioactive seed irradiate local cancerous lesions. In both biopsy and brachytherapy, needles are manually inserted into the prostate under TRUS guidance.

Ultrasound-guidance is the gold standard method for prostate biopsy and brachytherapy since it is real-time, relatively inexpensive, non-invasive, and easy to use. However, the image quality is rarely sufficient to visualize the cancerous lesions and rather, it shows the prostate boundary. This results in a significant number of false-negative biopsies. The detection rate is between 20-40% [2]. In brachytherapy, the seeds are barely visible since they are very small and also because their visibility is hindered by the speckle shadow artifact [3].

MRI is a superior imaging modality for its excellent visualization of the prostate lesions, gland, surrounding tissues, and because it is non-invasive. Advances with endorectal and phased array

pelvic coils have significantly improved the ability of MRI to visualize prostate tissue [4]. MRI can even provide (near to) real-time imaging.

MRI-guided manual prostate biopsy was introduced in 1995 by Schenck *et al.* in [5]. The effectiveness of MRI-guided brachytherapy was initially reported by D'Amico in 1998 [6]. The manual procedures, however, have some shortcomings:

- 1) It is hard for access the patient since the MRI bore is a confined space. This means that the patient should be moved in and out twice for each biopsy: once for the needle insertion and once for sample removal after taking a confirmation image. This results in a longer and more expensive procedure (due to longer MRI time and personnel time) as well as being uncomfortable for the patient. It also increases the possibility of patient motion which can lead to targeting error.
- 2) In manual biopsy and brachytherapy, a grid template is used with a targeting accuracy limited to 5 mm. Also, it does not enable an angulated needle trajectory which would help avoid pubic arch interference (PAI). These deficiencies are motivations for a robot-assisted approach.

Since 2000 when the first robot was introduced to assist MRI-guided prostate biopsy and brachytherapy [7], a few robotic systems have been developed for MRI-guided prostate biopsy and brachytherapy. These robots can be categorized into two groups: 1) manually actuated devices, and 2) computer controlled systems [8]. The first group's main disadvantage is the numerous patient removals from the scanner needed for needle placement. The second group can be categorized into two subtypes:

- 1) Robots with manual needle insertion; these robots only orient the needle toward the target and the insertion is still performed manually. Similar to manually actuated devices, these systems require many in-and-out movements of patient during the procedure.
- 2) Robots with automated needle placement; the major concern regarding these systems is the exclusion of the clinician from the control loop thus potentially risking patient safety.

Table 2.2 in Chapter 2 listed previously reported robotic systems for MRI-guided prostate biopsy and brachytherapy and compares them from different perspectives. In particular, it can be observed that from all previously reported robotic systems for MRI-guided prostate needle placement, 80 percent use the manual approach and 20 percent use the automated approach.

Given the shortcomings of the previously reported robotic systems, this study seeks to develop a robotic system that keeps the patient inside the scanner and takes advantage of the real-time MRI imaging during needle advancement, while keeping the physician in the control loop.

5.1.1 Previous work on teleoperated needle insertion under MRI guidance

⁹[Kokes *et al.* in [9] reported a 1-DOF hydraulically actuated needle insertion robot for breast radio frequency ablation under MRI guidance using a commercial haptic device placed outside of the MRI room. They used a commercial non-MRI compatible force sensor on the slave side behind the needle to monitor the force applied to the needle as a tool for cancerous tissue detection. Yang *et al.* in [10] proposed a pneumatically actuated version of the 1-DOF system. They developed a 3-DOF MRI-compatible force sensor to monitor the insertion forces [11]. Elhawary *et al.* in [12] reported a 5-DOF robotic system using linear piezo-ceramic motors for transrectal prostate biopsy in 1.5T MRI. This system employed a remotely-driven touch-screen needle insertion console placed inside the scanner room. Tse *et al.* in [13] reported a 1-DOF

⁹ The materials provided between the brackets have some overlap with the Chapter 2. This is due to the fact that each chapter is a manuscript which is either published or to be published and therefore, should have a single complete story.

haptic device to command the needle insertion driver from outside of the scanner room. Su *et al.* in [14] reported design requirements of a system for teleoperated needle insertion under real-time MRI for prostate brachytherapy. They proposed using a commercial haptic device as the master robot to command the needle driver from outside the room. Seifabadi *et al.* in [15] reported the feasibility of teleoperated needle insertion with the use of a single-DOF piezo-actuated needle insertion device integrated with a 4-DOF pneumatically actuated robot for transperineal prostate biopsy and brachytherapy, commanding it remotely by an MRI-compatible manually actuated master device [15]. Piccin *et al.* in [16] reported development of a bilateral single-DOF non-MRI compatible master device to remotely command the needle driver module of a 5-DOF CT/MRI-guided patient-mounted needle placement robot from outside of the scanner room.

5.1.2 Case for teleoperated needle steering under MRI guidance

Different sources contributing to the overall needle placement error in MRI-guided robotic prostate needle placement were studied in [17]. Among various errors, those caused during needle insertion are relatively more significant. This is because prostate rotation is not completely constrained by the surrounding organs [18] and [19].

In literature, many studies have reported methods of error estimation/prediction and error compensation during needle insertion. Abolhassani *et al.* in [20] reviewed different methods of error estimation/prediction including:

- 1) Methods that estimate the error by modeling insertion forces [21];
- 2) Methods that estimate the error by modeling tissue deformation during needle insertion [22] and [23];
- 3) Methods that estimate the error by modeling needle deflection [24].

Methods of error estimation are not in the scope of this study. Instead, we are seeking an efficient robotic approach for error compensation.

We found the following methods of compensation in the literature to reduce the error caused during needle insertion:

- 1) Lagerburg *et al.* in [25] proposed a tapping method to decrease the insertion force. Tapping means small and fast oscillations of needle during insertion resulting in reduction of the force between the needle and tissue. The efficacy of tapping was investigated in 30 patients who underwent transperineal ultrasound-guided brachytherapy. The needle placement error reduced from a mean of 5.9 mm to 0.9 mm [range of 0-2.0 mm] as a result of tapping as reported in [26];
- 2) Patriciu *et al.* in [27] suggested fast needle insertion during MRI-guided transperineal prostate brachytherapy to reduce the error caused by prostate motion. The method was accurate to 1.15 mm in seed placement in gel phantom and 2.5 mm in a canine study. We think this method can place some risk on patient's safety;
- 3) Badaan *et al.* in [28] reported continuous spinning of the needle as a practical solution to lower insertion force. The main concern for this method is the potential for causing tissue damage as a result of needle spinning;

In addition to the mentioned limitations, these methods cannot entirely eliminate the error and rather reduce it to some extent assuming that target does not move during needle insertion. A more efficient approach that may solve this issue is:

- 4) Flexible needle steering, meaning maneuvering the needle tip inside tissue under image guidance until it reaches the target. Three methods have been proposed for steering a flexible needle inside tissue:

- 4-1) Moving laterally base of the needle during needle insertion [29]. Disadvantages of this method are large lateral displacement of the needle base and requirement of applying large forces to the tissue.
- 4-2) Multiple concentric tubing with pre-bent inner stylet was also proposed in [30] and [31]. The feasibility of multiple concentric tubing under MRI guidance was reported in [32]. This method is more effective when it is desired to reach a target in a cavity. If targets are deep inside tissues, it may not be as effective unless the needle is very close to the target [33].
- 4-3) Bevel-tip needle steering [34]: if a bevel-tip flexible needle is inserted into tissue, it bends due to the asymmetric forces applied to the tip. If the needle is rotated 180 degrees, the needle bends to the opposite direction. Compared to the method 4-1), this method is less traumatic and compared to the second approach, it has the advantage of using standard needles and a simple robotic system. In fact, it only requires the combination of translation and rotation of needle. Although this idea was initially proposed for obstacle avoidance during percutaneous interventions, it is used for error compensation in this study.

Robot-assisted bevel-tip needle steering can be performed automatically or human-controlled using a master-slave system. The automated approach may be faster and less traumatic to the patient since it requires a smaller number of insertions. However, it relies on the knowledge of tissue and needle deformation during needle insertion. There is no such model yet available which can precisely predict needle-tissue deformation and prostate motion. On the other hand, the human-operated needle steering does not require a model of the needle-tissue interactions since it is performed intuitively in a trial and error fashion. The biggest advantage, however, is having

continuous human supervision during the procedure. For the advantages mentioned above, master-slave bevel-tip needle steering seems to be a promising approach to compensate for the error caused during needle insertion.

In this study, we present an MRI-compatible robotic platform with full 6-DOF (x , y , z , yaw, pitch, and roll) for prostate needle placement. We present a novel 2-DOF MRI-compatible master robot and development of controller hardware and software to enable teleoperated needle steering. Also, a 2-DOF MRI-compatible force sensor is developed using Fiber Bragg Grating (FBG) sensors to address with the non-backdrivability of the master robot that originates from the inherent friction of the piezo actuators. MRI-compatibility results of the system are presented in a 3T MRI scanner. Accuracy of the slave robot in tracking the master robot is presented in an MRI room inside a phantom. The feasibility of bevel-tip needle steering in phantom is demonstrated under real-time MRI-guidance.]

5.2 System architecture and components

Figure 5.1 exhibits the entire system architecture. On the right side, the base robot system components are shown as black rectangles while on the left side, teleoperated needle steering system components developed in this study are shown in red.

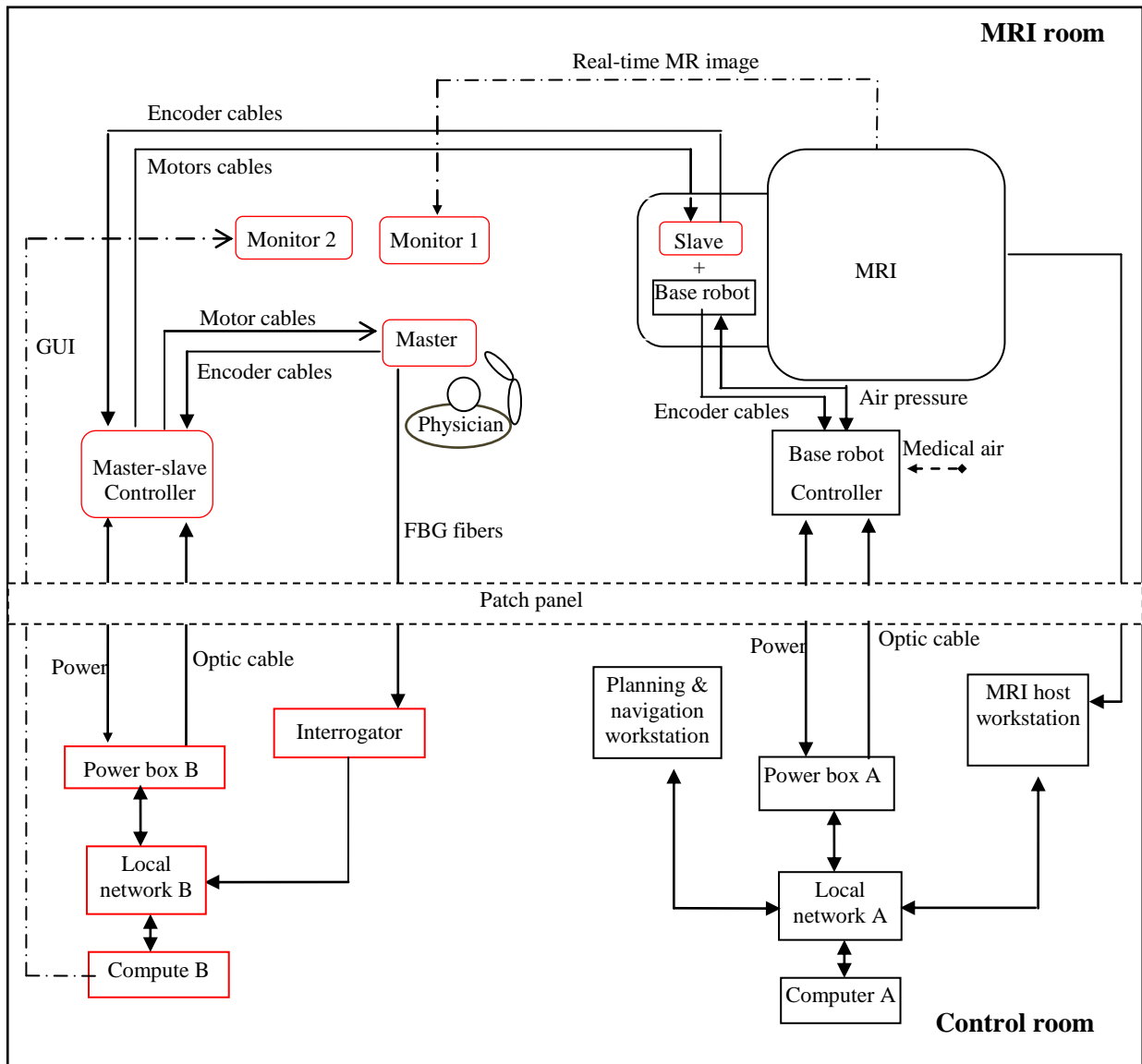


Figure 5.1: Schematic of the entire system components: Right: base robot system components are shown in black boxes. Left: teleoperation needle steering system components developed in this study are shown in red boxes.

5.2.1 Base robot system architecture and components

The base robot system consists of a 4-DOF parallel manipulator hereafter referred to as the base robot, base robot controller, planning and navigation workstation, power box A, MRI host

workstation, local network A, and computer A (Figure 5.1). The base robot and its controller are placed inside the MRI room while the rest are placed in control room.

Figure 5.2 shows the base robot. The robot is designed for manual needle insertion. 4 pneumatic actuators are used to move the four sliders. The movement of the 4 sliders enables translations and rotations of the needle in the x , y and R_x , R_y directions, respectively.

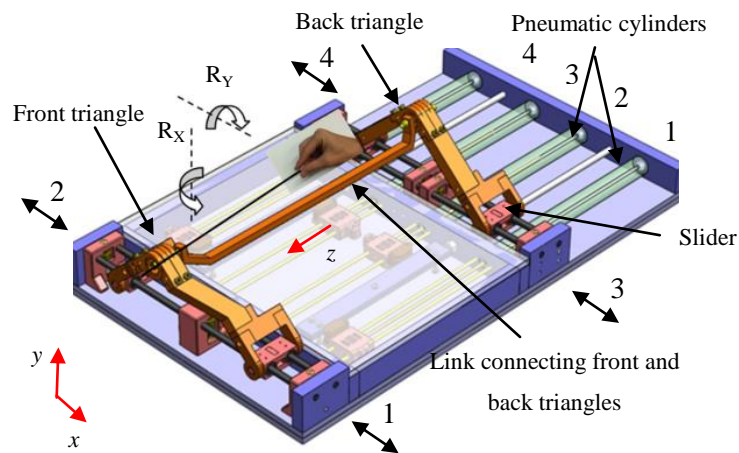


Figure 5.2: Base robot is a 4-DOF pneumatic robot for transperineal needle placement into prostate under MRI-guidance. It provides translations in x , and y directions as well as angulations in R_x and R_y directions. Insertion is performed manually.

The pneumatic linear actuators can be physically locked by brake mechanisms (not shown in Figure 5.2) to prevent the robot from accidentally moving during the needle insertion process due to human, software, or electrical errors.

The base robot controller consists of a linux PC, piezo electric valves, and a media converter all placed into a radio frequency shielded cage [35]. The controller uses medical air in a hospital to run the base robot. The power supply is placed in control room and is plugged to the controller through a patch panel (which is a RF shielded panel in MRI rooms).

The biopsy procedure using this robot is as follows:

- 1) The patient is placed on MRI table in lithomy position.
- 2) A Z-pattern fiducial frame as described in Chapter 2, (section 2.2.5) is placed on a predefined position on table and MR images are acquired. The images of Z-frame are sent from the MRI host workstation to the navigation and planning workstation on which 3D Slicer is running 3D Slicer calculates the robot-to-MR image coordinate transformation (called registration) and sends the transformation matrix (4×4) to the robot controller through the optical cable. This registration is performed once at the beginning of each procedure. All data between the controller and navigation workstation (or computer A) is transmitted through fiberoptic cables to minimize electro-magnetic interference (EMI).
- 3) The Z-frame is removed and the base robot is placed between the patients legs in a defined position.
- 4) The patient is moved to the scanner and images are acquired. The prostate images are sent from the MRI host workstation to 3D Slicer (planning and navigation workstation).
- 5) In 3D Slicer, a suspicious target is specified by the physician. Then, the target position along with a needle path in RAS coordinate are sent through the fiberoptic cable to the base robot controller. The needle path is chosen by physician within the reachable workspace of the robot and with the goal of avoiding pubic arch interference.
- 6) The robot controller applies the transformation matrix found in step 2) and calculates the target position and needle path in robot coordinate system. Next, robot controller solves the inverse kinematics, finds each actuator displacements, commands the piezo valves to apply pressure on each pneumatic cylinder, and move them accordingly.

- 7) After the actuators move, the position of each actuator is sent back to robot controller. The robot controller solves the forward kinematic and finds the target the needle path and compare them to the desired values. If the error is negligible, the needle is ready to be inserted.
- 8) Patient is removed from the scanner and needle is inserted manually.
- 9) The patient is placed back into the scanner and a confirmation image is taken to ensure the accuracy. If accuracy is satisfactory, the patient is removed and the needle is taken out. Otherwise, the patient is removed and needle is re-inserted. Procedure is repeated until all suspicious targets are sampled.

The monitor in control room displays the air pressure and the encoders' positions. Details of the base robot kinematics and system architecture can be found in [15], [36], and [37].

5.2.2 Teleoperated needle steering system architecture and components

A teleoperated needle steering system consists of: 1) a 2-DOF needle steering slave robot which is integrated with the base robot yielding a 6-DOF manipulator, 2) an MRI-compatible 2-DOF master robot, 3) master-slave controller, 4) two MRI-compatible monitors for real-time MR image and for graphical user interface (GUI), 5) an FBG interrogator for wavelength shift measurement (used in force measurement), 6) power supply box B, 7) local network B, and 8) computer B for force calculations, previewing GUI, and sending and receiving data to master-slave controller. Master-slave controller is placed next to the patch panel. The master robot and the monitor are placed next to the patient.

Data between the master-slave controller and computer B is transmitted thorough optical fiber cable. In fact, inside master-slave controller box and power box B, there are two identical media convertors that exchange data into optic signals and vice versa, meaning the data transmission

between the MRI room and the control room is in optical form with no interference with MRI. The local network in the control room aims to connect the FBG interrogator and master-slave controller to the computer B. The power cord is connected to master-slave controller through the patch panel to minimize EMI.

The first 8 steps of the biopsy procedure with use of the the proposed master-slave system is identical to the old system. The remaining steps are as follows:

- 9) The physician holds the needle mimicking stylet of the master robot and applies some force to start the motion. The FBGs embedded in the force sensor send the optical signal to the FBG interrogator which is placed in control room. These fibers are passed through the opening in the patch panel. The FBG interrogator measures the wavelength shifts and sends this information to computer B. In a MATLAB code, force and/or torque are calculated from the wavelength shifts and then sent to the master-slave controller in order to be used in the control loop.
- 10) The master-slave controller commands the master robot to move with a velocity proportional to the force applied.
- 11) The slave translates (rotates) the needle equal to the master translation (rotation). The physician observes needle advancement under real-time MRI and monitors the accuracy of tracking and the depth (or the needle rotation) on the GUI.
- 12) If the needle is deviating from the target, physician retracts the needle proportional to needle placement error and rotates the needle 180 degrees. Then, the insertion is resumed until reaching the target.
- 13) Next, the patient is removed and the needle is taken out. These steps are repeated until all targets are sampled.

In following sections, major components of the teleoperated systems are discussed in details.

5.3 Slave robot

The slave robot generates a combination of linear and rotary motions for the bevel-tip needle so that needle steering is enabled (Figure 5.3). This module replaces the linkage connecting the robot's front and back triangles (Figure 5.2) thus minimally changing the current design of the base robot. Figure 5.4 shows how easily the slave robot can be integrated with the base robot yielding a 6-DOF fully actuated robotic platform for MRI-guided prostate interventions. Switching between the manual insertion configuration (4-DOF robot) and teleoperated insertion configuration is therefore quick and easy.

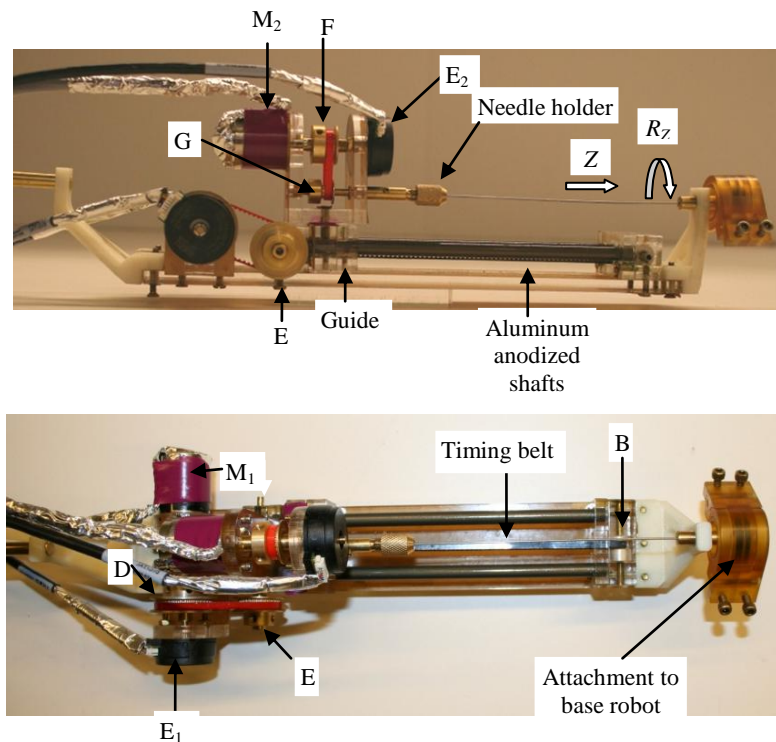


Figure 5.3: MRI-compatible needle steering slave robot with 2-DOF: translation along Z (superior-inferior) and rotation of the bevel-tip needle R_z . Cables are shielded carefully.

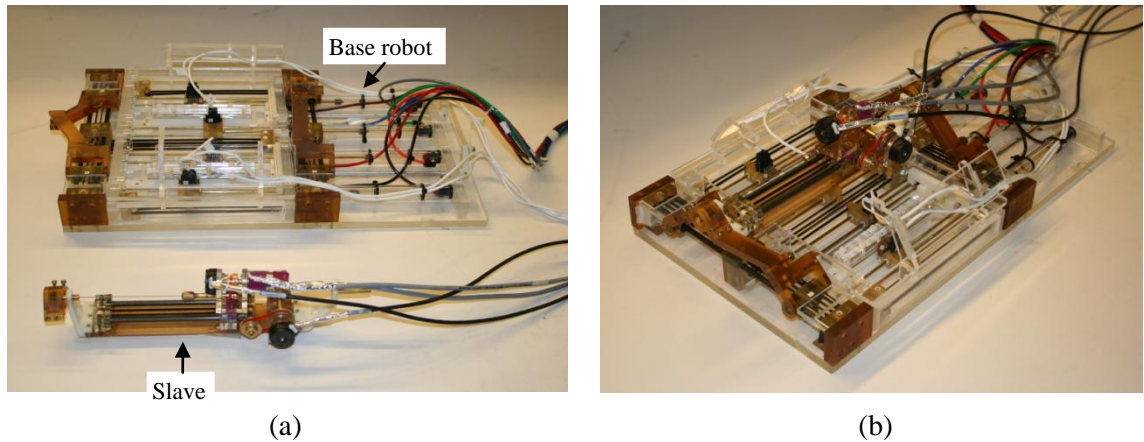


Figure 5.4: (a) The slave can be easily attached to the base robot and (b) the needle steering module is integrated with the base robot. The base robot provides the macro needle positioning and the slave provides insertion and final adjustments (i.e. steering).

5.3.1 Motors selection

Piezo motors were used in this study for their precise positioning and linear behavior which simplify the control of the position. However, minimizing the SNR deterioration related to these motors is a big challenge. Various piezo motors that are commercially available were compared: the Shinsei USR30-S ultrasonic motor (Shinsei Inc, Japan) is compact enough and provides high speed and torque (300 RPM and 100 Nmm, respectively). However, the driver provided with this motor had been reported to introduce significant noise on MR image [38]. Nanomotion motors (Nanomotion Ltd, Yokneam, Isreal) provide high speed and power. However, they only generate high frequency small-amplitude harmonic motion which is required to be combined with linear/rotary stages in order to be usable. These stages are usually bulky and expensive. Direct drive motors offered by Actuated Medical Inc (Bellefonte, PA, USA) are bulky and heavy even though they provide high power and speed. In this study, we used non-magnetic piezo motors (PiezoLEG Uppsala, Sweden) with PDA 3.1 drivers (nominal torque = 50 Nmm, nominal speed =

5.5 RPM). Some advantages of these motors are their high accuracy, small size, and availability of a standard driver (± 10 V analog input). Most importantly, SNR loss as a result of using this motor and driver was reported to be insignificant ($< 9\%$) [39] - this result cannot be utilized for our system directly). However, the maximum speed and torque of these motors is limited. According to our experiments, the piezo motor can provide 32 Nmm at its maximum speed of 5.5 RPM (the maximum torque decreased as the speed increases). This information will be used subsequently for power analysis.

It is preferred to design the slave robot to be non-backdrivable so that in the case of power failure, the needle holds its own position. This is naturally provided by the inherent friction of the piezo motor (55 Nmm static friction torque).

5.3.2 Linear stage

The linear motion is provided by a belt drive which consists of a timing belt, two small brass timing belt pulleys A and B (A is hidden), two aluminum anodized shafts, and a guide (Figure 5.3). Belt drive was chosen due to its smaller friction and minimum backlash. The guide for needle rotation stage and needle holder slides on two aluminum shafts and is fixed to the timing belt thus moving with the timing belt. Power is provided by piezo motor M_1 and is transmitted by another timing belt and a pair of pulleys (D, E). The gear ratio Gr_s between D and E was chosen to be 4:3 so that a speed of 2.5 mm/sec is attained with enough thrust force to easily penetrate into the prostate phantom. The travel is 140 mm enough to reach targets deep into the prostate (usually, targets are 70-110 mm deep). Optical encoder E_1 (EP8 OEM, US Digital, Vancouver, WA) is placed concentric to motor M_1 shaft in order to measure the linear displacement of the needle. All other parts are made of plastic (either 3D printing or cast acrylic) or brass.

5.3.3 Rotary stage

The rotary motion is generated by a second motor M_2 . The power is transmitted to the needle holder using two pulleys: F and G (Figure 5.3). The gear ratio between F, G is 2:1 to increase the speed of rotation. The needle is held by a hollow vice made of brass. The needle is loaded from behind for convenience. Optical encoder E_2 is used to measure needle orientation (EP8 OEM, US Digital, Vancouver, WA).

5.3.4 Needle

Typically, an 18G needle ($\varnothing = 1.3$ mm) is used for prostate biopsy and brachytherapy. In this study however, we used an MRI-compatible 20G \times 15 cm bevel-tip biopsy needle (Cook Inc, IN, USA) to achieve increased flexibility so that we can compensate for the errors caused by the needle-tissue interaction. The nominal angle of the bevel tip is 45 degrees.

5.3.5 Power analysis

The force applied to the needle during insertion can be found for 17G and 18G needles in the literature [41]. According to those studies, the maximum force for 17G and 18G needles are 14.5 N and 8.9 N, respectively. But in needle steering application, we propose using a 20G needle for better flexibility. In this study, we used a commercial prostate phantom (CIRS 053, Computerized Imaging Reference Systems, Inc., Norfolk, VA, USA) to roughly measure this force. It should be noted that since the inside gel is homogenous, the force variations may not precisely represent the actual forces. With the slave robot and a Nano 17 force sensor (National Instrument, NC, USA), the force was measured. Figure 5.5 shows the force profile for an insertion speed of 2.5 mm/sec. The force remains limited to 2.5N. Our slave robot can provide more than 5 N for the maximum insertion speed.

For the rotary motion, the required torque is small and the slave can provide superior torque to rotate the needle inside the prostate phantom.

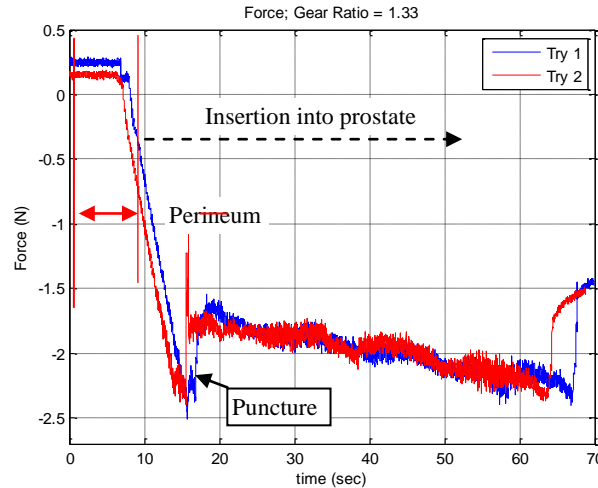


Figure 5.5: Force variation for inserting a 20G bevel-tip needle into prostate phantom CIRS 053. Experiment was repeated to ensure consistency.

5.4 Master robot

The master robot is designed to perform needle steering remotely while the physician is standing inside the MRI room next to the patient. Similar to the slave robot, the master has 2-DOF: needle insertion and needle rotation. Figure 5.6 shows the prototype of the proposed master robot. The physician grasps a small diameter cylinder (called stylus) that mimics the needle and manipulates it as if he or she is performing real needle steering. A force sensor is placed behind the stylus where the physician applies force and torque.

In the design of the master robot, we tried to minimize the inertia of moving parts and friction force since they distort kinesthetic sense. This means that actuators and encoders should be stationary. Also, prismatic joints were avoided in order to minimize friction.

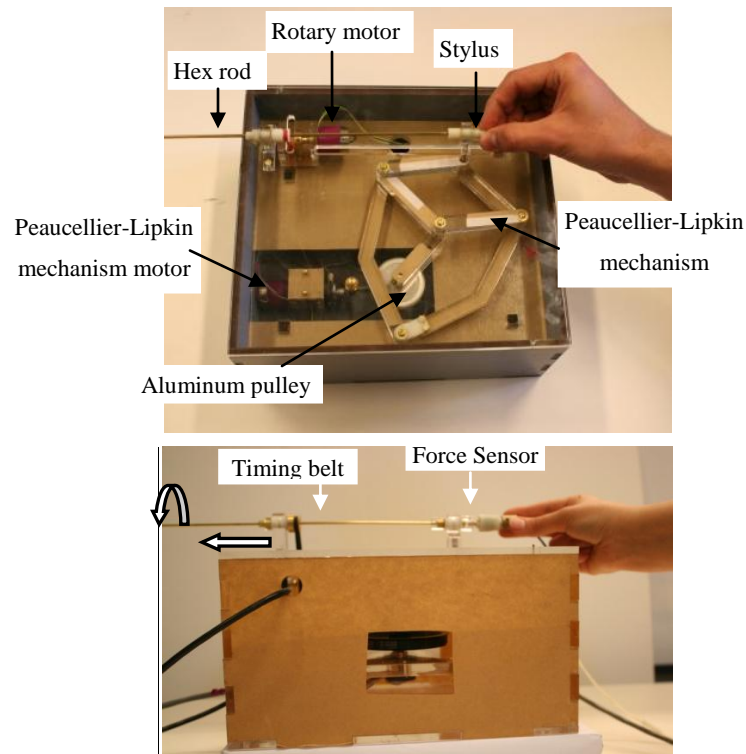


Figure 5.6: Prototype of the master robot: Peaucellier-Lipkin mechanism was employed to convert rotary motion of motor to linear motion. For rotation, the power was transmitted with a timing belt. Both motors and both encoders were fixed to the base.

5.4.1 Linear stage

Different mechanisms that convert rotary motion into linear motion with minimum friction were considered. Barbe *et al.* in [42] reported a slider-crank mechanism in the design of a single-DOF haptic device for remote needle insertion. In [27], an optimized configuration of a slider-crank mechanism was proposed for abdominal needle insertion. Other possibilities include using a four-bar mechanism that generates a straight trajectory such as Chebyshev, Hoeken, and Watt linkages. They are however bulky, the trajectory is not perfectly linear, and only a small portion of the whole trajectory is straight. In this study, a Peaucellier-Lipkin mechanism (Figure 5.7) was

chosen due to the following advantages: 1) there is no sliding joint in this mechanism meaning that friction is minimal; 2) its effector (point P) travels a perfect line throughout the workspace; 3) no counter balancing is necessary since the mechanism can be configured horizontally; The actuator is placed stationary at joint B. Links AE and AD are equal in length and so are CE, EP, PD, and DC. As BC rotates, P travels in an accurate straight line meaning that $P = (d, y)$ where d is a constant and y is variable.

Kinematic analysis: A and C lie on a circle which is centered at B. It can be proven that A, C, and P are collinear. Therefore, $\beta = 2\alpha$. Thus,

$$y = d \times \tan(\alpha) = d \times \tan(\beta/2) \quad (5-1)$$

Therefore,

$$\beta = 2 \operatorname{Atang}\left(\frac{y}{d}\right) \quad (5-2)$$

It can be shown that:

$$d = \frac{l_1^2 - l_3^2}{2l_2} \quad (5-3)$$

where $l_1 = AD$, $l_2 = BC$, and $l_3 = CD$.

Equation (5-1) and (5-2) express the relationship between β , as input, and translation of point P as output and vice versa. Equation (5-3) will be used for designing the sizes of linkages as well as power analysis.

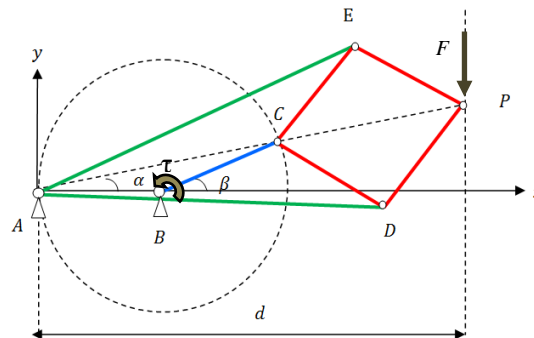


Figure 5.7: Peaucellier-Lipkin mechanism.

Dynamic analysis: Assuming the force F that physician applies to the master robot stylus is known, the required torque τ provided by the motor is desired. To use this haptic device, a physician inserts the needle with a maximum 2.5 mm/sec insertion speed and the linkages are light since they are made of plastic. Therefore, the quasi static assumption would be a reasonable assumption for a dynamic analysis. From the energy conservation law and assuming negligible friction loss in joints, one finds:

$$P_{in} = P_{out} \rightarrow \tau \times \dot{\beta} = F \times \dot{y} \rightarrow \tau = F \times \frac{\dot{y}}{\dot{\beta}} = F \frac{dy}{d\beta} \xrightarrow{\text{from (2)}}$$

$$\tau = F \frac{d}{2} \left(1 + \tan^2 \left(\frac{\beta}{2} \right) \right) = F \frac{d}{2} \left(1 + \left(\frac{y}{d} \right)^2 \right) \quad (5-4)$$

This indicates the required torque supplied by motor increases quadratically as y increases. We later use this equation for power analysis.

Link sizing and power analysis: Here, we have the following constraints:

- 1) $\dot{y} = \frac{d}{2} \dot{\beta} (1 + \tan^2(\frac{\beta}{2})) \geq 2.5 \text{ mm/sec}$ for all β ;
- 2) $F = \frac{\tau}{\frac{d}{2}(1+\tan^2(\frac{\beta}{2}))} = \frac{T \text{ (N.mm)} \times Gr}{\frac{d}{2}(1+\tan^2(\frac{\beta}{2}))} \geq 5N$
- 3) $-\pi/3 \leq \beta \leq \pi/3$;
- 4) $y_{max} = 70 \text{ mm}$;
- 5) $0 \leq \dot{\beta} \times Gr \leq 5.5 \text{ RPM}$;
- 6) $32 \text{ Nmm} \leq T \leq 50 \text{ Nmm}$.

The first constraint ensures that the master can generate a minimum speed of 2.5 mm/sec for the entire travel range so that needle insertion can be performed with maximum speed. Later, we put a constraint in the master-slave controller software so that master cannot move faster than slave. The second constraint makes certain that the master can develop enough force to match the physician's hand. This is similar to the force capability of slave robot. The third constraint is

considered to have a quasi-linear relationship between the motor shaft rotation, β and stylet displacement, y [27]. Figure 5.8 shows the relationship between β and y .

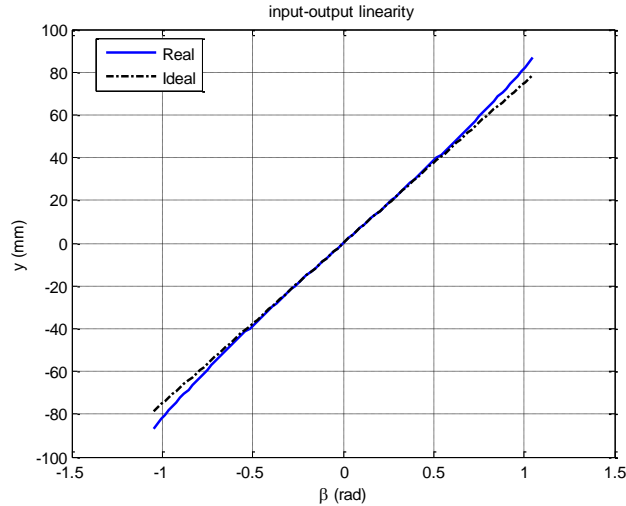


Figure 5.8: The input-output relationship remains satisfactorily linear if β is bounded to $[-\pi/3, \pi/3]$ ($d = 150$ mm).

For $\beta \in [-\frac{\pi}{3}, \frac{\pi}{3}]$, the relationship is fairly linear. We divide the 140 mm travel range symmetrically (± 70 mm) around the origin in order to maximize this linearity (Figure 5.8). The last two constraints show the motor speed and torque capability. T is motor output torque and Gr is the gear ratio between the motor shaft and joint B. If $d = 147$ mm and $Gr = 15$, the abovementioned requirements are met. Using equation (5-3) and $d = 147$ mm, the following dimensions for other links are found: $l_2 = 50$ mm, $l_1 = 140$ mm, and $l_3 = 70$ mm. The target gear ratio, $Gr = 15$, was realized using aluminum pulleys and timing belts (sdp/si.com). The timing belt has high efficiency for such a large speed reduction with minimal backlash. Figure 5.9 shows the inside view of the master robot.

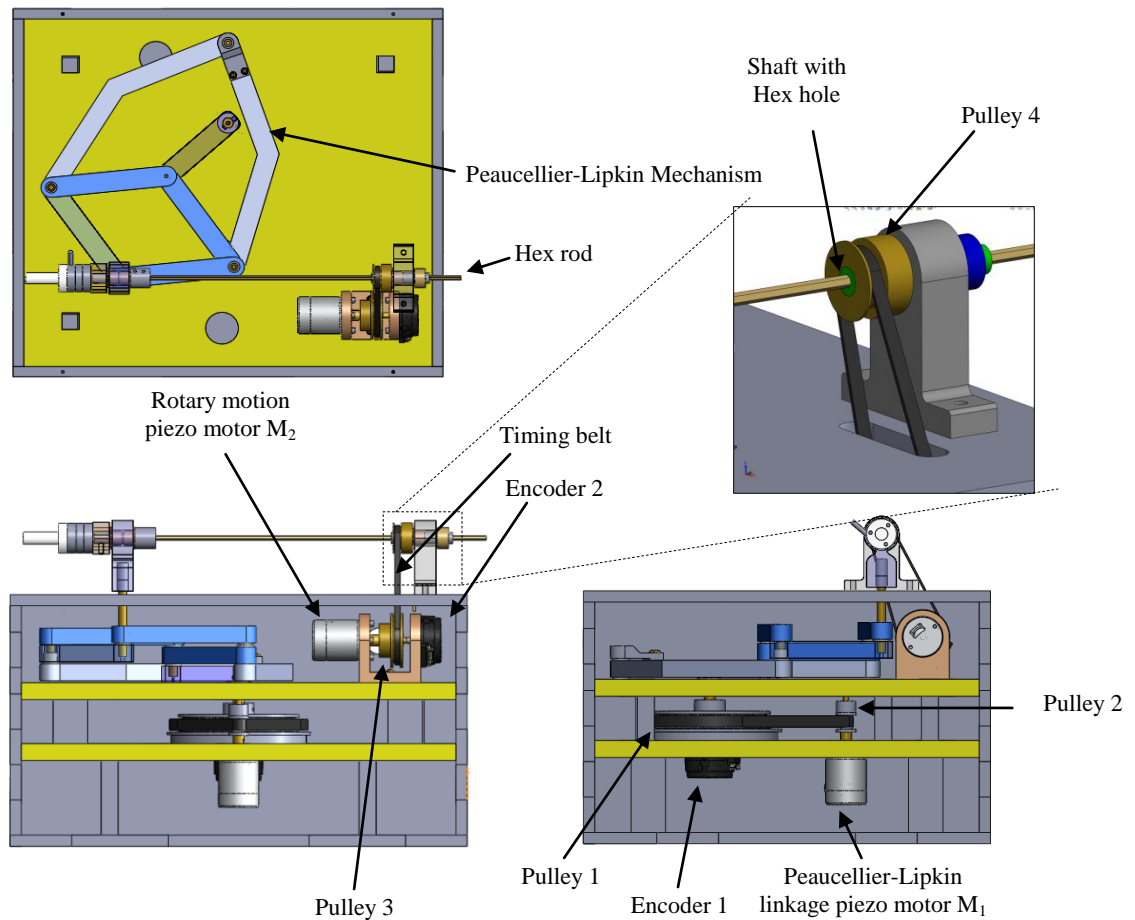


Figure 5.9: Top, front and side views of the master robot. The front and side views show the internal parts.

5.4.2 Rotary stage

Motor M_2 and its encoder are designed to be fixed to the base. The bar mimicking needle is selected to be hexagonal (made of brass) and passes through a small shaft with a hexagonal hole in the center. The shaft is press-fit at the center of pulley 4 (Figure 5.9). The shaft (made of brass with a wire EDM) allows needle to translate but constraints it from rotation. Pulley 4 is connected to pulley 3 which is concentric to the motor M_2 via a timing belt. As a result, the rotation of the stylus (the hexagonal bar) is transmitted to the rotary motor which is fixed to the base. In this

way, the motor and encoder of the rotary stage remain stationary in order to minimize the inertia of the moving parts. The gear ratio between these two pulleys is 1:2 (the larger pulley is attached to the motor), similar to the slave.

The box, linkages, and motor supports are made from cast acrylic sheet (mcmaster.com). All other parts are made from non-ferromagnetic metals (brass and aluminum) and plastic. Plastic and brass bearings were used for all rotary joints in order to minimize friction.

5.5 Controller

5.5.1 Controller hardware

Figure 5.10 shows the controller hardware and inside components. The controller hardware consists of four PDA 3.1 piezo motor drivers (PDA 3.1, PiezoMotor, Upsala, Sweden), a 4-axis DMC-2143 Ethernet motion controller (Galil Motion Control, Rocklin, CA, USA) which is the brain of the controller, a media converter (B&B Electronics Mfg. Co., Ottawa, IL, USA), and a 5 A 12 to 24 DC-DC converter (Linear power Inc., Pearl, MS, USA). All of these parts are placed inside an aluminum enclosure to minimize EMI. Ventilation is considered on top of the case. The encoders and motors are easily plugged using 9-pin connectors making the system installation quick and easy (Figure 5.10a). Also, the power and optical cable are plugged into the box. The motion controller communicates with the laptop in the control room through the optical cable. On computer B in Figure 5.1, GalilTools is used to command the controller. A 24 V DC power supply is used to run the controller, drivers, and media converter. Since the drivers work with a different voltage (12V) from Galil controller and media converter (24V), a DC-DC convertor is used.

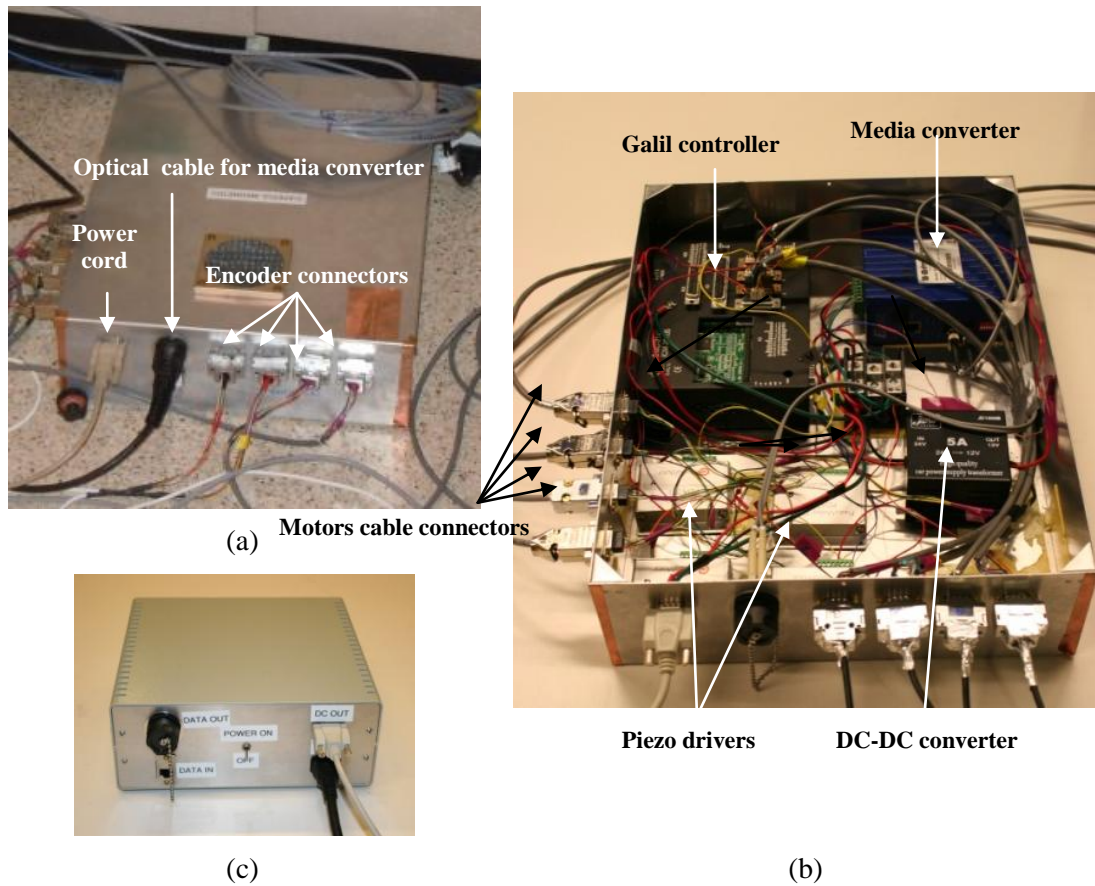


Figure 5.10: (a) Master-slave controller box outside view, (b) different components, and (c) Power supply box. Similar media converter is placed in power box.

Figure 5.10c shows the power supply box. It consists of a 24V power supply and a media converter. Media converter of power supply box gets the command from computer B through Ethernet cable and converts it to optical data. The optical data are transmitted through the optic cable to MRI room. At media converter inside the controller box, the optic data are converted back to electrical data and go to controller through an Ethernet cable. The opposite of this process is performed when Galil controller sends data to the computer B.

5.5.2 Controller architecture

The controller aims to maintain position tracking between the master and the slave robots. Since translation and rotation motions are independent, two separate controllers were considered, one for translation and another for rotation. One big challenge during controller design was the fact that master and slave robots are non-backdrivable as a result of the inherent friction of piezo motors. While it is an advantage for the slave (self-brake in case of power failure), it is the main drawback for the master since it is not possible to initiate the movement. In order to solve this problem, we developed an MRI-compatible force/torque sensor [43] and installed it on the master side as depicted in Figure 5.6. When the operator applies force or torque to the stylus, the stylus translates/rotates with a speed proportional to the amount of torque/force applied by the physician's hand. In fact, the controller and physician share the control of the master robot (referred to as cooperative control [44]). Figure 5.11 shows this concept. Force F_h (or τ_h) is multiplied to a constant k_f (k_τ). The output is the desired velocity (angular velocity). A PID controller ensures that the angular velocity of the master translational motor (rotational motor) will track this desired velocity. Now that the master's movement is initiated, another PID controller guarantees that the slave's position follows the master's position. Table 5.1 shows the controller gains and parameters. KD, KP, and KI are differential, proportional, and integral gains respectively. The gains were found by trial and error such that while the system remains stable at all time, the instantaneous error between the master and slave (i.e. $x_m - x_s$, $\theta_m - \theta_s$) is minimized both in free space motion and while inserting the needle into the phantom.

Table 5.1: Controller parameters.

	KD	KP	KI	k_f (SI)	k_r (SI)
Master linear	100	277	12	4.1e-3	2e-3
Slave linear	277	800	4	-	-
Master rotary	256	584	0.5	-	-
Slave rotary	250	500	4	-	-

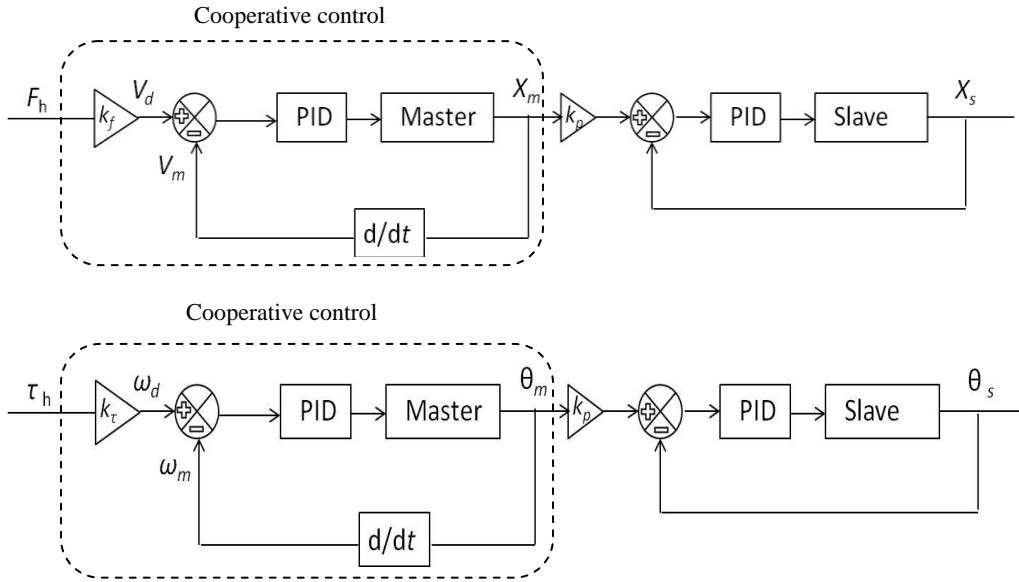


Figure 5.11: Controller architecture for master-slave system: cooperative control for the master and position tracking for slave. The top shows controller for needle translation and the bottom shows controller for needle rotation.

5.5.3 Controller software

The controller code was written in G-language (a language similar to Assembly developed by the Galil Co. for their controllers) and was compiled on the Galil controller using GalilTools, which is the software for Galil motion controllers. The input signals to the motion controller are F_h , τ_h , as well as position information coming from encoders, i.e. x_m , x_s , θ_m and θ_s . The encoders are directly connected to the controller while the force and torque information is received from the

MATLAB code running on computer B in control room. G-codes can be accessed within MATLAB using command *g.command* (.) making communication between the GalilTools and MATLAB possible [45]. This communication is bilateral, i.e. a MATLAB code sends force and torque to the controller and controller sends the position information of the robots to a GUI which is written in MATLAB.

5.6 MRI-Compatible force sensor

An MRI-compatible sensor which is capable of measuring axial force and torque is required on the master side in order to address the non-backdrivability of the master robot using the cooperative control as explained before. Since an MRI-compatible force sensor is not available commercially, such a sensor was developed using a Fiber Bragg Grating as strain sensors [43]. Figure 5.12 shows the 2-DOF force sensor prototype. Four FBGs are used to measure the axial force and torque.

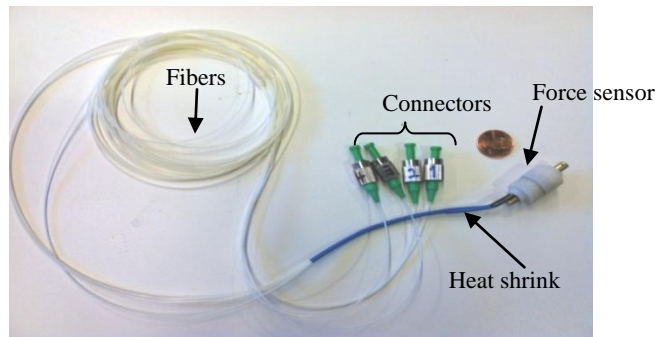


Figure 5.12: MRI-compatible force sensor prototype [43].

A Fiber Bragg grating (FBG) is a type of distributed Bragg reflector constructed in a short segment of an optical fiber (2 mm in our sensor) that reflects specific wavelengths of light and transmits the rest. This is attained by creating a periodic variation in the refractive index of the

fiber core. If the segment where the FBG is attached experiences normal strain due to force or change in temperature, the wavelength of the reflected light shifts proportionally. Optical fibers with 2 mm long FBGs, wavelength 1545nm, were purchased off the shelf from Technica SA (Beijing, China). A FBG interrogator is a device that generates light and measures the wavelength shift of the reflection. In this study, we used a 4 channel Micron Optics sm130 (Atlanta, GA, USA), with sampling rate of 2 KHz. The spectrum ranges from 1525 nm to 1565 nm. Each channel handles one fiber.

In order to use the sensor, we passed the fibers through the patch panel and plugged them into the FBG interrogator which is placed in the control room. Since the sensor is made of non-magnetic material (phosphor-bronze, and plastic for casing) and it only uses light, it is MRI-compatible by nature. The FBG interrogator sends the wavelength shifts with some other information to the computer B via an Ethernet port in real-time. In the MATLAB code, the wavelength shifts are extracted from the raw data and calibration coefficients (found after calibration procedure) are applied thus determining the axial force and torque. The axial force and torque measurements are then sent to the Galil controller in MRI room.

The force sensor can measure forces in the range ± 20 N and torques in the range of ± 200 Nmm with 0.1 N and 1 Nmm resolution, respectively. The sensor is compact ($\varnothing = 15$ mm, Height = 20mm). The sensor accounts for environment temperature changes.

5.7 Experiments and results

5.7.1 MRI-compatibility

MRI-compatibility can be defined as follows: 1) the device does not develop a risk to patient and clinicians' safety. This can either be a flying object due to the magnetic force or RF heating caused by metal parts. 2) The image quality deterioration as a result of putting the system in the

MRI room is insignificant. 3) The device can properly function inside the MRI room while the scanner is operating. In the following, MRI-compatibility from these perspectives is evaluated.

MRI safety: In this study, the master and the slave robots were made from nonmagnetic materials with minimal metal parts to avoid eddy current and therefore, RF heating. The controller components were placed into an aluminum enclosure and the controller box was placed next to the patch panel. The only object that touches the patient is the needle, meaning the risk of RF heating is minimized. During the MR imaging, no temperature change was observed by touching the needle.

Image quality: Ferromagnetic materials (even tiny set-screws) were eliminated in order to minimize EMI. The use of other metals was minimized to avoid eddy currents that results in RF heating and EMI. Cables of the piezo motors and encoders that have the most significant contribution to EMI were properly shielded and grounded. In our observation, the last few centimeters of unshielded cable (s) can knock out the entire signal (SNR dropped to only 4% in our first experiment). We realized that the encoder cables introduce significantly larger noise than motor cables. Since the encoders in this study are differential, we used shielded twisted-pair cables (US Digital, part No. CA-MIC6-SH-NC) in order to minimize this noise to the maximum extent possible. During the experiment, we observed that the encoders of the slave drop SNR up to 35% resulted from the interference of the MRI magnetic field with the unshielded encoder's PCB circuit. We fixed this issue by wrapping the encoder enclosures (black objects in Figure 5.3) using aluminum foil. The controller components were placed into an aluminum cage, and the box was placed next to the patch panel. Also, we used motors and drivers that were reported to be MRI-compatible with small SNR loss (< 9% [40]). The encoders were selected to be optical to minimize EMI.

With these considerations, we conducted an SNR test using a 3T GE Discovery MR750 (General Electric Healthcare, Waukesha, WI, USA). A cylindrical MRI phantom ($\varnothing = 110 \text{ mm} \times 230 \text{ mm}$) was placed in the isocenter and the robot placed so that the base robot front is 2 cm from the cylinder (similar to the relative position of the robot and patient). A round flex coil similar to those often used in prostate imaging was used. The phantom was imaged using three standard prostate imaging protocols:

- 1) T1 FGE: T1 weighted fast field gradient echo for diagnostic imaging;
- 2) T2 FSE: T2 weighted fast spin echo for diagnostic imaging;
- 3) TFE (FSPGR): “real-time” turbo field gradient echo.

Imaging parameters are provided in Table 5.2.

Table 5.2: Imaging parameters used for SNR tests.

Protocol	Thickness	FOV	#Slices	TE	TR	Flip Angle	NEX	Bandwidth
T1 FGE	3 mm	240 mm	10	2.2 ms	225 ms	75 deg	1	977 Hz/pixel
T2 FSE	3 mm	240 mm	10	88 ms	3000 ms	90 deg	1	244 Hz/pixel
FSPGR	3 mm	240 mm	10	4.2 ms	26 ms	70 deg	1	244 Hz/pixel

The following imaging series were taken: 1) phantom only (baseline); 2) System in (i.e. the master next to the scanner, the 6-DOF robot inside the bore, and controller inside the room next to the patch panel), but power off; 3) The power was turned on, but the cables of the motors and encoders remained unplugged; 4) The cables of the master robot we plugged only (2 for motors and 2 for encoders); 5) The cables of the slave robot we plugged only; 6) All cables were plugged; 7) The master and slave moved at the same time (teleoperation was enabled). Figure 5.13 shows the results.

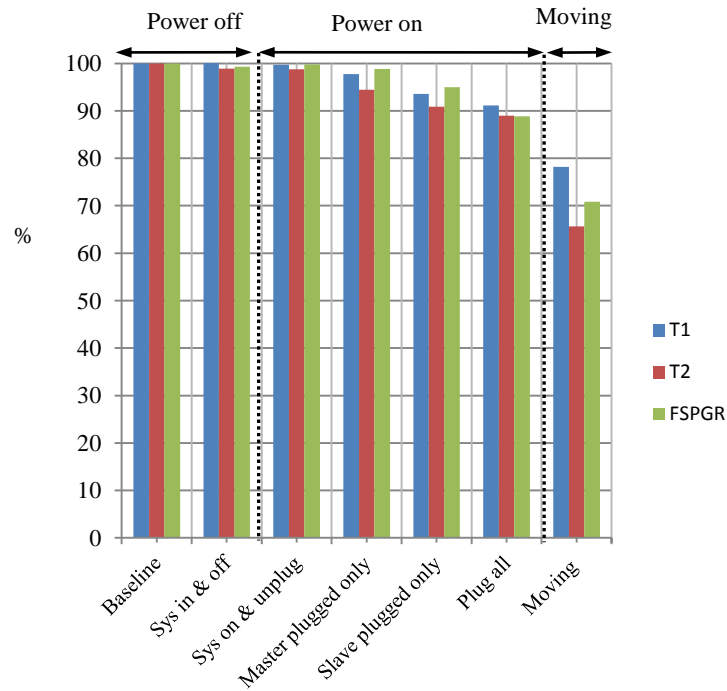


Figure 5.13: SNR results.

From Figure 5.13, the following observations can be made: 1) the system does not contribute any significant noise before moving (less than 10% SNR loss). 2) The SNR loss when the robots are moving is almost 30 percent. However, if we visually compare different imaging sequences for baseline with the system moving as shown in Figure 5.14, they are not very different. Since teleoperated needle steering is performed with a human operator, we think this SNR loss is quite acceptable.

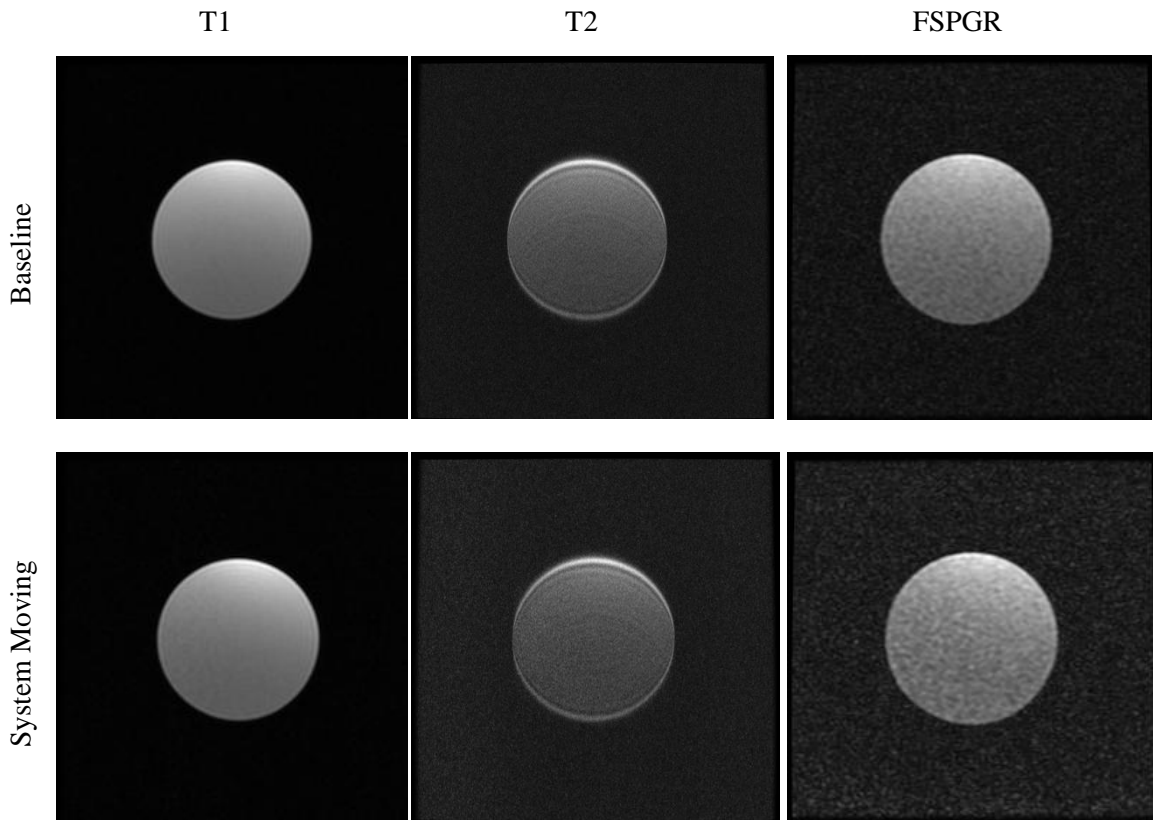


Figure 5.14: Visual comparison of different imaging sequences for the baseline with the system moving; the difference is insignificant.

5.7.2 System functionality

The functionality of the teleoperated needle steering system in MRI room was evaluated while the scanner is running. The 6-DOF robot was placed inside the bore, the master was placed next to the scanner and the system was powered on. The purpose of the following experiments is to demonstrate that the functionality of the system i.e. position tracking is not affected while MRI is running. Two experiments were conducted:

Free space motion: The purpose of this experiment is to evaluate the stability of the system as well as position tracking when the needle is moving outside tissue, and whether there is any delay for the slave in following the master. During this experiment, MRI was running at all time. Figure 5.15a and Figure 5.15b show the result.

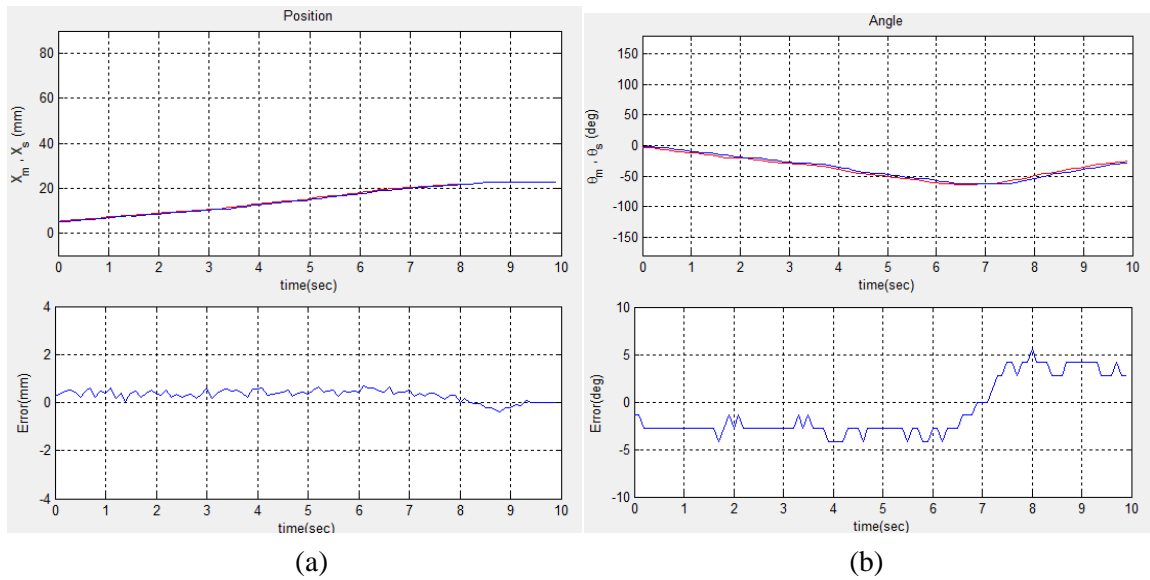
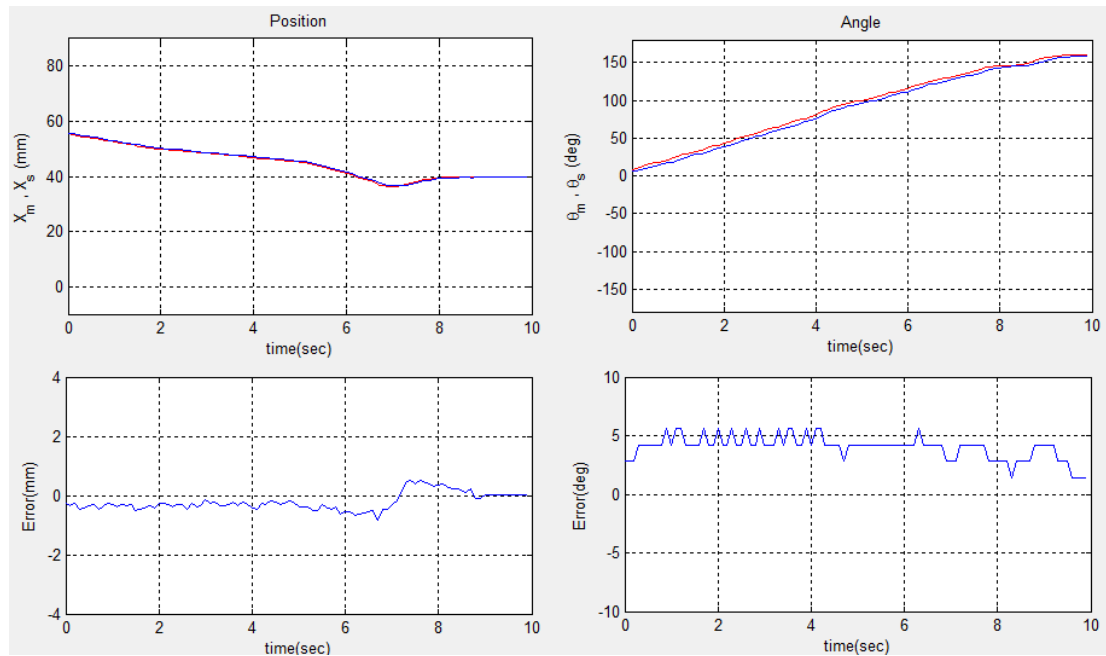


Figure 5.15: Position tracking when needle is moving in free space: (a) linear motion and (b) rotary motion. MRI was running during the experiment.

Needle insertion into prostate phantom: The purpose of this experiment is to evaluate the tracking accuracy when the needle is inserted into the tissue. Figure 5.16a and Figure 5.16b show the result.



(a)

(b)

Figure 5.16: Position tracking when the needle is inserted into the phantom: (a) Translational motion, and (b) rotary motion. The steady state error is approaching zero in both cases.

From Figure 5.15 and Figure 5.16, it can be observed that the slave robot can track the master robot with accuracy better than 0.5 mm in translation and 5 degrees in rotation during needle steering. The steady state error however was zero. These results demonstrated that MRI has no negative impact on the functionality of the system.

5.7.3 Feasibility of teleoperated needle steering in phantom trial on bench-top setup

In the previous section, we proved that the slave can follow the master with sufficient accuracy. Theoretically, needle insertion and rotation plus real-time image feedback enables physician to do bevel-tip needle steering. However, a more realistic experiment is sought to demonstrate the feasibility of needle steering using the proposed master-slave system and its capability in error

compensation. Figure 5.17 shows the experimental setup. This setup is almost the same as what was shown for the real experiment in MRI room (Figure 5.1) with the difference of having video feedback of the semi transparent soft plastic phantom instead of the real-time MRI image. It is assumed that the base robot has already oriented the needle toward the target (the accuracy of the base robot in needle orientation was reported previously in [17]). A semi transparent phantom was made using tissue mimicking soft plastic materials with the ratio of 5 to 1 (softener to hardener). The phantom box was created using a laser cutter ($70 \times 70 \times 20$ mm- dimensionally, this is different from the phantom used in the next section). On each two opposing faces of the box, 5 holes were made with the laser cutter with 0.1 mm accuracy. Each hole on one side was therefore precisely aligned with another hole on the opposite side.

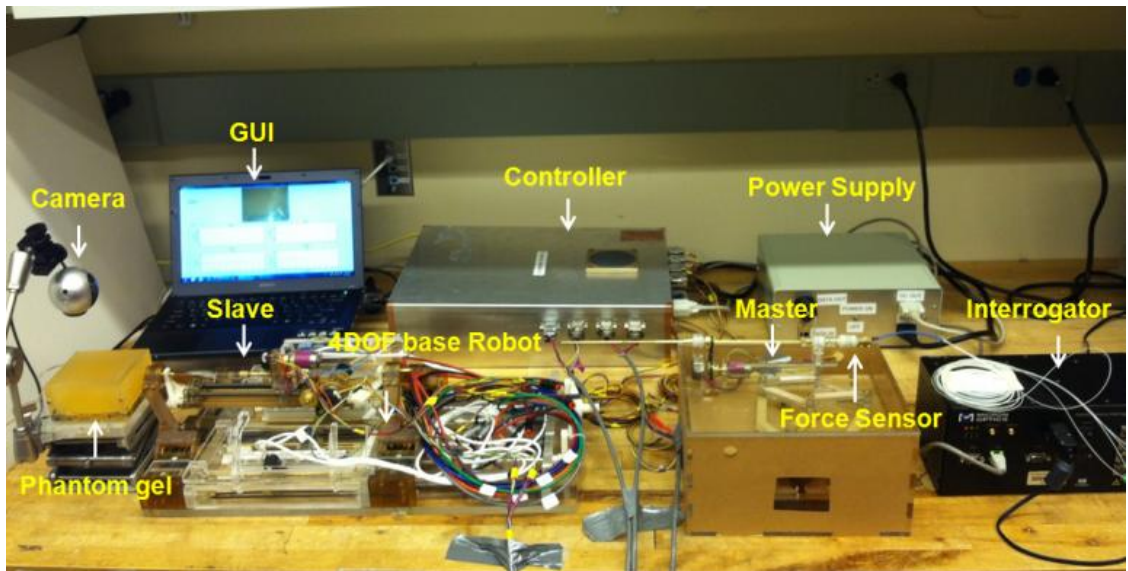


Figure 5.17. Bench-top phantom experiment to evaluate effectiveness of bevel-tip needle steering in error compensation.

The experiment was performed as follows using two users: for each target (5 targets in total), once the user inserted the needle without any steering until reaching the opposite wall of the

phantom and once with steering. Steering means to insert the needle almost half-way through, rotate the bevel-tip 20G needle for 180 degrees and then, continue the insertion until reaching the opposite side of the phantom. Figure 5.18 compares the errors. Since the needle leaves a path inside the phantom after the first insertion, user 2 used another 5 holes which were made on the other two opposing faces of the phantom.

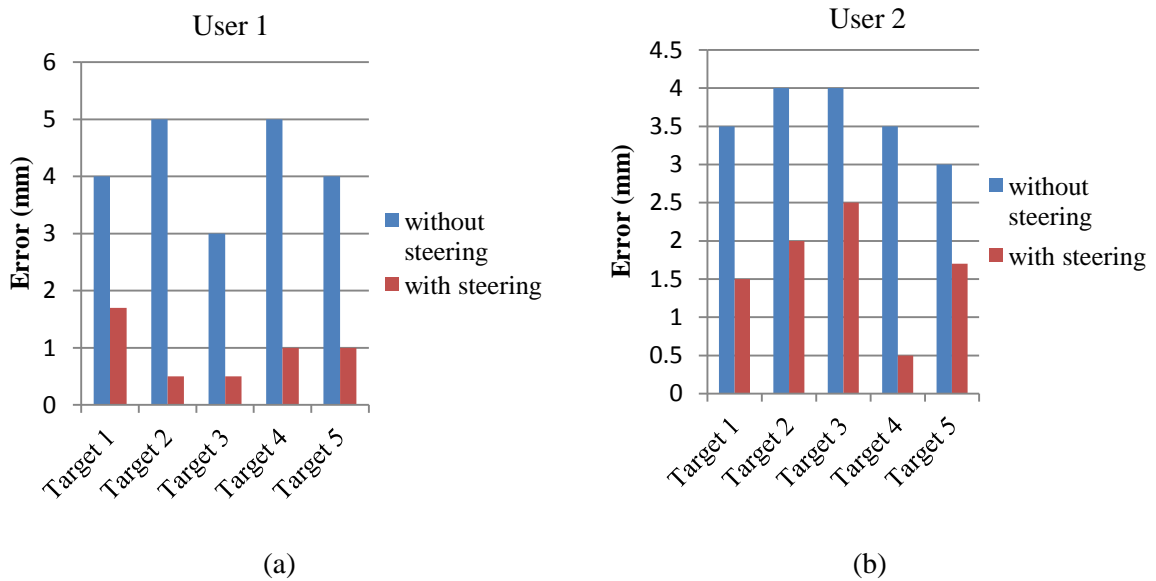


Figure 5.18. The effectiveness of a simple steering method: the blue bars show the errors without steering and the red bars show the errors with steering. Steering means the needle was stopped half-way through, rotated 180 deg, and the insertion was continued until reaching the opposite side of the phantom. The average error was reduced from 4.2 mm to 0.9 mm for User 1 and from 3.6 mm to 1.6 mm for User 2.

The results show that the error has significantly reduced as the result of this simple steering technique. Although the error numbers may not be quite representative of the human tissue, the relative reduction in error may still hold in the human tissue.

5.7.4 Feasibility of teleoperated needle steering under real-time MRI guidance

The feasibility of teleoperated needle steering under real-time MRI guidance was studied in a phantom experiment. FSPGR imaging with 2 slices per second was utilized for real-time visual feedback. Figure 5.19 shows the experimental setup. The system components used in this experiment are similar to what given in Figure 5.1. It was assumed that the base robot has already oriented the needle toward the target (the accuracy of the base robot in needle orientation was reported previously in [17], [38], and in Chapter 4). A semi-transparent phantom was made using tissue mimicking soft plastic materials (M-F Manufacturing, Inc., Ft. Worth, TX, USA). The phantom box was created using a laser cutter ($90 \times 90 \times 50$ mm). On the two opposing faces of the box, 8 holes were made with the laser cutter. Each hole on one side was therefore precisely aligned with another hole on the opposite side. The phantom is shown in Figure 5.20.

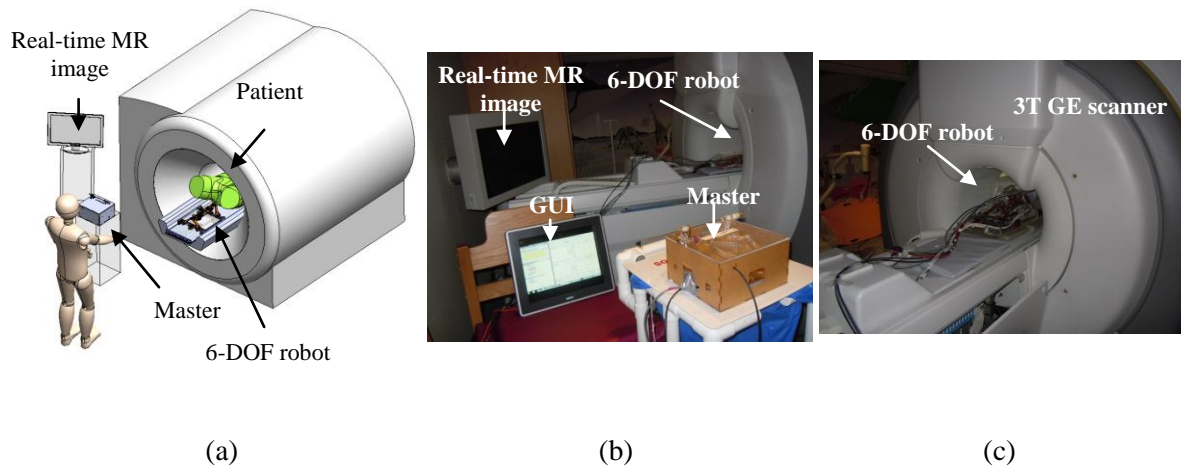


Figure 5.19: Experiment setup for teleoperated needle steering under MRI guidance: (a) physician steers needle remotely using the master robot under real-time MRI, (b) real experimental setup with phantom, one monitor for real-time MRI and one for GUI, and (c) 6-DOF robot is placed inside the bore.

The phantom was placed in front of the 6-DOF robot as shown in Figure 5.20. The needle was inserted partially into a hole before starting the experiment. Two visible markers (donut-shape) were placed concentric to those two holes made in the opposite walls of the phantom so that the

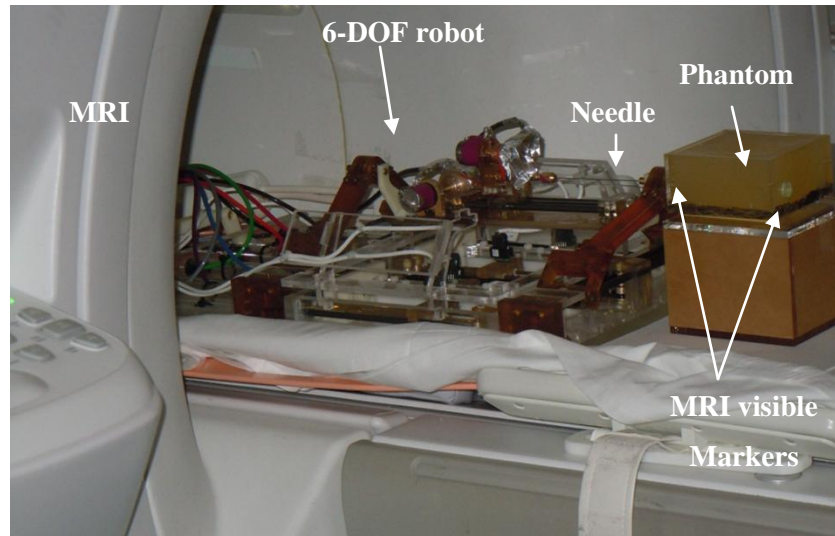


Figure 5.20: Phantom used in teleoperated needle steering experiment under MRI guidance.

entry point and the target are visible in the MR image. Therefore, the goal was to reach the other visible marker which was at 80 mm distance from the entry point. The operator held the master robot and inserted the needle under real-time MRI. Figure 5.21 shows the real-time MR image in which needle-tip artifact is visible as the needle was gradually inserted. The imaging plane was set so that it can capture the needle shaft and the visible markers (in a sagittal plane). The visible markers are missing in the image probably because they were expired. Only, the artifact of the needle tip is seen which was still adequate to continue this feasibility study. Since the artifact is a few millimeter thick, it cannot precisely represent the needle tip location (to solve this issue, see Chapter 6). Nevertheless, it was quite straightforward to follow the needle-tip in real-time MR image. When the needle reached almost half-way through, the operator rotated the needle 180

degrees and continued insertion. The needle was retracted after reaching the opposite wall of the phantom. Although this experiment was primitive, it proves that teleoperated needle steering under real-time MRI guidance with the proposed system and methodology is feasible. Figure 5.21 shows the needle tip at 4 intervals through insertion. At time step (c), the operator rotated the needle 180 degrees.

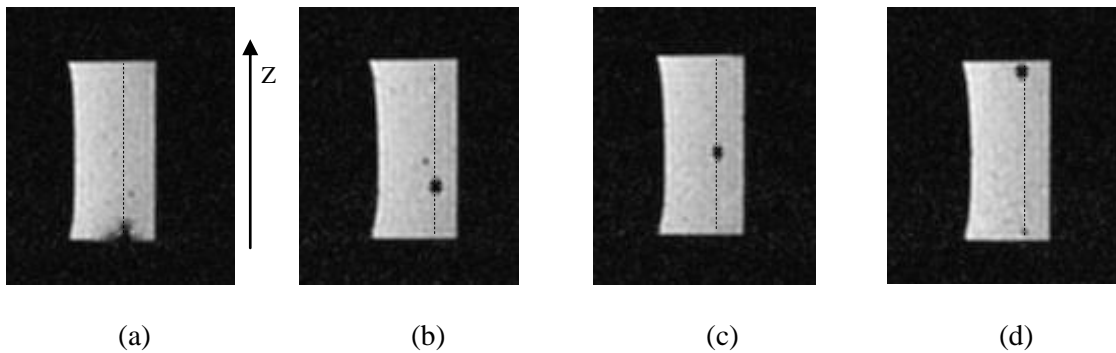


Figure 5.21: Real-time MR image of the needle during insertion: needle is gradually inserted toward the other side of the phantom. The dark spot is the needle tip artifact. The needle tip artifact is depicted in 4 intervals during needle insertion. At time step (c), the operator rotates the needle 180 degree to steer the needle tip toward the opposite direction. The phantom is shown in sagittal plane.

5.8 Conclusions and future work

In order to have continuous human supervision in the loop and to decrease the number of patient removals from the scanner, this study presented a master-slave approach for robot-assisted MRI-guided prostate needle placement. Teleoperated needle steering under real-time MRI guidance was proposed and enabled in order to compensate for errors introduced during needle insertion. For this purpose, a 2-DOF MRI-compatible needle steering module was developed and integrated with a 4-DOF transperineal robot, yielding a fully actuated 6-DOF robotic platform for prostate needle placement. A novel MRI-compatible 2-DOF haptic device was also developed to enable

teleoperated needle steering while the physician is standing inside the MRI room. A 2-DOF force sensor was developed to address the inherent friction of the piezo motors using a cooperative control architecture. Controller hardware and software were developed to perform this task with high sampling rate and no noticeable delay. MRI-compatibility results showed small SNR degradation of the system. Experiments in the MRI room proved that the system functionality is not affected by MRI. Also, the feasibility of teleoperated needle steering under real-time MRI was demonstrated in a phantom.

In this study, a static phantom was used with small target motion due to tissue deflection. In order to have a more realistic scenario, capability of needle steering should be experimented in a more realistic phantom such as one reported in [47], or ideally, in canine.

Since the surgical needle leaves a large artifact on real-time MR image, it is hard to track needle tip and therefore, compensate for the error. In addition, real-time MRI imaging involves some latency (typically, 500 msec). An alternative approach with higher accuracy and bandwidth in capturing the 3D shape of the needle is to track the needle using a Fiber Bragg Grating sensor. In chapter 6, this technology is developed.

Also, it is desired to replicate a similar force sensor and place it behind the needle on the slave side so that bilateral teleoperation with haptic feedback can be achieved during needle steering. However, this will introduce a new challenge: the 0.5 sec latency of the MR imaging may impact the system stability and transparency. This means more sophisticated controller architecture is necessary to make the system stable even in the presence of this time delay in visual feedback. This is not an issue and is addressable. However, the transparency of the system will be somewhat compromised because the operator is updated about the force at the slave side every 0.5 sec. This limitation cannot be addressed unless real-time MR imaging is offered. Currently,

real-time MR imaging with up to 33 msec latency has been achieved in research scanners. Therefore, this issue could be resolved in future [48].

This system will be modified for patient trials in near future after reconsidering sterilization and safety issues.

References

- [1] R. Siegel, D. Naishadham and A. Jemal, "Cancer statistics, 2012," *CA: A Cancer Journal for Clinicians*, 2012.
- [2] C. Tempany, S. Straus, N. Hata and S. Haker, "MR - guided prostate interventions," *Journal of Magnetic Resonance Imaging*, vol. 27, pp. 356-367, 2008.
- [3] B. H. Han, K. Wallner, G. Merrick, W. Butler, S. Sutlief and J. Sylvester, "Prostate brachytherapy seed identification on post-implant TRUS images," *Med. Phys.*, vol. 30, pp. 898, 2003.
- [4] A. Krieger. "Advances in magnetic resonance image guided robotic intervention". *Ph.D. dissertation, Dept. Mech. Eng., Johns Hopkins Univ.*, Baltimore, MD, 2008.
- [5] J. F. Schenck, F. A. Jolesz, P. B. Roemer, H. E. Cline, W. E. Lorensen, R. Kikinis, S. G. Silverman, C. J. Hardy, W. D. Barber, and E. T. Laskaris, "Superconducting open configuration MR imaging system for image-guided therapy," *Radiology*, vol. 195, pp. 805–814, 1995.

- [6] A. V. D'amico, C. Tempany, R. Cormack, N. Hata, M. Jinzaki, K. Tuncali, M. Weinstein and J. Richie, "Transperineal magnetic resonance image guided prostate biopsy," *J. Urol.*, vol. 164, pp. 385-387, 2000.
- [7] K. Chinzei, N. Hata, F. Jolesz and R. Kikinis, "Surgical assist robot for the active navigation in the intraoperative MRI: Hardware design issues," in *Intelligent Robots and Systems, 2000.(IROS 2000). Proceedings. 2000 IEEE/RSJ International Conference on*, 2000, pp. 727-732.
- [8] K. J. Macura and D. Stoianovici, "Advancements in Magnetic Resonance-Guided Robotic Interventions in the Prostate," *Topics in Magnetic Resonance Imaging: TMRI*, vol. 19, pp. 297, 2008.
- [9] R. Kokes, K. Lister, R. Gullapalli, B. Zhang, A. MacMillan, H. Richard and J. P. Desai, "Towards a teleoperated needle driver robot with haptic feedback for RFA of breast tumors under continuous MRI," *Med. Image Anal.*, vol. 13, pp. 445-455, 2009.
- [10] B. Yang, U. X. Tan, A. B. McMillan, R. Gullapalli and J. P. Desai, "Design and control of a 1-DOF MRI-compatible pneumatically actuated robot with long transmission lines," *Mechatronics, IEEE/ASME Transactions on*, vol. 16, pp. 1040-1048, 2011.
- [11] U. X. Tan, B. Yang, R. Gullapalli and J. P. Desai, "Triaxial MRI-compatible fiber-optic force sensor," *Robotics, IEEE Transactions on*, vol. 27, pp. 65-74, 2011.
- [12] H. Elhawary, Z. Tse, M. Rea, A. Zivanovic, B. Davies, C. Besant, N. de Souza, D. McRobbie, I. Young and M. Lamperth, "Robotic system for transrectal biopsy of the

- prostate: Real-time guidance under MRI," *Engineering in Medicine and Biology Magazine, IEEE*, vol. 29, pp. 78-86, 2010.
- [13] Z. Tse, H. Elhawary, M. Rea, I. Young, B. Davis and M. Lamperth, "A haptic unit designed for magnetic-resonance-guided biopsy," *Proc. Inst. Mech. Eng. Part H J. Eng. Med.*, vol. 223, pp. 159-172, 2009.
- [14] H. Su, W. Shang, G. A. Cole, K. Harrington and G. S. Fischer, "Haptic system design for MRI-guided needle based prostate brachytherapy," in *Haptics Symposium, 2010 IEEE*, 2010, pp. 483-488
- [15] R. Seifabadi, S. E. Song, A. Krieger, N. B. Cho, J. Tokuda, G. Fichtinger and I. Iordachita, "Robotic system for MRI-guided prostate biopsy: feasibility of teleoperated needle insertion and ex vivo phantom study," *International Journal of Computer Assisted Radiology and Surgery*, vol. 7, pp. 181-190, 2012.
- [16] O. Piccin, L. Barbé, B. Bayle, M. De Mathelin and A. Gangi, "A force feedback teleoperated needle insertion device for percutaneous procedures," *The International Journal of Robotics Research*, vol. 28, pp. 1154-1168, 2009.
- [17] R. Seifabadi, N. B. J. Cho, S. E. Song, J. Tokuda, N. Hata, C. M. Tempany, G. Fichtinger and I. Iordachita, "Accuracy study of a robotic system for MRI - guided prostate needle placement," *The International Journal of Medical Robotics and Computer Assisted Surgery*, 2012.

- [18] P. Blumenfeld, N. Hata, S. DiMaio, K. Zou, S. Haker, G. Fichtinger and C. Tempany, "Transperineal prostate biopsy under magnetic resonance image guidance: a needle placement accuracy study," *Journal of Magnetic Resonance Imaging*, vol. 26, pp. 688-694, 2007.
- [19] V. Lagerburg, M. A. Moerland, J. J. Lagendijk and J. J. Battermann, "Measurement of prostate rotation during insertion of needles for brachytherapy," *Radiotherapy and Oncology*, vol. 77, pp. 318-323, 2005.
- [20] N. Abolhassani, R. Patel and M. Moallem, "Needle insertion into soft tissue: A survey," *Med. Eng. Phys.*, vol. 29, pp. 413-431, 2007.
- [21] C. Simone and A. M. Okamura, "Modeling of needle insertion forces for robot-assisted percutaneous therapy," in *Robotics and Automation, 2002. Proceedings. ICRA'02. IEEE International Conference on*, 2002, pp. 2085-2091.
- [22] S. P. DiMaio and S. Salcudean, "Needle steering and motion planning in soft tissues," *Biomedical Engineering, IEEE Transactions on*, vol. 52, pp. 965-974, 2005.
- [23] R. Alterovitz, K. Goldberg, J. Pouliot, R. Taschereau and I. C. Hsu, "Needle insertion and radioactive seed implantation in human tissues: Simulation and sensitivity analysis," in *Robotics and Automation, 2003. Proceedings. ICRA'03. IEEE International Conference on*, 2003, pp. 1793-1799.
- [24] H. Kataoka, T. Washio, M. Audette and K. Mizuhara, "A model for relations between needle deflection, force, and thickness on needle penetration," in *Medical Image Computing and Computer-Assisted Intervention—MICCAI 2001*, pp. 966-974.

- [25] V. Lagerburg, M. A. Moerland, M. van Vulpen and J. J. W. Lagendijk, "A new robotic needle insertion method to minimize attendant prostate motion," *Radiotherapy and Oncology*, vol. 80, pp. 73-77, 2006.
- [26] V. Lagerburg, M. Moerland, M. Konings, R. Van de Vosse, J. Lagendijk and J. Battermann, "Development of a tapping device: a new needle insertion method for prostate brachytherapy," *Phys. Med. Biol.*, vol. 51, pp. 891, 2006.
- [27] A. Patriciu, D. Petrisor, M. Muntener, D. Mazilu, M. Schär and D. Stoianovici, "Automatic brachytherapy seed placement under MRI guidance," *Biomedical Engineering, IEEE Transactions on*, vol. 54, pp. 1499, 2007.
- [28] S. Badaan, D. Petrisor, C. Kim, P. Mozer, D. Mazilu, L. Gruionu, A. Patriciu, K. Cleary and D. Stoianovici, "Does needle rotation improve lesion targeting?" *The International Journal of Medical Robotics and Computer Assisted Surgery*, vol. 7, pp. 138-147, 2011.
- [29] S. DiMaio and S. Salcudean, "Needle steering and model-based trajectory planning," *Medical Image Computing and Computer-Assisted Intervention-MICCAI 2003*, pp. 33-40, 2003.
- [30] P. E. Dupont, J. Lock, B. Itkowitz and E. Butler, "Design and control of concentric-tube robots," *Robotics, IEEE Transactions on*, vol. 26, pp. 209-225, 2010.
- [31] D. C. Rucker, B. A. Jones and R. J. Webster, "A geometrically exact model for externally loaded concentric-tube continuum robots," *Robotics, IEEE Transactions on*, vol. 26, pp. 769-780, 2010.

- [32] H. Su, D. C. Cardona, W. Shang, A. Camilo, G. A. Cole, D. C. Rucker, R. Webster and G. S. Fischer, "A MRI-guided concentric tube continuum robot with piezoelectric actuation: A feasibility study," in *Robotics and Automation (ICRA), 2012 IEEE International Conference on*, 2012, pp. 1939-1945.
- [33] Walsh, "Image-guided robots for dot-matrix ablation," *PhD dissertation*, Dept. Mech. Eng., *Massachusetts Institute of technology (MIT)*, Chapter 5, 2010.
- [34] R. J. Webster III, J. S. Kim, N. J. Cowan, G. S. Chirikjian and A. M. Okamura, "Nonholonomic modeling of needle steering," *The International Journal of Robotics Research*, vol. 25, pp. 509-525, 2006.
- [35] G. S. Fischer, I. Iordachita, C. Csoma, J. Tokuda, S. P. DiMaio, C. M. Tempny, N. Hata and G. Fichtinger, "MRI-compatible pneumatic robot for transperineal prostate needle placement," *Mechatronics, IEEE/ASME Transactions on*, vol. 13, pp. 295-305, 2008
- [36] S. E. Song, N. B. Cho, G. Fischer, N. Hata, C. Tempny, G. Fichtinger and I. Iordachita, "Development of a pneumatic robot for MRI-guided transperineal prostate biopsy and brachytherapy: New approaches," in *Robotics and Automation (ICRA), 2010 IEEE International Conference on*, 2010, pp. 2580-2585.
- [37] R. Seifabadi, I. Iordachita and G. Fichtinger, "Design of a teleoperated needle steering system for MRI-guided prostate interventions," in *Biomedical Robotics and Biomechatronics (BioRob), 2012 4th IEEE RAS & EMBS International Conference on*, 2012, pp. 793-798.

- [38] J. Tokuda, S.E. Song, G.S. Fischer, I. Iordachita, R. Seifabadi, N.B. Cho, K. Tuncali, G. Fichtinger, C.M. Tempany, and N. Hata, "Preclinical evaluation of an MRI-compatible pneumatic robot for angulated needle placement in transperineal prostate interventions," *International Journal Of Computer Assisted Radiology And Surgery (IJCARs)*, DOI: 10.1007/s11548-012-0750-1, 2012.
- [39] H. Elhawary, Z. Tse, M. Rea, A. Zivanovic, B. Davies, C. Besant, N. de Souza, D. McRobbie, I. Young and M. Lamperth, "Robotic system for transrectal biopsy of the prostate: Real-time guidance under MRI," *Engineering in Medicine and Biology Magazine, IEEE*, vol. 29, pp. 78-86, 2010.
- [40] G.S. Fischer, A. Krieger, I. Iordachita, C. Csoma, L.L. Whitcomb, and G. Fichtinger, "MRI-compatibility of robot actuation techniques—a comparative study," *International Conference on Medical Image Computing and Computer Assisted Interventions (MICCAI)*, vol. 5242, pp.509-517, 2008.
- [41] T. K. Podder, D.P. Clark, J. Sherman, E.M. Messing, D. Fuller, D.J. Rubens, J. Strang, R. Brasacchio, L. Liao, W. Ng, and Y. Yu "In vivo Motion and Force Measurement of Surgical Needle Intervention during Prostate Brachytherapy," *Journal of Medical Physics*, vol. 33(8), pp. 2915-2922, 2006.
- [42] L. Barbé, B. Bayle, O. Piccin, J. Gangloff, and M. de Mathelin. Design and evaluation of a linear haptic device. *Proceedings IEEE International Conference on Robotics and Automation (ICRA)*, Italy, pp. 485 – 490, 2007

- [43] R. Monfaredi, R. Seifabadi, G. Fichtinger, and I. Iordachita, "Design of a decoupled MRI-compatible force sensor for robot-assisted prostate interventions," *In SPIE Medical Imaging*, pp. 867118-867118, 2013.
- [44] R.H. Taylor, P. Jensen, L.L. Whitcomb, A. Barnes, R. Kumar, D. Stoianovici, P. Gupta, Z. Wang, E. de Juan, and L. Kavoussi, "Steady-hand robotic system for microsurgical augmentation," *The International Journal of Robotics Research*, 18(12), pp. 1201-1210. 1999.
- [45] Application Note #4424, Programming MATLAB ® with Galil controllers. www.galilmc.com/support/appnotes/software/note4424.pdf
- [46] NEMA Standards Publication MS 1-2008: Determination of Signal-to-Noise Ratio (SNR) in Diagnostic Magnetic Resonance Imaging. *National Electrical Manufacturers Association*, www.nema.org.
- [47] N. Hungr, M. Baumann, J. Long and J. Troccaz, "A 3-D Ultrasound Robotic Prostate Brachytherapy System With Prostate Motion Tracking," *Robotics, IEEE Transaction on*, 2012.
- [48] S. Zhang, M. Uecker, D. Voit, K. D. Merboldt, and J. Frahm "Technical notes Real-time cardiovascular magnetic resonance at high temporal resolution: radial FLASH with nonlinear inverse reconstruction," *Journal of Cardiovascular Magnetic Resonance*, Open access, pp. 12-39, 2010.

Chapter 6

Needle tracking with embedded Fiber Bragg Gratings

This study presents one of the enabling technologies for teleoperated bevel-tip needle steering under real-time MRI guidance, i.e. capability of tracking the needle with higher accuracy and bandwidth than real-time MRI. Three fibers, each with three Fiber Bragg Grating (FBG) sensors were embedded into a 0.6 mm inner stylet of a 20G MRI-compatible biopsy needle. The axial force caused by the bevel-tip was considered in the analysis using beam-column theory. Due to the varying insertion depth, the minimum number of sensors and their optimal locations in the fibers were determined so that the tip position error estimation remains below 0.5 mm for all clinical insertion depths. A practical and accurate calibration method for the apparatus was presented. The instrumented needle was fabricated to fit in the needle driver unit of an MRI-compatible needle steering robot. The tracking apparatus was calibrated, including compensation for temperature changes in tissue during insertion. Experimental results illustrated needle tip tracking error below 0.5 mm at different insertion depths. Real-time 3D shape of the needle was visualized in 3D Slicer yielding navigation of the needle in real-time.

6.1 Introduction

Previously, I proposed human-operated in-room, master-slave needle steering under real-time MRI guidance to reduce number of patient removals from the scanner while having continuous human supervision in the loop (Figure 6.1) [1]. The purpose of bevel-tip needle steering is to compensate for the error occurring during needle insertion including prostate motion [2] and needle deflection [3]. To enable teleoperated bevel-tip needle steering under continuous MRI guidance, different technologies have to be developed including MRI-compatible haptic devices

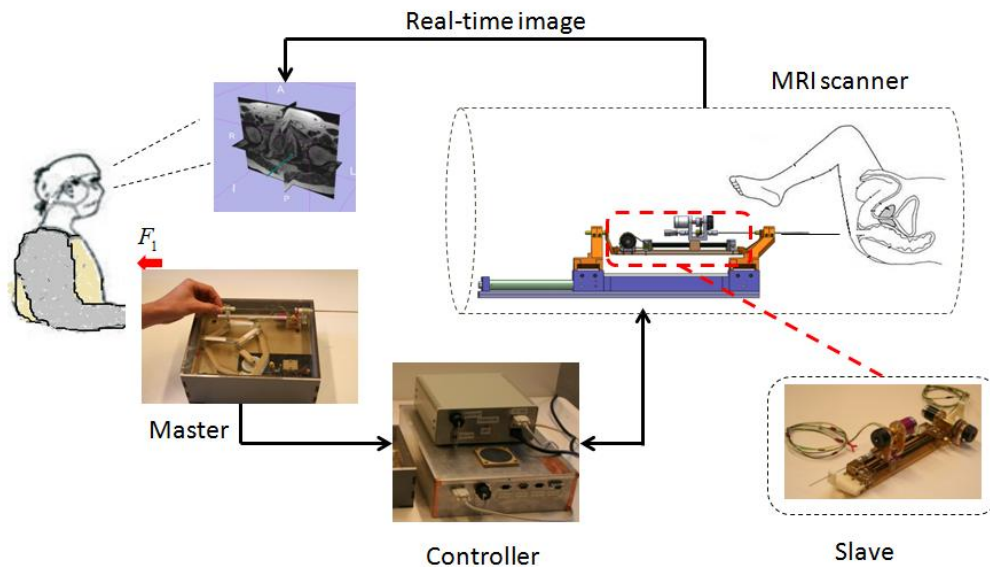


Figure 6.1: Teleoperated needle steering under real-time MRI guidance.

[4], MRI-compatible force sensors [5], target tracking [6], and needle tracking. This study focuses on needle tracking aspect.

A flexible bevel-tip needle bends during insertion due to asymmetric lateral forces applied to the bevel-tip. If it is rotated 180 degrees, the bending direction reverses making the needle tip deflect to the opposite trend. One dependency for enabling of this steering technique is providing visual information of the needle tip (and target) on the fly. The immediate solution would be real-time MR imaging. However, real-time MR imaging has some limitations: 1) needle leaves a large artifact on the image (few mm thick) and it is not straightforward to localize needle shaft within the artifact since it depends on many factors including imaging parameters [7]; 2) real-time imaging typically involves 500 msec latency in typical scanners, 3) for most of the scanners, it is difficult to interactively control the imaging plane so that the 3D shape of needle can be captured during insertion. In addition, using radio frequency tracking passive coils is not practical as it requires very tiny coils to be embedded into the 0.6 mm inner stylet of the needle.

An FBG sensor is a strain gauge consisting of an optic fiber with a short segment of grating mirrors in series. As the fiber experiences mechanical or thermal stresses, the distances between these mirrors change, allowing a different wavelength to be reflected and collected. This shift in wavelength is proportional to the strain applied [8]. On principle, FBG has no interference with MRI magnetic field. Some advantages of FBGs are high accuracy, fast response, robustness, biocompatibility, and sterilizability, making it a good solution for our application.

FBG technology has been previously used for a variety of needle and surgical tool applications. A needle having 3 embedded fibers in 120-degree configuration was proposed for measurement of below milli-Newton lateral force applied to a 25G tool shaft for vitreoretinal surgery [9]. A similar idea was used to capture the 3D shape of a diamond-tip 18G needle with fixed length [10]. FBGs have also been used to estimate 3D shape of the catheters and endoscopes in similar fashion [11] and [12].

We embedded 3 optical fibers ($\varnothing = 125 \mu\text{m}$) with constructed FBGs along the inner stylet of a 20G MRI-compatible bevel-tip needle (Figure 6.2). It was proven that minimum 3 FBGs along each fiber are required to render 3D shape of needle for all clinically possible insertion depths, i.e. depths in the range of 0-110 mm. The optimum locations of FBGs were found by mathematical modeling and computer simulation so that the error in tip estimation is below 0.5 mm for any insertion depth. Beam-column theory is employed in modeling of the needle deflection in order to account for the concentrated lateral and axial forces applied to the bevel-tip. The needle was custom designed to be used at the slave robot needle holder. After prototyping the needle, a simple and practical method for calibration was proposed without requirement of camera and image processing. Accuracy of the system in estimation of the needle tip for different insertion depths were demonstrated with experiments. Real-time 3D visualization of the needle

was enabled in 3D Slicer which is a software used in clinical procedures for prostate biopsy and brachytherapy [13].

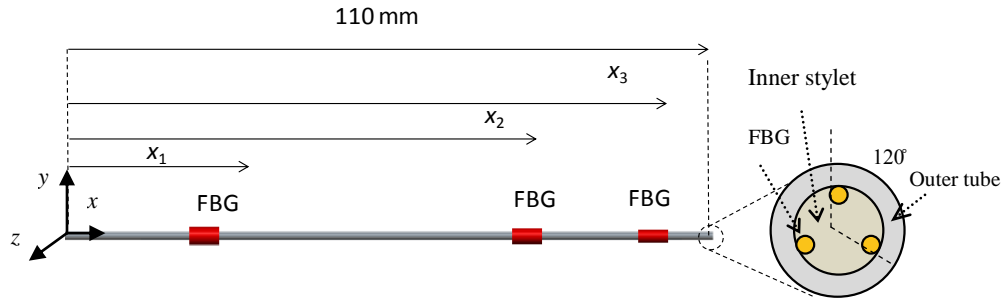


Figure 6.2: A 20G bevel-tip needle with 3 optical fibers at 120-degree configuration. Each fiber has 3 FBGs at x_1 , x_2 , and x_3 , respectively.

6.2 Design considerations

A 20G ($\phi = 0.9$ mm) needle was selected since it is flexible enough for steering purposes and still thick enough for embedding fibers into its inner stylet ($\phi = 0.6$ mm). We considered minimum and maximum insertion depths in transperineal prostate biopsy and brachytherapy to be 20 mm and 100 mm, respectively (most often in the range of 40-70 mm). The actual needle is longer considering the slave robot geometry (Figure 6.1). However, the length-of-interest, i.e. the length to be monitored is 110 mm (extra 10 mm was considered for the gap between the patient's premium and the robot).

Target displacement increases with insertion depth. We assumed that target displacement does not exceed 10 percent of the insertion depth which means up to 10 mm displacement when the needle is fully inserted (i.e. 100 mm). This is a fairly large displacement in comparison to the average 5.4 mm (1.6-11.1 mm) target displacement in transrectal prostate biopsy reported by Xu [14]. This assumption allowed us to use linear beam theory.

We defined the maximum tolerable tip estimation error to be 0.5 mm for all insertion depths. To cover most of the deflection scenarios, our method should be able to show the needle shape with at least two inflection points (Figure 6.3). This means a minimum 2 FBGs per fiber is required. The technology should be MRI-compatible. Lastly, it was desired not to have noticeable latency during needle monitoring using a high speed interrogator and a fast code and data streaming protocols.

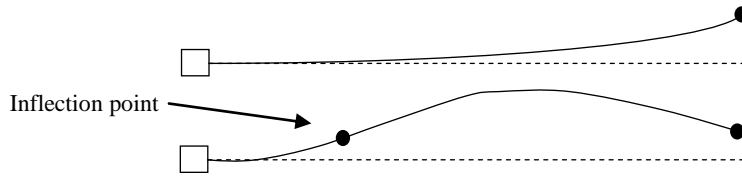


Figure 6.3: Needle with one and two inflection points. Tip is considered one of the inflection points.

6.3 Tip position estimation

Needle tip position can be defined as $[x, y, z]$ where x is the insertion depth measured by the slave robot encoder, and y and z are lateral deflections. We can use polynomial fit to estimate the needle profile. To find y , suppose that the needle is only deflected in x - y plane and the needle profile has $n+1$ inflection points (tip is one of them). This means a n -th order polynomial can be fitted to those n inflection points, i.e. the second derivative of the profile, can be represented by a n -th order polynomial. An n -th order polynomial has $n+1$ unknown ($a_1x^n + a_2x^{n-1} + \dots + a_{n+1}$). To find these unknowns, one needs to know the second derivative at n different locations along the profile other than the tip (tip gives us the $(n+1)$ -th constant). In order to measure the second derivative at the abovementioned n points, we can use n FBGs and find the corresponding second derivative from equation (1) [15]:

$$y''(x) = \frac{\varepsilon_{x-y}}{r} \quad (6-1)$$

where ε_{x-y} is strain in x - y plane and r is the radius of gyration (i.e. the needle radius). Then, we can solve a set of $n+1$ equations and attain the polynomial's coefficients. After finding the estimated second derivative polynomial, we double integrate and derive the approximate profile of the needle. In the equation, we put $x = l$ where l is insertion depth and find y . We found z in similar way using the set of sensors on the second fiber containing n FBGs located on the x - z plane. The set of n sensors on the third fiber are used for temperature compensation. These three fibers are placed at 120-degree-configuration [8].

The needle tip accuracy increases with a higher number of sensors along the needle length. However, a higher number of FBGs means higher manufacturing costs and increased susceptibility to fiber damage or malfunction. It also suggests higher complexity for calibration, and requires higher data processing time through the interrogator and streaming socket protocol, which will slow down real-time visualization of the needle profile and tip location. As a result, it was deemed necessary to find the minimum number of sensors that would be able to provide an error threshold smaller than 0.5 mm for all clinical depth configurations. As mentioned earlier, a minimum two sensors is required to estimate the shape of the needle in each plane with two inflection points. However, the localization analysis confirmed that for the case with only one active sensor, the error noticeably exceeds 0.5 mm. In order to compensate for this, three sensors were used along each fiber as will be discussed next.

For a three-sensor case, $y''(x)$ can be approximated as follows:

$$y''(x) = a_y x^3 + b_y x^2 + c_y x + d_y \quad (6-2)$$

To find a_y , b_y , c_y , and d_y , we use strain information at x_1 , x_2 , x_3 , from (6-1) and at the tip (which is equal to 0). Having $y''(x)$ at 4 locations, a_y , b_y , c_y , and d_y can be found as follows:

$$\begin{bmatrix} a_y \\ b_y \\ c_y \\ d_y \end{bmatrix} = \begin{bmatrix} x_1^3 & x_1^2 & x_1 & 1 \\ x_2^3 & x_2^2 & x_2 & 1 \\ x_3^3 & x_3^2 & x_3 & 1 \\ L^3 & L^2 & L & 1 \end{bmatrix}^{-1} \begin{bmatrix} y''(x_1) \\ y''(x_2) \\ y''(x_3) \\ 0 \end{bmatrix} \quad (6-3)$$

L is the instantaneous length of the needle. If we double integrate equation (6-2) and apply the boundary conditions, the approximated profile is obtained as follows:

$$y^{app}(x) = \frac{a_y}{20}x^5 + \frac{b_y}{12}x^4 + \frac{c_y}{6}x^3 + \frac{d_y}{2}x^2 \quad (6-4)$$

The approximate position of the needle tip then is $y(L)$. The profile on the x - z plane, $z(x)$, is found in the same manner. In the next section, sensor localization, i.e. finding optimum x_1 , x_2 , and x_3 , is discussed in detail.

6.4 Sensor localization

The needle tip pose estimation error can be defined as the difference between the approximated and the actual tip position:

$$\text{Error}(x_1, x_2, x_3) = |y^{actual} - y^{app}| \quad (6-5)$$

This error is a function of x_1 , x_2 , and x_3 . To minimize this error, the optimum sensor locations should be found for all insertion depths and possible needle profiles. For this reason, we should generate all possible needle profiles and insertion depths and see what sensor locations make the smallest error among all. The only practical method of searching among that infinite number of possibilities is development of a model for needle deflection. This model gives a function by which y^{actual} and y^{app} can be measured for any shape and depth and, as a result, the optimal sensor locations be determine based on Equation (6-5).

6.4.1 Modeling

The proposed free body diagram used in this study is shown in Figure 6.4.

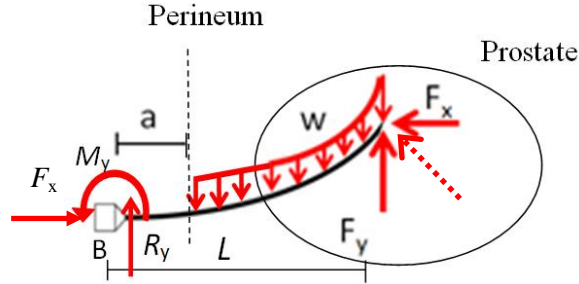


Figure 6.4: Free body diagram (FBD) for the bevel-tip needle during insertion.

Since the force necessary for buckling the needle (16 N- considering the module of elasticity of Inconel, 0.9 mm diameter of the needle, and the maximum length of needle which is 110 mm) is a few times higher than the maximum actual force applied to the needle (4N), the needle cannot buckle. F_y is the concentrated lateral force at the tip, F_x is the concentrated axial force at the tip due to the bevel-tip, w is the distributed load applied to the needle inside tissue, factor a is the needle length not inserted into the tissue but still deflected from the loads applied, and L is the present needle length. Here, we ignore torsion along the needle since we did not observe torsional lag between the base and the tip in phantom experiments. Although this free body diagram might not be the most accurate one, it is still adequate because it focuses not on what types of forces are applied but on what needle shapes can be created. As a result, a force configuration that generates a variety of needle shapes with up to two inflection points will allow derivation of mathematical models and optimization.

The needle can be modeled as an Euler-Bernoulli beam since the maximum tip deflection is limited to 10% of the length. We experimentally confirmed the linear relationship between the

force and tip deflection for the 20G needle used. The Euler-Bernoulli beam's governing differential equation is as follows:

$$y''(x) = \frac{M_y(x)}{EI} \quad (6-6)$$

where $M_y(x)$ is the moment as a function of x , and E is the equivalent module of elasticity, and I is the equivalent moment of inertia of the needle cross section. Due to the existence of the axial force at the tip of the cantilever beam, it should be considered as a beam-column not as a beam. This denotes that the moment caused by the $F(x)$ should be taken into account, as well:

$$M_y(x) = \begin{cases} R_y x + F_x y(x) - M_R, & 0 \leq x \leq a \\ M_R - F_x y(x) - R_y x + \frac{w(x-a)^2}{2}, & a \leq x \leq L \end{cases} \quad (6-7)$$

where R_y and M_R are the reaction force (in y direction) and moment at the support, respectively.

The solution of this differential equation is as follows:

$$y^{actual}(x) = \begin{cases} A_1 \cos(\lambda x) + B_1 \sin(\lambda x) + \overbrace{C_1 x + D_1}^{particular\ so}, & 0 \leq x \leq a \\ A_2 \cos(\lambda x) + B_2 \sin(\lambda x) + \underbrace{C_2 x^2 + D_2 x + E_2}_{particular\ sol}, & a \leq x \leq L \end{cases} \quad (6-8)$$

where $\lambda^2 = F_x/EI$. To find these 9 constant coefficients, we use the following 6 boundary conditions plus plugging the particular solutions into the differential equation (6-6):

$$\begin{aligned} y(0) &= y'(0) = y''(L) = 0; \\ y(a^-) &= y(a^+); \\ y'(a^-) &= y'(a^+); \\ y(a^-) &= y(a^+). \end{aligned} \quad (6-9)$$

It should be noted that all of A_1, B_1, \dots, E_2 are functions of $y(L)$. After finding A_2, B_2, \dots, E_2 , we put $x = L$ into (6-8) and solve for $y(L)$. In fact, $y(L)$ is the last found parameter. The procedure of finding $A_1, B_1, \dots, D_2, E_2$ and $y(L)$ is very cumbersome and was omitted for brevity. In order to find y^{app} , equation (6-4) was used. For the optimization, the second derivatives in (6-4) are

found from the mathematical model derived earlier (i.e. (6-8)). Having y^{actual} and y^{app} , error can be optimized against x_1 , x_2 , and x_3 .

6.4.2 Optimization

Having obtained a model, all parameters, i.e. a , L , F_x , F_y , and w are changed for any x_1 , x_2 , and x_3 . Then, locations providing the minimum approximation error are attained. Since insertion depth is varying in bevel-tip needle steering, the following scenarios are possible:

Case 1: no sensor is activated (insertion depth is very low);

Case 2: only one sensor is activated;

Case 3: only two sensors are activated;

Case 4: all three sensors are activated.

The following assumptions can be made during optimization: 1) the range of variation for F_x , F_y , and w will not deflect needle tip beyond 10% of the present length of the needle. 2) Since the error increases with insertion depth, optimization can be performed at the largest insertion depth for each case. Table 6.1 shows the parameters chosen for optimization.

Table 6.1: Parameters used for optimization.

F_x (N)	F_y (N)	w (N/m)	L (mm)
0.0 ~ 1.5	-5.0 ~5.0	-50 ~ 50	0~110

The range of change for x_3 (the sensor close to the tip) can be limited to the furthest quarter of the entire length (82.5-110 mm) in order to avoid cases with no sensor activated. The range of change for x_1 is the closest quarter of the needle length from the base (0-27.5 mm) because strain values are the highest close to the base. x_2 range of change is therefore middle half of the needle length (27.5-82.5 mm). In the following, the optimal locations are found for sensors within the suggested ranges.

Case 1: In this case, no sensor is activated due to the very low insertion depth and no tracking information is available. As a result, this situation should be avoided to possible extent. Luckily, prostate outer most point is 20 mm deep from perineum (see Figure 6.4), which means that the third sensor (closest to tip) can be localized within the first 20 mm of the needle. However, it is desired to minimize the depth of insertion without active sensors. We will make a decision on this in the next section.

Case 2: In this case, one out of three sensors is active. For this scenario, a set of 1st order equations was used to describe the estimated deflection polynomial to be compared with the mathematical model. We mentioned earlier that the range of change for x_3 is 82.5 to 110 mm. Yet, we must take into consideration the location of the second sensor x_2 in order to determine x_3 under the maximum insertion depth before the second sensor is activated. As a result, x_2 was selected to be very close to the upper acceptable limit at 79 mm. This means that the highest possible depth with only 1 active sensor is $110 - 79 = 31$ mm (we will further investigate this suggested value in Case 3 and Case 4). Taking this into account, we calculated and plotted “Error (x_3)” for the largest depth for any model parameters in Table 1 as shown in Figure 6.5.

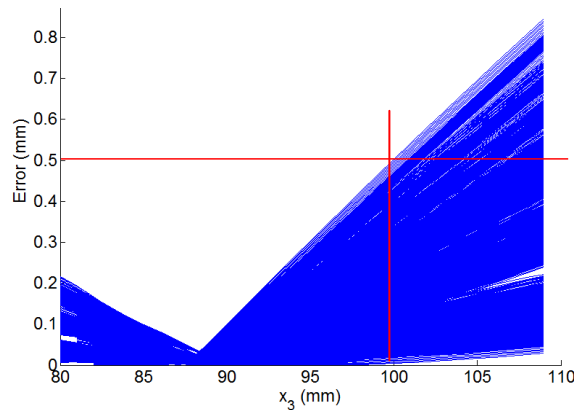


Figure 6.5: Case 2: maximum error for all force configurations and insertion depths up to 31 mm as a function of x_3 .

As seen, an optimal location for one active sensor is 89 mm. However, we chose 99 since it is the closest to the tip yet below 0.5 mm to avoid a situation without tip pose information.

Case 3: In this case, two out of three sensors are activated. For this case, a set of 2nd order equations was used to describe the estimated deflection polynomial. Figure 6.6 illustrates the 2D projection of the worst error surface as a function of x_2 and x_3 positions for all model parameters. The location of the third sensor x_3 must be taken into consideration in order to determine x_2 under the maximum insertion depth before the third sensor is activated. We start with $x_1 = 30$ mm (will further investigate by looking at Case 1 and Case 4). This entails the maximum depth with only two sensors activated is 80 mm from the tip. A range of values where the maximum error is below 0.5 mm is determined in Figure 6.6.

Case 4: All sensors are active. A set of 3rd order equations is used to describe the estimated deflection polynomial as shown in (6-2). Since Error (x_1, x_2, x_3) is a 4D surface, we represented its projection onto three planes, x_1 - x_2 , x_1 - x_3 , and x_2 - x_3 (Figure 6.7). The red area shows sensor locations where error is below 0.5 mm for all insertion depth and force configurations.

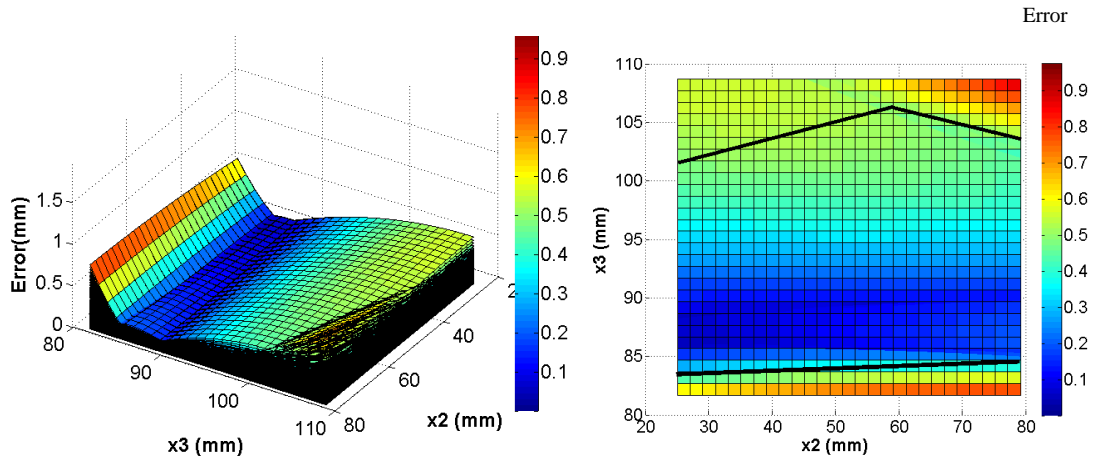


Figure 6.6: Case 3: maximum error for all model force configurations and depths from 31-79 mm as a function of x_2 and x_3 vary. The safe area is marked between two solid black lines.

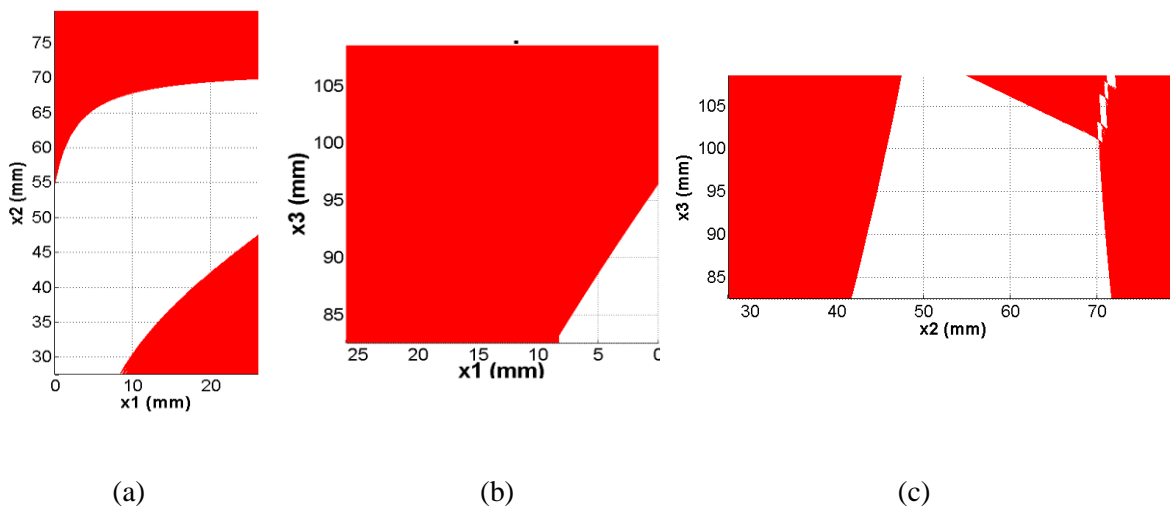


Figure 6.7: Case 4: error for all force configurations and insertion depth above 79 mm as a function of x_1 , x_2 , and x_3 . Red area shows locations with error below 0.5 mm.

Summary: From Case 1, $x_3 = 99$ was the optimum location. The suggested value for x_2 is 79. Figure 6.6 and Figure 6.7a, and Figure 6.7c confirm that this suggested value falls in the safe region. The suggested value for x_1 is 30. Figure 6.7a, Figure 6.7b confirm that this value is within the safe region. Table 2 shows the proposed sensor locations.

Table 6.2: Sensor optimal locations.

<i>Sensor location</i>	x_1	x_2	x_3
(mm)	30	79	99

After finding the sensor locations, we must ascertain whether the error remains below 0.5 mm for all force configurations. In Figure 6.8, we plotted the worst case error as a function of insertion depth for all force configurations, when x_1 , x_2 , and x_3 are chosen as specified in Table 2. As shown, the error increases as the insertion depth increases. It drops when another sensor is activated. The error remains below 0.5 mm for any insertion depth below 100 mm which is the deepest possible target.

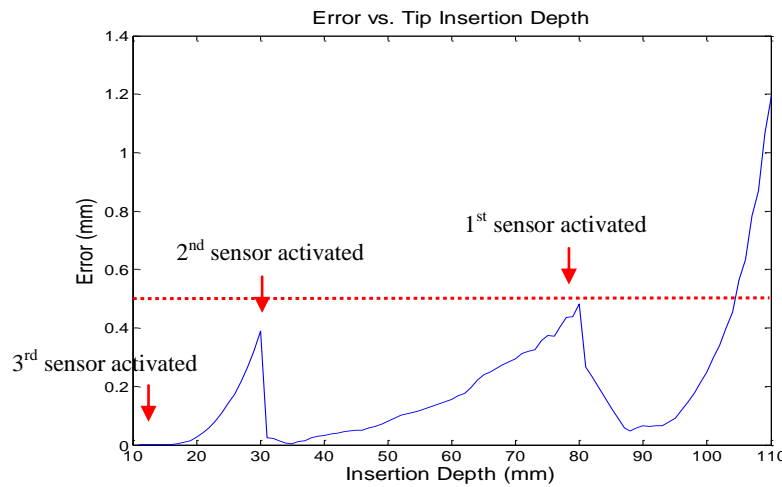


Figure 6.8: Maximum possible error in tip approximation for any load configuration as a function of insertion depth.

6.5 Fabrication

FBGs with 3 sensors at certain locations were custom made by Technica SA (Beijing, China). The sensors were 5 mm long, reflectivity > 70%, glass fiber, polyimide recoat, and the bandwidth

is 0.35-0.45 nm. The wavelengths were constructed at 1540, 1550, 1560 nm (± 0.5 nm) for x_1 , x_2 , and x_3 respectively. The fibers were 125 μ m in diameter and 5 m long. The accuracy of sensor placement was ± 0.5 mm.

The inner stylet was a 0.6 mm Titanium 6AL 4V Eli annealed wire with three grooves manufactured 170 mm along the length. The length of the inner stylet was 235 mm. The outer tube was obtained from a 20G \times 20 cm MRI biopsy needle (Cook Inc, IN, USA).

A jig was manufactured to carry out lateral milling of the stylet. Figure 6.9a shows the setup. Two stainless steel plates were overlaid and a channel of 0.6 mm diameter was machined at the corner of the interface between the plates. The channel was 235 mm long and used to hold the stylet to be machined. Once the needle was placed in the channel and the two plates were bolted together, a brass coin was attached along the stylet length that extended out of the plates. This coin was marked so that it points exact 120-degree rotations for cutting the three channels.

The fibers were glued to the inner stylet channels under microscope with instant adhesive Loctite 415 (Loctite Corp., CT, USA). The inner stylet was then passed through the outer tube. The 20G outer tube (175 mm long) was extended by another MRI-compatible 18G needle outer tube to increase the entire needle length to 235 mm. At the end, the handles were glued to the needle. Shrink tube was used to robustly attach the fibers to the needle. Figure 6.9b shows the needle prototype.

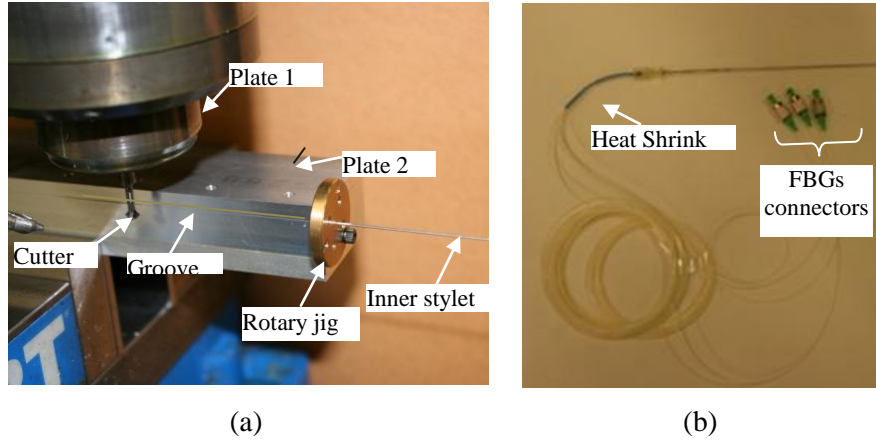


Figure 6.9: (a) Jigs and milling machine for making three grooves along the 0.6 mm needle at 120-degree configuration, (b) Needle prototype.

6.6 Calibration

In order to find strain values from wavelength shifts, calibration is required. At each location (i.e. x_1 , x_2 , and x_3), there are three sensors at 120 degrees. These sensors together give us ε_{xy} and ε_{xz} in that location. A calibration matrix is therefore defined at each x_i to link the wavelength shifts and strains as follows:

$$\begin{bmatrix} \Delta\lambda_1 \\ \Delta\lambda_2 \\ \Delta\lambda_3 \end{bmatrix}_i = \begin{bmatrix} c_{xy,1} & c_{xz,1} \\ c_{xy,2} & c_{xz,2} \\ c_{xy,3} & c_{xz,3} \end{bmatrix}_i \begin{bmatrix} \Delta\varepsilon_{xy} \\ \Delta\varepsilon_{xz} \end{bmatrix}_i \quad (6-10)$$

where $i = \{1, 2, 3\}$. These calibration matrices neither depend on the shape of the needle nor the load configuration applied to it. For this reason, we find these matrices for the basic load configuration when a concentrated force at the tip is applied at the maximum length of the needle (110 mm). $c_{xy, j}$ are found when the needle is deflected in xy plane (i.e. when $\varepsilon_{xz} = 0$) while $c_{xz, j}$ are found when the needle deflects in xz plane (i.e. when $\varepsilon_{xy} = 0$) and $j = \{1, 2, 3\}$. From linear beam theory for concentrated lateral load at the tip of a cantilever beam ((6-1) and (6-6)), one has:

$$y''(x) = \frac{\varepsilon_{xy}(x)}{r} = \frac{F_y x}{EI} \quad (6-11)$$

$$F_y = \frac{3EIy(L)}{L^3} \quad (6-12)$$

where F_y is the lateral load. From these equations, the strain as a function of x is derived:

$$\varepsilon_{xy}(x_i) = \frac{3ry(L)x_i}{L^3} \quad (6-13)$$

r is the distance between the central axis of the fiber and the needle axis. This means we only should measure $y(L)$ in order to find $\varepsilon_{xy}(x_i)$. In order to have a calibration matrix which represents the entire range of needle deflection, we apply different deflections $y(L) = 1, 2, 3, \dots, 10$ mm once in xy , and once in xz using the experimental setup shown in Figure 6.10 and next:

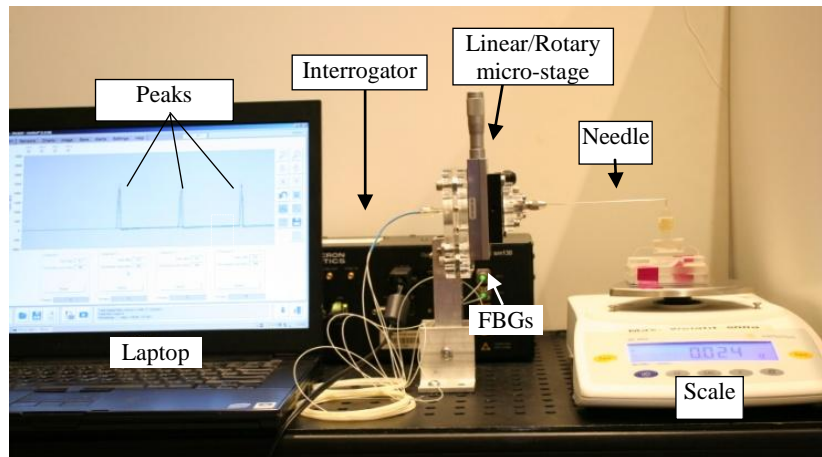


Figure 6.10: Calibration and experimental setup.

The needle was held by a pin vice in the center of a 2-DOF micro-stage. The stage can translate vertically with 10 micron resolution thus enabling needle-tip deflection with high accuracy. The rotary stage with 1 degree resolution makes it possible to deflect the needle in different planes. In order to detect the first moment of starting deflection, a scale with 0.001gram resolution was

used. A sharp blade was placed on top of the scale to enable point contact between the scale and the needle. The micro-stage and the scale were firmly bolted to an anti-vibration table. The interrogator was a 4 channel Micron Optics sm130 (Atlanta, GA, USA), with sampling rate of 2 KHz. The spectrum range is from 1525 nm-1565 nm. Each channel handles one fiber with many sensors (3 sensors in our case). We collected and analyzed data in MATLAB 7.

Now that ε_{xy} and $\Delta\lambda_j$ are found separately, $c_{xy,j}$ is found by fitting the best line to the graph of $\Delta\lambda_j$ vs. $\varepsilon_{xy,j}$ using least square method and find the slope as $c_{xy,j}$. In order to eliminate the effect of temperature change, we subtract $\Delta\lambda_{mean}$ at each x_i from sensor readings. We performed temperature compensation during real-time data collection, as well. The results are provided below:

$$C_1 = \begin{bmatrix} 1127.05 & 315.79 \\ -544.97 & -1111.77 \\ -582.08 & 795.97 \end{bmatrix}, C_2 = \begin{bmatrix} 1145.81 & 302.09 \\ -605.81 & -1150.97 \\ -540.00 & 848.88 \end{bmatrix}, C_3 = \begin{bmatrix} 1234.71 & 466.98 \\ -593.17 & -1283.92 \\ -641.54 & 816.93 \end{bmatrix}.$$

After finding the calibration matrices, strains can be calculated as follows:

$$\Delta E = C_i^+ \Delta A \quad (6-14)$$

where C_i^+ is the pseudo-inverse of C_i .

6.7 Preliminary evaluation with one inflection point

In order to evaluate tip estimation accuracy for different insertion depths, we chose maximum insertion depth for each case (worst scenario), applied known deflections to the tip in xy and xz planes using the setup shown in Figure 6.10, and compared them with the estimated value.

One sensor active: The purpose of this experiment was to evaluate needle-tip tracking when only one sensor is active, i.e. when depth < 31 mm. The needle length-of-interest was 27 mm once in xy plane and once in xz plane. The tip was deflected with the micro-stage from 0 up to 3 mm (10

percent of the depth) once forward (loading) and once backward (unloading). The results of 0 degree are shown in Figure 6.11a and the results for the needle placed at 90 degree are shown in Figure 6.11b. The 0 degree means that the needle is deflected in xy plane (i.e. $z(x) = 0, 0 \leq x \leq 110$ mm) and 90 degree means that the needle is deflected in xz plane (i.e. $y(x) = 0, 0 \leq x \leq 110$ mm).

Two sensors active: The purpose of this experiment was to evaluate needle-tip tracking when two out of three sensors are active, i.e. when $31 < \text{depth} < 80$ mm. The cantilever support was placed close to the end of this range at 75 mm. The tip was deflected with the micro-stage from 0 up to 7.5 mm (10 percent of the depth) once forward (loading) and once backward (unloading). The results of 0 degree are shown in Figure 6.11c and the results for 90 degree are shown in Figure 6.11d.

Three sensors active: The purpose of this experiment was to evaluate needle-tip tracking when all of three sensors are active, i.e. when $\text{depth} > 80$ mm. The needle was placed 110 mm outside of the vice. The tip was deflected with the micro-stage from 0 up to 10 mm once forward (loading) and once backward (unloading). The results of needle at 0 degree are shown in Figure 6.11e, the results for 90 degree are shown in Figure 6.11f.

The preliminary results confirmed below 0.5 mm accuracy in needle-tip estimation for almost all insertion depths. Only in case (e), the error goes slightly above the threshold. The error variation was quite consistent in the repeated tests. Therefore, it is possible to compensate for the error by curve fitting. Nevertheless, an insertion depth of 100 mm is less likely to occur since most of targets are 60-90 mm deep from perineum.

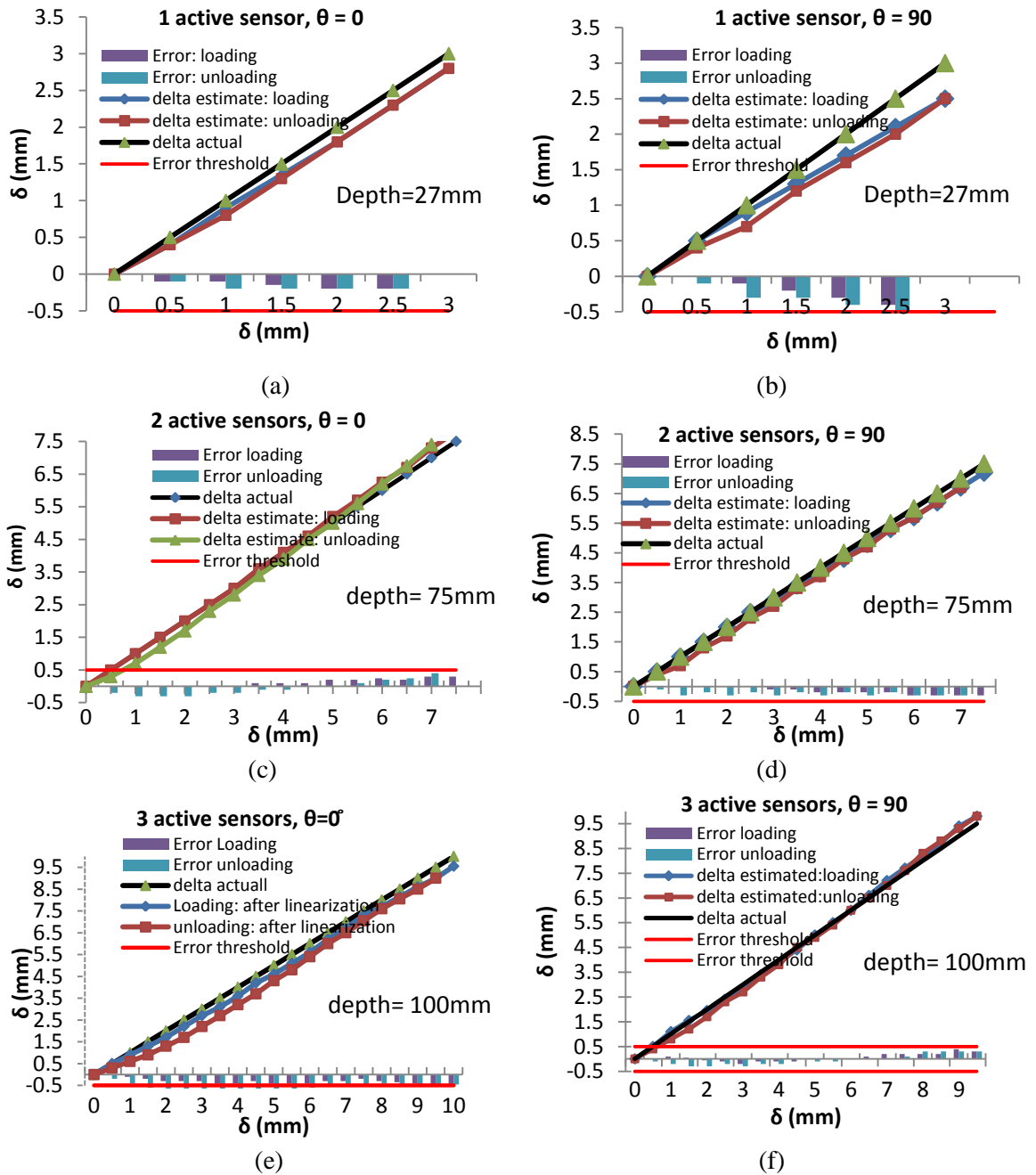


Figure 6.11: Experimental results for needle tip position estimation for different depths and needle orientations. (a), (b): one sensor active, (c), (d): two sensors active, and (e), (f): three sensors active. θ is the orientation of the needle. $\theta = 0$ means needle deflection in xy plane and $\theta = 90$ means needle deflection in xz plane.

6.8 Real-time visualization

For targeting purposes, prostate anatomy is acquired from the intraoperative MRI so that physician can specify target locations within prostate capsule. Here, our goal is to overlay the 3D shape of the needle on the prostate anatomy in real-time. This feature helps physicians to precisely track needle shape and tip in order to compensate for any deviation of the tip from the target.

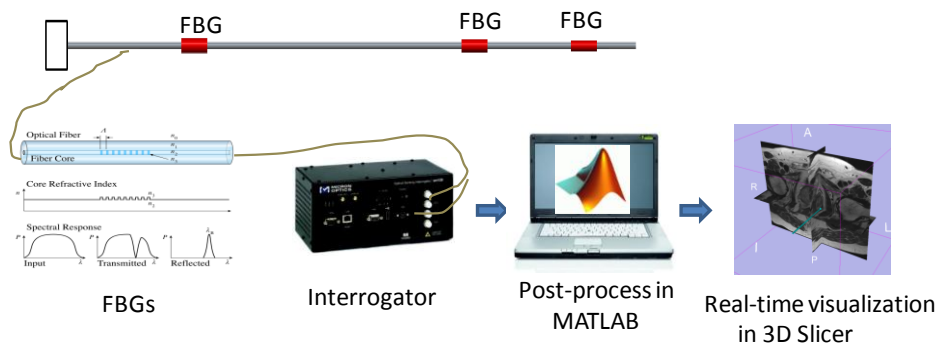


Figure 6.12: Data flow from FBGs to 3D Slicer.

“3D Slicer is a free open-source software application for medical image computing. As a clinical research tool, 3D Slicer is similar to a radiology workstation that supports versatile visualizations but also provides advanced functionality such as automated segmentation and registration for a variety of application domains. Unlike a typical radiology workstation, 3D Slicer is free and is not tied to specific hardware. As a programming platform, 3D Slicer facilitates translation and evaluation of the new quantitative methods by allowing the biomedical researcher to focus on the implementation of the algorithm and providing abstractions for the common tasks of data communication, visualization and user interface development. Compared to other tools that provide aspects of this functionality, 3D Slicer is fully open source and can be readily extended

and redistributed. In addition, 3D Slicer is designed to facilitate the development of new functionality in the form of 3D Slicer extensions. [16]”. This effort has been enabled by the participation of several large scale United States national institute of health (NIH) funded efforts. It has been used on multi-modality imaging including, MRI, CT, US, nuclear medicine, etc and for many organs from head to toe. Slicer has been used in clinical research. In particular, in our teleoperated needle steering system, we use 3D slicer for robot-to-MRI registration and targeting [17].

Figure 6.12 shows the data flow from the FBGs until the needle shape is visualized in 3D Slicer. For targeting purposes, prostate anatomy is acquired from the intraoperative MRI so that physician can specify target locations within prostate capsule. Wavelength shifts are measured by interrogator and sent to MATLAB for post process. Needle profile estimation is performed in MATLAB as explained before. In order to send the 3D shape profile of the needle from MATLAB to Slicer, we used OpenIGTLink ([http:// openigtlink.org/](http://openigtlink.org/)). OpenIGTLink is a library for communications among computers and devices in operating rooms (OR) for wide variety of image-guided therapy (IGT) applications. In our application, it provides communication between Slicer and MATLAB. Since OpenIGTLink is written in C++, MEX files were necessary to make possible calling OpenIGTLink commands in MATLAB that have recently been developed¹⁰. In Slicer, the needle was visualized as a group of fiducials placed next to each other. Figure 6.13 shows visualization software when needle is deflected with two inflection points.

¹⁰ <http://www.na-mic.org/Wiki/index.php/OpenIGTLink/Matlab> [Accessed on November 2012].

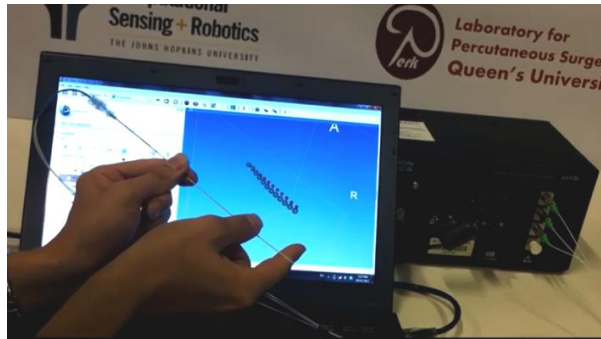


Figure 6.13: Real-time visualization of a $20\text{G} \times 110\text{ mm}$ needle in 3D Slicer: a screen shot showing needle shape with 2 inflection points.

6.9 Conclusions and future work

This chapter presented development of one of the key technologies for teleoperated bevel-tip needle steering under real-time MRI guidance, i.e. 3D tracking of the needle tip with better accuracy and higher bandwidth than continuous MR imaging. Results showed needle tip tracking error below 0.5 mm for all insertion depths, covering all clinically relevant insertion depths in transperineal prostate needle placement procedures. Real-time 3D shape of the needle was overlaid on the intraoperative prostate MR image using 3D Slicer. This technology has been incorporated to the master-slave system.

References

- [1] R. Seifabadi, I. Iordachita and G. Fichtinger, "Design of a teleoperated needle steering system for MRI-guided prostate interventions," in *Biomedical Robotics and Biomechatronics (BioRob)*, 2012 4th IEEE RAS & EMBS International Conference on, 2012, pp. 793-798.

- [2] V. Lagerburg, M. A. Moerland, J. J. Lagendijk and J. J. Battermann, "Measurement of prostate rotation during insertion of needles for brachytherapy," *Radiotherapy and Oncology*, vol. 77, pp. 318-323, 2005.
- [3] R. Seifabadi, N. B. Cho, S. E. Song, J. Tokuda, N. Hata, C. M. Tempany, G. Fichtinger, and I. Iordachita,. Accuracy Study of an MRI-guided Robotic System for Prostate Needle placement. *The International Journal of Medical Robotics and Computer Assisted Surgery*, Published online June 2012, DOI: 10.1002/rcs.1440.
- [4] G. S. Fischer, and H. Su, "apparatus and methods for MRI-compatible haptic interface," *U.S. Patent* No. 20,120,265,051, 2012.
- [5] R. Monfaredi, R. Seifabadi, G. Fichtinger, and I. Iordachita, "Design of a decoupled MRI-compatible force sensor for robot-assisted prostate interventions," *In SPIE Medical Imaging*, pp. 867118-867118, 2013.
- [6] M. Ries, B. D. de Senneville, S. Roujol, Y. Berber, B. Quesson and C. Moonen, "Real - time 3D target tracking in MRI guided focused ultrasound ablations in moving tissues," *Magnetic Resonance in Medicine*, vol. 64, pp. 1704-1712, 2010.
- [7] S. E. Song, N. B. Cho, I. I. Iordachita, P. Guion, G. Fichtinger and L. L. Whitcomb, "A study of needle image artifact localization in confirmation imaging of MRI-guided robotic prostate biopsy," in *Robotics and Automation (ICRA), 2011 IEEE International Conference on*, 2011, pp. 4834-4839.

- [8] K. O. Hill, and G. Meltz, "Fiber Bragg grating technology fundamentals and overview," *Journal of Lightwave Technology*, vol. 15(8), pp. 1263–1276 (1997).
- [9] I. Iordachita, Z. Sun, M. Balicki, J. Kang, S. Phee, J. Handa, P. Gehlbach, R. Taylor. A sub-millimetric, 0.25 mm resolution fully integrated fiber-optic force-sensing tool for retinal microsurgery. *International Journal of Computer Assisted Radiology and Surgery (IJCARS)*, vol. 4(4), pp. 383–390.
- [10] Y. L. Park, S. Elayaperumal, B. Daniel, S. C. Ryu, M. Shin, J. Savall, R. J. Black, B. Moslehi, and M. R. Cutkosky. Real-time estimation of 3-D needle shape and deflection for MRI-guided interventions. *Mechatronics, IEEE/ASME Transaction on*, vol. 15(6), pp. 906–915, 2010.
- [11] ENDOSENSE. Medical apparatus system having optical fiber load sensing capability, 2006.
- [12] L. Zhang, J. Qian, Y. Zhang, and L. Shen. On SDM/WDM FBG sensor net for shape detection of endoscope. in *Robotics and Automation (ICRA), 2005 IEEE International Conference*, 4:1986–1991, 2005.
- [13] J. Tokuda, G. Fischer, C. Csoma, S. DiMaio, D. Gobbi, G. Fichtinger, C. Tempny and N. Hata, "Software strategy for robotic transperineal prostate therapy in closed-bore MRI," *Medical Image Computing and Computer-Assisted Intervention–MICCAI 2008*, pp. 701-709, 2008.
- [14] H. Xu, A. Lasso, S. Vikal, P. Guion, A. Krieger, A. Kaushal, L. Whitcomb, and G. Fichtinger. Accuracy validation for MRI-guided robotic prostate biopsy. *SPIE Medical Imaging: Visualization, Image-Guided Procedure, and Modeling*, vol. 7625, pp. 762517-762517, 2010.
- [15] S. P. Timoshenko, "History of strength of materials". *Dover publications*, 1983.

- [16] A. Fedorov, R. Beichel, J. Kalpathy-Cramer, J. Finet, J. C. Fillion-Robin, S. Pujol, C. Bauer *et al.*, "3D Slicer as an image computing platform for the Quantitative Imaging Network," *Magnetic Resonance Imaging*, vol. 30 (9), pp. 1323-1341, 2012.
- [17] J. Tokuda, G. S. Fischer, S. P. DiMaio, D. G. Gobbi, C. Csoma, P. W. Mewes, G. Fichtinger, C. M. Tempany, and N. Hata. "Integrated navigation and control software system for MRI-guided robotic prostate interventions," *Computerized medical imaging and graphics: the official journal of the Computerized Medical Imaging Society*, vol. 11(2), pp. 701-709, 2009.

Chapter 7

Conclusions and future work

7.1 Conclusions

This thesis presented the development of enabling technologies for human-operated in-room master-slave needle placement under real-time MRI guidance, while the patient is kept in the scanner and having the needle placement process under continuous control of the physician. For this purpose:

- 1- A teleoperated MRI-compatible single-DOF needle insertion system was developed and integrated with an existing 4-DOF base robot for prostate needle placement. The slave robot was a single-DOF needle insertion module actuated with linear piezo motors while the master was an MRI-compatible master device with manual actuation. The feasibility of this system in remote needle insertion was demonstrated.
- 2- In an accuracy study, different error sources in MRI-guided robotic prostate needle placement were identified and quantified. A calibration procedure was proposed to reduce the error associated with the 4-DOF base robot. In a phantom study, the overall system error in needle placement was reduced to 2.5 mm which is within the clinically acceptable range. Also, this study highlighted the significance of errors occurring during needle insertion, including errors caused by prostate motion, deformation, and needle deflection.
- 3- In order to compensate for the error occurring during needle insertion and in continuation with the teleoperated needle placement approach, teleoperated needle steering under real-time MRI guidance was developed. An MRI-compatible 2-DOF needle steering module

was developed using piezo electric motors and integrated with the 4-DOF base robot, yielding a fully actuated 6-DOF MRI-compatible robotic platform intended for prostate biopsy and brachytherapy. The base robot provides the macro needle positioning while the slave provides the insertion and the fine adjustments (macro-micro approach). In order to let physician stay in room during needle steering, a novel 2-DOF MRI-compatible master robot was developed with associated controller software and hardware. MRI-compatibility tests showed insignificant SNR deterioration of the system. Experiments in an MRI room indicated that the system functionality is not affected by the MRI magnetic field in any way. Phantom experiments demonstrated that the bevel-tip needle steering could significantly reduce the targeting error. The feasibility of teleoperated needle steering under real-time MRI was also studied.

- 4- A method for real-time tracking of the 3D shape of a needle with better accuracy and higher bandwidth than continuous MRI imaging was achieved by embedding Fiber Bragg Grating strain sensors along the inner stylet of a 20G needle that we used for bevel-tip needle steering. Mathematical modeling and computer simulations were performed to find the optimal locations of the FBGs along the needle. The needle was modeled as a beam-column in order to account for lateral and axial concentrated forces applied to the asymmetric beveled tip. The needle was prototyped and calibrated using a simple and practical method. Results showed that the needle tip tracking error was below 0.5 mm for different insertion depths, covering all clinically relevant insertion depths in transperineal prostate needle placement procedures. The needle shape was overlaid on the intra-operative prostate MR image helping the physician to keep precise track of the needle tip and shape during teleoperated bevel-tip needle steering.

- 5- A 2-DOF decoupled MRI-compatible force-torque sensor was co-developed using a Fiber Bragg Grating in order to be used with the master robot. The sensor aimed to address the non-backdrivability of the master robot caused by the inherent friction of the piezo motors using a cooperative control architecture. This small foot-print sensor was able to measure axial forces in the range of $\pm 10\text{N}$ and axial torques in the range of $\pm 100\text{Nmm}$ with resolution of 0.1 N and 1 Nmm , respectively. The sensor was designed, prototyped and calibrated. Experiments demonstrated the accuracy of the sensor in comparison with a commercial sensor as ground truth and proved that the sensor reading is not affected by temperature changes in the environment. The sensor was successfully tested in the teleoperated needle steering system in an MRI room.

7.2 Future work

- 1- For teleoperated needle steering under real-time MRI guidance, the following are proposed as future directions: a) it is desired to replicate the force sensor and place it behind the needle on the slave side, so that bilateral teleoperated needle steering can be achieved. This also requires modification to the control architecture. Algorithms such as the one reported in [1] appear to be possible solutions and I have tested them in MATLAB SIMULINK. b) In this thesis, a static phantom was used with small target motion. Needle steering should be evaluated in a more realistic phantom such as what was reported in [2], or even better, in vivo (typically a canine). It is desired to integrate the needle tracking technique described in Chapter 6 with the teleoperated needle steering system and testing it in an MRI room. Implementation of this idea can be achieved in a short time frame. The main limitations of the existing design before using it for human are as follows:

- Sterilizability: this requires approval from designated companies and redesigning the sterilizable parts such as the needle guide.
 - Safety: adding emergency buttons, limit switches, and home positioning sensors could improve the safety of the system.
 - Animal studies: before human study, the system functionality should be evaluated in an animal such as a canine.
 - Institutional review board (IRB) approval must be taken for testing the system on humans.
- 2- The ex vivo accuracy study reported in Chapter 2 on MRI-guided robotic prostate needle placement can be repeated in vivo where prostate motion and deflection are more realistic. The experiment can also be repeated for the 6-DOF robotic system (vs. the 4-DOF system used) in order to demonstrate the effectiveness of needle steering in error compensation and to measure the error of both the base robot and the needle steering slave robot at the same time.
 - 3- The 2-DOF MRI-compatible force sensor reported in Appendix A is sufficient for the needle steering purpose reported in this study. However, it is desired to extend it to 4-DOF and 6-DOF force sensing in future.
 - 4- The robotic system presented in this thesis aims to place the needle into the desired target under the contiguous control of physician. However for real biopsy and brachytherapy procedures, an MRI-compatible automated biopsy system with multiple sampling capabilities and an MRI-compatible automated seed injector system are sought to perform the final task after the needle reaches the desired target.

References

- [1] O. Piccin, L. Barbé, B. Bayle, M. De Mathelin, and A. Gangi. "A force feedback teleoperated needle insertion device for percutaneous procedures," *The International Journal of Robotics Research*, vol. 28 (9), pp. 1154-1168, 2009.
- [2] N. Hungr, M. Baumann, J. A. Long, and J. Troccaz. "A 3-D Ultrasound Robotic Prostate Brachytherapy System with Prostate Motion Tracking," in *Robotics, IEEE Transactions on*, vol. 28 (6), pp. 1382-1397, 2012.

Appendix A

The materials presented in this Appendix have been published with the citation as follows:

R. Monfaredi, R. Seifabadi, G. Fichtinger, and I. Iordachita, “Design of a decoupled MRI-compatible force sensor for robot-assisted prostate interventions,” *In SPIE Medical Imaging*, pp. 867118-867118, 2013.

The materials have also been submitted to Johns Hopkins University Patent Office to be filed as a United States patent with the following reference information:

R. Monfaredi (35%), I. Iordachita (35%), and R. Seifabadi (30%), “MRI-compatible force/toque sensor with fiber Bragg gratings”, JHU reference #C12338, March 2013, to be filed as a *United States Patent*.

Contributions:

R. Monfaredi performed the mechanical design and FE analysis of the force sensor. I developed the calibration and evaluation experimental setup including a code to analyze FBG data from the interrogator, data acquisition system for the Nano 17 force sensor, and a graphical user interface (GUI) for data collection. R. Monfaredi and I built the sensor and collected data.

Design of a decoupled MRI-compatible force sensor using fiber Bragg grating sensors for robot-assisted prostate interventions

During prostate needle insertion, the gland rotates and displaces resulting in needle placement inaccuracy. To compensate for this error, we proposed master-slave needle steering under real-time MRI in a previous study. For MRI-compatibility and accurate motion control, the master (and the slave) robot uses piezo actuators. These actuators however, are non-backdrivable. To address this issue, a force sensor is required. A force sensor is also required on the slave side to reflect the insertion force to the clinician's hand through the master robot. Currently, there is no MRI-compatible force sensor commercially available. In order to generate a combination of linear and rotary motions for needle steering, this study is seeking to develop an MRI-compatible 2 -degrees of freedom (DOF) force/torque sensor. Fiber Bragg Grating (FBG) strain measuring sensors are used. The active element is made of phosphor bronze and other parts are made of brass. The force and torque measurements are designed to be mechanically decoupled. The sensor measures -20 to 20 N axial force with 0.1 N resolution, and -200 to 200 Nmm axial torque with 1 Nmm resolution. Analytical and Finite Element (FE) analyses are performed to ensure the strains are within the measurable range of the FBG sensors. The sensor is designed to be compact (diameter = 15 mm, height = 20 mm) and easy to handle and install. The proposed sensor is fabricated and calibrated using a commercial force/torque sensor.

A.1 Introduction

In the last decade, robot assisted MRI-guided prostate needle placement has gained a lot of interest due to the MRI superior imaging capabilities. MRI-compatible force/torque sensor can be an important part of robotic systems for prostate percutaneous interventions under MRI. Despite the advances reported recently in MRI-compatible systems, developing a proper MRI-compatible

sensor is still a challenging task. To the best of our knowledge, there is no commercially available MRI-compatible sensor in the market and recent research in this field does not provide an applicable solution.

The application (Figure A.1) for which we are developing a force sensor is teleoperated needle steering under real-time MRI guidance proposed in [1].

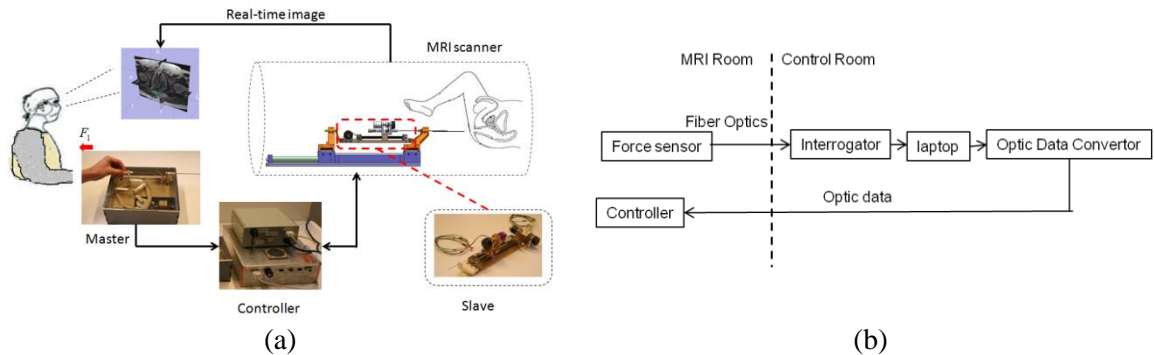


Figure A. 1: (a) Motivation: teleoperated needle steering under real-time MRI guidance is proposed to compensate for needle placement error, (b) MRI-compatibility: the electronic parts for force measurement are placed outside of the MRI room thus eliminating interference with magnetic field.

The clinician interacts with a master robot which is placed next to the scanner and therefore, must be MRI-compatible. The slave robot (which is installed on the base robot [2], [3] - the base robot orients the needle toward the target) follows the motions of the master.

Slave and master have 2-DOF: linear motion for the needle plus the rotary motion. Since the needle is beveled, the combination of these two motions enables needle steering. Visual feedback is provided by real-time MRI. A controller is developed to enable communication between the master and the slave. The idea of teleoperation is proposed to enable the surgeon to remotely perform the task while the patient is inside the scanner for real-time imaging. Since the master

robot uses piezo motors for the MRI-compatibility and ease of control, it is non-backdrivable. Therefore, a 2-DOF force-torque sensor is required to enable movement. In addition, to feedback the needle insertion force to the clinician's hand, a force sensor should be placed on the slave side behind the needle. MRI-compatibility for sensors indicates that: 1) the sensor should be able to operate in a high magnetic field, and 2) it has minimal disturbance to the MR images. This means that usage of any non-magnetic metallic part should be reduced to minimum, and ferromagnetic materials must be avoided. In addition, it implies that the conventional strain gauges cannot be used since they distort the magnetic field and the RF pulse emitted by the scanner thus drastically degrading the image quality. Shielding of strain gauges does not resolve the image degradation.

In previous studies, hydrostatic pressure, differential light intensity, differential optic fiber, optical micrometry, and absolute light intensity have been proposed as alternatives to the conventional strain gauges [4]. Tada *et al.* [5] developed an optical 2-axis force sensor without any metal and electronic components in the sensing element using photo sensors and optical fibers. The sensor was a 2-DOF sensor which measures forces in the x and y directions. The sensor was rather bulky since it used photo sensors.

Chapuis *et al.* [6] designed a simple and efficient torque sensor based on light intensity measurement over optical fibers. This sensor allowed the electronic components to be placed outside of the scanner room. The sensitivity of transverse torque was reduced to 0.03% of the desired output torque by using a self-guiding flexible structure and optimal mirror placement. This sensor was a single-DOF sensor for torque sensing and utilized optical technology for the compactness and being sensitive to precise placement of the mirrors.

An MRI-compatible 3-axis force sensor was developed in [7]. Differential measure of light intensity was used using a new MRI-compatible optical micrometry. Optoelectronic devices and

pairs of optical fibers were used to measure forces in three directions. Two micrometers were aligned in orthogonal directions in order to realize 3-axis force sensitivity.

Parallel plate structure was used to develop an MRI-compatible optical force sensor. It utilized an optical micrometry based on differential measures of light intensity [8]. The sensor's head components were made of glass fiber reinforced poly-ether-ether-ketone to reduce axial interference and hysteresis behavior of plastic resin. This was a 1-DOF sensor for axial force sensing.

An optical fiber sensing method was designed and fabricated in [9]. The sensor was based on an optical sensing principle and measured forces by deforming a 3-DOF flexible structure. By using an optical sensing scheme, minute deflection of the structure was detected. Then the magnitude and direction of the applied force were determined. This sensor measured only forces. The sensor was bulky because of the sensing principal.

Polygerinos *et al.* in [10] presented a prototype design and development of a small MRI-compatible fiber-optic force sensor to measure forces during MRI-guided cardiac catheterization. A fiber-optic cable interrogated a reflective surface at a predefined distance inside a catheter shaft based on light intensity modulation.

Tan *et al.* developed a 3-DOF axial force sensor with small coupling effects between DOFs [11]. Using materials with hysteretic behavior, it was necessary to use Prandtl–Ishlinskii theory to address this behavior. The sensor was bulky for its forces range capability.

Hao Su *et al.* [4] developed a sensor for torque measurement in 2 directions and force measurement in one direction. This sensor was developed based on fiber-optic and spherical mirror technology. The sensor was bulky and was not able to measure axial torque which is necessary for needle steering in prostate intervention.

Iordachita *et al.* designed and analyzed a force measurement device that measures distal forces interior to the sclera using FBGs embedded in a 0.5 mm diameter tool shaft. Utilizing FGB technology in this design made the device small necessary for retinal microsurgery. This device was suitable for force sensing in 2 directions especially for microsurgery procedures [12].

In this study, we propose using FBG sensors as the strain measuring elements. FBG is a type of distributed Bragg grating constructed in a short segment of an optical fiber that reflects a particular wavelength of light and transmits all others [13]. If FBG experiences strain which can be caused either by mechanical stress or thermal stress (i.e. external force/torque or temperature change), the distance between two consecutive layers changes, resulting in the shift of the reflected wavelength. This wavelength shift is a linear function of strain. Previously, FBG was used for needle shape tracking [14] and force measurement applied to the needle tip in retinal surgery [12]. However, no force/torque sensor with FBG has been reported. The advantages of FBG sensors are as follows: 1) they can measure a very high strain up to 5000 (even 10000) $\mu\text{m}/\text{m}$ and therefore, offer a higher sensitivity; 2) they are bio-compatible; 3) they are sterilizable, and 4) they are easy to install.

Since the optic fibers are utilized not only for strain measurement, but also for data transmission, they do not create any interference with the MRI magnetic field. The interrogator (which is the signal analyzer device and generates the light and computes the wavelength shift based on the reflected signal) is placed outside of the MRI room, thus having no impact on MR image (Figure A.1b). The calibration matrices are applied to the wavelength shift readings in a MATLAB code running on a laptop next to the interrogator in order to generate the force data. Force measurements are then sent to the controller in MRI room to produce the control law which will

move the master and the slave robots. This procedure ensures no interference of the force sensing with MRI since it requires no electric signal transmission.

In this Appendix, we present a novel mechanically decoupled 2-DOF sensor using FBG sensors. In section 2, the design procedure is described. Section 3 demonstrates the fabrication stage and FBG installation. Section 4 discusses the calibration setup and results. Section 5 concludes the Appendix.

A.2 Sensor design

A.2.1 Mechanical design

The following criteria were considered while designing the mechanical structure of the sensor:

- 1) *Mechanically decoupled sensor*: This will simplify the calibration procedure for the sensor.
This criterion was fulfilled by utilizing a ball bearing and square cross section shaft to separate axial force and axial torque flow.
- 2) *Small size sensor*: This is necessary for the placement of the sensor in the intervention device.
This criterion is considered by compact mechanical design and utilizing of FBGs with 2 mm length.
- 3) *Limitations of FBG installation*: There are a few limitations which should be considered while designing the sensor
 - *FBG curvature limitation*: The FBG is embedded in a fiber and should not be over bent.
 - *Beam-to-FBG length ratio*: There are some specific FBGs with standard lengths available in the market. In this design, FBGs with 2 mm length were selected. There is no standard for beam-to-FBG length ratio, but due to the stress concentration on the two extremities of the beam on which the FBG are installed and to avoid the effect of this inconsistency on the FBG performance, beam-to-FBG length ratio must be fairly larger than 1. In our design, this ratio

was selected to be 2. The FBG length and the beam-to-FBG length ratio directly affect the size of the sensor and determine how small the sensor can be.

- 4) *Avoiding hysteresis and fatigue:* Hysteric behavior is one of the potential problems which can be encountered in the sensor development. This problem is caused by the material used for the active elements. On the other hand, it should be noted that the active element is exposed to dynamic loading and unloading that can result in fatigue and failure of the sensor. In our design, phosphor bronze was considered as the material for active elements due to its hysteresis-free characteristic, high strength against dynamic loading and fatigue, and good machinability.
- 5) *Temperature compensation:* FBGs are very sensitive to temperature variation. To address this issue, a set of two FBGs were used for each DOF. Using two FBGs and considering differential calculation, the temperature variation effect was compensated for.

In this section, two different decoupled designs are proposed and compared (Figure A.2 and Figure A.3).

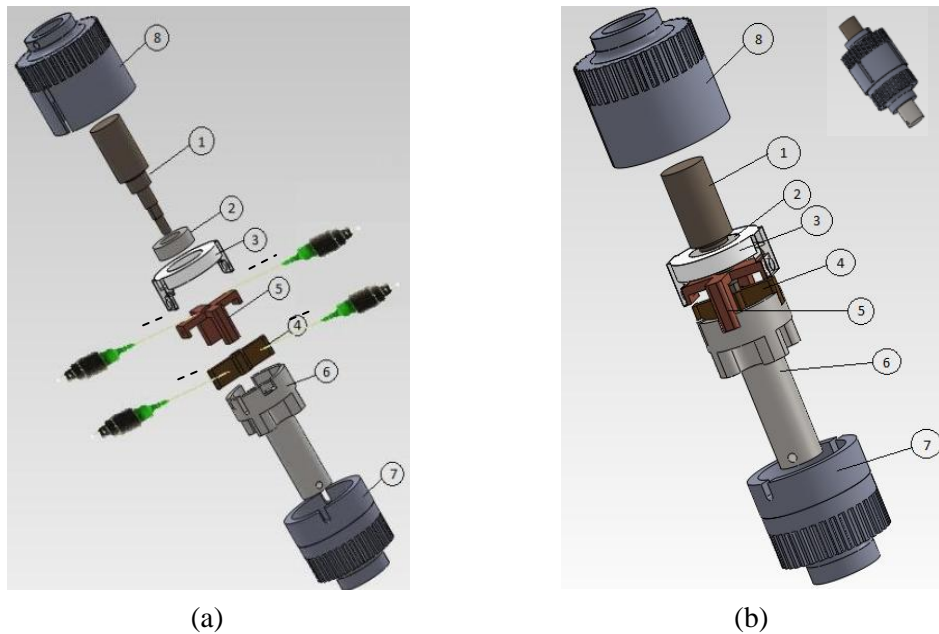


Figure A. 2: 2-DOF force/torque sensor with radial FBG installation, first design: (a) exploded view, (b) assembled sensor (1- square cross section shaft for torque transmitting; 2- ball bearing; 3- part for transmitting axial force; 4- active element for axial torque; 5- active element for axial force; 6- base and shaft; 7 and 8 are casings).

Figure A.2a and Figure A.3a show the exploded view of the proposed designs and where the FBGs are installed. As shown in these figures, an extra FBG is used for each DOF in order to compensate for environment temperature variation. In these figures, parts 1 and 6 are used to connect the sensor to the test bed. Part 2 is a ball bearing and is used to decouple the force and torque. Part 3 exerts the axial force to the corresponding FBGs. Part 4 has a square hole at the center which transmits torque but not the axial load. In the first design (Figure A.2), FBGs for axial force measurement are installed on part 5 and FBGs measuring the torque are installed on part 4. In the second proposed structure (Figure A.3), all FBGs are installed on part 5. Figure A.2b shows the assembled sensor for the first design. Figure A.3b shows how the force and

torque are separated using ball bearing for the second design and Figure A.3c shows how the torque flows from part 1 to part 6.

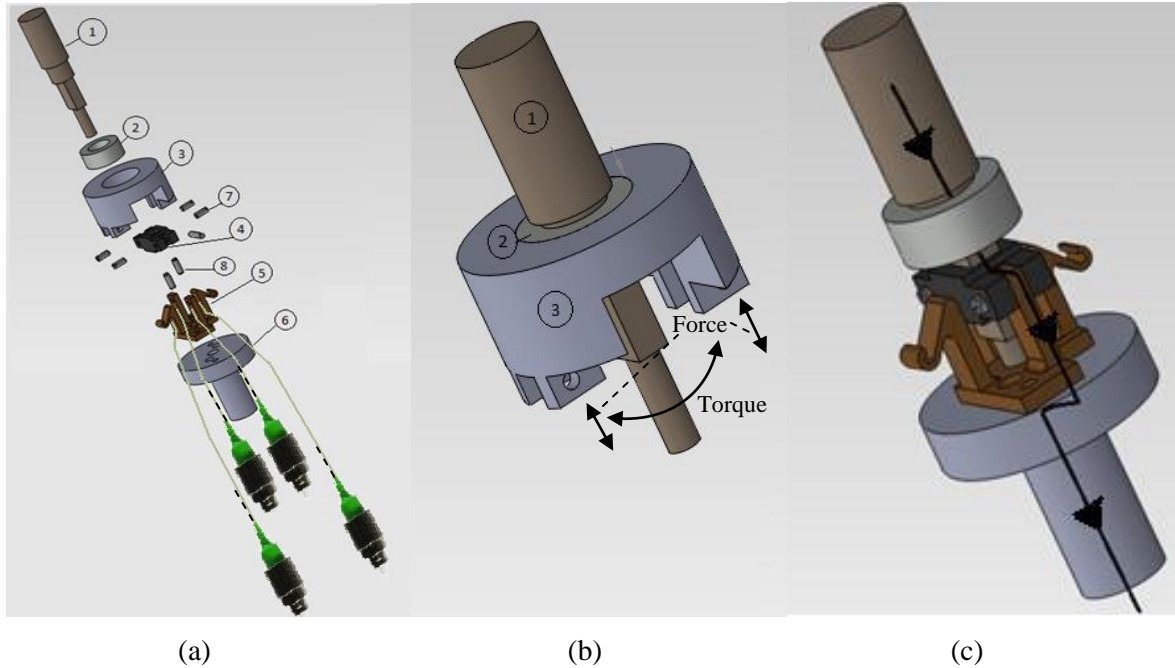


Figure A. 3: Modified sensor with axial FBG installation configuration: (a) exploded view, (b) ball bearing (part 2) connects part 1 to part 3 with minimum friction thus making force and torque measurements decoupled, and (c) the solid line shows how the torque flows from part 1 to part 6. (1- square cross section shaft for torque transmitting; 2- ball bearing; 3- part for transmitting axial force; 4- part for transmitting axial torque; 5- active element for axial force and torque; 6- base and shaft).

Mechanical decoupling of the sensor simplifies calibration of the sensor since the calibration matrix becomes diagonal in this case:

$$\begin{bmatrix} \Delta\lambda_1 \\ \Delta\lambda_2 \end{bmatrix} = \overbrace{\begin{bmatrix} c_{11} & 0 \\ 0 & c_{22} \end{bmatrix}}^{\mathbf{c}} \begin{bmatrix} f_z \\ \tau_z \end{bmatrix} \quad (\text{A-1})$$

where C is the calibration matrix. Each element of this matrix are found independently. f_z and τ_z are the axial force and torque, respectively. $\Delta\lambda_1$ and $\Delta\lambda_2$ are the wavelength shifts corresponding to the force and torque active elements, respectively.

The functionality of both proposed designs are the same. However, in the second design, Figure A.3, the FBGs are installed axially rather than radially. Second design is advantageous to our application since it makes handling of the sensor easier and prevents the FBGs from damage. This is the preferred solution we built and calibrated.

Part 5 (active element in Figure A.3) was made of phosphor bronze which is an MRI-compatible material and has hysteresis free behavior. The module of elasticity is $E = 1.1 \times 10^{11} \text{N/m}^2$. The force range of -20 to +20N and torque range of -200 to 200 Nmm were considered as the working ranges of the sensor. The resolution was considered to be 0.1 N and 1 Nmm, respectively. The strain range of 5 to 1000 $\mu\epsilon$ was selected for the FBG sensor. Considering the desired forces and strains, the thickness and the lengths of the beams can be calculated using the following equation from Euler-Bernoulli theorem:

$$\epsilon = \frac{3FL}{2Et^2w} \quad (\text{A-2})$$

where F is the concentrated force applied to the tip of the beam, L is the length of the beam, E is the module of elasticity, and t and w are the thickness and width of the beam, respectively. From equation (A-2), the following values were found: $L = 4\text{mm}$, $t = 1, \text{mm}$ and $w = 2 \text{mm}$. Figure A.4a shows these parameters on the active element.

A.2.2 Finite element analysis

The finite element (FE) analysis is used to investigate the strengths as well as linear behavior of the part on which the FBGs are installed (referred to as active elements). Figure A.4b illustrates FE results for part 5 when axial force is exerted on the sensor. Figure A.4a shows the location for installing FBGs for axial load. The results show that actual stress is below the yield stress (Figure A.4b). Since axial force causes bending of the active elements, it is important to keep the arm d in Figure A.4b constant and to prevent the lateral displacement of the applied force which will lead to inaccuracy in force measurement. Therefore, the beams were designed to have that specific shape as shown in Figure A.4b. Simulation results in Figure A.4b show negligible lateral displacement.

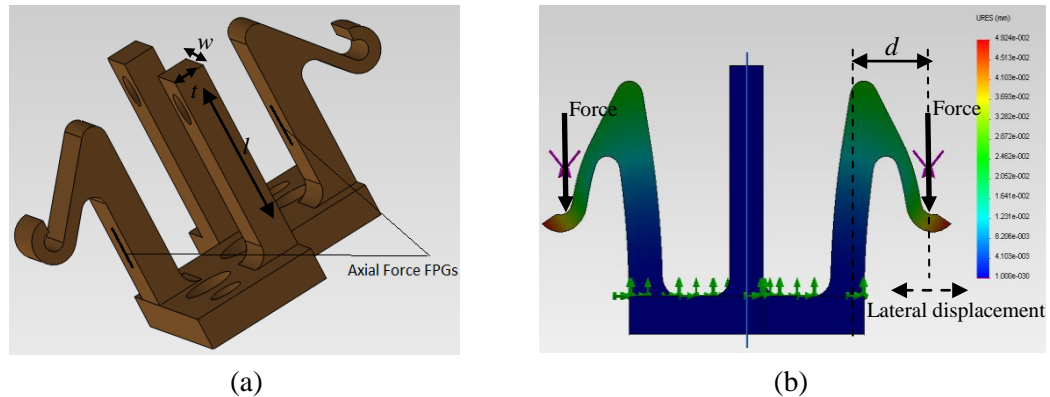


Figure A. 4: FE analysis for the axial force active elements: (a) Active element, (b) FE results when axial force is applied: simulation shows that the tips of the L-shaped beams do not move in lateral direction, i.e. the arm d remains constant after applying the force.

Figure A.5a shows why parts 4 and 5 were designed to be separate pieces. Because of torsion, the gradient of stress varies in lateral direction as well as longitudinal direction, which is not proper for the beam that FBGs are installed on. The stress distribution along the beam is shown in

Figure A.5b when part 4 and part 5 are connected with four set screws in order to apply concentrated force at contact points (Figure A.5c).

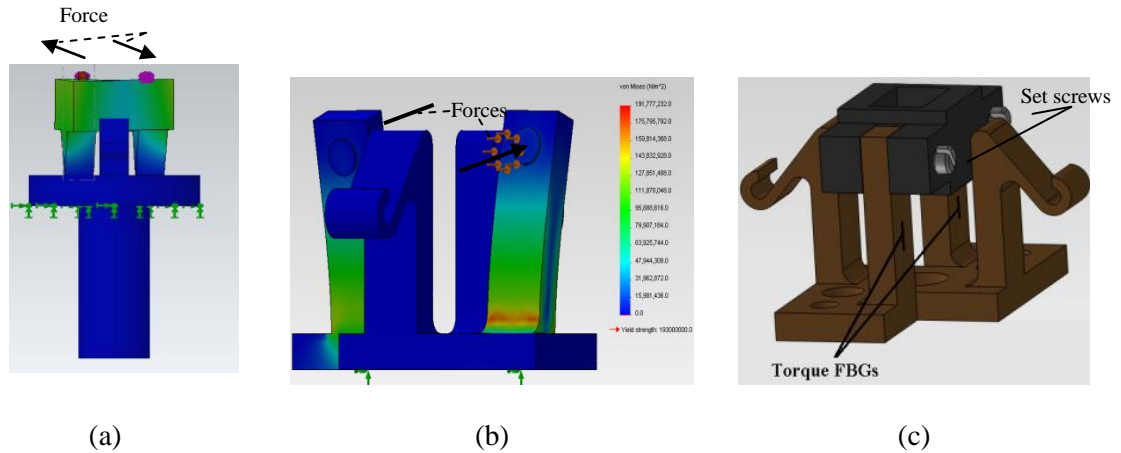


Figure A. 5: FE analysis for the active elements involved in axial torque measurement: (a) Stress distribution when part 4 and part 5 are one piece, (b) stress distribution when two separate parts are used for torque transfer, and (c) close-up view of parts 4 and 5. Set screws ensure a concentrated force distribution.

A.3 Sensor fabrication and FBG installation

Since the sensor is not a rigid structure and a simple calibration procedure is sought for sensor calibration due to the decoupled structure of the sensor, the dimensional and geometrical tolerances of the parts can affect the performance of the sensor. Therefore, a precise fabrication technology should be used, especially for the active element.

Figure A.6a illustrates five different pieces of the active element cut with wire EDM machine and were attached together using high strength (2600 psi) plastic steel epoxy (ITW Devcon, Danvers, MA). Figure A.6b shows an exploded view of the manufactured parts. For the active element, phosphor bronze was used. Other metallic parts were made of brass. The casings were made of ABS material using rapid prototyping.

The ball bearing is made of ceramic. Figure A.7a demonstrates the fabricated and assembled sensor. Figure A.7a shows that the size of our sensor is small. Figure A.7b shows the final sensor which is ready to be plugged into the interrogator for use.

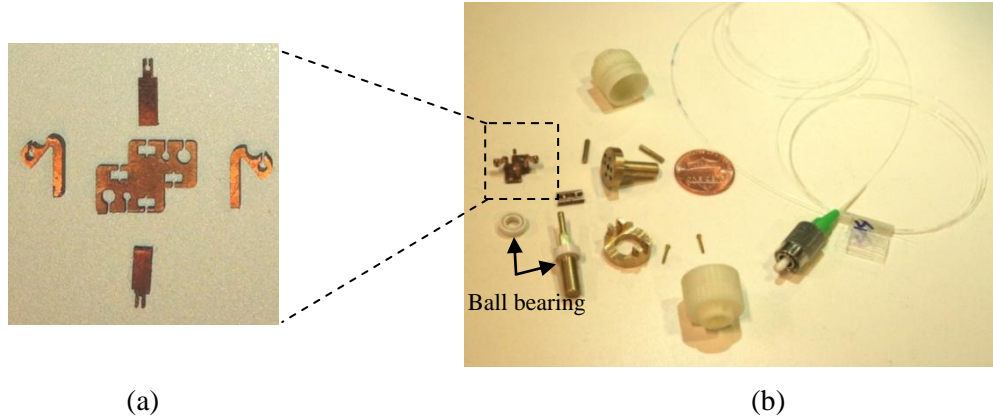


Figure A. 6: (a) Different pieces of the active element were fabricated by wire EDM and were glued to each other, (b) The exploded view of the final fabricated parts (see Figure A.3a for labels of each part).

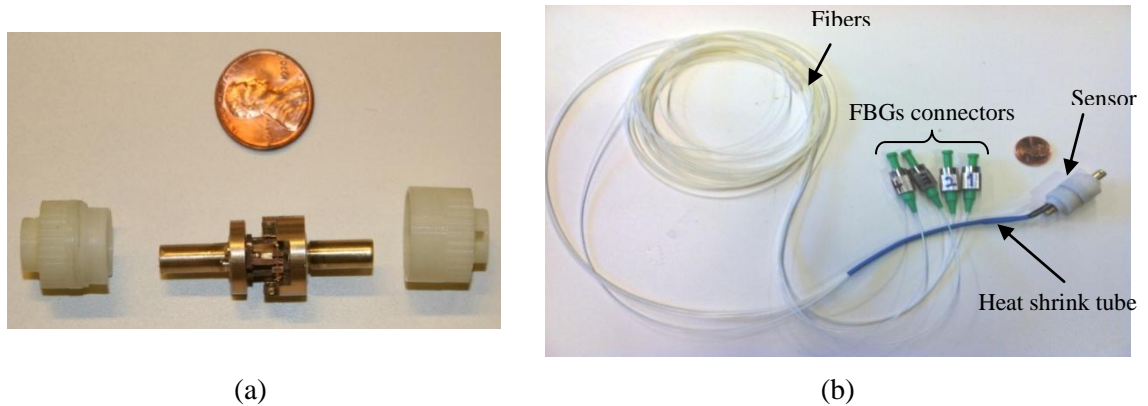


Figure A. 7: (a) Assembled sensor (without FBG), (b) Sensor prototype after installing the FBGs.

The proper design of the sensor and placement of the FBGs have simplified the handling of the sensor since fibers are well secured using heat shrink tubes (Figure A.7b).

A.4 Sensor calibration and results

Our sensor is structurally decoupled and as a result, it was easy to be calibrated. A small size lathe (Model 4410, Sherline Products, Inc., Vista, CA, USA) was used to calibrate the sensor. We needed two DOFs for our calibration setup, one axial motion and one axial rotation to apply axial force and torque to the sensor. As shown in Figure A.8a, a commercial 6-DOF Nano 17 sensor (ATI Industrial Automation, Apex, NC, USA) was used as a ground truth for calibration. Nano 17 sensor and our MRI-compatible sensor were attached in series by using a flexible coupling to protect both sensors against overload. This set of sensors was fixed to the lathe machine between lathe jaw chuck and tailstock chuck as an integrated part. Then, it was possible to apply torque to the sensors by applying torque to the jaw chuck and to apply axial force by moving the tailstock chuck in lathe's axial direction by rotating the handwheel.

Figure A.8b shows the complete setup for our sensor calibration procedure. FBGs were connected to the interrogator (sm 130, Micron Optics, Inc., Atlanta, GA) and the interrogator was connected to the laptop/Matlab via Ethernet port. The Nano 17 sensor was connected to the laptop/Matlab via a Galil 2143 controller (DB 28040, Galil Motion Control, Rocklin, CA, USA) as the data acquisition system. The 2143 Galil controller was equipped with a daughter board DB-28040 to read Nano 17 analog signals in single-ended configuration. In a program written in G-code (the language of Galil controller), calibration matrix was multiplied by the analog inputs in order to produce force and torque in different directions (i.e. x , y , and z). The outputs of the Nano 17 sensor and MRI-compatible sensor were processed in Matlab software to estimate the calibration matrix.

For calibration of the axial force, we used the handwheel to move the tailstock chuck and to increase the axial force gradually. The output of the Nano 17 sensor was plotted versus $\Delta\lambda_1$. The

slope of the obtained calibration line was considered as the calibration coefficient, i.e. $F_{\text{MRI Sensor}} = C_1 \cdot \Delta\lambda_1$, where C_1 is the above mentioned coefficient. The same procedure was conducted for the calibration of the axial torque.

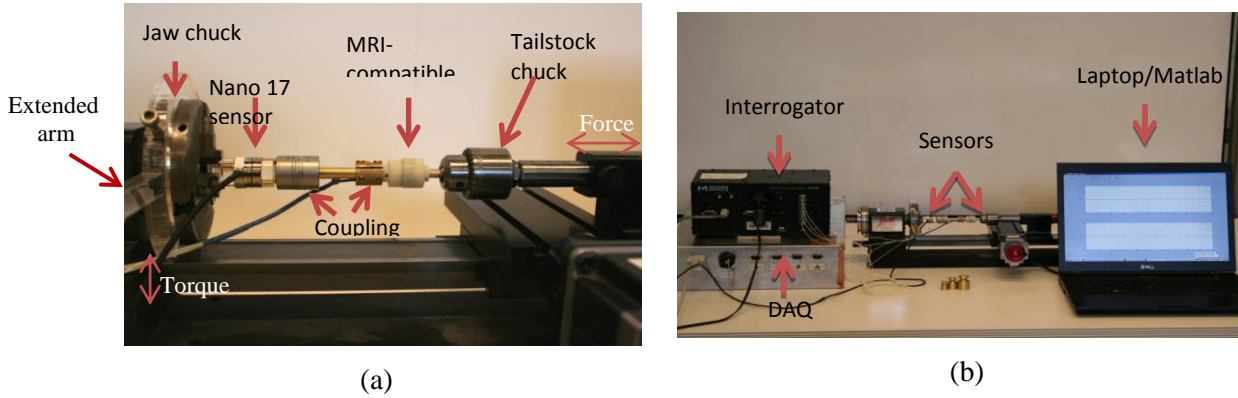


Figure A. 8: Calibration setup: a) close-up view of sensors and b) overall view.

For this case, a range of standard weights were used to apply torque on the jaw chuck by an extended arm. The axial force and torque were applied in both directions. Figures A.9a and Figure A.9b show the calibration results for the axial force and axial torque, respectively.

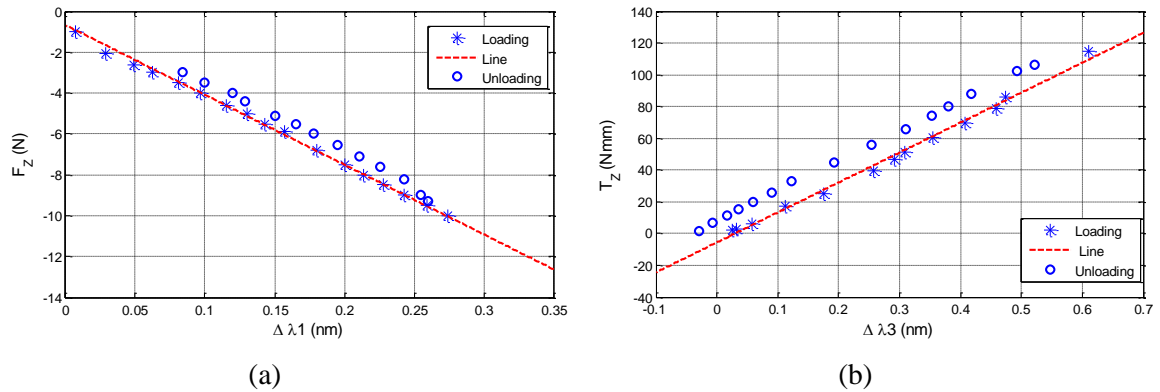


Figure A. 9: Calibration results: (a) axial force and (b) axial torque.

Figure A.9 show linear behavior of the sensor for axial force and axial torque loading and unloading. In these figures, there are some shifts between loading and unloading both in axial force and axial torque which should not be mistaken with hysteresis. These shifts are because of several reasons: 1) installation of the FBGs on two beams instead of four beams that caused asymmetric structure and made the sensor sensitive to lateral force and force distribution, 2) manufacturing errors especially, an undesired clearance between part 1 and 6 (Figure A.3) which caused undesired sensitivity of the sensor to lateral forces, and 3) the assembling inaccuracy of the sensors in the calibration setup which can lead to lateral forces.

A.5 Conclusions

A structurally inherent decoupled MRI force/torque sensor was designed, fabricated, and calibrated to be used in a master-slave needle steering procedure under real-time MRI utilizing Fiber Bragg Grating technology. Mechanically decoupled sensor prevented interference of force and torque in different directions, thus making calibrated easier. Sensor design requirements were studied and two designs were proposed and compared. Finally FE analysis was performed to finalize the configuration and dimensions of the preferred design. The proposed sensor was fabricated and calibrated using a commercial force/torque sensor. The calibration results show linear behavior of the sensor, but it also demonstrates a shift in the diagram in loading and unloading which was due to manufacturing errors and calibration setup and will be addressed in the future.

References

- [1] R. Seifabadi, I. Iordachita and G. Fichtinger, "Design of a teleoperated needle steering system for MRI-guided prostate interventions," in *Biomedical Robotics and Biomechatronics (BioRob), 2012 4th IEEE RAS & EMBS International Conference on*, 2012, pp. 793-798.
- [2] R. Seifabadi, N. B. J. Cho, S. E. Song, J. Tokuda, N. Hata, C. M. Tempany, G. Fichtinger and I. Iordachita, "Accuracy study of a robotic system for MRI - guided prostate needle placement," *The International Journal of Medical Robotics and Computer Assisted Surgery*, 2012.
- [3] J. Tokuda, S. E. Song, G. S. Fischer, I. I. Iordachita, R. Seifabadi, N. B. Cho, K. Tuncali, G. Fichtinger, C. M. Tempany and N. Hata, "Preclinical evaluation of an MRI-compatible pneumatic robot for angulated needle placement in transperineal prostate interventions," *International Journal of Computer Assisted Radiology and Surgery*, vol. 7(6), pp. 949-957, 2012.
- [4] H. Su and G. S. Fischer, "A 3-axis optical force/torque sensor for prostate needle placement in magnetic resonance imaging environments," in *Technologies for Practical Robot Applications, 2009. TePRA 2009. IEEE International Conference on*, 2009, pp. 5-9.
- [5] M. Tada, S. Sasaki and T. Ogasawara, "Development of an optical 2-axis force sensor usable in MRI environments," in *Sensors, 2002. Proceedings of IEEE*, 2002, pp. 984-989.

- [6] D. Chapuis, R. Gassert, L. Sacher, E. Burdet and H. Bleuler, "Design of a simple MRI/fMRI-compatible force/torque sensor," in *Intelligent Robots and Systems, 2004.(IROS 2004). Proceedings. 2004 IEEE/RSJ International Conference on*, 2004, pp. 2593-2599.
- [7] M. Tada and T. Kanade, "Design of an MR-compatible three-axis force sensor," in *Intelligent Robots and Systems, 2005.(IROS 2005). 2005 IEEE/RSJ International Conference on*, 2005, pp. 3505-3510.
- [8] T. Tokuno, M. Tada and K. Umeda, "High-precision mri-compatible force sensor with parallel plate structure," in *Biomedical Robotics and Biomechanics, 2008. BioRob 2008. 2nd IEEE RAS & EMBS International Conference on*, 2008, pp. 33-38.
- [9] P. Puangmali, K. Althoefer and L. D. Seneviratne, "Novel design of a 3-axis optical fiber force sensor for applications in magnetic resonance environments," in *Robotics and Automation, 2009. ICRA'09. IEEE International Conference on*, 2009, pp. 3682-3687.
- [10] P. Polygerinos, P. Puangmali, T. Schaeffter, R. Razavi, L. D. Seneviratne and K. Althoefer, "Novel miniature MRI-compatible fiber-optic force sensor for cardiac catheterization procedures," in *Robotics and Automation (ICRA), 2010 IEEE International Conference on*, 2010, pp. 2598-2603.
- [11] X. Tan, B. Yang, R. Gullapalli and J. P. Desai, "Triaxial MRI-compatible fiber-optic force sensor," *Robotics, IEEE Transactions on*, vol. 27, pp. 65-74, 2011.
- [12] I. Iordachita, Z. Sun, M. Balicki, J. Kang, S. Phee, J. Handa, P. Gehlbach, R. Taylor. A sub-millimetric, 0.25 mm resolution fully integrated fiber-optic force-sensing tool for

retinal microsurgery. *International Journal of Computer Assisted Radiology and Surgery (IJCARS)*, vol. 4(4), pp. 383–390.

- [13] K. O. Hill, and G. Meltz, "Fiber Bragg grating technology fundamentals and overview," *Journal of Lightwave Technology*, vol. 15(8), pp. 1263–1276 (1997).
- [14] Y. L. Park, S. Elayaperumal, B. Daniel, S. C. Ryu, M. Shin, J. Savall, R. J. Black, B. Moslehi and M. R. Cutkosky, "Real-time estimation of 3-D needle shape and deflection for MRI-guided interventions," *Mechatronics, IEEE/ASME Transactions on*, vol. 15, pp. 906-915, 2010.

Appendix B

The materials presented in this Appendix have been published with the citation as follows:

J. Tokuda, S. E. Song, G. S. Fischer, I. I. Iordachita, R. Seifabadi, N. B. Cho, K. Tuncali, G. Fichtinger, C. M. Tempny, and N. Hata, "Preclinical evaluation of an MRI-compatible pneumatic robot for angulated needle placement in transperineal prostate interventions," *International Journal of Computer Assisted Radiology and Surgery*, vol. 7(6), pp. 949-957, 2012.

Contributions:

I performed the robot calibration. I implemented the code for forward and inverse kinematic of the robot based on the calibration results. I performed robot workspace analysis and implemented a feature to help the clinicians ensure that the selected target and needle trajectory are within the robot's reachable workspace. I participated in the MRI phantom experiment.

Preclinical evaluation of an MRI-compatible pneumatic robot for angulated needle placement in transperineal prostate interventions

Purpose: To evaluate the targeting accuracy of a small profile MRI-compatible pneumatic robot for needle placement that can angulate a needle insertion path into a large accessible target volume. **Methods:** We extended our MRI-compatible pneumatic robot for needle placement to utilize its four degrees-of-freedom (4-DOF) mechanism with two parallel triangular structures and support transperineal prostate biopsies in a closed-bore magnetic resonance imaging (MRI) scanner. The robot is designed to guide a needle toward a lesion so that a radiologist can annually insert it in the bore. The robot is integrated with navigation software that allows an operator to plan angulated needle insertion by selecting a target and an entry point. The targeting error was evaluated while the angle between the needle insertion path and the static magnetic field was between -5.7° and 5.7° horizontally and between -5.7° and 4.3° vertically in the MRI scanner after sterilizing and draping the device. **Results:** The robot positioned the needle for angulated insertion as specified on the navigation software with overall targeting error of 0.8 ± 0.5 mm along the horizontal axis and 0.8 ± 0.8 mm along the vertical axis. The two-dimensional root-mean-square targeting error on the axial slices containing the targets was 1.4 mm.

Conclusions: Our preclinical evaluation demonstrated that the MRI-compatible pneumatic robot for needle placement with the capability to angulate the needle insertion path provides targeting accuracy feasible for clinical MRI-guided prostate interventions. The clinical feasibility has to be established in a clinical study.

B.1 Introduction

MRI-guided prostate biopsy and brachytherapy are active areas of research [1]–[16], reflecting a strong demand for the precise and minimally invasive care of prostate cancer. It is the most common cancer among men in the United States [17]. Although transrectal ultrasound (TRUS) [18] and [19] is the current standard modality for guiding biopsy and brachytherapy, MRI is ideal due to its excellent visualization of the prostate gland, focal lesions, and surrounding prostatic tissues. MRI is particularly useful if combined with a transperineal approach because it provides better access to the anterior and apical regions of the prostate [20] and can be applied to patients who cannot undergo TRUS-guided biopsy due to previous total colectomy. Given that the MRI-guided approach includes angulated needle paths, it can avoid pubic arch interference; thus, it also offers the ability to treat large volume glands that are too large for TRUS-guided procedures. Researchers have been continuously demonstrating the clinical feasibility of transperineal prostate biopsy and brachytherapy guided by intraprocedural MRI [1], [2], [5], [13], and [14]. One of the major challenges in MRI-guided transperineal prostate interventions is performing procedures in the in-bore space of an MRI scanner and taking full advantage of the intraprocedural imaging to precisely guide a needle to the target. Unfortunately, a conventional 60-cm closed-bore MRI scanner does not allow keeping the patient in the lithotomy position with the legs widely open for easy access to the perineum. Therefore, the patient table is repeatedly withdrawn from the scanner bore: inside for imaging and outside for needle placement, unless a wide-bore MRI scanner is used [16] and [21]. This precludes the ability to monitor the needle insertion process using real-time MRI, which is becoming available in modern MRI scanners [21]–[23]. To assist transperineal procedures in the bore, several groups have developed MRI-compatible robotic devices to numerically guide a needle into the prostate. This idea was first

demonstrated in an open-configuration MRI scanner [24] and [25] and then adapted to closed-bore MRI systems [26]–[28]. These robotic devices, however, do not secure a workspace for a physician to safely access the perineum. Even for robots equipped with needle insertion and tissue sampling or seed deployment mechanisms for a fully automated process, it is crucial to secure safe access to the patient in the bore. To address these issues, we have been developing an MRI-compatible pneumatic robot for needle placement with a 4-DOF parallel kinematic structure that effectively utilizes the space under the legs of the patient in the lithotomy position [29] and [30]. The robot is designed to guide a needle toward a lesion so that a radiologist can manually insert it in the bore. The parallel kinematic structure can position a needle in parallel to the static magnetic field as well as with angulation from the field. While most targets in the prostate can be reached without angulation as practiced in conventional transperineal interventions with needle-guiding templates, some targets require angulated needle placement because of obstacles, for example the pubic arch. Those targets cannot be reached by using needle-guiding templates, because they only guide the needle in parallel to the MRI scanner’s B_0 field. In spite of its small profile, the robot has kinematics that achieves a range that sufficiently covers the entire prostate gland of most patients by providing the capability to angulate the direction of needle insertion with respect to the static magnetic field. In this study, we extended the user interface of our robot to allow a physician to plan angulated needle insertions by fully utilizing our unique 4-DOF parallel kinematic structure. Although the kinematic structure was designed for an angulated insertion, it has never been validated with an MRI scanner in our past studies [29]–[31] due to the lack of a practical user interface to plan an angulated needle insertion intuitively. The user interface was integrated with our navigation software, 3D Slicer with ProstateNav software plug-in module, which has been used in our ongoing clinical trial of MRI-guided manual prostate

biopsy using a template [23]. We performed a preclinical evaluation of the robot in the same setting as a clinical procedure, including sterilization and draping, and examined if the robot can achieve the targeting accuracy required for transperineal prostate biopsy [9].

B.2 Materials and Methods

B.2.1 Pneumatic robot with 4-DOF parallel kinematic structure

Figure B.1 shows the overview and configuration of the robot with the 4-DOF parallel kinematic structure. The robot has two parallel triangular planar positioning mechanisms parallel to the axial plane of the scanner: one positioned at the front of the robot (front triangular mechanism), facing the perineum, and the second on the feet side of the robot (back triangular mechanism). Those triangular mechanisms are connected by a linkage, which functions as a needle insertion platform. Four pneumatic linear actuators are placed in parallel to the static magnetic field under the kinematic structure to drive the front and the back triangular mechanisms independently. The linear actuation is transmitted to the in-plane positioning of the front and back triangular mechanisms using timing belts. Subsequently, mechanically connecting the summit of the triangular mechanisms (ball joint connections) creates the needle insertion axis, resulting in a 4-DOF angle guide (needle insertion and rotation about its axis are not actuated). The pneumatic linear actuators can be physically locked by brake mechanisms to prevent the robot from accidentally moving during the needle insertion process due to human, software, or electrical errors. Most of the robot's components are constructed of fully MRI-compatible plastic, with a minimal amount of nonferrous metal including brass (alloy 260 and 360) and anodized aluminum (alloy 6061) to avoid eddy currents and deterioration of magnetic field homogeneity. The linear motion of four pneumatic linear actuators is transmitted to the two triangular mechanisms for

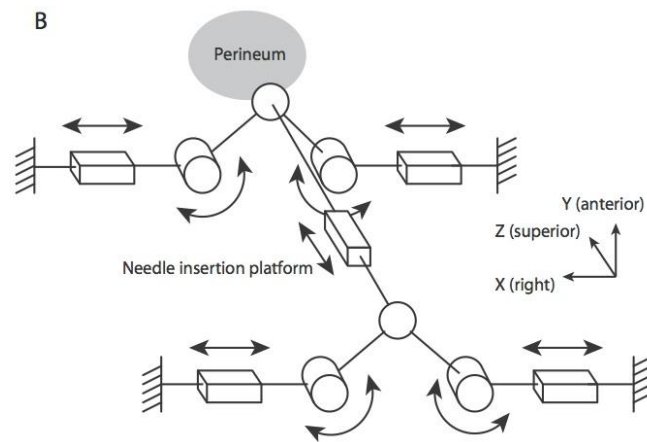
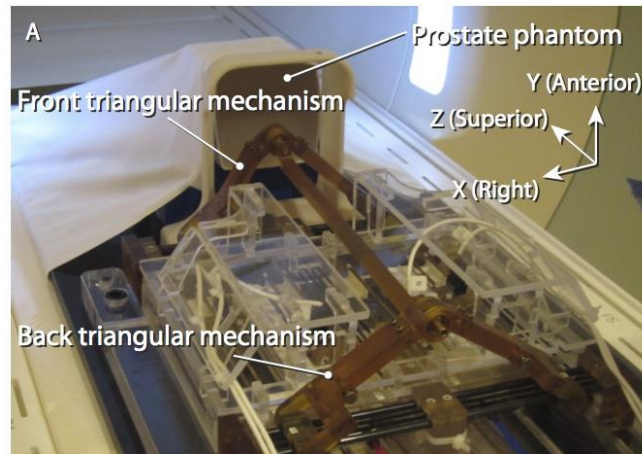


Figure B. 1: 4-DOF pneumatic robot: (a) The photo shows an overview of the 4-DOF MRI-compatible pneumatic needle placement robot and the agar phantom placed on the patient table of the MRI scanner. The phantom was removed from the scanner during the needle placement in the experiment and (b) The robot with 4-DOF parallel kinematic structure has two identical triangular planar positioning mechanisms that move within the x - y plane (axial in patient coordinate system) and are connected by a linkage as a needle insertion platform. The needle is manually inserted into the prostate through the perineum after the robot positions and orients the needle insertion platform.

planer motion via timing belts (MXL type, trapezoidal teeth, urethane body, Kevlar core, 1/8" width, 0.08" pitch) and pulleys (MXL type, 1/8" width, 0.08" pitch, aluminum body, brass setscrew). Ultem and cast acrylic are used for most of the robot structure, and some parts are fabricated from commercial Stereolithography Apparatus (SLA) rapid-prototype service using Acura ® 60 plastic (Acu-Cast Technologies, LLC, Lawrenceburg, TN). Optical encoders with shielded differential signals (EM1-0-500-I, US Digital, Vancouver, WA) are used to sense the pneumatic actuator positions.

B.2.2 System configuration

The system consists of the following primary components (Figure B.2): (1) the robot with in-room robot controller for low level servo control; (2) navigation workstation that allows physician and operator to visualize the anatomy and robot workspace and to define targets and entry points for needle placement on MR images transferred from the scanner; (3) 3 Tesla MRI scanner (MAGNETOM Verio, Siemens Healthcare, Erlangen, Germany). The robot controller is equipped with a computer running Linux-based real-time operating system (RTLinux, Wind River Systems, CA), four pairs of piezoelectric pressure regulator valves to control each of the four pneumatic actuators, and a fiber-optic Ethernet interface enclosed in an EMI-shielded Faraday cage. The controller is connected to the medical air supply connector on the wall of the scanner room to pneumatically drive the robot. Electric power is supplied through a grounded and filtered patch panel on the wall of the scanner room. Thus, the controller can be operated inside the scanner room, approximately 3 m from the isocenter of the MRI scanner without interfering with imaging, while communicating with the navigation workstation located outside of the scanner room [27] during image acquisition. The navigation workstation is a Linux-based workstation running open-source medical image computing and visualization software, 3D Slicer

[32]. The 3D Slicer software incorporates a plug-in module that adds functionalities to plan targets on an intraprocedural MRI, registers the robot to an image coordinate system using a specially designed fiducial marker [22], and sends the coordinates of the planned target to the robot controller through a network using the OpenIGTLink protocol [33]. The navigation workstation also runs a Digital Imaging and Communication in Medicine (DICOM) listener (DCMTK¹¹) to receive intraprocedural MRI from the host computer of the MRI scanner through the network. The robot controller and the navigation workstation are connected via the fiber-optic network, while the navigation workstation and the host computer of the MRI scanner are connected via 1000-Base T Ethernet.

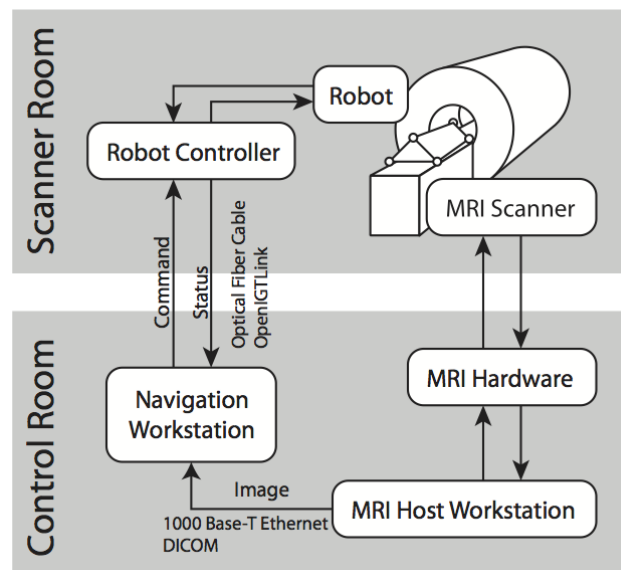


Figure B. 2: System architecture and components: The configuration of the robot system for MRI-guided prostate interventions. Robot controller for low-level servo control of the robot is placed in the scanner room, while the navigation workstation is placed next to the host workstation of the MRI scanner system in the control room. Optical fiber Ethernet is used for network communication between the robot controller and navigation workstation to shut off electromagnetic (EM) noise from outside of the EM shielded scanner room.

¹¹ <http://dicom.offis.de/>

B.2.3 User interface for needle insertion path planning

Figure B.3 shows the graphical user interface used to define a needle insertion path on the navigation software. The interface provides two methods to specify needle insertion paths: (1) “parallel insertion”, which is parallel to the static magnetic field, by specifying a target point in the prostate on an intraprocedural MRI; (2) “angulated insertion”, by specifying a needle insertion point on the perineum and a target point to define the intended insertion angle. The navigation

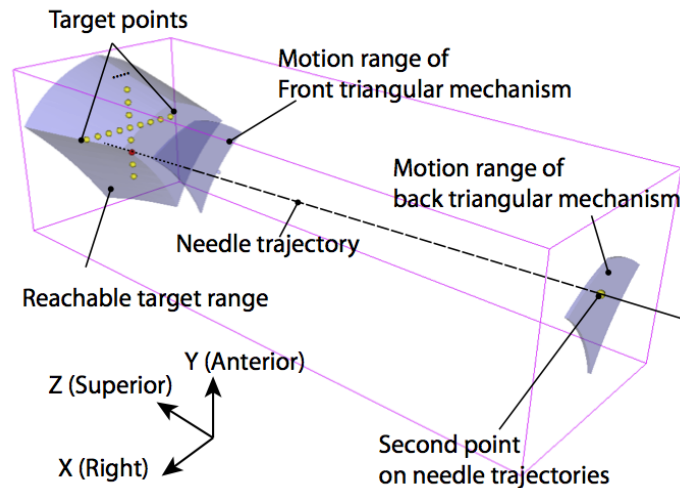


Figure B. 3: The screenshot of the navigation software based on 3D Slicer shows the 3D models representing reachable target range and motion range of the front and back triangular-shaped links.

software calculates the orientation of the needle insertion based on the two points specified and sends it to the controller in a quaternion. Before actual robot operation, the software also overlays 3D models representing a volume reachable by the needle tip onto the images to confirm that the target and the needle insertion angle are within the range of motion of the robot. This feature will

allow the physician and operator to decide whether to reposition the robot or the patient before starting the procedure.

B.2.4 Targeting experiment

Targeting accuracy of the angulated insertion was evaluated in the 3T MRI scanner as follows:

Table setup: We placed a prostate intervention tabletop setup with built-in leg supports that allows the subject to be positioned in feet-first lithotomy position in the scanner. The tabletop setup has been used in our ongoing clinical trial of MRI-guided prostate biopsy [16] and [21]. The tabletop consists of a baseboard, leg holders, and attachments to fix the robot and a Z-frame fiducial marker [22] and [23]. The baseboard is made of a cotton-resin plate designed to fit on the patient table of the MRI scanner. The leg holders, attach to the baseboard by an adjustable attachment, keep the legs apart and are raised to secure the workspace between the legs. Two saline phantoms in bottle containers were placed on the right and left of a cubical free space with a dimension of approximately $100 \times 100 \times 100$ mm, the anticipated location of the prostate in a clinical case. The needle can be placed in this cubical free space in this experiment.

Calibration: We first registered the robot to the image coordinate system by localizing the Z-frame fixed to the tabletop as previously described [22] and [23]. The Z-frame has seven rigid MR-visible marker tubes with 7.5 mm inner diameters filled with a contrast agent (MR Spots, Beekley, Bristol, CT, USA) placed on three adjacent faces of a 60 mm cube, thus forming 7 bright spots on an axial image. The navigation software automatically detects the seven rigid tubes on cross sectional MR images of the Z-frame acquired with the 2D Fast Spin Echo imaging sequence for calibration (TR/TE: 3,000/116 ms; acquisition matrix: 256×256 ; echo train length: 27; flip angle 140° ; field of view: 160×160 mm; slice thickness: 2 mm; receiver bandwidth: 250

Hz/pixel; acquisition time: approx. 1min). After localization of the Z-frame, it was replaced by the robot so that the robot was registered to the image coordinate system.

Robot setup: To take any factor that may impact the targeting accuracy into account, we tested the robot in a clinical setting. As shown in Figure B.4, we draped the base of the robot with a sterilized plastic cover designed for use in clinical cases. The base of the robot includes all but the top ball joints of the front and back triangular mechanisms, which guide the needle, and the top linkage with the needle insertion platform. Sterilization of those parts was validated and certified (Nelson Laboratories, Salt Lake City, UT, USA) for the full STERRAD_ NX advanced short sterilization cycle to a sterility assurance level (SAL) of $\leq 10^{-6}$ using the biological indicator (BI) overkill method. The sterilized parts were not attached to the robot until the base part of the robot was draped after being placed onto the tabletop.

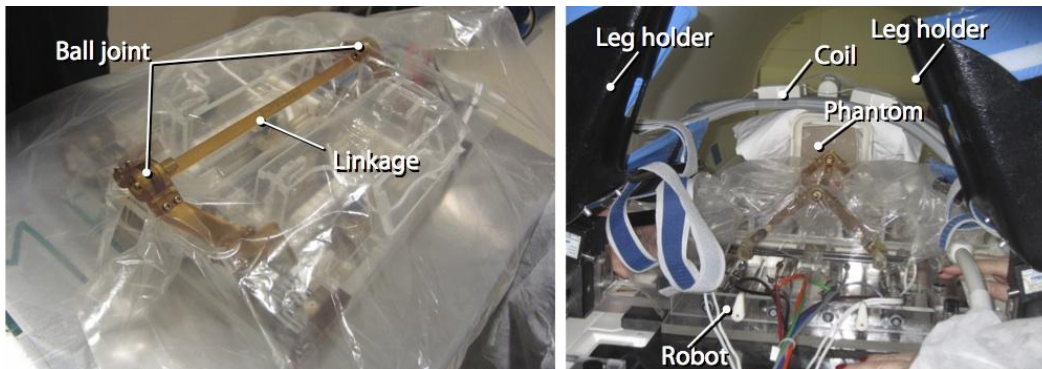


Figure B. 4: Robot sterilization: The robot was draped with a transparent plastic cover for sterilization of the interventional workspace. Only the base of the robot, which is not sterilizable, is draped. The linkage that connects the two triangular mechanisms and the ball joints that hold the needle were sterilized before the procedure and attached to the base part of the robot. The four links of the front and back triangular mechanisms penetrate the cover.

Planning: A multi-slice planning image of the phantom was acquired using a TSE sequence (TR/TE: 5, 250/100 ms; acquisition matrix: 320×224 ; echo train length: 20; flip angle 150° ; field of view: 140×140 mm; slice thickness: 3 mm; receiver bandwidth: 203 Hz/pixel) that has been used for intraoperative imaging in our ongoing clinical trial. The acquired images were transferred to the navigation workstation and loaded into the software. On the planning image, we defined 16 targets in the cubical space; eight were aligned along the vertical axis, and eight were aligned along the horizontal axis, as shown by the points in Figure B.3. The targets were placed every 10 mm for the both vertical and horizontal lines. All targets were placed on the same plane to avoid an error variation due to differences in needle insertion depth and to reveal the relationship between the needle placement error and the angulation. The distance between the plane and the Z-frame was 100 mm, which is a typical distance between the Z-frame and targets in the prostate in our ongoing clinical trial of manual MRI-guided prostate biopsy. In addition, one fixed point was defined in the motion range of the back triangular mechanism as a remote center of the needle angulation for evaluation purposes - this point was selected to generate upward insertion paths as would be required to avoid the pubic arch, not as a putative entry point. The distance between the fixed point and the plane that includes the targets was 400 mm. The fixed point was aligned to the cross point of the vertical and horizontal rows of the targets as shown in Figure B.3, resulting in angulated insertion with ranges of $[-5.7^\circ, 5.7^\circ]$ horizontally and $[-5.7^\circ, 4.3^\circ]$ vertically. The needle insertion paths were calculated based on those points and transferred to the controller, where the inverse kinematics of the robot was computed. The robot moved the needle guide to align with each target position and orientation. In the future clinical applications, the physician and operator will confirm that the target and the needle insertion angle are within the range at this stage and decide whether to reposition the robot or the patient before

proceeding to the next step. If the robot needs to be repositioned, the operator will perform the calibration and robot set up steps again.

Needle placement: Before we positioned the robot at each target, we positioned it at a randomly selected target to take positioning errors due to large robot motion into account. Once the needle insertion path was confirmed on the navigation software, the kinematic structure was physically locked with the brake safety mechanisms. An 18G \times 15 cm MRI-compatible core biopsy needle (MRI Bio Gun, E-Z-EM, Westbury, NY, USA) was manually inserted through the robot's guide sleeve to the needle insertion depth determined by the controller and placed in the cubical free space. The tip of the needle was covered by an MR-visible marker (MR Spots, Beekley, Bristol, CT) to identify the tip of the needle in the cubical free space on confirmation images without inserting the needle into a phantom, which often leads to a needle placement error due to needle deflection. The tip of the needle was identified as a signal void within the marker on the MR images acquired from planes perpendicular to the needle (Figure B.5).

Validation: A confirmation image of the needle in the target location was acquired using a multislice TSE sequence (TR/TE: 3,000/106 ms; acquisition matrix: 320 \times 200; echo train length: 27; flip angle 140 $^\circ$; field of view: 280 \times 224 mm; slice thickness: 2 mm; receiver bandwidth: 252 Hz/pixel) after each needle insertion. The center of signal void of the MR-visible marker due to the existence of the needle was identified as the location of the needle manually on the same slice as the target (Figure B.5). The two-dimensional (2D) needle placement error was evaluated by measuring the distance between the defined target and the center of the needle.

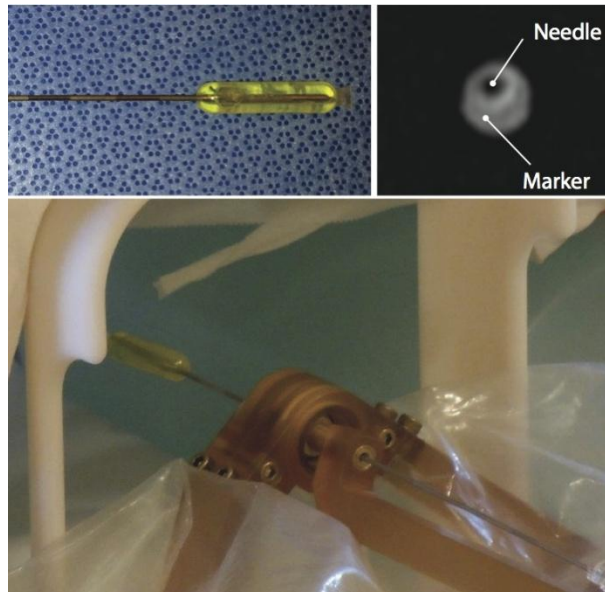


Figure B. 5: MRI needle placement accuracy: the tip of the needle was covered by an MRI-visible marker (upper left) so that the tip of the needle can be identified as an artifact on an MR image acquired from a plane perpendicular to the needle (upper right). The bottom photo shows the needle with the marker placed at the target by the robot.

B.3 Results

We can specify the target points with angulation with the newly developed software, achieving a wider range of motion than our previous system, which only allowed parallel insertion. The robotic controller successfully positioned the needle holder with angulated insertion as specified on the navigation software. All needle placements for 16 targets were carried out successfully with target errors less than 3.1 mm. The calibration process was completed instantly without any failure. Figure B.6 shows the relationship between the targeting error and the angle of the needle from the static magnetic field. The overall targeting error was 0.8 ± 0.5 mm along the horizontal x axis and 0.8 ± 0.8 mm along the vertical y axis. The 2D root-mean-square (RMS) targeting error evaluated on the same axial slices as the targets was 1.4 mm. The total procedure time for 16

targets was 99 min, including MR imaging. The time to set up the system and the phantom in the scanner was 31 min. The Z-frame image and the planning image were acquired in 6 min. The calibration was performed during the acquisition of the planning image. The planning process lasted approximately 5 min. The mean duration for targeting, including selection of the target and positioning of the needle, was 128 ± 59 s.

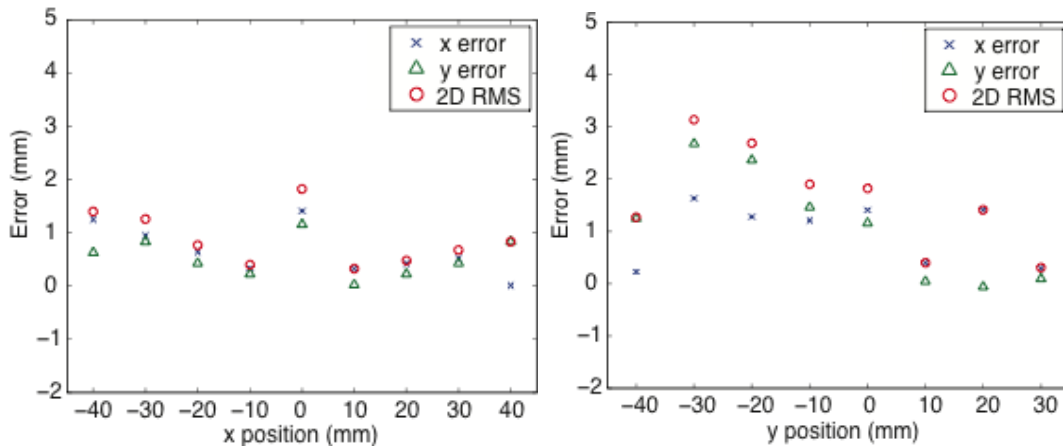


Figure B. 6: Accuracy results: the plots show the error of needle placement in the x-axis (horizontal: right-left axis of the patient) and y-axis (vertical: anterior-posterior axis of the patient) with respect to the needle angle from the static field.

B.4 Discussion

In this study, we demonstrated our MRI-compatible needle placement robot with angulated needle placement capabilities and evaluated the targeting accuracy in the MRI scanner. The capability to place a needle with angulated insertion paths is particularly useful when a target in the prostate is not reachable from the perineum with a parallel insertion due to the limited range of target or obstacles between the perineum and the target. Angulated insertion allows the anterior gland to be reached avoiding the pubic arch for large volume glands, for example. The targeting

accuracy with angulated insertion was comparable to parallel insertion (1.3 mm) we evaluated in our previous study [31]. Although the study is limited to the evaluations of single oblique (either horizontal or vertical) angulation, we expect the targeting accuracy with a double oblique angulation will be strongly affected by the vertical angulation, because the targeting error was relatively constant for the horizontal angulation. It is also expected that the vertical and horizontal angulations will not affect each other, because they can be decomposed in the difference and the mean displacements of the two linear actuators for the front triangular structure if the back triangular mechanism is fixed as a remote center of rotation.

Targeting errors in prostate biopsies performed with 18G needles in previously published clinical studies were 6.5 mm for a transperineal approach with a needle-guiding template [9] and 5.8 mm for a transrectal approach with a commercially available device [15]. Although we did not take into account deflection of the needle in this study, we expect that the targeting accuracy of 1.4 mm is within an acceptable range for clinical applications, given the targeting accuracies in the existing studies and the contribution of needle deflection evaluated in a previous study using animal tissues, which revealed that the contribution of needle deflection was 0.6 mm for bovine liver and 1.1 mm for bovine muscle tissue at the target 120 mm from the entry point with an 18-gauge symmetrical bevel needle [9]. It should also be noted that the targeting accuracy of 1.4 mm is beyond the theoretical limit for a conventional needle-guide template with a 5-mm interval. The needle placement accuracy we found in this study is comparable to other preclinical studies on image based evaluation of MRI-compatible robots, which have been used clinically: Schouten *et al.* achieved needle placement accuracy of 3.0 mm with their pneumatic robot for transrectal biopsy [34]; Krieger *et al.* published their robotic system with hybrid tracking for transrectal biopsy with needle placement accuracy of 1.5 mm [35]; Nuntener *et al.* reported that their MRI-

compatible robot for fully automated transperineal seed placement achieved seed placement accuracy of 0.72 mm [36]. Besides deflection of the needle, there are other factors that may degrade the targeting accuracy of our robot for needle placement. First, air/tissue interfaces near the imaging volume and deoxygenated blood potentially distort the static magnetic field, causing inaccurate localization of targets and the Z-frame; the prostate is adjacent to the rectal wall and also close to the perineum; the Z-frame is placed in a narrow free space surrounded by the thighs and the perineum of the patients. However, it is still important to validate such an effect with a human subject. Second, shrinkage of the plastic mechanical parts due to repeated sterilization may lead to mechanical inaccuracy. It is important to select a sterilization method that has a minimum impact on the robot's material and to evaluate it thoroughly with the device before clinical application. Our recent work has shown that the selected sterilization method did not affect the needle positioning accuracy in a laboratory setting [37]. Third, the targets cannot be assumed to stay at the same position throughout, because the patient moves during the procedure. The positions of the targets have to be updated. This can be achieved by registering the initial planning image and the images acquired for verification of needle placement. Such an imaging protocol is clinically feasible: our previous report on a clinical trial of manual MRI-guided prostate biopsy with a needle guiding template demonstrated that a multi-slice turbo spin echo image of the prostate can be acquired after each needle insertion without noticeable image distortion caused by the location of the needle. This image can be used for evaluation of error between the designated target position and the actual needle position [21]. We found one unanticipated issue with angulated insertion that we had not encountered in our previous studies: a larger needle insertion angle was associated with a larger targeting error in the vertical direction. This can be explained by the nature of our triangular kinematics: the ratio of vertical

displacement of the triangular mechanism to the displacement of the pneumatic linear actuator is larger at the lower range than the higher range; therefore, a larger error can be observed at the lower position if the back triangular mechanism is fixed. Furthermore, if the front and back triangular mechanisms are positioned independently to angulate the needle, the overall error in the front or back triangular mechanism is geometrically scaled up at the tip of the needle. Because the relationship between displacement of the actuator/encoder and the tip of the triangular mechanism is not linear, calibration of the encoder at the zero position of the triangular mechanism is critical. Further testing is required to tune the kinematic software to improve the calibration accuracy. We also found that the use of drape with the device in the preclinical evaluation is crucial to identify any possible problems in the clinical workflow before a clinical trial. We experienced a reduction in the range of needle placement due to insufficient slack of the drape during our rehearsal session before the experiment. If the drape is not properly attached, it might be trapped by the mechanism, impeding normal operation. Pubic arch interference has been a major technical limitation during transperineal prostate interventions, especially for the anterior and lateral portion of the prostate. Although we only evaluated needle angulations of approximately 5° by fixing the back triangular mechanism, the robot can achieve angulation of more than 10° upward by lowering the back triangular mechanism. Needle angulation of 10° would dramatically reduce pubic arch interface; Tincher *et al.* reported that the mean maximum interferences in patients in lithotomy position with 0° and 20° needle angulations were 7.8 and 1.0 mm, respectively [38]. Because of the linear trend between targeting error and angulation shown in Figure B.6, we expect that the targeting accuracy at the maximum angulation would still be the same level as manual needle placement with template [9]. There are a number of MRI-compatible actuator technologies, such as pneumatic stepping motors [39] and [40], air motors [41],

ultrasonic motors [42], and piezoelectric motors [43] for MRI-compatible devices. We chose the pneumatic cylinders to drive our parallel triangular mechanism to achieve the low-profile kinematic structure that allows the radiologist to manually insert a needle into the patient at the imaging position. Securing in-bore workspace for the radiologist is particularly important for the smooth transition from the manual procedure to the robotic procedure, and for patient safety. In conclusion, our preclinical evaluation demonstrated that the MRI-compatible pneumatic robot for needle placement with 4-DOF parallel kinematic structure provides better targeting accuracy than the theoretical limit of conventional manual needle-guiding templates even with angulated needle insertion path, suggesting that this robotic device can be used in clinical practice. The clinical feasibility has to be established in a clinical study.

References

- [1] R. Cormack, A. V. D'Amico, N. Hata, S. Silverman, M. Weinstein and C. Tempany, "Feasibility of transperineal prostate biopsy under interventional magnetic resonance guidance," *Urology*, vol. 56, pp. 663-664, 2000.
- [2] A. V. D'amico, C. M. Tempany, R. Cormack, N. Hata, M. Jinzaki, K. Tuncali, M. Weinstein and J. Richie, "Transperineal magnetic resonance image guided prostate biopsy," *J. Urol.*, vol. 164, pp. 385-387, 2000.
- [3] R. C. Susil, A. Krieger, J. A. Derbyshire, A. Tanacs, L. L. Whitcomb, G. Fichtinger and E. Atalar, "System for MR Image-guided Prostate Interventions: Canine Study1," *Radiology*, vol. 228, pp. 886-894, 2003.

- [4] C. Ménard, R. C. Susil, P. Choyke, G. S. Gustafson, W. Kammerer, H. Ning, R. W. Miller, K. L. Ullman, N. Sears Crouse and S. Smith, "MRI-guided HDR prostate brachytherapy in standard 1.5T scanner," *International Journal of Radiation Oncology* Biology* Physics*, vol. 59, pp. 1414-1423, 2004.
- [5] R. C. Susil, K. Camphausen, P. Choyke, E. R. McVeigh, G. S. Gustafson, H. Ning, R. W. Miller, E. Atalar, C. N. Coleman and C. Ménard, "System for prostate brachytherapy and biopsy in a standard 1.5T MRI scanner," *Magnetic Resonance in Medicine*, vol. 52, pp. 683-687, 2004.
- [6] S. Zangos, K. Eichler, K. Engelmann, M. Ahmed, S. Dettmer, C. Herzog, W. Pegios, A. Wetter, T. Lehnert and M. G. Mack, "MR-guided transgluteal biopsies with an open low-field system in patients with clinically suspected prostate cancer: technique and preliminary results," *Eur. Radiol.*, vol. 15, pp. 174-182, 2005.
- [7] K. Engelhard, H. Hollenbach, B. Kiefer, A. Winkel, K. Goeb and D. Engehausen, "Prostate biopsy in the supine position in a standard 1.5-T scanner under real time MR-imaging control using a MR-compatible endorectal biopsy device," *Eur. Radiol.*, vol. 16, pp. 1237-1243, 2006.
- [8] R. C. Susil, C. Ménard, A. Krieger, J. A. Coleman, K. Camphausen, P. Choyke, G. Fichtinger, L. L. Whitcomb, C. N. Coleman and E. Atalar, "Transrectal prostate biopsy and fiducial marker placement in a standard 1.5T magnetic resonance imaging scanner," *J. Urol.*, vol. 175, pp. 113-120, 2006.

- [9] P. Blumenfeld, N. Hata, S. DiMaio, K. Zou, S. Haker, G. Fichtinger and C. Tempany, "Transperineal prostate biopsy under magnetic resonance image guidance: a needle placement accuracy study," *Journal of Magnetic Resonance Imaging*, vol. 26, pp. 688-694, 2007.
- [10] T. Hambrock, J. J. Fütterer, H. J. Huisman, C. Hulsbergen-vandeKaa, J. van Basten, I. van Oort, J. A. Witjes and J. O. Barentsz, "Thirty-two-channel coil 3T magnetic resonance-guided biopsies of prostate tumor suspicious regions identified on multimodality 3T magnetic resonance imaging: technique and feasibility," *Invest. Radiol.*, vol. 43, pp. 686-694, 2008.
- [11] M. Rea, D. McRobbie, H. Elhawary, Z. T. H. Tse, M. Lampérth and I. Young, "System for 3-D real-time tracking of MRI-compatible devices by image processing," *Mechatronics, IEEE/ASME Transactions on*, vol. 13, pp. 379-382, 2008.
- [12] F. Lakosi, G. Antal, C. Vandulek, A. Kovacs, R. Garamvolgyi, O. Petnehazy, G. Bajzik, J. Hadjiev, I. Repa and P. Bogner, "Technical feasibility of transperineal MR-guided prostate interventions in a low-field open MRI unit: canine study," *Pathology & Oncology Research*, vol. 15, pp. 315-322, 2009.
- [13] C. Menard, P. Chung, J. Abed, A. Simeonov, J. Lee, K. Brock, W. Foltz, G. O'Leary, C. Elliott and M. Milosevic, "Online guidance of tumor targeted prostate brachytherapy using histologically referenced MRI," in *Proc Intl Soc Mag Reson Med*, 2010, pp. 6693.
- [14] C. Menard, D. Iupati, J. Lee, A. Simeonov, J. Abed, J. Publicover, P. Chung, A. Bayley, C. Catton and M. Milosevic, "MRI and biopsy performance in delineating recurrent

- tumor boundaries after radiotherapy for prostate cancer," in *Proc Intl Soc Mag Reson Med*, 2011, pp. 3072.
- [15] M. Schouten, J. Bomers, D. Yakar, H. Huisman, T. Scheenen, S. Misra and J. Futterer, "Transrectal MRI-guided prostate biopsy: Evaluation of a novel robotic technique," in *Proc Intl Soc Mag Reson Med*, 2011, pp. 1060.
- [16] K. Tuncali K, J. Tokuda, A. Fedorov, I. Iordachita, S. Song, S. Oguro, A. Lasso, F. M. Fennessy, Y. Tang, N. Hata, C. M. Tempany, "3T MRI-guided Transperineal Targeted Prostate Biopsy: Clinical Feasibility, Safety, and Early Results," in *Proc Intl Soc Mag Reson Med*, 2011, pp. 7-13.
- [17] R. Siegel, D. Naishadham, A. Jemal, "Cancer statistics," *CA Cancer J Clin*, vol. 62 (1), pp. 10-29, 2012.
- [18] K. K. Hodge, J. E. McNeal, M. K. Terris, T. A. Stamey, "Random systematic versus directed ultrasound guided transrectal core biopsies of the prostate," *J Urol*, vol. 142 (1), pp. 71-74, 1989.
- [19] D. S. Scherr, J. Eastham, M. Otori, P. T. Scardino, "Prostate biopsy techniques and indications: when, where, and how," *Semin Urol Oncol*, vol. 20(1), pp. 18-31, 2002.
- [20] A. O. Sartor, H. Hricak, T. M. Wheeler, J. Coleman, D. F. Penson, P. R. Carroll, M. A. Rubin, P. T. Scardino, "Evaluating localized prostate cancer and identifying candidates for focal therapy," *Urology*, vol. 72 (6), pp. S12-24.

- [21] K. Chinzei, N. Hata, F. A. Jolesz and R. Kikinis, "MR compatible surgical assist robot: System integration and preliminary feasibility study," in *Medical Image Computing and Computer-Assisted Intervention–MICCAI 2000*, 2000, pp. 921-930.
- [22] S. DiMaio, S. Pieper, K. H. Chinzei, S. Haker, D. Kacher, G. Fichtinger, C. M. Tempany, R. Kikinis, "Robot-assisted needle placement in open MRI: system architecture, integration and validation," *Comput Aided Surg*, vol. 12, pp. 15-24, 2007.
- [23] A. Patriciu, D. Petrisor, M. Muntener, D. Mazilu, M. Schar and D. Stoianovici, "Automatic brachytherapy seed placement under MRI guidance," *Biomedical Engineering, IEEE Transactions on*, vol. 54, pp. 1499-1506, 2007.
- [24] G. S. Fischer, I. Iordachita, C. Csoma, J. Tokuda, S. P. DiMaio, C. M. Tempany, N. Hata and G. Fichtinger, "MRI-compatible pneumatic robot for transperineal prostate needle placement," *Mechatronics, IEEE/ASME Transactions on*, vol. 13, pp. 295-305, 2008.
- [25] van den Bosch, Michiel R, M. R. Moman, M. van Vulpen, J. J. Battermann, E. Duiveman, L. J. van Schelven, H. de Leeuw, J. J. Lagendijk and M. A. Moerland, "MRI-guided robotic system for transperineal prostate interventions: proof of principle," *Phys. Med. Biol.*, vol. 55, pp. N133, 2010.
- [26] S. Song, N. Cho, J. Tokuda, N. Hata, C. Tempany, G. Fichtinger and I. Iordachita, "Preliminary evaluation of an MRI-compatible modular robotic system for MRI-guided prostate interventions," in *Biomedical Robotics and Biomechatronics (BioRob), 2010 3rd IEEE RAS and EMBS International Conference on*, 2010, pp. 796-801.

- [27] S. Song, N. B. Cho, G. Fischer, N. Hata, C. Tempany, G. Fichtinger and I. Iordachita, "Development of a pneumatic robot for MRI-guided transperineal prostate biopsy and brachytherapy: New approaches," in *Robotics and Automation (ICRA), 2010 IEEE International Conference on*, 2010, pp. 2580-2585.
- [28] R. Seifabadi, S. Song, A. Krieger, N. B. Cho, J. Tokuda, G. Fichtinger and I. Iordachita, "Robotic system for MRI-guided prostate biopsy: feasibility of teleoperated needle insertion and ex vivo phantom study," *International Journal of Computer Assisted Radiology and Surgery*, vol. 7, pp. 181-190, 2012.
- [29] J. Tokuda, G. S. Fischer, C. Csoma, S. P. DiMaio, D. G. Gobbi, G. Fichtinger, C. M. Tempany and N. Hata, "Software strategy for robotic transperineal prostate therapy in closed-bore MRI," in *Medical Image Computing and Computer-Assisted Intervention—MICCAI 2008* Anonymous Springer, 2008, pp. 701-709.
- [30] D. T. Gering, A. Nabavi, R. Kikinis, N. Hata, L. J. O'Donnell, W. E. L. Grimson, F. A. Jolesz, P. M. Black and W. M. Wells, "An integrated visualization system for surgical planning and guidance using image fusion and an open MR," *Journal of Magnetic Resonance Imaging*, vol. 13, pp. 967-975, 2001.
- [31] S. P. DiMaio, E. Samset, G. Fischer, I. Iordachita, G. Fichtinger, F. Jolesz and C. Tempany, "Dynamic MRI scan plane control for passive tracking of instruments and devices," in *Medical Image Computing and Computer-Assisted Intervention—MICCAI 2007* Anonymous Springer, 2007, pp. 50-58.

- [32] J. Tokuda, G. S. Fischer, X. Papademetris, Z. Yaniv Z, L. Ibanez, P. Cheng, H. Liu, J. Blevins, J. Arata, A. J. Golby, T. Kapur, S. Pieper, E. C. Burdette, G. Fichtinger, C. M. Tempany, N. Hata, "OpenIGTLink: an open network protocol for image-guided therapy environment," *Int J Med Robot*, vol. 5(4), pp. 423-434.
- [33] J. Tokuda, K. Tuncali, I. Iordachita, S. Song, A. Fedorov, S. Ogur, A. Lasso, F. Fennessy, Y. Tang, C. M. Tempany, N. Hata, "Preliminary Accuracy Evaluation of 3T MRI-guided Transperineal Prostate Biopsy with Grid Template," in *Proc Intl Soc Mag Reson Med*, 2011, pp. 7-13.
- [34] M. G. Schouten, J. Ansems, W. K. Renema, D. Bosboom, T. W. Scheenen, J. J. Futterer, "The accuracy and safety aspects of a novel robotic needle guide manipulator to perform transrectal prostate biopsies," *Med Phys*, vol. 37(9), pp. 4744-4750, 2010.
- [35] A. Krieger, I. Iordachita, P. Guion, A. K. Singh, A. Kaushal, C. Menard, P. A. Pinto, K. Camphausen, G. Fichtinger, L. L. Whitcomb, "An MRI-compatible robotic system with hybrid tracking for MRI-guided prostate intervention," in *Biomedical Engineering, IEEE Transaction on*, vol. 58(11), pp. 3049-3060, 2011.
- [36] M. Muntene, A. Patriciu, D. Petrisor, D. Mazilu, H. Bagga, L. Kavoussi, K. Cleary, D. Stoianovici, "Magnetic resonance imaging compatible robotic system for fully automated brachytherapy seed placement," *Urology*, vol. 68(6), pp. 1313-1317, 2006.
- [37] R. Seifabadi, N. B. J. Cho, S. E. Song, J. Tokuda, N. Hata, C. M. Tempany, G. Fichtinger and I. Iordachita, "Accuracy study of a robotic system for MRI - guided prostate needle

placement," *The International Journal of Medical Robotics and Computer Assisted Surgery*, 2012.

- [38] S. A. Tincher, R. Y. Kim, M. P. Ezekiel, T. Zinsli, J. B. Fiveash, D. A. Raben, A. J. Bueschen, and D. A. Urban, "Effects of pelvic rotation and needle angle on pubic arch interference during transperineal prostate implants," *Int J Radiat Oncol Biol Phys*, vol. 47(2), pp. 361-363, 2000.
- [39] D. Stoianovici, D. Song, D. Petrisor, D. Ursu, D. Mazilu, M. Mutener, M. Schar and A. Patriciu, "'MRI Stealth" robot for prostate interventions," *Minimally Invasive Therapy & Allied Technologies*, vol. 16, pp. 241-248, 2007.
- [40] H. Elhawary, A. Zivanovic, M. Rea, Z. T. H. Tse, D. McRobbie, I. Young, M. Paley, B. Davies and M. Lampérth, "A MR compatible mechatronic system to facilitate magic angle experiments in vivo," in *Medical Image Computing and Computer-Assisted Intervention–MICCAI 2007* Anonymous Springer, 2007, pp. 604-611.
- [41] E. Taillant, J. Avila-Vilchis, C. Allegrini, I. Bricault and P. Cinquin, "CT and MR compatible light puncture robot: Architectural design and first experiments," in *Medical Image Computing and Computer-Assisted Intervention–MICCAI 2004* Anonymous Springer, 2004, pp. 145-152.
- [42] T. Suzuki, H. Liao, E. Kobayashi and I. Sakuma, "Ultrasonic motor driving method for EMI-free image in MR image-guided surgical robotic system," in *Intelligent Robots and Systems, 2007. IROS 2007. IEEE/RSJ International Conference on*, 2007, pp. 522-527.

- [43] H. Elhawary, A. Zivanovic, M. Rea, B. Davies, C. Besant, D. McRobbie, N. de Souza, I. Young and M. Lampérth, "The feasibility of MR-image guided prostate biopsy using piezoceramic motors inside or near to the magnet isocentre," in *Medical Image Computing and Computer-Assisted Intervention–MICCAI 2006* Anonymous Springer, 2006, pp. 519-526.